On focusing of shock waves

by

Veronica Eliasson

September 2007
Technical Reports from
Royal Institute of Technology
KTH Mechanics
SE-100 44 Stockholm, Sweden

Akademisk avhandling som med tillstånd av Kungliga Tekniska Högskolan i Stockholm framlägges till offentlig granskning för avläggande av teknologie doktorsexamen fredagen den 21 september 2007 kl 10.15 i sal F3, Kungliga Tekniska Högskolan, Valhallavägen 79, Stockholm.

©Veronica Eliasson 2007

Universitetsservice US–AB, Stockholm 2007

On focusing of shock waves

Veronica Eliasson
KTH Mechanics, Royal Institute of Technology (KTH)
SE-100 44 Stockholm, Sweden

Abstract

Both experimental and numerical investigations of converging shock waves have been performed. In the experiments, a shock tube was used to create and study converging shock waves of various geometrical shapes. Two methods were used to create polygonally shaped shocks. In the first method, the geometry of the outer boundary of the test section of the shock tube was varied. Four different exchangeable shapes of the outer boundary were considered: a circle, a smooth pentagon, a heptagon, and an octagon. In the second method, an initially cylindrical shock wave was perturbed by metal cylinders placed in various patterns and positions inside the test section. For three or more regularly spaced cylinders, the resulting diffracted shock fronts formed polygonal shaped patterns near the point of focus. Regular reflection was observed for the case with three cylinders and Mach refection was observed for cases with four or more cylinders. When the shock wave is close to the center of convergence, light emission is observed. An experimental investigation of the light emission was conducted and results show that the shape of the shock wave close to the center of convergence has a large influence on the amount of emitted light. It was found that a symmetrical polygonal shock front produced more light than an asymmetrical shape.

The shock wave focusing was also studied numerically using the Euler equations for a gas obeying the ideal gas law with constant specific heats. Two problems were analyzed; an axisymmetric model of the shock tube used in the experiments and a cylindrical shock wave diffracted by cylinders in a two dimensional test section. The results showed good agreement with the experiments. The temperature field from the numerical simulations was investigated and shows that the triple points behind the shock front are hot spots that increase the temperature at the center as they arrive there.

As a practical example of shock wave focusing, converging shocks in an electrohydraulic lithotripter were simulated. The maximum radius of a gas bubble subjected to the pressure field obtained from the lithotripter was calculated and compared for various geometrical shapes and materials of the reflector. Results showed that the shape had a large impact while the material did not influence the maximum radius of the gas bubble.

Descriptors: converging shock, Euler equations, imploding shock, Mach reflection, regular reflection, shock focusing, shock tube

Preface

This doctoral thesis in fluid mechanics is a paper-based thesis of both experimental and numerical character. The thesis is divided into two parts in where the first part, starting with an introductory essay, is an overview and summary of the present contribution to the field of shock wave focusing. The second part consists of six papers. In chapter 9 of the first part in the thesis the respondent's contribution to all papers are stated.

September 2007, Stockholm
Veronica Eliasson

Nothing shocks me. I'm a scientist.

Indiana Jones (1984)

Contents

Part I

Overview and summary

CHAPTER 1

Introduction

The title of this thesis is 'On shock wave focusing' and this may cause you to ask yourself *what is a shock wave?*, *where do they occur?* and *what is meant by shock wave focusing?*

A shock wave is a thin discontinuous region in which quantities like pressure, temperature, and velocity make an abrupt "jump" from one state in front of the shock to another state behind the shock. Think of the difference in the two states as the difference in a stretch of a highway with free flow, compared to the same stretch when it is jammed up with cars, not moving at all. A shock wave propagates faster than the local speed of sound. Consider a fluid particle in a flow where a shock wave would pass, it would not know it before the shock arrives, because no information (except the shock itself) propagates faster than the local speed of sound. Further, shock waves are dissipative, which means that the entropy increases as the shock travels and its strength is reduced.

Shock waves are encountered many times during a normal day. Let us assume you wake up in the morning and go to the bathroom to brush your teeth. You turn on the water, and as it flows out and hits the sink, you see a roughly circular region with a very thin water layer centered around the streaming water. Further out from the center, the depth of this thin layer abruptly increases. This "jump" is an example of a shock wave. Later, you might drive your car to work. When the traffic flow is interrupted, say by red lights or traffic jams during rush hour, the vehicles slow down to a stop. You brake as soon as the car in front of you brakes and then the car after you brakes; car after car behind you brakes to a stop. This "braking motion" that propagates behind you, against the direction of the traffic, can be viewed as a shock wave. Later, the same evening, you find yourself in the middle of a thunderstorm. Lightning streaks across the sky, followed by a loud crack and low rumblings. The noise is caused by a shock wave. The lightning produces extremely hot air which expands into the cool surrounding air faster than the speed of sound. The shock wave expands radially for about 10 m and then becomes an ordinary sound wave called thunder.

Perhaps you played outdoors with a magnifying glass when you were a child. By focusing the rays of the sun onto a piece of paper with the magnifying glass, the paper starts to smoke, then turn brown and maybe even catch fire.

In our work we use the same idea, but instead of the sun, we use a shock wave and the magnifying glass is replaced by a shock tube.

In addition to the aforementioned examples, shock waves occur in many more situations, ranging from tiny bubble implosions to supernova explosions. Shock waves have been the source of many accomplishments, from the medical treatment of shock wave lithotripsy (i.e. breaking of kidney stones) to the devastating consequences caused by explosions.

This thesis is a result of both experimental and numerical studies of converging shock waves. The first part of the thesis is organized as follows: the basic preliminaries for shock wave focusing are discussed in chapter 2. A review of earlier work on shock wave focusing, both experimental and numerical, is given in chapter 3. The experimental setup used in the present study is explained in chapter 4 followed by a summary of the experimental results in chapter 5. The numerical simulations are discussed and the results are presented in chapter 6. Chapter 7 contains simulations on weak shock wave focusing in shock wave lithotripsy. Finally, conclusions of the present work and an outlook of the future is presented in chapter 8. The contribution of the author to the papers in section 2 of this thesis is stated in chapter 9.

FIGURE 1.1. Left: a traffic jam, photograph © Miha Skulj. Upper right: lightning during a thunderstorm, photograph © Anna Tunska. Lower right: flowing water in a sink.

CHAPTER 2

Basic concepts

2.1. Governing equations

The analysis of compressible flow is based on three fundamental equations, as discussed in Anderson (1990). They are the continuity equation, the momentum equation and the energy equation, presented here in integral form:

$$\iiint_{\mathcal{V}} \frac{\partial}{\partial t}\rho \mathrm{d}\mathcal{V} + \iint_{S} \rho \mathbf{V}\cdot \mathrm{d}\mathbf{S} = 0, \tag{2.1}$$

$$\iiint_{\mathcal{V}} \frac{\partial}{\partial t}\Big[\rho \mathbf{V}\Big]\mathrm{d}\mathcal{V} + \iint_{S} (\rho \mathbf{V}\cdot \mathrm{d}\mathbf{S})\mathbf{V} = \iiint_{V} \rho \mathbf{f}\mathrm{d}\mathcal{V} - \iint_{S} p\mathrm{d}\mathbf{S}, \tag{2.2}$$

$$\begin{aligned} &\iiint_{\mathcal{V}} \frac{\partial}{\partial t}\Big[\rho\Big(e+\frac{V^2}{2}\Big)\Big]\mathrm{d}\mathcal{V} + \iint_{S} \rho\Big(e+\frac{V^2}{2}\Big)\mathbf{V}\cdot \mathrm{d}\mathbf{S} \\ &= \iiint_{\mathcal{V}} \dot{q}\rho \mathrm{d}\mathcal{V} - \iint_{S} p\mathbf{V}\cdot \mathrm{d}\mathbf{S} + \iiint_{\mathcal{V}} \rho(\mathbf{f}\cdot \mathbf{V})\mathrm{d}\mathcal{V}. \end{aligned} \tag{2.3}$$

Here $\mathcal{V}$ is a fixed volume, $\mathbf{V}$ is the velocity vector $\mathbf{V} = (u, v, w)$ in the x, y and z directions, ρ is the density, S is the surface area of the volume $\mathcal{V}$, p is the pressure acting on the surface S, $\dot{q}$ is the heat rate added per unit mass, f represents the body forces per unit mass and e is the internal energy. The system of equations, (2.1)–(2.3), is closed with an equation of state. One of the simplest equations of state is the ideal gas law, which is valid for moderate temperatures and low pressures. It is given by

$$p = \rho RT, \tag{2.4}$$

where R is the specific gas constant and T is the temperature in kelvin. There exist a number of more intricate equations of state that model more complex situations, such as low temperature or high pressure flows where the intramolecular forces become important and cannot be neglected.

Because a shock wave has a width of only a few mean free paths, it can be described as a discontinuity. A shock wave is an irreversible process, and by the second law of thermodynamics, the entropy increases across the discontinuity.

This cannot be seen from equations (2.1)–(2.4), so an entropy relation must be added, as in Courant & Friedrichs (1948) or Zel'dovich & Raizer (1966).

2.2. Shock tube theory

Shock tubes are experimental devices used to study shock waves as well as thermodynamic and chemical properties. Usually, a shock tube consists of a long tube closed at both ends and separated into two parts by a thin membrane; see Figure 2.1. The two parts are the high pressure part, called the driver section, and the low pressure part, called the driven section. The pressure in the low pressure part, p_1, is usually lower than the atmospheric pressure, often on the order of a few kPa. The high pressure part, contains the highest possible pressure, p_4, usually on the order of MPa.

To produce a shock wave, the driven section is evacuated from gas to a given pressure. Then the driver section is filled with gas. At a given pressure difference between the two sections, the membrane rapidly breaks, and the compressed gas in the high pressure part flows into the low pressure part. A shock wave travels forward through the low pressure part and a rarefaction wave, starting at the broken membrane, travels backwards through the high pressure part.

The flow conditions in the shock tube are shown in Figure 2.1. The subscripts in the figure indicate various regions: '1' represents the undisturbed low pressure gas, '2' is the region just behind the shock, and '3' is the gas from the high pressure part which has passed through the rarefaction wave. Region '4' indicates the high pressure gas not disturbed by the rarefaction wave and '5' is the region behind the reflected shock.

Just before the membrane breaks, the pressure difference reaches its maximum value; see Figure 2.1 (a). When the membrane breaks, a shock wave travels downstream in the low pressure part and a rarefaction wave travels upstream in the high pressure part. The pressure and temperature distributions are shown in Figure. 2.1 (b)–(c). Next, the shock wave reflects from the rear (provided it is a closed shock tube) and returns. The reflected shock produces a very high pressure and temperature behind it; see Figure 2.1 (d)–(e). The dotted line, visible in Figure 2.1 (b)–(e), represents the contact surface between the high and low pressure gas. Across the contact surface there is no flow of gas, and the pressure and velocity are continuous.

The shock Mach number, M_s, depends on the pressure ratio between the high and low pressure part, p_4/p_1, the choice of gas used in the different parts of the tube, and the respective temperatures of the gases. The relation between the pressures p_1 and p_4 can be derived from equations (2.1) – (2.3) and is given by equation (2.5). A derivation can be found in Liepmann & Roshko (1957).

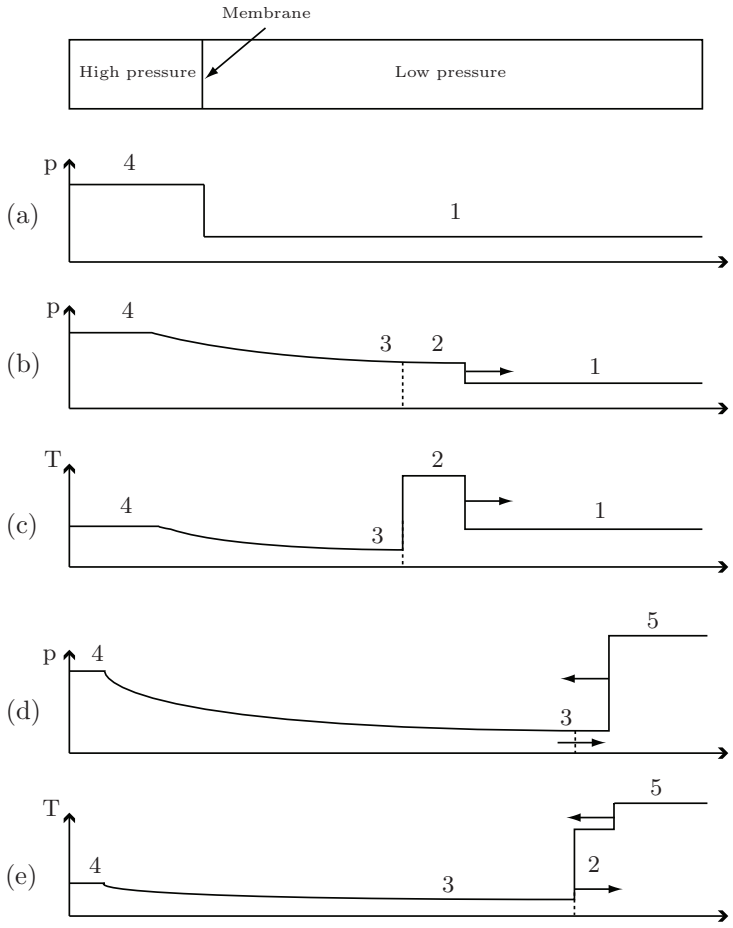

FIGURE 2.1. Conditions in a shock tube; on top is the high and low pressure parts, separated by a membrane. (a) is the initial pressure distribution. (b) and (c) show the pressure and temperature distribution respectively after the membrane has broken and the shock has started to travel down stream in the low pressure part. (d) and (e) show the pressure and temperature distribution just after the shock has reflected from the rear wall.

$$\frac{p_4}{p_1} = \frac{2\gamma_1 M_s^2 - (\gamma_1 - 1)}{\gamma_1 + 1}\left[1 - \frac{\gamma_4 - 1}{\gamma_1 + 1}\frac{a_1}{a_4}\left(M_s - \frac{1}{M_s}\right)\right]^{-\frac{2\gamma_4}{\gamma_4 - 1}} \tag{2.5}$$

Here $\gamma = c_p/c_v$ is the ratio between the specific heats for constant pressure and constant volume respectively, and a is the speed of sound. The subscripts denote the region in which the property is valid. Different methods can be used to create stronger shocks in a shock tube, such as heating the gas in the high pressure section, increasing the pressure difference between the high and low pressure part, and choosing a light gas in the low pressure part (so when the membrane bursts, the high pressure gas flows into a state close to vacuum).

Because a shock induces flow, meaning that the gas behind the shock propagates in the direction of the shock, shock tubes can sometimes be used as wind tunnels to look at aerodynamic aspects of high enthalpy flow. Using the shock tube as a wind tunnel has an advantage; it is relatively easy to create high pressures and high temperature flows that can be studied. A limitation is that the test time is short, on the order of micro seconds, because the test is run during the time when the shock has passed until either the contact surface or the reflected wave arrives.

For a more detailed explanation of shock tubes and the conditions during operation see Anderson (1990).

2.3. Shock reflection

When a shock wave interacts with a solid surface or another shock, there are several possible types of shock reflections that can occur. They can be divided into two groups: *regular reflection* and *Mach reflection*. A regular reflection consists of an incoming shock, i, and a reflected shock, r, and is the simplest configuration possible; see Figure 2.2 (a). For large angles between the flow and the solid surface, a single shock cannot turn the flow to a direction parallel to the wedge, so a three shock system is necessary. This is called a Mach reflection; see Figure 2.2 (b). A three shock system consists of an incoming shock and a reflected shock connected to a Mach shock, m, in a point called a triple point. Between the Mach shock and the reflected shock there is a slip line, denoted s in Figure 2.2 (b). The velocity of the gas on different sides of the slip line is in the same direction but not necessarily of the same magnitude. The flow deflection angle, θ, and the Mach number, M, behind an oblique shock are functions of the free stream Mach number, M_∞, the gas constant, γ, and the shock angle, α, and are given by

$$\theta(M_\infty, \gamma, \alpha) = \cot^{-1}\left[\left(\frac{(\gamma+1)M_\infty^2}{2(M_\infty^2 \sin^2\alpha - 1)} - 1\right)\tan\alpha\right], \tag{2.6}$$

and

$$M(M_\infty, \gamma, \alpha) = \sqrt{\frac{(\gamma+1)^2 M_\infty^4 \sin^2\alpha - 4(M_\infty^2 \sin^2\alpha - 1)(\gamma M_\infty^2 \sin^2\alpha + 1)}{[2\gamma M_\infty^2 \sin^2\alpha - (\gamma-1)][(\gamma-1)M_\infty^2 \sin^2\alpha + 2]}}. \tag{2.7}$$

These equations can be found in NACA Report 1135 (1953).

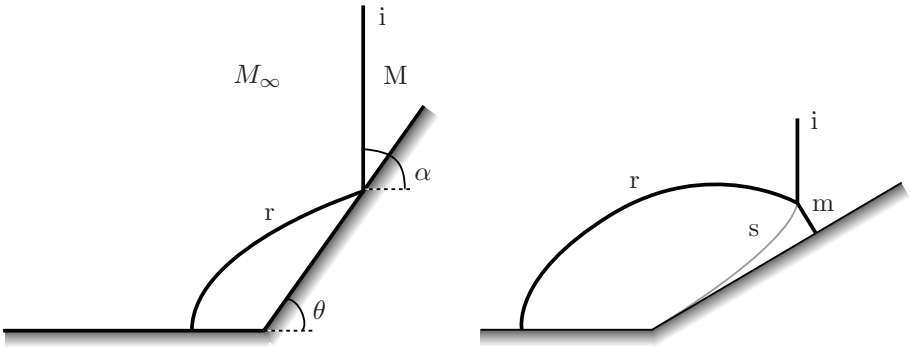

FIGURE 2.2. Shock reflection for a pseudo steady shock. (a) Regular reflection and (b) Mach reflection. M_∞: free stream Mach number, M: Mach number after shock, i: incident shock, r: reflected shock, s: slip stream, m: Mach shock, θ: wedge angle, α: shock angle.

The type of reflection that occurs is dependent on M_∞, γ, and θ. It is possible to determine the regions where the various types of reflections occur by computing lower and upper boundaries for these. The lower boundary, i.e. the minimum shock angle for a flow with a free stream Mach number M_∞, is given by the Mach wave angle, α_{MW}:

$$\alpha_{MW} = \arcsin(1/M_\infty). \tag{2.8}$$

If the incident shock is strong, (the flow behind the incident shock is subsonic), it is not possible for a reflected shock to exist and there cannot be any shock reflection. This is the criterion for the upper boundary of the reflection domain. The boundary is defined by a subsonic flow behind the incident shock and α is obtained by solving equation (2.7) with the right hand side equal to one. The solution is called the sonic incident criterion and is given by

$$\alpha_S = \arcsin\sqrt{\frac{\gamma - 3 + M_\infty^2(\gamma+1) + \sqrt{(\gamma+1)[(M_\infty^2-3)^2 + \gamma(M_\infty^2+1)^2]}}{4\gamma M_\infty^2}}. \tag{2.9}$$

The upper boundary for regular reflections is defined as the maximum angle such that the flow turning angle of the reflected shock equals the flow turning angle of the incident shock. This criterion is called the detachment criterion and is found by computing the maximum angle $\alpha^{\theta_{\max}}$ from equation (2.6) and then solving

$$\theta(M_\infty, \gamma, \alpha) = \theta(M_{1D}, \gamma, \alpha^{\theta_{\max}}(M_{1D}, \gamma)). \tag{2.10}$$

The solution to equation (2.10) is a fifth-degree polynomial in terms of $\sin^2\alpha$:

$$D_0 + D_1 \sin^2\alpha + D_2 \sin^4\alpha + D_3 \sin^6\alpha + D_4 \sin^8\alpha + D_5 \sin^{10}\alpha = 0, \quad (2.11)$$

where coefficients D_0–D_5 are given by

$$\begin{aligned}
D_0 &= -16, \\
D_1 &= 32M^2 - 4M^4 - 48M^2\gamma - 16M^4\gamma + 16\gamma^2 - \\
&\quad 16M^4\gamma^2 + 16M^2\gamma^3 + 4M^4\gamma^4, \\
D_2 &= -16M^4 + 4M^6 - M^8 + 104M^4\gamma + 16M^6\gamma - \\
&\quad 4M^8\gamma - 64M^2\gamma^2 - 32M^4\gamma^2 + 8M^6\gamma^2 - 6M^8\gamma^2 - \\
&\quad 56M^4\gamma^3 - 16M^6\gamma^3 - 4M^8\gamma^3 - 12M^6\gamma^4 - M^8\gamma^4, \\
D_3 &= M^8 - 64M^6\gamma + 4M^8\gamma + 96M^4\gamma^2 + 64M^6\gamma^2 + \\
&\quad 14M^8\gamma^2 + 64M^6\gamma^3 + 20M^8\gamma^3 + 9M^8\gamma^4, \\
D_4 &= 8M^8\gamma - 64M^6\gamma^2 - 32M^8\gamma^2 - 24M^8\gamma^3, \\
D_5 &= 16M^8\gamma^2.
\end{aligned}$$

Only one root of equation (2.11) is real and bounded and gives the detachment criterion. The shock reflection domain is usually plotted for parameters (M, α) and is shown in Figure 2.3. Here, only the upper and lower boundaries for the reflection are plotted, along with the detachment criterion, above which no regular reflection can occur. However, Mach reflection can occur below the detachment criterion. As mentioned earlier, there are several possible shock reflection configurations, such as regular reflection with subsonic or supersonic downstream flow, Mach reflection with subsonic or supersonic flow downstream of the reflected shock, Mach reflection with a forward reflected shock, inverted Mach reflection and von Neumann reflection. Detailed descriptions of these configurations can be found in Mouton (2006) or Hornung (1986).

Several criteria for transition from a regular reflection (RR) to a Mach reflection (MR) exist. Three of these were proposed in von Neumann (1943) and since then many more have been suggested; see Ben-Dor (1992, 2006). The length scale concept was introduced in Hornung *et al.* (1979) and is the criterion that agrees best with pseudo steady flow in experimental shock tube facilities. The ongoing research on transition conditions for RR↔MR is motivated by difficulties in matching theoretical and experimental results. One problem is the persistence of regular reflections well past the theoretical maximum limit and many publications address this problem; see Barbosa & Skews (2002).

2.4. Definition of stable converging shock waves

It is well known that a converging cylindrical shock wave is easily perturbed from its original shape if there are any disturbances present in the flow. However, there is a certain measure of stability in these shock waves, because they do not break up into several individual pieces. Instead, the regions with higher

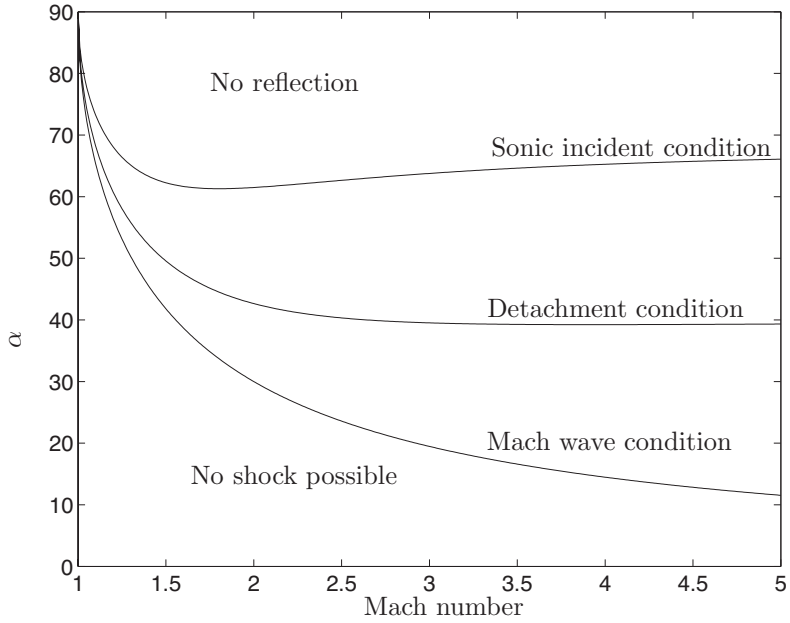

FIGURE 2.3. Shock reflection domain for γ=1.4. Above the sonic incident condition, no reflection is possible. Regular reflection is only possible in the region between the Mach wave and the detachment condition.

curvature travel faster than the planar parts, and the shock evolves into another shape. Several measures of stability were proposed by Fong & Ahlborn (1979):

(i) radial stability: $\Delta r/R$, the perturbation radius normalized by the instantaneous radius of the converging shock,
(ii) area (or volume) stability: $\Delta A/A$, perturbation area (or volume) normalized by the instantaneous area $A = \pi R^2$ (or volume $V = 4\pi R^3/4$),
(iii) form stability: where the angle, δ, between the wave normal and the radius is measured.

The measure of stability is divided into two categories: *absolute stability*, in which case $\Delta r/R$, $\Delta A/A$, and δ tend to zero before the shock wave has focused and *partial stability*, where the parameters converge to a value much less than unity.

A polygonal converging shock wave is always assumed to be stable. If a polygonal shock wave undergoes regular reflection, then its shape will be

preserved and will not change during the focusing process. Alternatively, it may undergo Mach reflection, thus changing its shape continuously as it focuses, but in a completely predictable way.

2.5. The schlieren technique

Schlieren techniques are often used when visualizing density gradients, e.g. in shock waves. The methods are rarely used for quantitative measurements of density gradients but are very useful for the qualitative understanding of the flow.

Optical methods for inhomogeneous media have been used for a long time. In the early 1670's Robert Hooke (1635-1703) demonstrated a simple version of what is known today as the shadowgraph method to observe the convective plume of a candle for several members of the Royal Society. Christiaan Huygens (1629-1695) invented a version of the schlieren technique to look for striae in glass blanks prior to making lenses from them. Jean Paul Marat (1743-1793) published the first shadowgram of thermal plumes from hot objects. Marat did not connect the thermal plumes with density gradients of a fluid; he interpreted it as a proof of an "igneous fluid". The invention of the schlieren imaging technique is usually attributed to August Toepler (1836-1912), who named the technique after the german word for optical inhomogenities in glass: 'Schlieren'[1]. He used a light source, a knife edge, and a telescope, not too different from today's most common schlieren setups. Ernst Mach (1838-1916) confirmed in 1877, by using schlieren optics, that non-linear waves of finite strength could travel faster than the speed of sound, as earlier predicted by Riemann (1860). Since then, many gas dynamics phenomena have been visualized by the schlieren image technique. For a historical outlook and a detailed description of the schlieren optics method, see Settles (2001).

The speed of light, c, and the refraction index, n, will vary with the density, ρ, of the medium in which it is passing through. This means that light passing through a region of compressible flow is diffracted due to the density changes in the gas. The refraction index, n, can be written as a function of the density, ρ,

$$n \equiv \frac{c}{c_0} = 1 + \beta \frac{\rho}{\rho_n}. \tag{2.12}$$

Here β is a dimensionless constant, c_0 is the speed of light in vacuum, and ρ_n is the density at the standard state. The idea of the schlieren method is to cut off part of the deflected light before it reaches the registry device and thus produce darker (or brighter) regions on the photograph. If the density change takes place over a distance which is less than the wave length of the light then the optical method is sufficiently accurate.

[1] 'Schlieren' is the plural form of 'Schliere' and is capitalized in German but not in English.

A schematic diagram of the schlieren method is shown in Figure (2.4). A light source is placed at *(A)* and the light becomes parallel after passing the lens L_1. After passing the test section, the light is focused by the second lens L_2. The focal plane of L_2 is where the image of the light source appears, *(A')*. A schlieren edge is placed at *(A')* to cut off parts of the light. Depending on how the light is intercepted, it will appear darker or brighter at the image plane of the test section. It is important to notice that the *point* where the light hits the focal plane of the test section does not change, it is just the *amount of light* that changes.

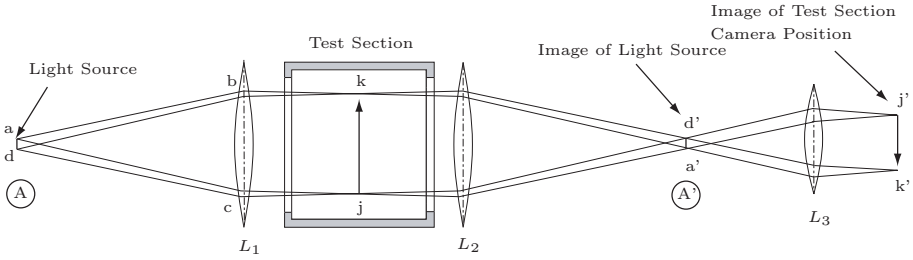

FIGURE 2.4. Schematic diagram of a schlieren system.

Depending on how the schlieren edge is shaped, the inhomogeneous media under consideration will appear in various ways. The most commonly used schlieren edge is a straight edge, which shows the density gradient in the flow normal to the edge. Usually, a knife edge is placed normal or parallel to the flow direction. It is possible to change the schlieren edge into other shapes to enhance various properties. For example, a dark-field edge produces bright higher-order features against a dark background. The dark-field filter can be set up by a spherical schlieren edge, e.g. a pin-head. The quality and the properties of the light source are also of importance for the quality of the final schlieren photograph. Usually, incandescent lamps, flash lamps, or lasers are used as light sources; see Vasil'ev (1971) and Settles (2001). Lasers are expensive tools and not necessarily better for schlieren imaging. The typical schlieren concept deals with a light source composed of individual rays that do not interact with any other rays. This is not true for a laser because it produces a parallel, monochromatic, and coherent light. A common problem is that schlieren systems with coherent laser light sources become schlieren-interferometers. This problem is further discussed and solutions are suggested by Oppenheim *et al.* (1966).

In the present study, we use schlieren optics to study shock waves in a gas. However, there are many other applications for schlieren optics, even for phenomena in liquids. This technique can be used to study everything from air flows in model green houses (see Settles (2000)) to supersonic jets.

CHAPTER 3

Review of earlier work on shock wave focusing

3.1. Previous work on shock wave focusing

Guderley (1942) was first to analytically investigate the convergence of cylindrical and spherical shock waves. Guderley derived a self similar solution for the radius of the converging shock wave as a function of time, which can be written as

$$\frac{R}{R_c} = \left(1 - \frac{t}{t_c}\right)^{\alpha}. \tag{3.1}$$

Here R is the radius of the converging shock wave, R_c is the radius of the outer edge of the test section, t is the time, and t_c is the time when the shock wave arrives at the center of convergence. Guderley found the self similar power law exponent for cylindrical shock waves to be $\alpha = 0.834$. Since then, many more investigations of the self similar exponent have been performed, and some of the results are summarized in Table 1.

	Self similar exponent
Guderley (1942)	0.834
Butler (1954)	0.835217
Stanyukovich (1960)	0.834
Welsh (1967)	0.835323
Mishkin & Fujimoto (1978)	0.828
Nakamura (1983)	0.8342, $M_s = 4.0$
	0.8345, $M_s = 10.0$
de Neef & Nechtman* (1978)	0.835±0.003
Kleine* (1985)	0.832 + 0.028, -0.043
Takayama* (1986)	0.831 ±0.002

TABLE 1. Self similarity exponents for converging cylindrical shock waves. *Experiments.

The first experimental study on shock wave focusing was done by Perry & Kantrowitz (1951). They used a horizontal shock tube with a tear-drop inset in the test section to create cylindrical shocks. They studied converging and

reflecting shocks, visualized by the schlieren technique, at two different shock Mach numbers (1.4 and 1.8). They found that creating perfect cylindrical shocks was more difficult for higher Mach numbers because the shock strength was increased. Perry & Kantrowitz suggested that this could be explained by irregular membrane opening times and bad membrane material. Also, a cylindrical obstacle was placed in the flow, and the result showed that the center of convergence was displaced toward the disturbed side of the shock wave. Another interesting observation was the presence of light in the center of the test section during the focusing process. This was interpreted to be an indicator of the presence of high temperatures, as the light was believed to be caused by ionized gas.

Sturtevant & Kulkarny (1976) performed experiments on plane shock waves which focused in a parabolic reflector mounted at the end of a shock tube. Different shapes of parabolic reflectors were used. Results showed that weak shock waves focused with crossed and looped fronts while strong shocks did not. It was concluded that the shock strength governed the behavior during the focusing process and that nonlinear phenomena were important near the focal point.

Plane shocks diffracted by cones, a cylinder and a sphere were experimentally investigated by Bryson & Gross (1961). A plane shock with a Mach number of 2.82 was diffracted by a cylinder with a diameter of 1.27 cm. The diffraction was followed through about seven diameter downstream of the cylinder and was visualized by a schlieren optics system. Results showed that when the shock wave impinged upon the cylinder, at first a regular reflection occurred. Between 40° and 50° from the forward stagnation point on the cylinder, Mach reflection begins. As the Mach shocks collide behind the cylinder, a second Mach reflection is created. The experimental results were compared to Whitham's theory, Whitham (1957, 1958, 1959) and showed good agreement.

3.1.1. *Design of annular shock tubes*

In annular shock tubes used to produce and study converging shock waves, the shock must turn through a 90° bend in order to reach the test section and begin the convergence process. A simplified sketch of the annular part of a shock tube is shown in Figure 3.1. Arrows indicate the direction of the flow, the 90° bend is indicated by a circle and the test section is indicated by an oval. The design of the 90° bend has a big influence on the resulting flow after the shock passes it. The reflection and diffraction around 90° bends were investigated experimentally by Takayama (1978). To find an optimal shape for the bend, six different bends were tested, from sharp to smooth corners. Shock Mach numbers ranged from 1.1 – 6.0. Results for the sharp bend showed that the transmitted shock did not stabilize before it reached the end of the exit duct. The exit was located at X/L=8.0, where X was the distance along the duct and L was the height of the shock tube. Also, the flow

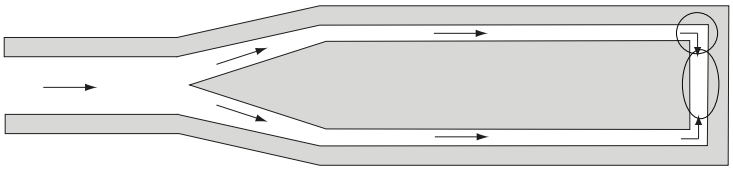

FIGURE 3.1. A simplified sketch of an annular shock tube. The 90° bend is indicated by a circle and the test section is indicated by an oval.

behind the shock never became uniform. Takayama stated that a sharp bend "may be useless to obtain stable shock transmission." A radius of curvature larger than $(R_o + R_i)/2L$, where R_o and R_i are the outer and inner radius of curvature of the walls, was enough for stable shock transmission. Converging-diverging bends with smooth walls were also investigated and results showed that they produced stable transmitted shocks. The best performance for a converging-diverging bend was obtained for $R_o = 120$ mm and $R_i = 20$ mm. Another design consisting of several contraction corners was studied by Wu *et al.* (1980). Each contraction made sure that the Mach became an incident shock in the succeeding element. With this design, the flow separation and the strong pressure gradients behind the transmitted shock can be avoided. The method used by Wu *et al.* was found to be useful even if the Mach reflection was a double Mach reflection; see Ben-Dor (1981).

Smooth 90° bends were investigated both experimentally and theoretically by Edwards *et al.* (1983). They used two bends (rectangular cross-section, 22x47.4 mm) with different radii of curvature, 75 mm and 150 mm. Incident planar shocks with Mach numbers in the range of $1.2 < M_s < 2.8$ were investigated. A multi-spark light source together with a schlieren optics system enabled five recordings of the shock position during each run. Hence, it was possible to obtain the velocity of the shock at four times in the bend. As the shock entered the bend, it suffered Mach reflection at the outer wall, and the recovery time to a planar profile was faster for the shape with larger radius of curvature. The velocity of the shock at both the inner and the outer walls was influenced by the sharpness of the bend. The maximum velocity at the outer wall and the minimum velocity at the inner wall were both obtained for the sharper of the two bends. The results were compared to Whitham's ray theory and showed adequate agreement of both the enhancement of the shock at the outer wall and the attenuation at the inner wall.

3.1.2. *Stability of cylindrical shocks*

An annular shock tube was used by Wu *et al.* (1981) to investigate the stability of converging cylindrical shocks. Wu *et al.* perturbed the converging shock with two kinds of artificial disturbances. The first disturbance consisted of

four rectangular webs upstream of the cylindrical test section. Results showed that a smooth square-shaped shock was formed, which later transformed into a sharp rectangular shape. As the shock expanded, vortex pairs were observed behind the shock front, and this was taken as a sign of the instability of the converging shock. The second type of artificial disturbance utilized a cylindrical rod with a diameter of 4.4 mm placed inside the test section at a radial distance of 2.54 cm from the center. As the shock wave was diffracted by the cylindrical rod, two pairs of Mach shocks and a reflected shock were generated. The shape of the cylindrical shock was perturbed, and it did not regain its symmetry during the focusing process. However, there was no observable shift in the focal point of the converging shock as compared to the case without artificial disturbances.

Both strong and weak converging shocks were investigated experimentally and theoretically by Neemeh & Ahmad (1986). An annular shock tube with a diameter of 152 mm was used to produce converging cylindrical shocks. Perturbations were produced by cylindrical rods of various diameters placed in the path of the converging shock. The results showed that for a strong shock perturbed by a cylinder, the focal region of the collapse shifted toward the rod because the undisturbed part of the shock front traveled faster than the disturbed part. On the contrary, for a weak shock, the focal region was located outside the geometrical center because the disturbed part traveled faster than the undisturbed part. For both cases, the size of the focal region was dependent on the rod diameter. Neemeh & Ahmad defined a perturbation factor for initially strong cylindrical shocks, $\epsilon = \Delta R/R_S$, where ΔR is the distance by which the perturbed part of the shock front is displaced from its undisturbed position and R_S is the instantaneous radius of the cylindrical shock wave. The perturbation factor was measured for the experimental results and then a mathematical equation was fitted to those results:

$$\epsilon = [F(\xi)](\frac{R_S}{R_0})^{-G(\xi)}. \tag{3.2}$$

Here $\xi = d/R_0$, where d is the diameter of the cylindrical rod, R_0 is the radius at which the rod is placed, and the functions F and G are given by

$$F(\xi) = 0.182(\xi) - 24.59(\xi)^2 + 349.19(\xi)^3 - 118.6(\xi)^4, \tag{3.3}$$

$$G(\xi) = 0.67 + 3.22(\xi) - 38.7(\xi)^2 + 121.4(\xi)^3. \tag{3.4}$$

Takayama *et al.* (1984) used a horizontal annular shock tube to produce converging shock waves with initial shock Mach numbers in the range of 1.10 – 2.10. The supports for the inner tube consisted of cylindrical rods with a diameter of 12 mm and the area contraction due to the supports was less than 7%. A double exposure holographic interferometer was used to visualize the converging shock wave and the flow behind it. Close to the center of convergence, the initially cylindrical shock wave became square-shaped. This

was referred to as a mode-four instability. No relation was found between the position of the four supports for the inner tube of the annular shock tube section and the square shaped shock. Artificial disturbances in the form of 12 cylindrical rods were introduced just after the 90° corner. Close to the focal point, a square-shaped shock was again observed, and the authors concluded that an instability of mode four existed near the center. The diverging shock resumed a stable cylindrical shape.

Takayama *et al.* (1987) used two different horizontal annular shock tubes to investigate the stability and behavior of converging cylindrical shock waves. One shock tube was located in the Stoßwellenlabor, RWTH Aachen, and one in the Institute for High Speed Mechanics, Tohoku University in Sendai. One of the goals was to find out if a stable converging cylindrical shock wave could be produced. The results showed that the shape of the shock wave was very sensitive to disturbances in the flow. Both shock tubes were equipped with supports for the inner body, and these supports caused disturbances that changed the shape of the shock wave. The Aachen shock tube had three supports, near the center of convergence, the shock wave was always triangular, showing a mode-three instability. The Sendai tube had two sets of four supports. Although the area contraction from these supports was rather small, the converging shock showed a mode-four instability as a result of their presence. To investigate the effect of disturbances, cylindrical rods were introduced upstream of the test section in the Sendai shock tube. It was found that the shock wave was significantly affected by these rods during the first part of the converging process. Later, as the shock wave reached the center of convergence, the mode-four instability was again observed. Takayama *et al.* concluded that the disturbances caused by the supports could not be suppressed by the cylindrical rods. Also, the instability, i.e. the deviation from a cylindrical shape, was found to be more significant for stronger shocks.

To minimize disturbances in the flow, a vertical shock tube with an unsupported inner body was used by Watanabe *et al.* (1995). Special care was taken to minimize possible disturbances in the shock tube to enable production of perfect cylindrical converging shock waves. The results showed that the cylindrical shock waves tended to be more uniform than in horizontal shock tubes with supports. Still, when the shock wave reached the center of convergence, it was not perfectly cylindrical. This was believed to be caused by small changes of the area in the co-axial channel between the inner and outer body of the shock tube. To study the influence of artificial disturbances, a number of cylindrical rods were introduced in the flow. Different numbers of rods were used, and Watanabe *et al.* concluded that when there was a combination of modes, the lowest mode was strongest and suppressed the other ones.

3.1.2a. *Numerical simulations.* A numerical study of initially weak cylindrical converging shock waves was done by Book & Löhner (1990). The authors

simulated the experiments of Takayama *et al.* (1987) and tried to verify that a mode-four instability was present in the simulations as well. A finite element scheme with triangular grid cells and adaptive mesh refinement was used for the simulations. Results showed that weak shocks with an initial Mach number of 1.1 became square-shaped close to the focal point, while shocks with an initial Mach number of 2.1 only vaguely became square-shaped. The authors explained that this was caused by a mode-four instability growing faster than other modes. It should be noted that the square is aligned with the principal directions in the grid, and it should not be ruled out that the shape is due to discrete effects.

A numerical study by Demmig & Hehmsoth (1990) also compared results to experiments by Takayama *et al.* (1984, 1987). The initial conditions of the numerical simulations were taken from the experiments. The initial shape of the shock front was not circular, but was given a mode-four deformation to match the experimental results. As the shock reflected, the shock front approached a circular shape. The simulation agreed well with the experimental results. Also, converging shock waves with higher Mach numbers were studied and electron density profiles were computed. Results showed that ionization took place behind the incident shock close to the focal point and that it increased after the reflected shock had passed.

3.1.3. *Polygonal shock waves*

Schwendeman & Whitham (1987) used the approximate theory of geometrical shock dynamics by Whitham (1957) to study the behavior of converging cylindrical shocks. They showed that a regular polygon undergoing Mach reflection will keep reconfiguring with successive intervals, i.e. transforming from an n-corner polygon to a $2n$-corner polygon and then back again. Further, Schwendeman & Whitham showed that the shock Mach number for polygonal converging shock waves, subjected to Mach reflection, will increase exactly as that for a circular converging shock. They also showed that perturbed polygonal shock waves with smooth corners (without plane sides), first form plane sides and sharp corners. Then the shock wave oscillates between the two configurations until it reaches the center of convergence and starts to reflect. This behavior was later confirmed by Apazidis & Lesser (1996) and Apazidis *et al.* (2002) for a smooth pentagonal converging shock wave in both experiments and in numerical simulations. The experiments were performed in a two dimensional chamber with a smooth pentagonal shape. A diverging shock wave was produced in the center of the chamber by an exploding device, either an exploding wire or an igniting spark. The diverging shock propagated outward until it was reflected off the walls of the chamber and then started to converge. It was observed that the shock wave assumed the same shape as the smooth pentagonal shape of the boundary where the reflection occurred. The curved sides became planar, but the transforming process (five corners to ten corners

and back again etc.) was not observed due to disturbances at the center of the chamber caused by the initial explosion that created the shock. A detailed explanation and the results obtained in this study are given in Johansson (2000).

The focusing and reflection behavior of initially regular polygon-shaped shocks were investigated by Aki & Higashino (1990). A finite difference scheme was used to solve the two dimensional compressible Euler equations. The gas was assumed to be ideal and inviscid. The initial Mach numbers were constant along the sides of the polygon, and they ranged from 1.4 to 2.1 in a series of various tests. An equilateral triangle regular reflection was observed and the shape of the triangle was preserved during the focusing process. For polygons with more than three sides, Mach reflection and thus a reconfiguration process was observed. All of the regular polygons tested in that study focused at the geometrical center of the initial polygonal shock. As the shock started to reflect, the shock front became rounded and straight sides were not observed anymore.

A self similar solution for the focusing process of two dimensional equilateral triangular shock waves was investigated in Betelu & Aronson (2001). This solution shows that the corners of the triangular shock wave undergo regular reflections and preserve the triangular shape during the whole focusing process for certain values of Mach numbers and initial conditions. The energy density is bounded for this solution, which means that the Mach number will approach a constant value at the focus. This is in contrast to symmetric polygonal shocks that suffer Mach reflection at the vertices, in which case the Mach number increases as the shock approaches the focus. However, if the criteria for regular reflections for the triangular shock wave are violated, then a reconfiguring process with Mach reflection takes place.

3.1.4. *Three dimensional shock wave focusing*

All the previously mentioned experiments have been performed for cylindrical shock waves. Production of spherical, converging, shock waves was studied by Hosseini & Takayama (2005). A test section with transparent walls and an inner diameter of 150 mm was used. The diverging shock wave was generated by small explosives in the center of the test section. The shock wave was not spherical immediately after the explosion, but as it propagated further out it quickly approached a spherical shape. Hosseini & Takayama concluded that a diverging shock wave was always stable. The diverging shock wave reflected off the wall of the test section and started to converge. The converging shock wave kept its spherical shape until it started to interact with the detonation products. Comparisons were made with both Guderley's similarity law and the Chester-Chesnell-Whitham method. Both methods showed a reasonable agreement with the experimental data. However, the methods overestimated the speed of the shock wave, since neither of them take into account the flow ahead of the shock wave. The shock wave in the experiments was visualized in two different ways, both by double-exposure holographic interferometry and by a high-speed

video camera (100 sequential images with a frequency of 1,000,000 images/s) with the shadowgraph method. The usage of a high speed camera was a new method to visualize the entire focusing process for an individual shock wave. Previously, only one photograph was taken for an individual shock wave. Thus it was hard to keep exactly the same experimental conditions (Mach number, pressure, etc.) for each shock wave.

3.1.5. *Imploding detonation waves*

Imploding detonation waves were generated and investigated in Knystautas *et al.* (1969). The authors produced a two dimensional shock front in the shape of a regular polygon consisting of 30 sides, see Knystautas & Lee (1967) for further experimental details. Knystautas *et al.* followed the wave structure as the detonation wave converged. It was reported that Mach reflections occurring between the sides of the polygonal wave induced a smoothing effect on the shape and that it eventually became cylindrical; the detonation wave was stable. A spectroscopic analysis suggested that high temperatures, $1.89 \cdot 10^5$ K, were obtained as the shock reflected from the center, and at the same time, a bright flash was generated at the center of convergence.

The stability of cylindrical imploding detonation waves was further investigated by Knystautas & Lee (1971). A coaxial tube was used and the detonation wave was initiated by a high-energy spark plug at the beginning of the tube. A cylindrical implosion chamber, with a diameter of 80 mm and a thickness of 10 mm, was mounted at the rear end of the coaxial tube. The implosion wave entered the cylindrical chamber through a converging-diverging 90° bend to minimize the attenuation effects. In this work, an artificial disturbance in the form of a cylindrical rod with a diameter of 3.2 to 9.6 mm was introduced in the implosion chamber. The authors concluded that cylindrical converging detonation waves were stable since the bright spot at the focal point appeared at the same location in every experiment. Also, for the case with a rod of diameter 3.2 mm placed at the rim of the implosion chamber, the disturbances on the detonation front decreased and the wave regained its cylindrical symmetry before it collapsed.

Further investigations of imploding shock waves were made by Roig & Glass (1977) in a hemispherical chamber. A blast wave was produced at the center of the chamber. It decayed into a detonation wave and travelled outward and reflected from the walls, resulting in a converging detonation wave. The measured peak temperatures were around 5,000 K. Roig & Glass (1977) also indicated that the temperatures obtained in Knystautas *et al.* (1969) were overestimated due to the invalid use of Wein's law, and they postulated that the actual peak temperature probably lay below 10,000 K. A spectroscopic temperature measurement at an implosion focus in a 20 cm diameter hemispherical cavity was performed by Saito & Glass (1982). They measured the radiation intensity distributions and fitted these to black-body curves. Results

showed that temperatures were 10,000-13,000 K for imploding shock waves and 15,000-17,000 K for imploding detonation waves.

A spectroscopical study of the light emission seen during the convergence process was also performed by Matsuo *et al.* (1985). Light emission was observed as the shock wave collapsed and the full width at half maximum of the light pulse was 2.0-2.5 μs. The luminous diameter of the plasma core from the spectrograph recordings was 5 mm and the corresponding diameter observed with a camera recording was 5-8 mm. The larger value from the camera recording was due to the longer exposure time, which allowed the shock wave to travel a distance of up to 3 mm during the recording. Temperature measurements ranged from 13,000-34,000 K depending on the initiation energy.

Still, after more than six decades of ongoing research in the field of shock wave focusing, open questions remain and are summarized below.

- Can a stable and repeatable converging shock be created?
- How does the shape of the shock wave influence the focusing and reflection behavior?
- What causes the light emission during the focusing process?
- What is the spectrum of the emitted light?
- What parameters influence the amount of light emission?
- What models should be used for numerical simulations of shock wave focusing?

Questions marked • are considered in this thesis.

CHAPTER 4

Experimental setup

The experiments were carried out at the Fluid Physics Laboratory at KTH Mechanics. The experimental setup consists of a horizontal shock tube, a light source, and a schlieren optics system. The shock tube has a test section where shock waves are focused and reflected. The process is visualized by the schlieren system with a camera. The experimental setup is shown in Figure 4.1.

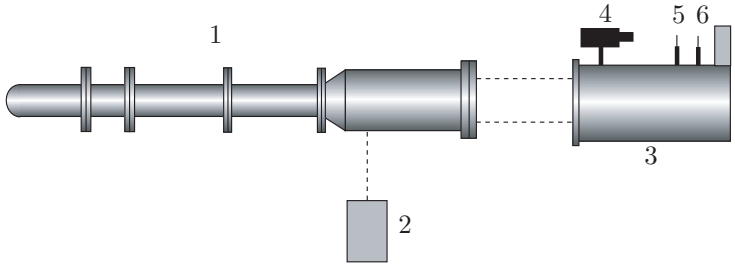

FIGURE 4.1. Schematic overview of the experimental setup: 1. Shock tube, 2. Pulse laser, 3. Schlieren optics, 4. PCO CCD camera, 5. Lens, 6. Schlieren edge.

4.1. The shock tube

The shock tube used in the present experimental studies is a typical setup for analysis of converging shocks. Similar setups have been used by several other investigators, see for example Perry & Kantrowitz (1951); Takayama *et al.* (1984); Neemeh & Ahmad (1986). The new feature with this shock tube is that the outer boundary of the test section is exchangeable and various geometrical shapes can be used.

The 2.4 m long circular shock tube consists a high pressure part and a low pressure channel which are separated by a 0.5 mm thick aluminum membrane. An illustration of the shock tube and its main elements is shown in Figure 4.2. To create a shock wave, the low pressure channel is evacuated of gas to a given pressure. Then the high pressure part is filled with gas, and at a given pressure difference between the two parts, the membrane bursts. The shock wave becomes planar as it travels downstream in the inlet section of the low pressure

channel. The pressures in the high and low pressure parts are monitored by sensors, see Figure 4.2.

To control the membrane opening, a knife-cross is placed in the inlet of the low pressure channel. The knife-cross helps the membrane to open evenly, shortens the time until a fully developed shock has formed, and prevents unnecessary disturbances. It helps prevent pieces of the membrane from coming loose.

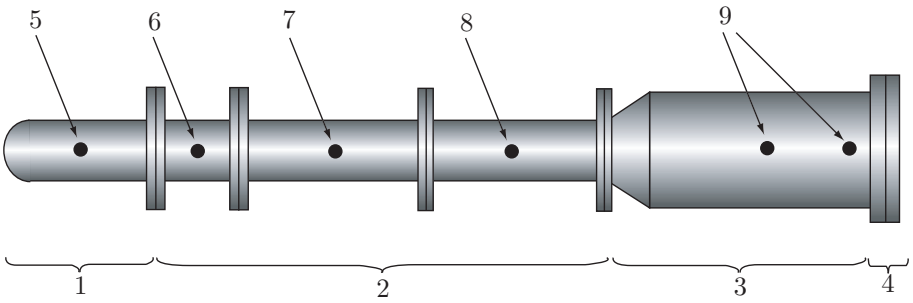

FIGURE 4.2. Schematic overview of the shock tube setup: 1. High pressure part, 2. Low pressure channel: inlet section, 3. Low pressure channel: transformation section, 4. Low pressure channel: test section, 5. High pressure sensor, 6. Low pressure sensor, 7. Vacuum valve, 8. Vacuum pump, 9. Shock sensors.

When the plane shock wave reaches the transformation section, the shock wave is forced to become annular by a conically diverging section where the diameter increases from 80 mm to 160 mm; see Figure 4.3. The cross-sectional area is held constant from the inlet section through the transformation section. The annular section is formed by an inner body mounted coaxially inside the wider diameter outer tube.

The 490 mm long inner body, with a diameter of 140 mm, is held in place by two sets of four supports. The two sets are placed 30.75 cm apart, and the supports are shaped as wing profiles to minimize the disturbances on the flow. Also, the second set of supports is rotated 45° relative to the first set. The shock speed, U_s, is measured by sensors placed in the annular section. The sensors are triggered by the temperature jump caused by the passage of the shock wave.

The test section is mounted at the end of the annular part of the shock tube. After a sharp 90° bend, the annular shock wave enters the test section and the focusing and reflection process begins. The gap between the two facing glass windows in the test section is 5 mm, reducing the cross-sectional area to half of that in the annular part.

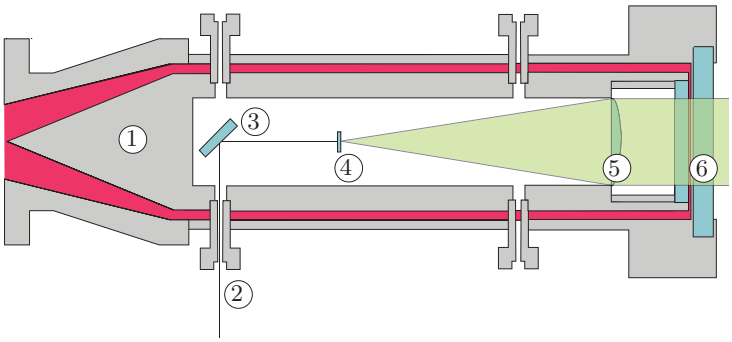

FIGURE 4.3. The annular part of the shock tube: 1. Inner body with a cone, 2. Supports, 3. Mirror, 4. Lens, 5. Glass windows for visualization, 6. Test section.

4.2. Method to shape the shock waves

Two different methods are used to create a polygonally shaped converging shock wave. In the first method, the shape of the shock wave is determined by the shape of the outer boundary of the test section. Four different outer boundaries of the test section are been used in the present experiments: a circle, a smooth pentagon, a heptagon and an octagon. The radius for the circular reflector boundary is 80 mm. The shape for the smooth pentagonal boundary is given by the following equation:

$$r = \frac{r_0}{1 + \varepsilon \cos(5\theta)} \tag{4.1}$$

where r is the radius, $\varepsilon = 0.035$ and $r_0 = 77$ mm. The radius for the circumscribed circle is 80 mm, both for the heptagonal and the octagonal reflector boundaries. The four reflector boundaries are shown in Figure 4.4.

(a) Circular. (b) Pentagonal. (c) Heptagonal. (d) Octagonal.

FIGURE 4.4. The four outer boundaries for the test section used in the experiments.

In the second method, an initially cylindrical shock wave produced by the circular outer boundary is perturbed by metal cylinders placed in various patterns and positions between the two facing glass windows inside the test section. The cylinders have three different diameters: 7.5, 10 or 15 mm. The cylinders are equipped with rubber rings on one end and glue on the other end and are held in place by the pressure between the two facing glass windows. The method to place these cylindrical obstacles in the test section is both safe and adjustable. An example with 16 cylinders (two octagonal patterns of radius $r = 46$ mm) where the cylinders alternate between diameters of 10 mm and 15 mm is shown in Figure 4.5.

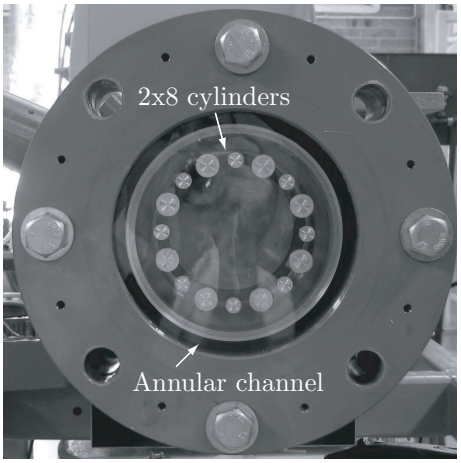

FIGURE 4.5. Rear part of the shock tube with 2x8 cylinders, where every other cylinder has 15 mm and 10 mm diameter, placed in the test section at $r = 46$ mm.

It is worth noting that the supports were adjusted to produce a minimal disturbance for the experiments with the heptagonal reflector boundary; for the other shapes, two of the supports were not optimally positioned. The optimal position is where the chord of the wing profile is aligned with the flow, so that the wing profile is an aerodynamic body. The case with a not optimal position was obtained when the wing profile was placed so that the chord of the profile was perpendicular to the direction of the flow, thus creating a bluff body.

4.3. The shock visualization

The facing surfaces in the test section consist of glass windows, and the convergence and reflecting process is visualized by the schlieren optics method. An air-cooled Nd:Yag (NewWave Orion) laser is used as a light source. The laser is operated in single shot mode with 5 ns light pulses. The laser is placed

outside the shock tube, either parallel or normal to the axis of the shock tube. If the laser is placed parallel to the axis, then a mirror is used to deflect the light through the laser light entrance on the shock tube.

The laser light entrance is a hole with a diameter of 6 mm through one of the upstream positioned supports for the inner body. When the laser light beam has entered the shock tube, it is deflected in the axial direction by a mirror placed inside the inner body. To simplify the adjustments of the optical setup, an electric motor is attached to the mirror in order to fine tune it after the equipment is in place. After hitting the mirror, the laser light enters a beam expander that produces a parallel light. The beam expander consists of two lenses. The first lens is biconcave with a diameter of 6 mm and a focal length of –8 mm. The second lens is plane convex with a diameter of 95 mm and a focal length of +300 mm. After the beam expander, the parallel light passes the first glass window, enters the test section, and then leaves the shock tube via the rear end glass window to enter the schlieren optics system.

4.3.1. *The schlieren optics*

The receiver part of the schlieren optics system is placed 1150 mm from the rear glass window of the shock tube. The receiver system consists of a large lens, 185 mm in diameter, with a focal length of 1310 mm and two mirrors that deflect the light into the section located at the top of the system.

The schlieren edge is placed in the image plane of the light source to cut off parts of the deflected light beams. Usually, the schlieren edge is a straight edge, but in this experiment, a spherical needle-point with a radius of 1 mm was used. This schlieren edge was chosen to match the shape of the shock wave, and it also produces a so called dark-field filter, which gives bright higher-order features against a dark background; see Settles (2001).

After passing the schlieren edge, the light goes through a lens and then enters the camera. The camera is a CCD PCO SensiCam (12 bits, 1280 x 1024 pixels, pixel size: 6.7 x 6.7 μm) equipped with a Canon lens with a focal length of 80 mm.

For experiments with the heptagonal reflector boundary and the cylindrical obstacles, special care was taken to avoid spurious light reflections inside the inner body by adding a light-absorbing coating to the interior of the inner body. This was done to obtain higher quality photographs.

4.3.2. *The shock speed measuring device and time control*

Two units, each containing a sensor and amplifier, are placed in the wall of the outer tube in the annular part of the shock tube. The sensor element is a 70 mm long glass plug with a diameter of 17 mm and a thin strip of platinum paint at the end. The glass plug is mounted in a hole so that the end surface (with the platinum paint) is flush with the inner surface of the tube.

The resistance of platinum is temperature dependent, so when the shock wave passes the sensor, the resistance of the platinum is changed due to the temperature increase caused by the shock wave. This change in resistance is transformed to a voltage pulse via an electric circuit which can be monitored on an oscilloscope. The electric circuit consists of an amplifier, an AD845 operational amplifier with a settling time of 350 ns to 0.01%. The glass plug is shown in Figure 4.6 and the circuit diagram of the electric circuit is shown in Figure 4.7.

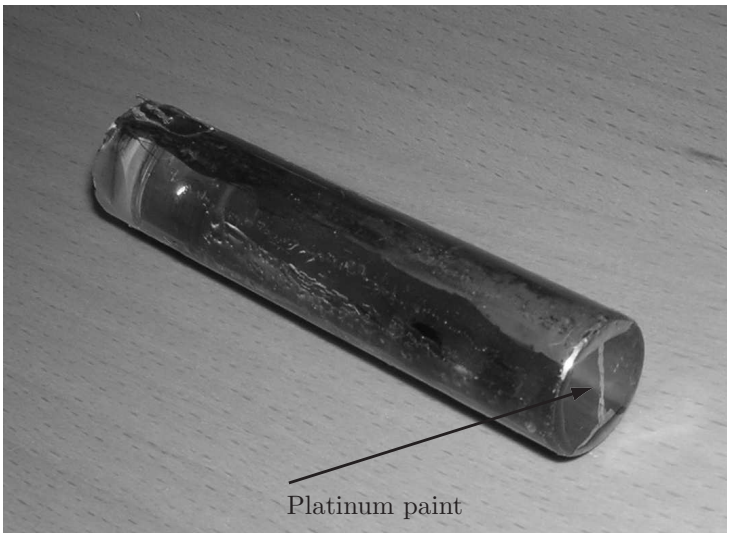

FIGURE 4.6. A sensor for shock speed measurement consisting of a glass plug with a thin strip of platinum paint at the end surface.

A time delay unit (Stanford Research System, DG535) is used to control the laser and the camera to enable exposures of the converging shock wave at predetermined time instants. This is necessary because it is not possible to take more than one photograph during each run.

4.4. The light measurements

During the light emission measurements, a photomultiplier (PM) tube is connected to the rear end of the shock tube. The PM tube (RCA 4526) is a light detector, and the time resolved output signal is proportional to the number of photons detected at each moment. The PM tube is placed in a light-sealed plastic cover to ensure that the detected light is originating from the converging shock wave and not from light sources within the laboratory. It is possible to mount the PM-tube in two different positions inside the cover, and one of these

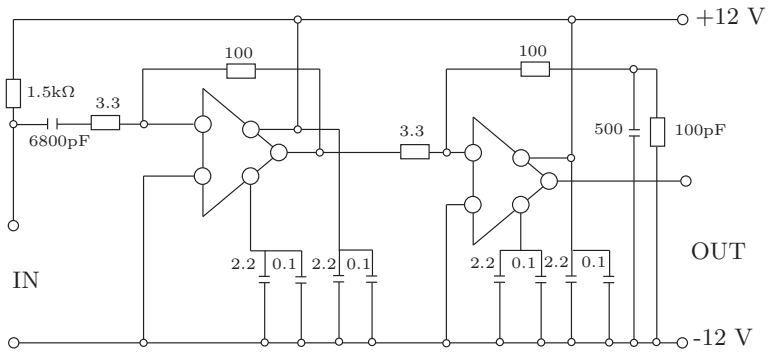

FIGURE 4.7. Circuit diagram for the amplifier. Resistances in $k\Omega$ and capacitances in μF.

will allow the use of schlieren optics and the PM-tube simultaneously. The PM tube is operated at -1,100 V during all experiments.

CHAPTER 5

Experimental results

In this chapter, the results from the experiments on shock wave focusing are presented briefly. The goals of the experimental study were to find out if we could create stable and repeatable converging shocks and to analyze how the shape of the shock wave influenced the focusing behavior. Furthermore, we continued to investigate the light emission that appeared during the focusing process. The questions we investigated were *i*) "When does the light appear?", *ii*) "What parameters are important for the amount of light emitted?", and *iii*) "Why is there light?"

The experimental results are divided into two sections. First, results from the two methods to generate polygonal shock waves are discussed. In the second section, the results from the light emission experiments are evaluated. Papers 1–5 enclosed in the second part of this thesis provide more details and further discussions on the results presented in this chapter.

5.1. Generation of polygonal shock waves

Two different methods were used to create polygonal converging shock waves. The first method consisted of changing the geometrical shape of the outer boundary of the test section. In the second method, an initially cylindrical shock wave was perturbed by cylindrical obstacles placed in various patterns and positions inside the test section.

Figure 5.1 shows schlieren photographs of a converging shock wave, shaped by the heptagonal outer boundary in Figure 4.4 (c), are shown. At first, the converging shock assumes the shape of the boundary, a heptagon, as in Figure 5.1 (a). Next, the heptagon-shaped shock will transform into a double heptagon because the corners consists of Mach shocks that propagate faster than the adjacent planar sides; this is shown in Figure 5.1 (b). The double heptagon transforms back to a heptagon when the faster moving Mach shocks consume the planar sides. At this configuration, the resulting heptagon is oriented opposite to the original one, see Figure 5.1 (c). This reconfiguration process will, according to theoretical and numerical results, continue during the rest of the convergence process if there are no disturbances present. Finally, the shock converges, reflects in the center, and starts to diverge. At first, the reflected shock assumes a circular shape, but it will later be influenced by

the flow ahead of it and transform into a smoother version of the initial shape. To see this, compare Figures 5.1 (e) and (a).

The same behavior is observed for all polygonal converging shocks produced by the four different reflector boundaries. More results can be found in Eliasson *et al.* (2006) and Eliasson (2006); these are Papers 1 and 3 in the second part of the thesis.

A typical series of schlieren photographs of a polygonal converging shock wave is shown in Figure 5.2. The converging shock wave is perturbed by eight cylinders with diameters of 15 mm placed in an octagonal pattern centered about the focal point. The shock wave diffracts over the obstacles, and Mach shocks and triple points form between the converging shock, the reflected shock, and the Mach shocks. As the shock wave passes the obstacles, an octagon-shaped shock with curved sides will form; see Figure 5.2 (a). The curved sides eventually become planar and the shock reconfigures as mentioned previously: a double octagon, shown in Figure 5.2 (b), transforms back into an octagonal shape, in (c), which is oriented opposite to the octagon in (a). After the shock wave has reflected, it will assume a circular shape; see Figure 5.2 (d). The main conclusions from the experiments with cylindrical obstacles are the following: the size of the cylinder determines how much the shock will be perturbed, and while the shape of the shock is easily perturbed, it is hard to move the position where the shock wave will focus. More results and further discussions on experiments with cylindrical obstacles are presented in Eliasson *et al.* (2007); see Paper 2 in section two of this thesis.

Schlieren photographs of a heptagonal converging shock are shown in Figure 5.3. In this figure, it is possible to see that the sides of the polygonal shock are, at first, rather planar; see Figure 5.3 (a). Then, as the reflected shock interacts with the converging shock, the plane sides become more curved; see Figure 5.3 (b). When the reflected shock has passed by the converging shock, the curved sides become planar, as mentioned earlier. Then, the transformation process takes place; see Figures 5.3 (c)–(d).

5.2. Shape of the shock wave close to the center of focusing

The various geometrical shapes that we investigated and compared to each other can be divided into three groups: a cylindrical shock, an initially cylindrical shock perturbed by cylindrical obstacles, and polygonal shock waves created by changing the shape of the outer boundary of the test section.

Figure 5.5 shows close-ups of various geometrical shapes from shock waves in the three groups mentioned above. The geometrical configurations of the obstacles for the photographs in Figure 5.5 (b)–(j) are shown in Figure 5.4. The scale used in all photographs in Figure 5.5 is nearly identical, except that the scale used in (j) is 25% larger than those used in the other photographs. A cylindrical shock wave is unstable, and hence it will be influenced even by small

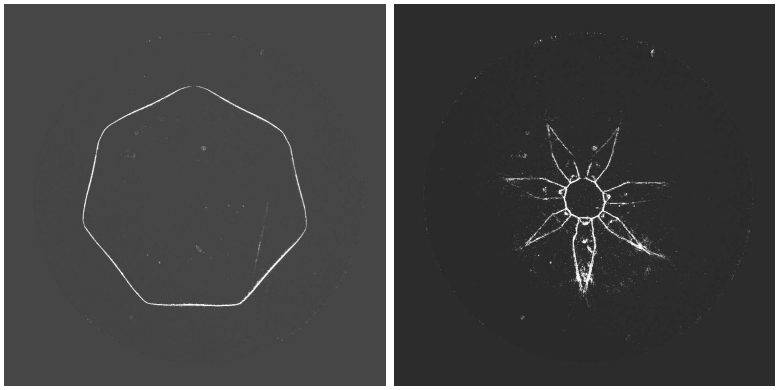

(a) $t = 0$ μs

(b) $t = 20$ μs

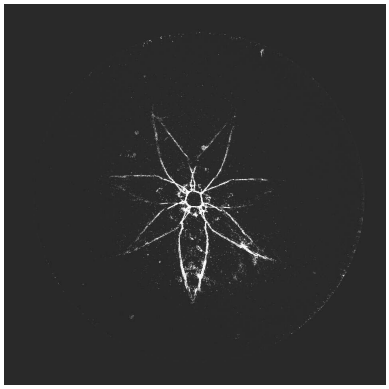

(c) $t = 22$ μs

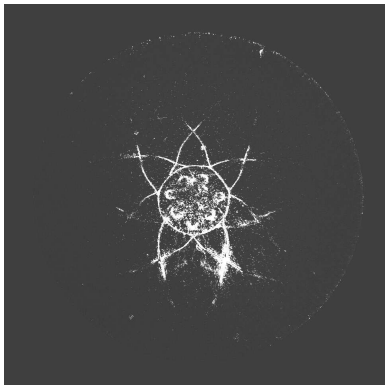

(d) $t = 35$ μs

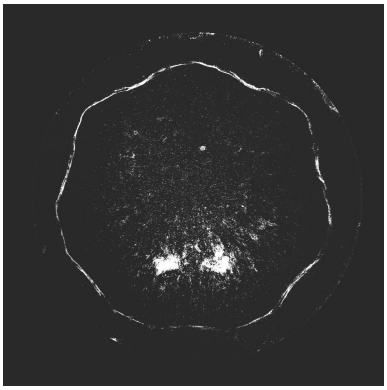

(e) $t = 75$ μs

FIGURE 5.1. A polygonal shock wave transforming between a heptagonal and a double heptagonal shape during the focusing process. In (a)-(c) the shock is converging and in (d) and (e) it has reflected and is diverging.

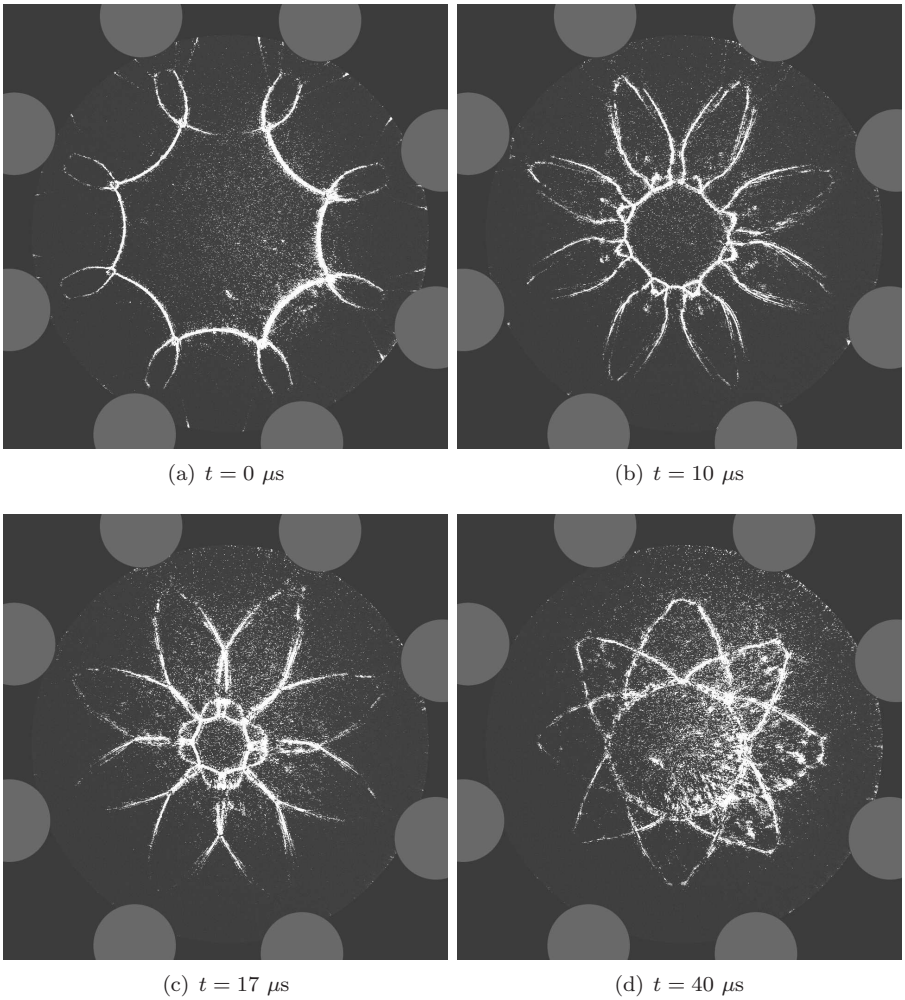

(a) $t = 0$ μs (b) $t = 10$ μs

(c) $t = 17$ μs (d) $t = 40$ μs

FIGURE 5.2. An initially cylindrical converging shock wave perturbed by eight cylinders placed in an octagon pattern. In (a)-(c) the shock is converging and in (d) it has reflected and is out-going.

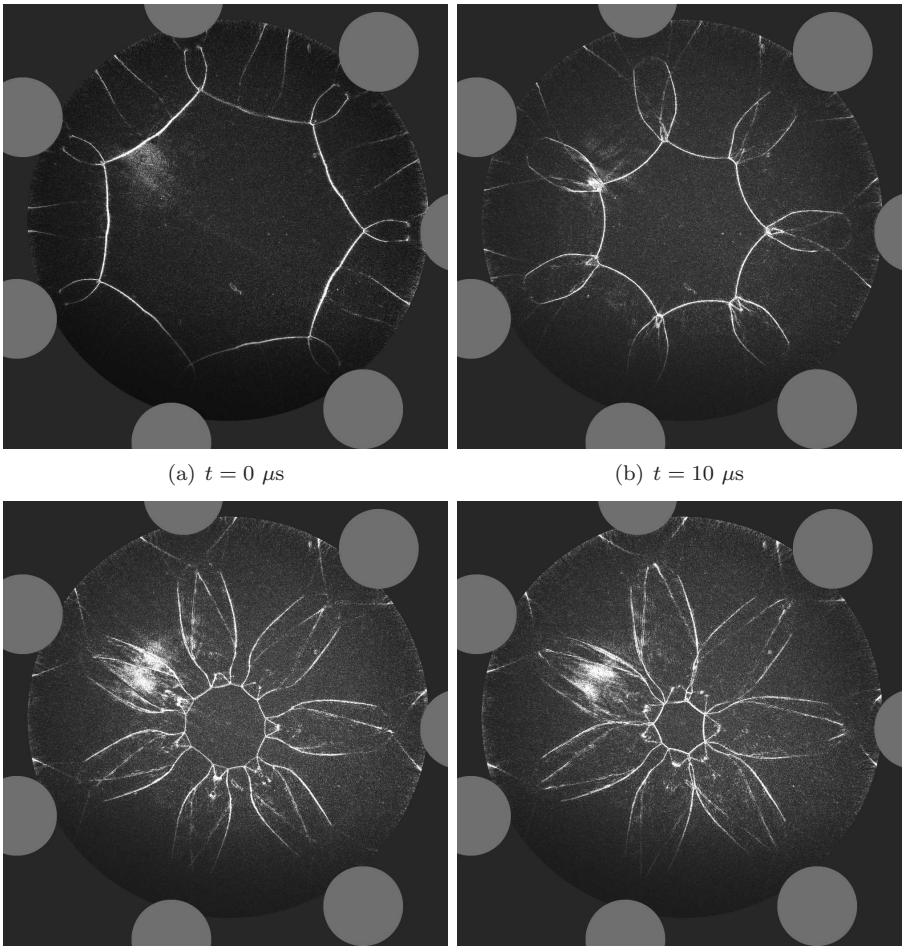

(a) $t = 0$ μs (b) $t = 10$ μs

(c) $t = 15$ μs (d) $t = 20$ μs

FIGURE 5.3. An initially cylindrical converging shock wave perturbed by seven cylinders placed in a symmetric heptagon pattern. The shock is converging.

disturbances present in the shock tube. Disturbances are generated by the supports for the inner body of the annular part of the shock tube. Although the supports are shaped as wing profiles to minimize disturbances, they still affect the flow. Owing to the inherent instability of converging cylindrical shocks, an initially cylindrical shock wave becomes square-shaped close to the center of convergence; see Figure 5.5 (a). The square-like shape becomes visible close to the focal point. For the case with one 15 mm diameter cylinder, the shape resembles a teardrop; see (b). In Figure 5.5 (c) and (d), two cylinders are placed opposite each other; in (c) both of them were 15 mm in diameter, and in (d) one was 15 mm and one was 7.5 mm in diameter. Here it is possible to see that the undisturbed parts travel faster than the disturbed parts, resulting in an elongated diamond-shaped shock. For the case with cylinders of different sizes, the second Mach shock, (resulting from a collision between the first two Mach shocks), is more developed. Three cylinders, placed in a triangular pattern, produced a triangular shock close to the center of convergence; see Figure 5.5 (e). For this case, the shock undergoes regular reflection and thus maintains the same shape through the convergence process. The cylinders are located opposite to the corners of the triangle. In the next example, where four cylinders are placed in a square formation, a square-shaped shock is created and Mach reflection takes place; see Figure 5.5 (f). At this instant, the plane sides are located opposite the corners, and one full cycle of the reconfiguration process has taken place. The square in (f) is oriented differently compared to the square in (a), suggesting that the four cylinders are the reason for the final shape, rather than the four supports. Seven and eight obstacles placed in symmetric polygons created heptagonal and octagonal shapes respectively; see Figure 5.5 (g) and (h). A shock wave perturbed by sixteen cylinders, where every other cylinder has a diameter of 10 mm and 15 mm (see Figure 4.5), is shown in Figure 5.5 (i). The disturbances from the larger cylinders overtake the disturbances from the smaller cylinders and the shock becomes octagon-shaped close to the center. Five of the cylinders (in a row) from the configuration in (i) are kept and and three smaller cylinders (7.5 mm diameter) are added at the same radial position as the larger cylinders, see Figure 5.5 (j). The shock shape close to the center is elongated, and its center point is hardly moved. The pentagonal outer boundary is used in Figure 5.5 (k), and a pentagonal shape is observed. A heptagonal reflector boundary creates a heptagonal shape close to the center of focusing, while an octagonal reflector boundary creates a square-like shape, see (l) and (m), respectively. The square-like shape in (m) originates due to the disturbances from the supports for the inner body, as opposed to the circular case in (a).

In summary, the results show that converging shock waves with an even number of sides generated by the reflector boundaries will be influenced by the four supports and become square-shaped close to the center of convergence. However, shock waves with an even number of sides generated by cylindrical

obstacles will not be influenced by the four supports. All shocks with an odd number of sides will also remain unaffected by the four supports.

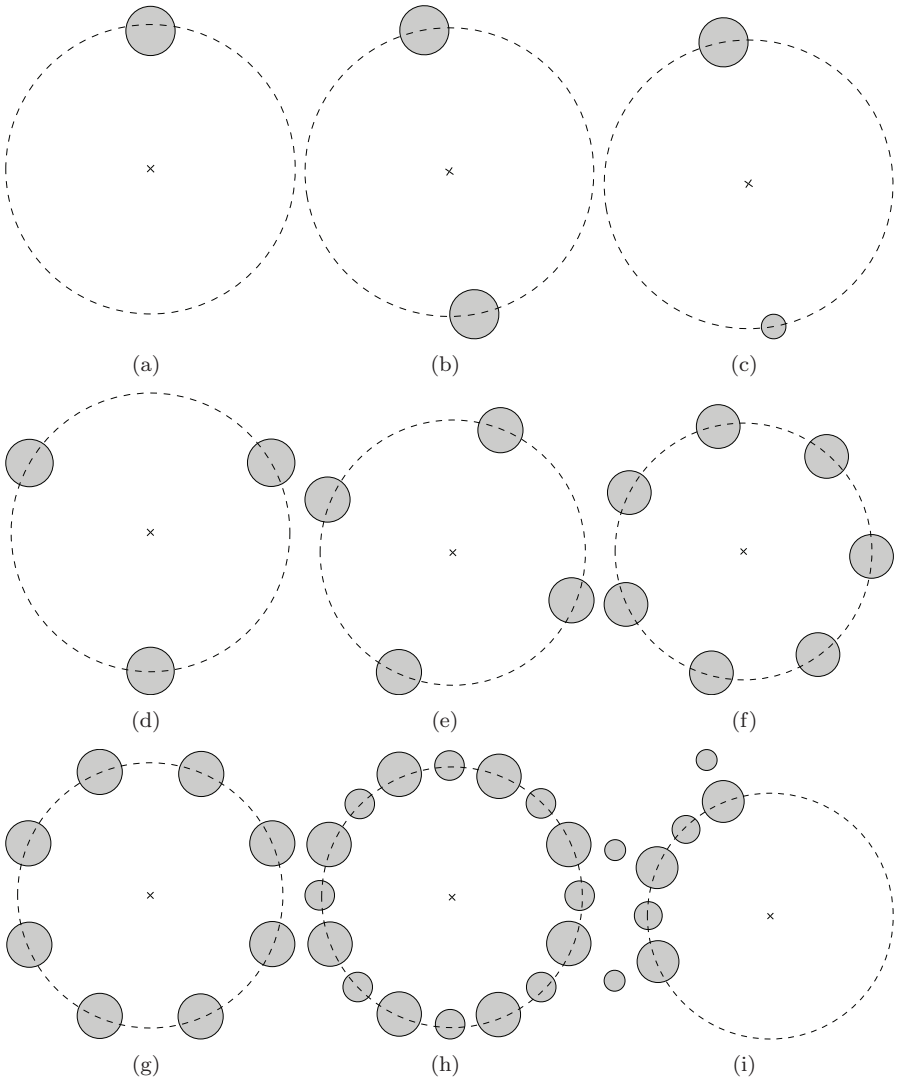

FIGURE 5.4. Obstacle configuration for the schlieren photographs in Figure 5.5: (a) one cylinder, (b) two cylinders, (c) two cylinders, (d) three cylinders, (e) four cylinders, (f) seven cylinders, (g) eight cylinders, (h) 16 cylinders and (j) 3x15 mm, 2x10 mm and 3x7.5 mm.

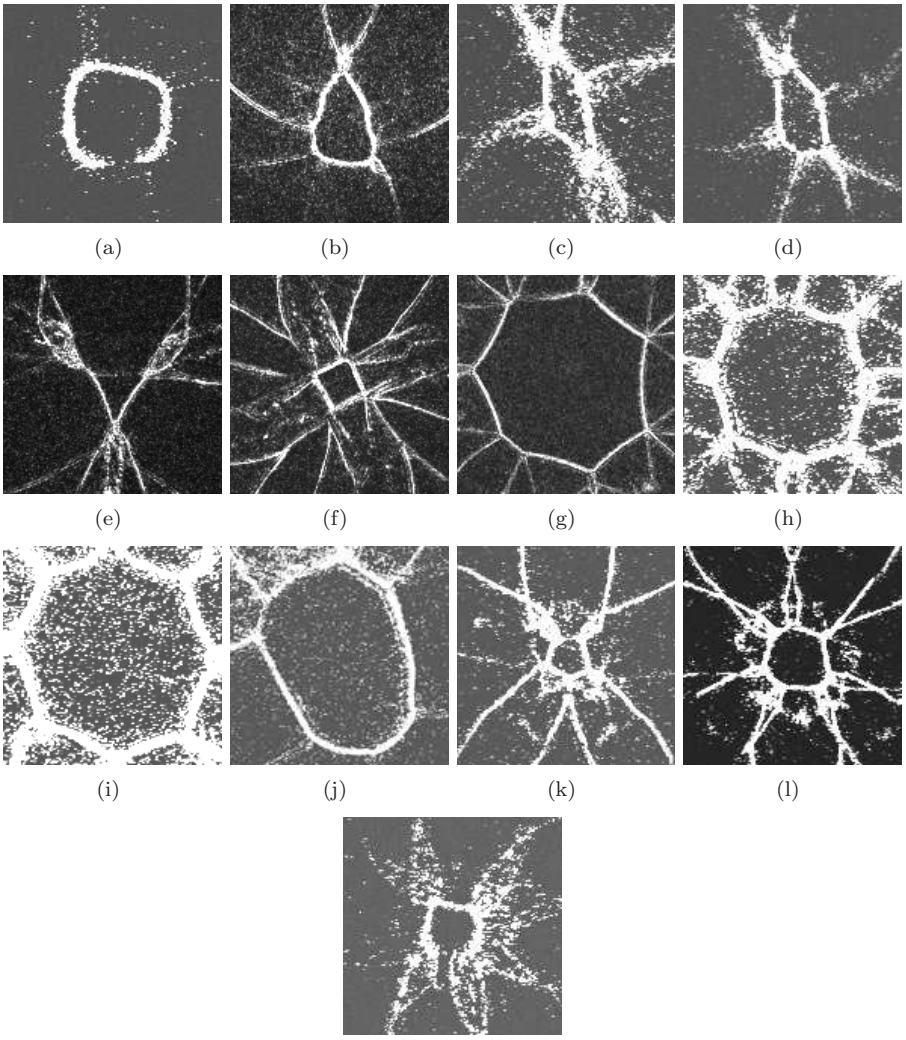

FIGURE 5.5. Schlieren photographs of shock waves close to the center of convergence for different shapes (a) cylindrical outer boundary, (b) one cylinder, D=15 mm, (c) two cylinders, D = 15 mm, (d) two cylinders, D=7.5 mm and 15 mm, (e) three cylinders D=15 mm, (f) four cylinders, D=15 mm, (g) seven cylinders D=15 mm, (h) eight cylinders D=15 mm, (i) 16 cylinders, 8x15 mm and 8x10 mm in diameter, (j) 3x15 mm, 2x10 mm and 3x7.5 mm, (k) pentagonal outer boundary, (l) heptagonal outer boundary and (m) octagonal outer boundary.

5.3. Light emission from converging shock waves in air and argon

A series of experiments have been conducted to investigate the light emission caused by converging shock waves. In particular, we looked at where the shock was positioned when the light appeared, how long the light was emitted, and how the shape of the converging shock wave influenced the light emission. Also, two different gases were tested, air and argon. To study the light emission, we looked at the light intensity as a function of time by using a photo multiplier (PM) tube. Also, the spatial appearance of the light emission was studied by taking photographs of the light spots, with the same CCD camera as used to obtain the schlieren photographs.

A typical time signal from the PM tube is shown in Figure 5.6. The signal from the PM tube shows the light intensity level as a function of time. At first nothing happens; it is dark in the test section of the shock tube. As soon as light is detected, the signal from the PM tube decreases below zero. The deviation from the reference voltage level, (the reference level is when there is no light), is proportional to the intensity of the detected light and also dependent on the voltage operating the PM tube. The same voltage level (-1100 V) was used for all experiments. The full width at half maximum (FWHM) of the light emission signal is about 200 ns for this case. This is considerably longer than the FWHM for a sonoluminescence pulse, which is on the order of several hundred picoseconds; see experimental results by Gompf *et al.* (1997) and simulations by Vuong & Szeri (1996).

A comparison of the amount of emitted light was made for various shapes of converging shock waves. If we ignore the fact that a different amount of the shock wave is reflected back due to various shapes of reflectors or numbers of obstacles, the unperturbed cylindrical converging shock wave is the best at producing light. The geometrical shapes which are far from cylindrical, i.e. the triangular and the one-obstacle case, produce the least amount of light. We believe that this is due to the fact that the various parts of the shock front arrive at the focal point at different time instants. Also, the triangular case will undergo regular reflection during the focusing process. This means that the shape will remain the same and the Mach number remains bounded, which leads to a bounded energy as the triangular shock converges; see Betelu & Aronson (2001).

Photographs of the light emission were taken with the CCD camera. The CCD photographs were saved as 16-bit grayscale data, where only 12 bits were used for the actual data (because the camera sets the highest four bits to zero), resulting in 4096 shades of gray. The exposure time for the CCD camera was set to 1 ms, a long time compared to the actual length of the light pulse. This means that the shock wave will hit the focal point and reflect back and disappear outside of the photograph frame before the CCD camera stops

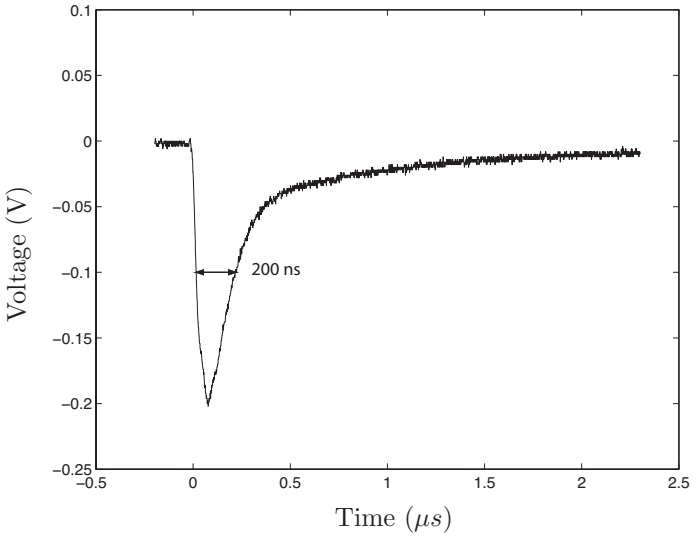

FIGURE 5.6. A typical signal from the PM-tube in the case with the cylindrical shock.

recording. An example is shown in Figure 5.7 for argon as test gas and the octagonal outer boundary. The size of the light spot is approximately 1 mm in diameter, which is smaller than the results obtained by Matsuo *et al.* (1985). In that case, the light spot was about 5–8 mm, taken with an exposure time of 0.4 μs. The upper right corner of the graph shows the gray level values in a cut through the center of the photograph.

5.4. Remarks

There is a restriction when using reflector boundaries to change the shape of the shock: it is not possible to use polygonal shapes with less than seven planar sides and corners. The boundary would then block parts of the 90° corner where the shock is propagating when it turns into the test section. The second method, with obstacles, is more flexible because it allows one to place the objects in any geometrical pattern.

The various methods to create polygonal shock waves will reflect back a different amount of the shock front, and hence the wave energy reaching the focal point will vary for the different cases. It would be desirable to ensure that the same amount of energy would reach the focal point by varying the initial conditions from the separate geometrical setups. Also, the reflector boundaries reflect back parts of the flow before the shock wave has turned around the 90°

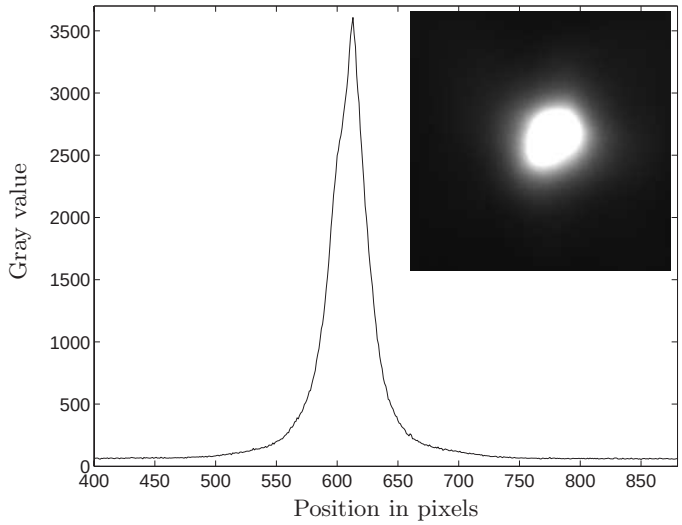

FIGURE 5.7. Light emission from argon in the low pressure channel. High gray value - bright pixels, low gray value - dark pixels. The octagonal outer boundary is used.

corner, so the amount of flow entering the test section is reduced compared to the case with obstacles.

CHAPTER 6

Numerical simulations

Shock front propagation problems are often solved numerically using geometrical acoustics, geometrical shock dynamics (GSD) or the full set of Euler equations. Geometrical acoustics is a linear method used to solve shock propagating problems for weak shocks and is similar to the way light rays are treated in optics. This method cannot be used for problems with stronger shocks for which the nonlinear effects become important. GSD was introduced by Whitham (1958) and the method is further described in Whitham (1974). The original GSD method does not account for the influence of the flow ahead of the shock. A detailed explanation on how to use GSD for shock propagating problems can be found in Henshaw *et al.* (1986), which shows results from different cases of shock propagation such as shock wave diffraction, shock waves in channels, and shock wave focusing.

Two numerical methods have been used in the present study to simulate the flow in the shock tube and the two dimensional test section. The first method is an Artificially Upstream Flux vector Splitting (AUFS) scheme for the Euler equations, suggested by Sun & Takayama (2003). This numerical scheme discretizes the Euler equations according to the direction of wave propagation. Results obtained with the AUFS scheme are presented in Paper 1 and Paper 2 in the second part of the thesis. In the second method, we use the Overture suite from Chesshire & Henshaw (1990), which is further described in the next section.

There are three main reasons for doing numerical simulations of converging shock waves: *i*) It is hard to do quantitative measurements in experiments on shock wave focusing because you often rely on qualitative visualization methods and get results in the context of density gradients as functions of time. Hence, the numerical simulations are a useful complementary tool to get more data. Quantities like temperature, pressure, velocity, and Mach number are easy to calculate via numerical simulations for the whole flow field. *ii*) One can save both time and money by doing numerical simulations, because one can predict the results and therefore do not need as many experimental results to validate the hypothesis. *iii*) A validation of the models and the numerical schemes used for the present problem is important. If the numerical results agree well with

experimental results, one can expect the model and the numerical scheme to be valid.

6.1. Simulations in Overture

Numerical simulations of two problems have been performed. The first problem is an axisymmetric model of the shock tube used in the previously mentioned experiments; see chapters 4 and 5. The second problem consists of simulations of converging shock waves diffracted by cylinders in a two dimensional test section; see Papers 5 and 6 in the second part of this thesis.

For the numerical simulations, we used the two dimensional Euler equations as a model for both the flow in the shock tube and for the converging shock wave inside the test section. In conservative form they read

$$\mathbf{u}_t + \mathbf{f}(\mathbf{u})_x + \mathbf{g}(\mathbf{u})_y = 0, \tag{6.1}$$

$$\mathbf{u} = \begin{bmatrix} \rho \\ \rho u \\ \rho v \\ E \end{bmatrix}, \ \mathbf{f} = \begin{bmatrix} \rho u \\ \rho u^2 + p \\ \rho uv \\ u(E+p) \end{bmatrix}, \ \mathbf{g} = \begin{bmatrix} \rho v \\ \rho vu \\ \rho v^2 + p \\ v(E+p) \end{bmatrix}. \tag{6.2}$$

Here ρ is the density, u and v are the velocities in the horizontal and vertical directions respectively, p is the pressure, and the total energy, E, is given by

$$E = \frac{p}{\gamma - 1} + \frac{1}{2}\rho(u^2 + v^2). \tag{6.3}$$

In the computations we assume the gas obeys the ideal gas law with constant specific heats. This assumption is valid away from the center of convergence, however near the center the temperature reaches such high values that it no longer behaves as a calorically perfect gas. The assumption of constant specific heats is valid up to 1000 K for air; beyond this, the vibrational motion of O_2 and N_2 molecules affect the specific heats and they are no longer constant, see Anderson (1990). For argon, the assumption of specific heats is valid up to temperatures where the gas undergoes ionization.

The complex geometry of the experimental setup requires a sophisticated numerical flow solver. An intrinsic numerical difficulty of the converging shock wave problem is the different scales associated with the focusing process. The change in scales justifies the use of adaptive mesh refinement (AMR). The Overture suite that we used for the numerical simulations has support for both geometry (through body fitted overset grids) and AMR, and it includes various flow solvers. Overture is a free software package available for download at `http://www.llnl.gov/CASC/Overture/`. For the experiments presented here, we used the OverBlown solver for the Euler equations, based on the second order accurate Godunov method, discussed in Henshaw & Schwendeman (2003, 2006). Artificial viscosity was added to the numerical scheme to stabilize the

method and to give sharp shocks without overshoots; this is further explained in Henshaw (2003).

The numerical 'schlieren' plots, i.e. plots of the density gradient, are calculated using:

$$I_{sch} = \alpha \exp(-\beta s(\mathbf{x})), \tag{6.4}$$

$$s(\mathbf{x}) = \frac{\tilde{s} - \min \tilde{s}}{\max \tilde{s} - \min \tilde{s}}, \ s \in [0,1] \tag{6.5}$$

$$\tilde{s}(\mathbf{x}) = \sqrt{\rho_x^2 + \rho_y^2}, \tag{6.6}$$

where α and β are set to 1 and 15 respectively; see Henshaw & Schwendeman (2006). These parameters can be adjusted to change the contrast of the schlieren plot.

6.2. Problem formulation and setup

6.2.1. *Shock tube simulations*

To simulate the flow in the shock tube, we used an axisymmetric grid. The initial grid is depicted in Figure 6.1. The whole grid is shown in Figure 6.1 (a), and detailed views of the front and rear part of the inner body and the test section are displayed in Figure 6.1 (b)–(d). The proportions for the grid are, in principle, the same as for the shock tube used in the experiments. The main difference is that the front of the cone on the inner body and the 90° corner are not exactly sharp, but have a small curvature. This guarantees that the normal to the corner is well defined everywhere, which would not be the case for a sharp corner.

The initial conditions in the low pressure part are set to room temperature, (294 K) at 13.3 kPa (100 torr), and the density is given by the ideal gas law $\rho = p/RT$, where R is the gas constant (287.06 J/kgK). The initial pressure in the high pressure part is set to 1450 kPa, the temperature is set to room temperature, and the density is given by the ideal gas law.

6.2.2. *Results*

Results show that the 90° corner has a large impact on the flow. For a straight 90° corner, there will be a large amount of reflection and the shock loses strength as it turns the corner. This is seen in Figures 6.2–6.4 which show 'schlieren', pressure, and speed plots of the flow field during the instant when the shock turns the corner. In Figure 6.2, it is seen that the diffracted shock never becomes planar again; instead, a Mach shock bounces back and forth as the shock wave propagates in the test section. The pressure field is shown in Figure 6.3. As soon as the reflected shock has passed the gap to the test section, the incoming flow will be more or less stopped and no gas will enter the test section. The speed of the gas is plotted in Figure 6.4, and it is clear from

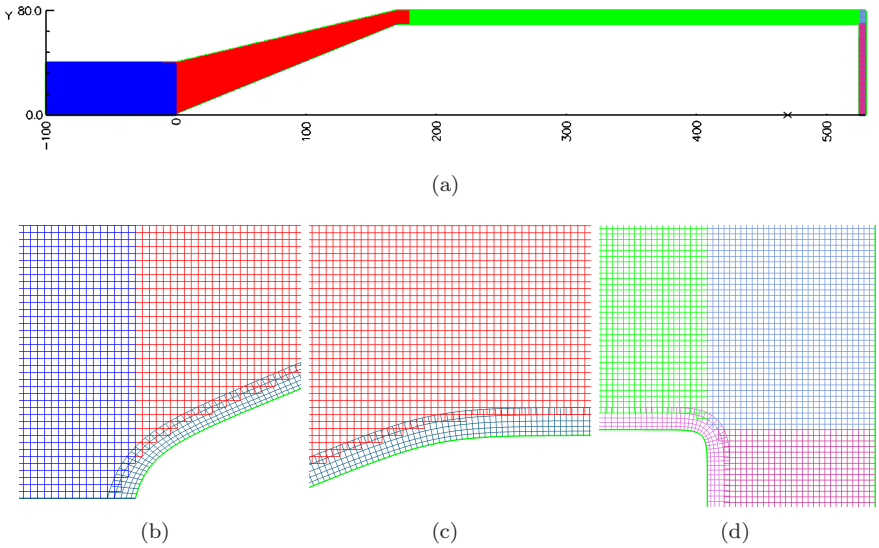

FIGURE 6.1. Grids for the shock tube simulations. The shock tube (a) and enlargements of the tip of the cone (b), the end of the cone (c) and the 90° corner (d).

Figure 6.4 (g)–(i) that the reflected wave stopped the motion of the incoming gas, so a large amount of the gas never reached the test section.

The conclusion is that the corner used in the simulations, based on the experimental setup, is not optimal for a focusing process. Large parts of the incoming gas never reach the test section, instead the flow becomes stopped by the reflected shock caused by the corner. A redesign of the corner would lead to a larger amount of gas reaching the test section and thus the focal point.

6.2.3. *Simulations of converging shocks*

The two dimensional model of the test section consists of two background grids, one Cartesian and one annular, and optional cylindrical obstacles described by individual annular grids. The grid spacing of the annular grids are adjusted to conform with the grid spacing, h, of the Cartesian grid.

Several cases were simulated: a circular converging shock wave, a circular converging shock perturbed by one cylinder, three cylinders placed in a equilateral pattern, and four cylinders placed in a square formation; this is described in Paper 5. The cylinder surfaces are set to be perfectly reflecting, which is not the case in the experimental setup, but we assume the errors due to this

choice are small and can be neglected. The boundary condition on the outer perimeter of the domain is set to a supersonic outflow condition, which is one of the simplest non-reflecting boundary conditions.

Given the initial conditions in front of the converging shock, the state behind the shock can be parameterized by the Mach number. Here we set the initial conditions in front of the shock to be a gas at rest at room temperature. We then adjust the initial Mach number so that the radius of the converging and reflecting circular shock, matches the experimental results as a function of time; see Paper 5.

6.2.4. *Results*

Schlieren plots of the converging shocks close to the center of convergence are shown in Figure 6.5. In (a), one cylinder has been used to diffract the converging shock. The shape of the shock resembles a teardrop. In (b), three cylinders were used to create a triangular shape undergoing regular reflection, thus the same shape remains during the focusing process. Figure 6.5 (c) shows a square shock created by four cylinders placed in a square formation. In (d), two symmetric octagons, one with 15 mm diameter cylinders and the other with 10 mm cylinders. Close to the center, the influence of the eight larger cylinders are dominating, creating an octagon shock. In (e) and (f) two cylinders are placed opposite each other. In (e) the cylinders are 7.5 mm and 15 mm in diameter and in (f) they are both 15 mm in diameter. The second Mach shock, resulting from the collision of the first two Mach shocks, has progressed more for the part of the shock wave diffracted by the smaller (7.5 mm) cylinder. Seven cylinders are placed in a heptagonal pattern in Figure 6.5 (g). The reconfiguration process has gone through one cycle and a heptagon shock is visible; its corners are located opposite to the location of the cylinders. The same behavior is observed in (h) for the case with an octagon shock. The last picture shows a shock wave diffracted by several cylinders placed in a dense formation. The shape gets elongated and the center of the converging shock is moved just a small distance. The numerical simulations agree well with the experimental results discussed earlier; compare figures 5.5 and 6.5. Also, the locations of triple points and Mach shocks match the experimental results. The numerical 'schlieren' plots are more detailed than the corresponding schlieren photographs from the experimental studies, and because of this, they are a useful complement.

A full reconfiguration cycle for the heptagonal case is shown in Figure 6.6. In the beginning, the sides of the polygonal shock are at first rather planar; see Figure 6.6 (a). Then, as the reflected shock starts to interact with the converging shock, Figure 6.6 (b), the plane sides become more curved; see (c). When the reflected shock has passed by the converging shock, the curved sides become planar, as mentioned earlier. Then, the transformation process takes

place (see Figure 6.6 (e)–(i)), resulting in a heptagon shock with plane sides placed opposite the cylindrical rods.

Diffraction of a cylindrical shock wave hitting a single cylinder is shown in Figure 6.8. At first, a regular reflection occurs, shown in (a)–(b), and as the reflection point moves past the cylinder, it transforms into a Mach reflection containing a triple point at the intersection of the Mach shock, the incoming shock, and the reflected shock; see (c)–(f). The angle where the transition from regular to Mach reflection occurs is dependent on the Mach number of the incoming shock. For plane shock diffraction on cylinders this angle is about 45° for Mach number 1.3 and 40° for Mach number 2.8.

The dimensionless pressure and temperature near the focal point were measured for a cylindrical converging shock perturbed by 0-16 cylinders. Figure 6.8 shows the maximum pressure and temperature as a function of the number of cylinders. The maximum pressure is non-dimensionalized with the initial pressure in the low pressure part, here 13.3 kPa. The temperature is made dimensionless with respect to the gas constant γ and the room temperature, in this case 294 K. The results show that the undisturbed cylindrical shock gives the highest pressure and temperature near the focal point. This is expected, because in all other cases, part of the flow is reflected by the obstacles and never reaches the focal point. For a low number of cylinders, 1–6, the maximum values are low. This is most likely caused by the fact that all parts of the shock front do not reach the focal point at the same time, and hence the focusing effect is lost. Higher pressures and temperatures are obtained for the cases with a larger number of obstacles, 7–13.

6.3. Remarks

We have used a simplified model with an ideal gas assumption where the ionization and real gas effects are ignored. This simplification is valid when the shock wave is away from the convergence center; at the center, the temperatures become so high that real gas effects and ionization must be accounted for.

An advantage of the numerical simulations is the increased level of detail and the flexibility to follow the convergence process closely through animations.

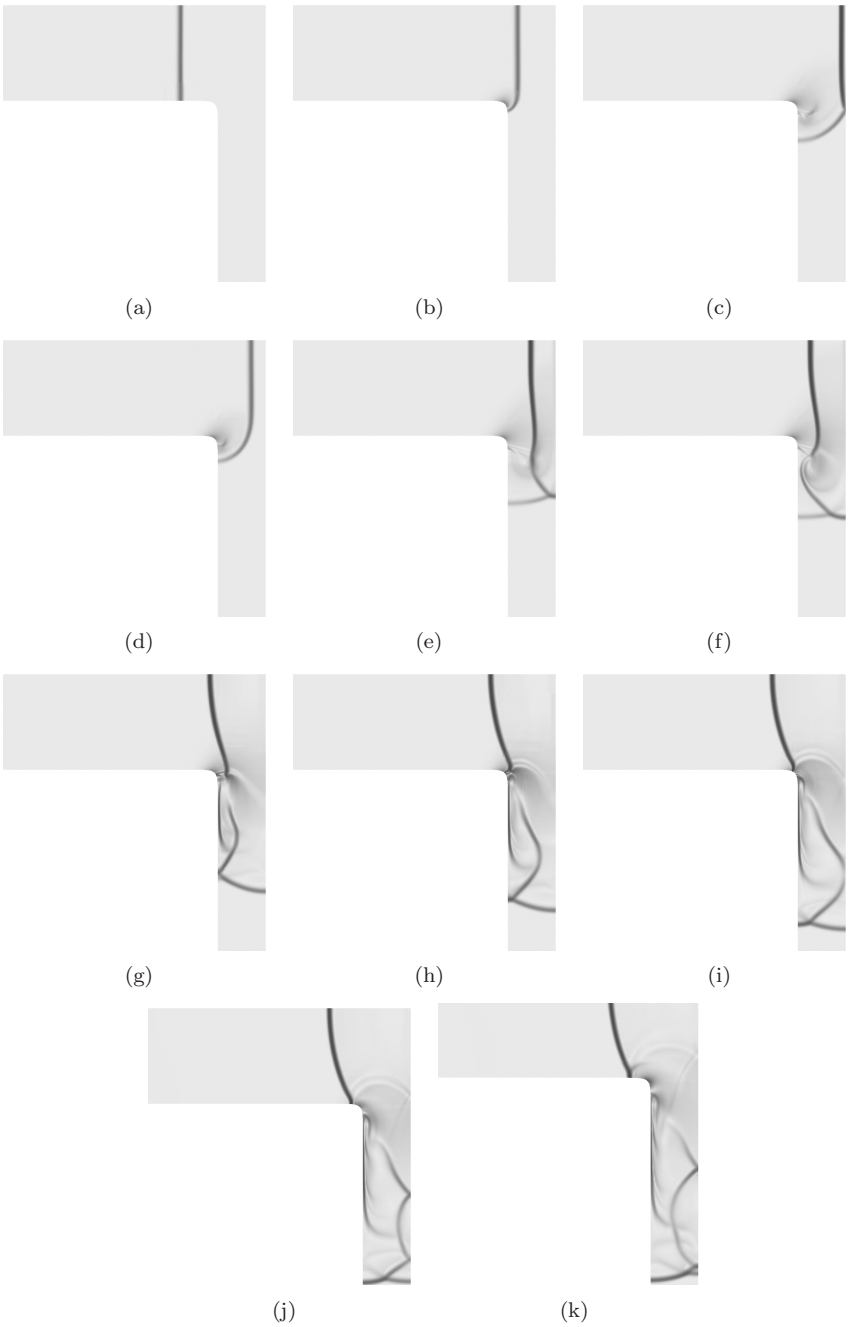

FIGURE 6.2. Schlieren images from simulations in Overture showing the shock wave as it passes the 90° corner of the test section.

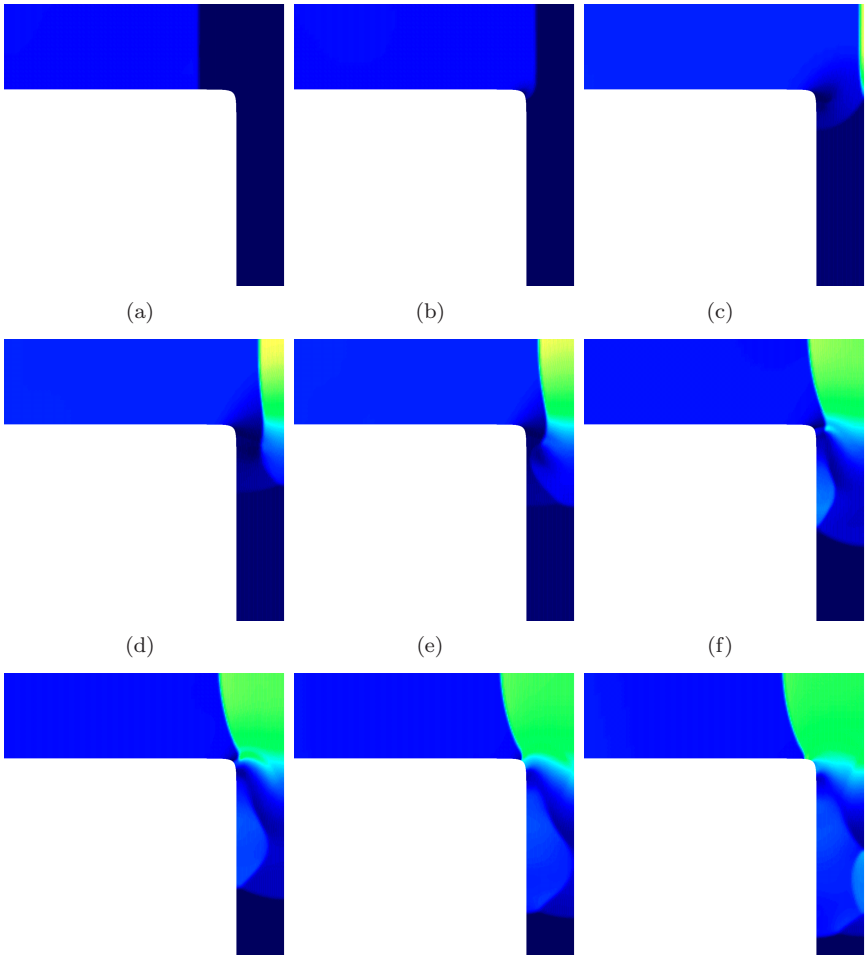

FIGURE 6.3. Pressure plots from simulations in Overture showing the shock wave as it passes the 90° corner of the test section.

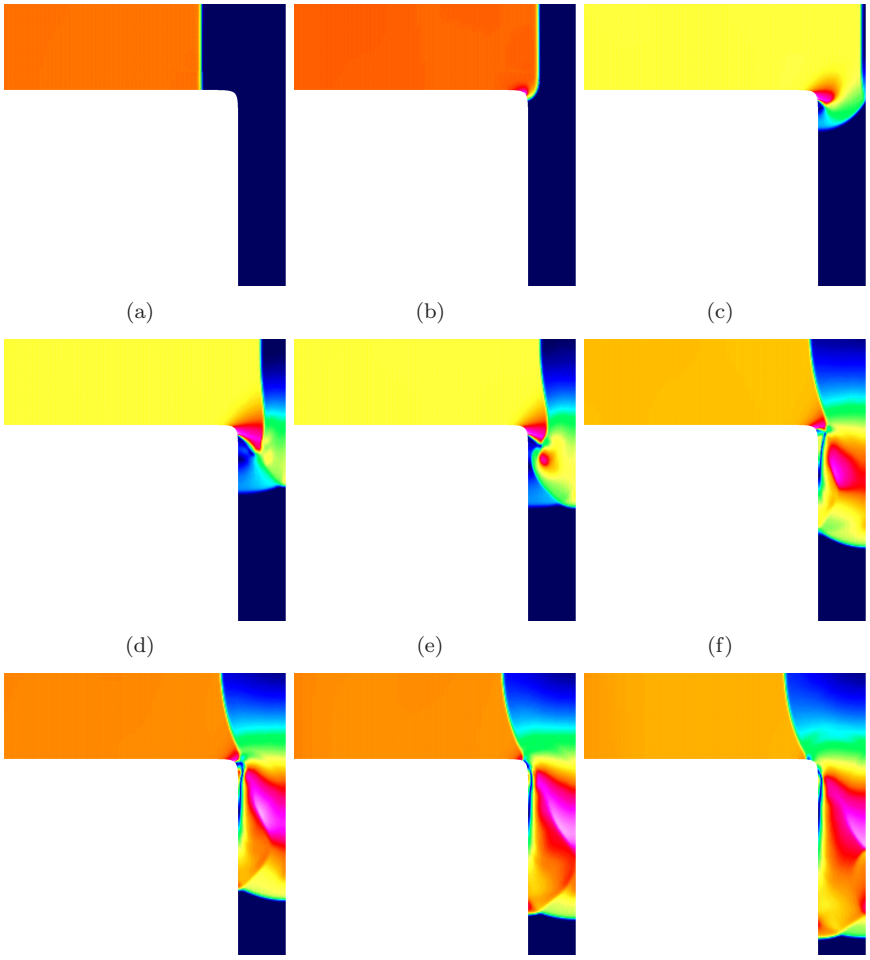

FIGURE 6.4. Simulations in Overture showing the speed of the flow as the shock wave passes the 90° corner of the test section.

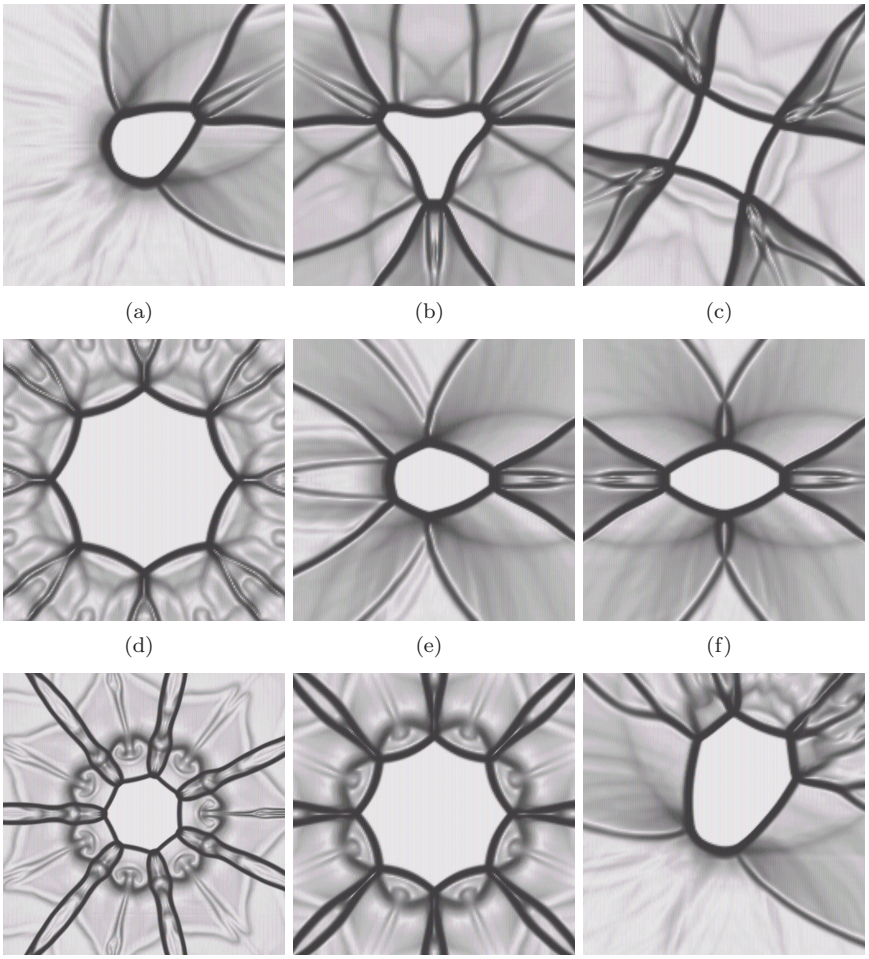

FIGURE 6.5. Schlieren images from simulations in Overture showing shock waves close to the center of convergence for (a) one cylinder, (b) three cylinders, (c) four cylinders, (d) 16 cylinders, (e) two cylinders, 7.5 mm and 15 mm diameter, opposite each other, (f) two cylinders opposite each other, (g) seven cylinders, (h) eight cylinders, and (i) a dense formation of cylinders in one radial direction. The diameter of the cylinders is 15 mm unless otherwise specified.

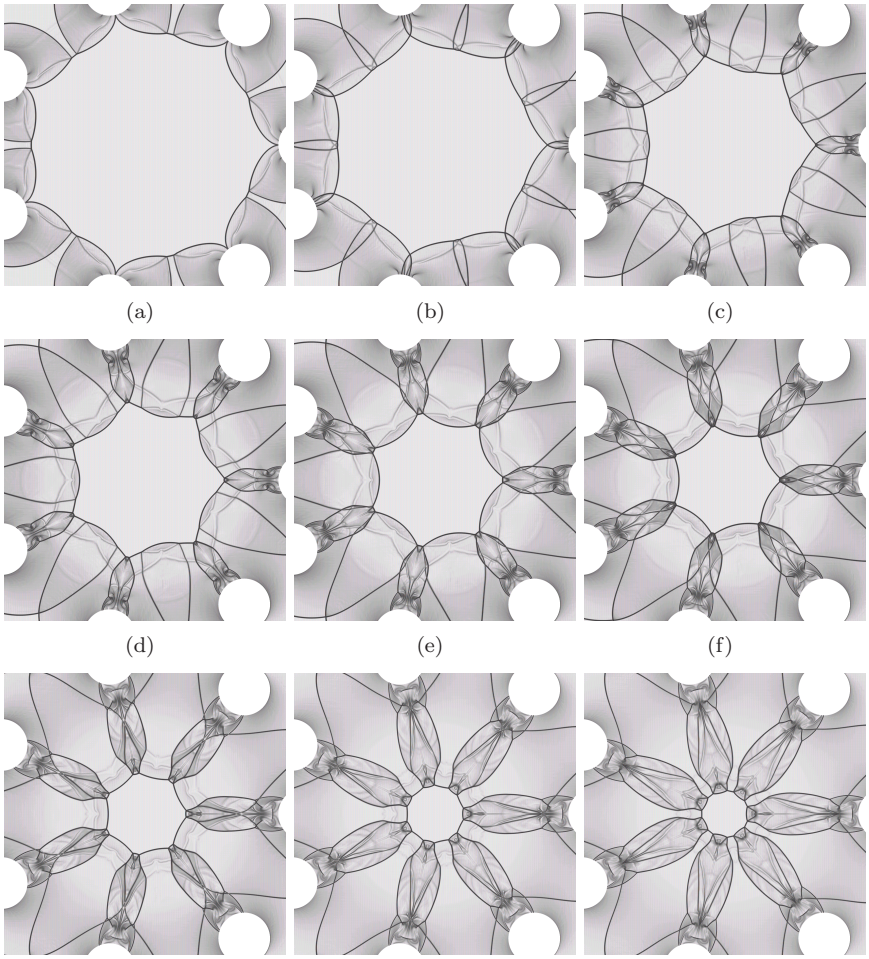

FIGURE 6.6. Schlieren images from simulations in Overture showing an initially cylindrical shock wave diffracted by seven cylinders placed in a symmetric heptagonal pattern. The diameter of the cylinders is 15 mm.

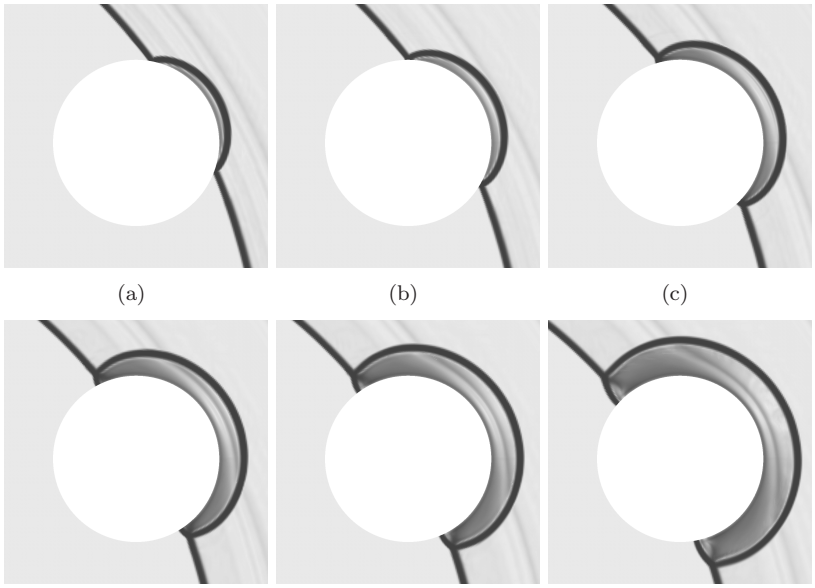

FIGURE 6.7. Schlieren images from simulations in Overture showing the development of the diffracted shock from a cylindrical shock wave hitting a 15 mm diameter cylinder. Regular reflection in (a)–(b) and Mach reflection in (c)–(f).

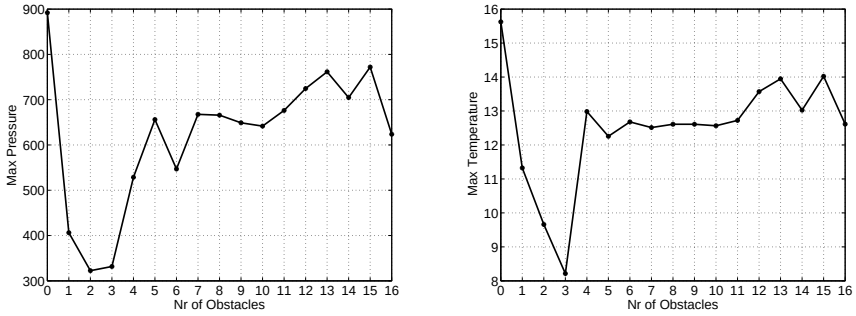

FIGURE 6.8. Maximum dimensionless pressure and temperature near the focal point as a function of the number of cylinders.

CHAPTER 7

An application of shock wave focusing

An application of shock wave focusing is shock wave lithotripsy (SWL), which is a non-invasive treatment to eliminate kidney stones. SWL was developed in the early 1980's and is now the primary treatment for stones in the upper urinary tract. In SWL, shock waves shatter the kidney stones to small fragments which can be passed naturally. This method of removing kidney stones has proven to be very attractive over the alternative method, surgical removal, because it is felt to be safer and more cost-effective. However, SWL is not without adverse effects, such as hemorrhaging, vasoconstriction, and ischemia, occurring especially in young and elderly patients. These problems have inspired researchers during the last two decades to improve lithotripsy technology to minimize tissue injury in SWL.

Three types of lithotripters are in use today: electrohydraulic (EH), piezoelectric (PE), and electromagnetic (EM). The working principles for current lithotripters are all fundamentally the same, and they differ from each other only in terms of overall performance. A lithotripter generates a pressure wave and repeatedly focuses it onto the kidney stone. The pressure wave that hits the kidney stone can be characterized by a leading compressive shock front followed by a long trailing tensile wave. An acoustic wave can be focused to an ideal focal point by an elliptic reflector. Due to hyperbolic effects, the pressure wave in a lithotripter will not focus at a point; instead, the focal point will grow to a region increasing in size with shock strength. Approximately 2000 lithotripter shock waves (LSWs) are generated and focused on the stone during a typical procedure. The frequency is usually 2 Hz. Recent studies, e.g. Pishchalnikov *et al.* (2006), have shown that the stones break better when the shock wave rates are lowered.

The standard lithotripter is an EH reflector called Dornier HM-3. The reflector-based EH lithotripters consist of an ellipsoidal reflector body where a spark generates an outgoing weak shock wave at one of the focal points. This shock wave focuses at the second focal point and is aimed at the kidney stone. In most cases, the working medium inside the reflector is water in the most cases, to mimic the impedance in the human body.

There are five potential mechanisms involved in stone breakage: (1) erosion, (2) spallation, (3) dynamic fatigue, (4) shear, and (5) circumferential

compression. Erosion results from cavitation because impurities in the fluid serve as nucleation sites for bubbles, and the bubbles subjected to an LSW will expand quickly and then collapse violently. The stone erodes as the cavitation clouds collapse against its surface. Spallation is caused by high tensile stresses due to the internal reflections in the stone from the LSW. Dynamic fatigue occurs because the material in the stone is not homogenous, and micro cracks are formed during the repeated cycles of the LSW. Shear forces can be caused by the pressure gradients that exist in the stone as a result of the focusing of the shock wave. Circumferential compression is a result of the velocity difference between the compression pulse in the stone (faster wave speed) and in the surrounding fluid. For further discussions on mechanisms behind stone breakage see Bailey *et al.* (2003) and Lingeman *et al.* (2003). At first, the stone is reduced to smaller chunks, which then grind down to sand-sized particles, which can be passed from the body in a natural way.

The major mechanisms for tissue damage are believed to be cavitation clouds (pre-exsisting bubbles expand and destroy small capillaries, and when they collapse, the formation of strong jets can destroy larger vessels) and shear stresses. To reduce the damage, it is important to understand the mechanisms.

In this chapter, we simulate the wave propagation from a EH reflector. We tested several shapes of the reflector and various materials. To characterize the different cases, we looked at the maximum radius of that a gas bubble would have after being subjected to the resulting pressure field. Furthermore, we investigated the size, location and shape of the region where the largest bubbles occur. The idea was to better understand how the low pressure region could be reduced to a region close to the kidney stone. To remove the low pressure region completely reduces the success in stone fragmentation.

The nonlinear effects in SWL make this subject into an interesting research area for anyone fascinated by shock wave focusing. In the earlier chapters of this thesis, we were mainly interested in the shock front itself but in this chapter we turn our attention to the rarefaction wave, that both helps to fragment the kidney stone and causes tissue damage in the kidney through cavitation.

7.1. Reflection between a liquid-liquid and a liquid-solid interface

The reflection coefficient, R, for an oblique wave hitting an interface between a liquid-liquid layer can be found in Blackstock (2000), and is given by

$$R \equiv \frac{p^-}{p^+} = \frac{Z_2 \cos\theta_i - Z_1 \cos\theta_t}{Z_2 \cos\theta_i + Z_1 \cos\theta_t} = \frac{\sqrt{\frac{p_2}{p_1}\frac{\rho_2}{\rho_1}}\cos\theta_i + \sqrt{1 - \frac{p_2}{p_1}\frac{\rho_1}{\rho_2}\sin^2\theta_i}}{\sqrt{\frac{p_2}{p_1}\frac{\rho_2}{\rho_1}}\cos\theta_i - \sqrt{1 - \frac{p_2}{p_1}\frac{\rho_1}{\rho_2}\sin^2\theta_i}}, \quad (7.1)$$

where $Z_j = \rho_j c_j$ is the impedance of medium j, θ_i is the angle of incidence, and θ_t is the angle of transmission. The index 1 refers to the working medium

and 2 to the reflector. The speed of sound is given by $c_j = \sqrt{np_j/\rho_j}$, where n comes from Tait's equation of state; see chapter 7.4. Snell's law gives the relation between the angles of incidence and transmission as

$$\theta_t = \arcsin(\frac{c_2}{c_1}). \tag{7.2}$$

The reflection coefficient for a liquid-solid interface is given in Brekhovskikh (1960):

$$R = \frac{Z_1 \cos^2 2\gamma_1 + Z_t \sin^2 2\gamma_1 - Z}{Z_1 \cos^2 2\gamma_1 + Z_t \sin^2 2\gamma_1 + Z}, \tag{7.3}$$

where Z, Z_1, and Z_t are the impedances of sound waves in the liquid, and longitudinal and transverse waves in the solid:

$$Z = \frac{\rho c}{\cos\theta}, Z_1 = \frac{\rho_1 c_1}{\cos\theta_1}, Z_1 = \frac{\rho_1 b_1}{\cos\gamma_1}. \tag{7.4}$$

Three different cases will occur depending on how large the angle θ is. For $0 < \sin\theta < c/c_1$, the angles γ_1 and θ_1 are both real; the reflection coefficient is given by equation (7.3) and only transverse waves are present. For the interval $c/c_1 < \sin\theta < c/b_1$, γ_1 is real and θ_1 is complex, which gives the reflection coefficient

$$R = \frac{-i|Z_1| \cos^2 2\gamma_1 + Z_t \sin^2 2\gamma_1 - Z}{i|Z_1| \cos^2 2\gamma_1 + Z_t \sin^2 2\gamma_1 + Z}, \tag{7.5}$$

and there are both transverse and longitudinal waves present. Finally, the interval $c/c_b < \sin\theta$ gives complex angles γ_1 and θ_1 and $|R| = 1$, which means that total internal reflection occurs.

Regular reflection for shock waves in water can be analyzed in the same way as for shock waves in gases, except that the chosen equation of state is different; see Sommerfeld & Miller (1988). The angle of reflection as a function of the incident angle is shown in Figure 7.1. Results show that the maximum value for the angle of reflection decreases when the shock strength is increased. The pressure jump over the reflected shock is greater than the pressure jump for the incident shock, and it increases for increasing angles of incidence.

7.2. The maximum bubble radius

The maximum bubble radius is important because it gives a good measure of how much damage bubbles can potentially do during SWL. The expression for the maximum radius, r_{max}, of an air bubble immersed in a liquid surrounded by a pressure field, $P(t)$, is given in Iloreta *et al.* (2007) and will be summarized here for the convenience of the reader. The work, W, done on a fluid through a spherical bubble is defined as

$$W = \int F dr = \int (PA)\dot{r} dt = 4\pi \int P r^2 \dot{r} dt, \tag{7.6}$$

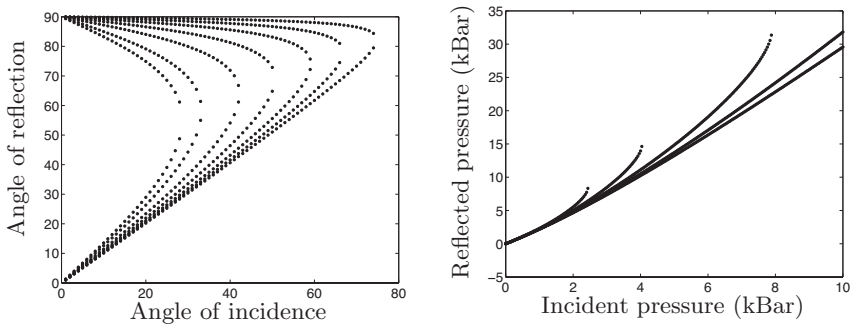

(a) (b)

FIGURE 7.1. (a) The reflection angle as a function of the incidence angle, (b) the reflected pressure as a function of incidence pressure for different angles of of incidence: 20°, 25°, 30°, 35°, 40°. The higher the incidence angle, the higher the reflected pressure.

where $r(t)$ is the radius of the bubble and $\dot{r}(t)$ is the bubble wall velocity. A large range of parameters for typical lithotripters were used to define the expression for the maximum bubble radius as

$$r_{max} = 0.01382 W^{0.337}. \tag{7.7}$$

An energy balance gives an explanation for this expression. At first, before the LSW hits the bubble, the bubble has zero energy. The amount of work done on the liquid, W, by an LSW is the sum of potential, ΔPE, and kinetic energy, ΔKE, $W = \Delta\mathrm{PE} + \Delta\mathrm{KE}$. When the bubble reaches maximum radius, the kinetic energy is converted to potential energy,

$$W = \Delta\mathrm{PE} = \int (\mathrm{p}_\infty - \mathrm{p_b})\mathrm{dV} \approx (\mathrm{p}_\infty - \mathrm{p_v})\frac{4}{3}\pi \mathrm{r}^3_{\mathrm{max}}. \tag{7.8}$$

The bubble pressure, p_b, is the sum of the vapor pressure, p_v and the gas pressure, p_g, within the bubble: $p_b = p_g + p_v$. For the case of an LSW acting on a bubble, the vapor pressure is much larger than the gas pressure, so the gas pressure is neglected in equation (7.8). Now, we see that the exponent 1/3 in equation (7.7) comes from equation (7.8). The coefficient in equation (7.7) is found by using a theoretical reference room temperature of 18°C in equation (7.8), and this gives a slightly different value of 0.01331.

7.3. The Rayleigh-Plesset equation

The Rayleigh-Plesset (RP) equation is a reduction of the Navier-Stokes equations to an ordinary differential equation. It is used to describe bubble dynamics for spherical gas bubbles surrounded by an incompressible liquid. Rayleigh's

theories for bubbles might seem inappropriate at first, because he considered a bubble in an incompressible fluid subject to a spatially uniform pressure. In the case of a lithotripter, the flow can be considered incompressible, but the pressure is changing during the passage of the LSW. However, the bubble radius (on the order of microns) is much smaller than the focal region (a couple of millimeters) where the maximum pressures occur; see Howle *et al.* (1998). Hence, the Rayleigh theory is widely used for bubble dynamics in lithotripsy.

To describe the bubble dynamics, we use a simplified version of the RP equation given by Hilgenfeldt *et al.* (1998):

$$\rho_l\left(r\dot{r}+\frac{3}{2}\dot{r}^2\right)=P(t). \tag{7.9}$$

This simplified version gives good results and works well for determining the work done by the bubble on the fluid, and thus it gives the maximum bubble radius, as explained by Iloreta *et al.*

7.4. Problem setup

The two dimensional Euler equations with radial symmetry are used to model the wave propagation inside the lithotripter:

$$\frac{\partial}{\partial t}\mathbf{q}+\frac{\partial}{\partial r}\mathbf{F}(\mathbf{q})+\frac{\partial}{\partial z}\mathbf{G}(\mathbf{q})=\mathbf{S}(\mathbf{q}), \tag{7.10}$$

where

$$\mathbf{q}=\begin{pmatrix}\rho\\ \rho u\\ \rho v\\ \rho e\end{pmatrix},\ \mathbf{F}(\mathbf{q})=\begin{pmatrix}\rho u\\ \rho u^2+p\\ \rho uv\\ (\rho e+p)u\end{pmatrix}, \tag{7.11}$$

$$\mathbf{G}(\mathbf{q})=\begin{pmatrix}\rho v\\ \rho uv\\ \rho v^2+p\\ (\rho e+p)v\end{pmatrix},\ \mathbf{S}(\mathbf{q})=\begin{pmatrix}-\frac{1}{r}\rho u\\ -\frac{1}{r}\rho u^2\\ -\frac{1}{r}\rho uv\\ -\frac{1}{r}(\rho e+p)u\end{pmatrix}, \tag{7.12}$$

and ρ is the fluid density, u is the axial velocity, v is the radial velocity, and p is the pressure. As equation of state, we use the Tait equation,

$$p_{\text{Tait}}\equiv p+B=(B+1)\big(\frac{\rho}{\rho_0}\big)^n. \tag{7.13}$$

This is the isentropic relationship between the density and the pressure for water. In our numerical experiments, we used $B=3000$ and $n=7$. The values for densities and wave speeds in the reflector and the working media, used for the numerical simulations, are shown in Table 1.

Media	density (kg/m^3)	c (m/s)	c_1 (m/s)	$b_1(m/s)$
water	1000	1482	–	–
brass	8600	–	4073	2114

TABLE 1. Density and wave speed for the reflector and the water used in the numerical simulations.

7.4.1. *CLAWPACK*

The numerical simulations have been performed with CLAWPACK. CLAWPACK (Conservation LAW PACKage) is a free package of `FORTRAN77` subroutines suitable for solving hyperbolic partial differential equations numerically. The software can solve linear and nonlinear problems in one, two, and three space dimensions; see Leveque (2002). The package can be downloaded from the CLAWPACK site, `http://www.amath.washington.edu/~claw/`. A finite volume method is used where a Riemann problem is solved at each grid cell interface by the Godunov method.

7.4.2. *The reflector*

An axisymmetric model is used to represent the lithotripter reflector. The reflector is modeled by a density jump across the prescribed reflector boundary. First, the reflection coefficient is calculated as described in section 7.1. The value of the reflection coefficient is a function of the axial position and the incident angle, θ_i, between a ray emanating from F_1 and the point on the reflector. The reflection coefficient for the original case is shown in Figure 7.2. The density ratio across the reflector boundary is given by equation (7.1). If the density ratio approaches infinity, then $R \to 1$, and to keep the code stable we set $R = 0.993$. The shape of the reflector is varied by changing the eccentricity of the elliptical shape. The material of the reflector was set by changing the density, longitudinal and transversal wave speeds of the material. A list of all tested cases are shown in Table 2.

The size of the computational domain in the serial simulations was set to 1025x350 cells corresponding to 32.8x11.2 cm^2. The time step was set to a fixed value of $4.0 \cdot 10^{-8}$ s. The 'save domain', i.e. the domain where pressure data in every time step was saved to compute the maximum bubble radius, was a 60x7.5 mm^2 region, shown in Figure 7.3 as the dark gray region. For the parallel simulations, the computational domain was set to 3600x2400 cells corresponding to 36x24 cm^2, and the time step was set to $2.5667 \cdot 10^{-8}$ s. The save domain in the parallel simulations was a 21.8x7.75 cm^2 region, and is the light gray region in Figure 7.3. Five cases of the modified reflector are shown in Figure 7.4.

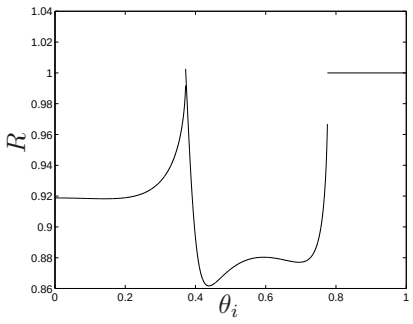

FIGURE 7.2. The reflection coefficient, R, as a function of the incident angle, θ_i, for a water-brass interface, for the original case.

Case	Eccentricity	b	c	ρ
I	0.81	2114	4073	8600
II	0.82	2114	4073	8600
III	0.83	2114	4073	8600
IV	0.84	2114	4073	8600
V	0.85	2114	4073	8600
VI	0.8274	2114	4073	8600
VII	$0.80 + f(x)$	2114	4073	8600
VIII	$0.85 - f(x)$	2114	4073	8600
IX	0.8274	2236	4237	8800
X	0.8274	2148	4803	8670
XI	0.8274	2165	4842	8530
XII	0.8274	2032	4668	8470
XIII	0.8274	3181	5850	7850
XIV*	0.8274	2114	4073	8600

TABLE 2. A list of all cases in the numerical simulations. Here $f(x) = 0.05\,(x - x_{\min})/(x_{\max} - x_{\min})$, where $x \in [x_{\min}, x_{\max}] = [0.004, 0.128]$. Case XIV had a reflection coefficient close to unity, $R = 0.993$.

7.5. Results

The maximum bubble radius, given by equation (7.7), was calculated for the various cases shown in Table 2. The initial bubble radius was set to 4.5 μm and the time interval for the integration of the work W was set to 20 μs; see equation (7.6). The results show that the eccentricity influences both the region

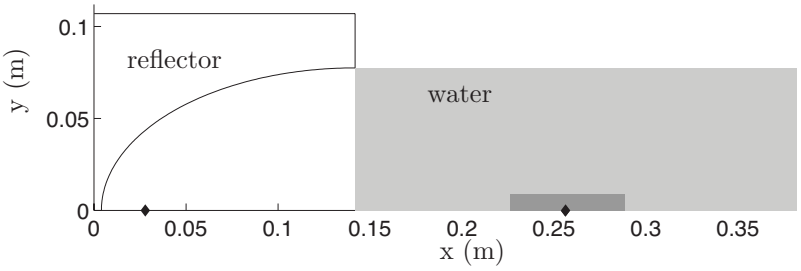

FIGURE 7.3. The computational domain. The light gray region is the save domain for the parallel simulations and the dark gray region is the save domain for the serial simulations.

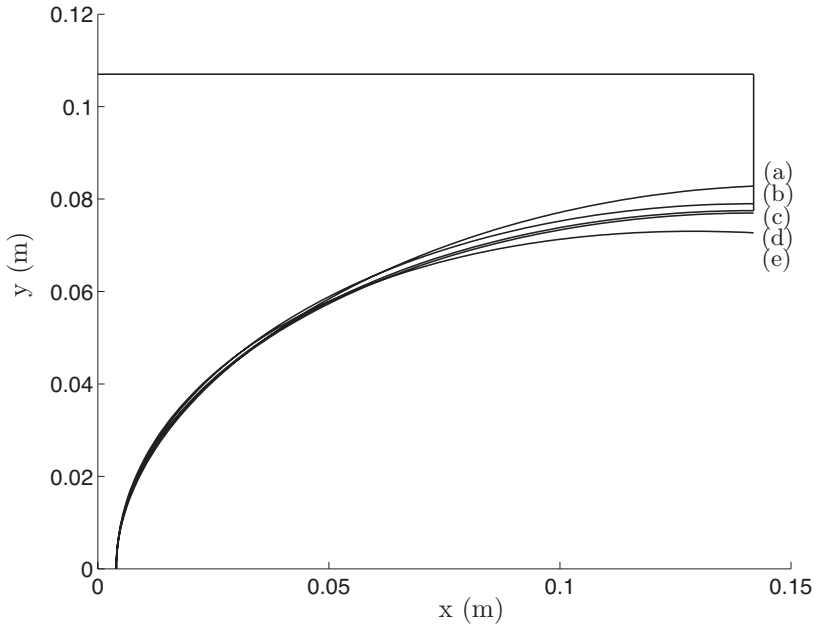

FIGURE 7.4. Examples of various reflectors used in the simulations; (a) $e = 0.85 - f(x)$, (b)$e = 0.82$, (c)$e = 0.8274$, (d) $e = 0.83$, and (e) $e = 0.80 + f(x)$.

where the maximum bubble radius exists and the value of the maximum radius. Contour plots of the maximum bubble radius from the serial simulations are shown in Figures 7.5 and 7.6. The results from the cases with different

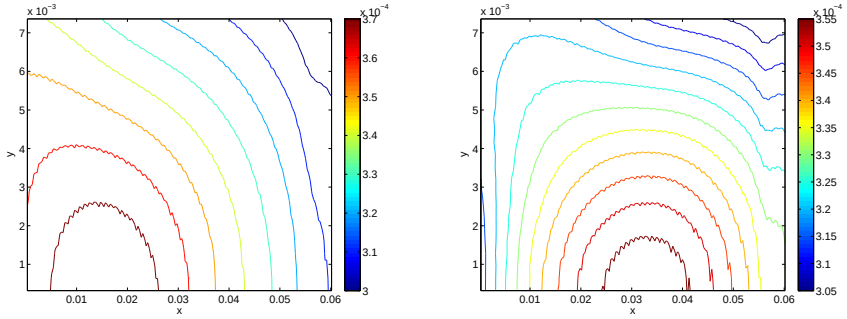

(a) Case VI, $e = 0.8274$

(b) Case I, $e = 0.81$

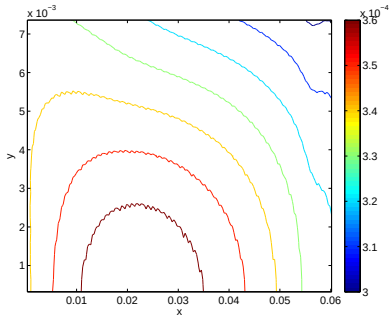

(c) Case II, $e = 0.82$

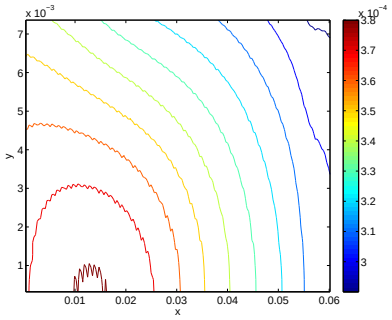

(d) Case III, $e = 0.83$

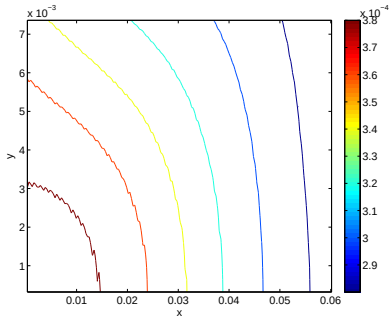

(e) Case IV, $e = 0.84$

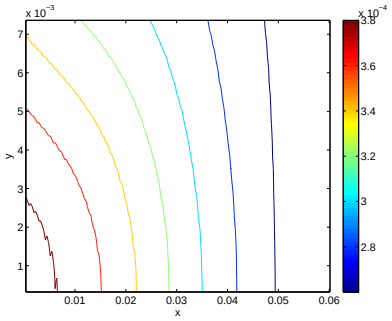

(f) Case V, $e = 0.85$

FIGURE 7.5. The maximum bubble radius for reflectors with a constant eccentricity, e. Serial simulations.

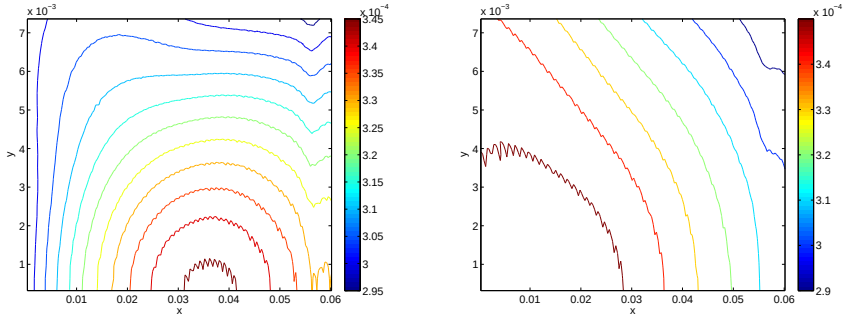

(a) Case VII, $e = 0.80 + f(x)$ (b) Case VIII, $e = 0.85 - f(x)$

FIGURE 7.6. The maximum bubble radius for reflectors with an eccentricity as a function of x, $e(x)$. Serial simulations.

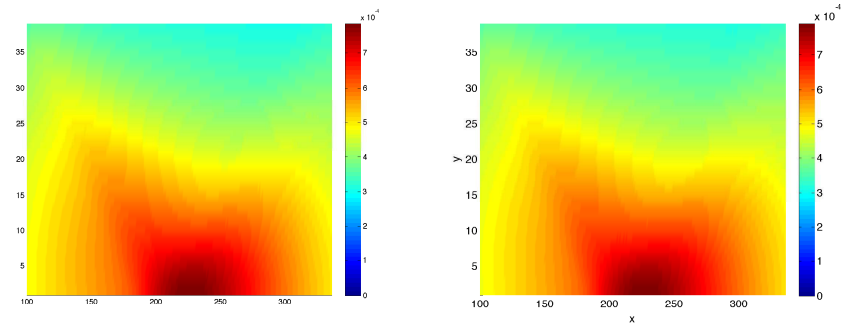

(a) Case VI, $R = R(\theta_i)$. (b) Case XIV, $R = 1$.

FIGURE 7.7. The maximum bubble radius for the original reflector shape with (a) $R = R(\theta_i)$, and (b) $R = 0.993$. Parallel simulations.

materials showed no variation in the maximum bubble radius, as compared to the original case. Results from the parallel simulations for the original reflector shape with both a varying reflection coefficient (see Figure 7.2) and a reflection coefficient close to unity, $R = 0.993$, are shown in Figure 7.7. The maximum bubble radius is about 1 mm.

Results from serial simulations of cases IX-XIV showed no difference in the pressure field as compared to case VI with the original setup. This means that the value of the material and thus the reflection coefficient of the reflector do not have a large influence on the maximum bubble radius.

The criteria for choosing a reflector with better characteristics are (1) the size of the low pressure region should be decreased and (2) the focal point can not be translated towards the first focal point; it should either be at the same place as for the original case or translated towards increasing x-values. If the focal point would be translated towards negative x-values, it might not be possible to fragment kidney stones as far into the human body as in the original reflector, thus reducing the range of patients were it could be used. The results from the serial simulations show that the best choice is case VII (see Table 2), since the maximum bubble radius is minimized and the focal point is moved slightly towards increasing x-values.

7.6. Remarks

The assumption of a bubble inside the computational domain will cause a disturbance in the flow field, and we do not take that disturbance into account. Since the choice of material does not seem to influence the maximum bubble radius, it is possible that the reflection coefficient does not matter, and we could use a reflection coefficient equal to unity everywhere on the reflector.

The parallel simulations were run on DataStar at San Diego Supercomputer Center, USA. A typical simulation used 600 processors during a total run time of 20 minutes. If the computation time could be reduced, say by using adaptive mesh refinement, then it would be useful to optimize the shape of the reflector by some well-known optimization method, such as the adjoint method.

CHAPTER 8

Conclusions and outlook

In this chapter, we summarize the most important conclusions and contributions from the present study. For more details and further discussions, the reader is referred to the papers in section 2 of this thesis.

8.1. Experiments on shock wave focusing

- Polygonal converging shock waves can be produced by an appropriate choice of the shape of the reflector boundary or by introducing cylindrical obstacles in a specific pattern in the flow. Polygon-shaped shock waves are stable in the sense that the evolution of the shape is predictable and bounded.
- Regular reflection has been observed for an equilateral triangular-shaped converging shock. This is in agreement with earlier numerical studies by Aki & Higashino (1990); Betelu & Aronson (2001).
- Mach reflection has been observed for polygonal shapes with more than three sides: square pentagon, heptagon, octagon and double octagon formations. The experimental results agree well with earlier analytical and numerical results from Schwendeman & Whitham (1987); Apazidis & Lesser (1996); Aki & Higashino (1990).
- The final form of the converging shock, close to the center of convergence, is square-like for the circular and octagonal reflector boundaries. This is caused by the perturbations in the flow due to the four supports in the annular part of the shock tube. The square-like shape is not present when the pentagonal and heptagonal reflector boundaries are used. A possible explanation is that a disturbance with an even number of modes cannot overtake a disturbance with an uneven number of modes if the size of the disturbance is approximately the same in both cases. Also, the square-like shape is missing in all cases when the cylindrical obstacles are present. This means that the disturbances from the obstacles are stronger than the disturbances from the supports. Disturbances from the supports were also observed in experiments performed in Takayama *et al.* (1984, 1987); Watanabe *et al.* (1995).
- The reflected shock initially has a circular symmetry for all four reflector boundaries. The shock wave retains its circular symmetry in the case of the circular reflector. For the other reflectors, the shape of the

outgoing shock is influenced by the flow field created by the converging shock. The shape of the shock approaches the same shape it had when it converged but with smooth features. This is in agreement with the numerical simulations by Aki & Higashino (1990). When the cylindrical obstacles were present, the reflected shock was circular; no photographs were taken late enough to show if the shape of the shock front becomes influenced by the flow ahead of it.

- Light emission is always produced when the shock collapses. Light emission was also observed in earlier experiments by Perry & Kantrowitz (1951); Saito & Glass (1982); Matsuo *et al.* (1985). The full width at half maximum of the light pulse was longer in the experiments by Matsuo *et al.* A reasonable explanation is that the conditions in the two experiments were not the same; gas mixtures, pressures, shapes of the shock wave, etc. were different.
- The amount of light emission depends on three main parameters:
    - The shape of the shock close to the center of focusing: a shape as close as possible to a circle produces more light than for example an asymmetric shape. For example, an octagonal shaped shock produces more light than a shock shaped as a tear-drop, as in the case with one cylinder.
    - The test gas: as test gas, argon produces more light during the focusing than air. This is in agreement with experiments on shock wave focusing by Perry & Kantrowitz (1951) and correlates with results of experiments on sonoluminescence by Hiller *et al.* (1994).
    - Number of cylindrical disturbances: the unperturbed circular shock produces the most light. For all other cases a certain amount of the flow is reflected back before it reaches the focal point, and hence the energy density at the focal point is maximized for the circular case.

8.1.1. *Outlook*

A big experimental challenge that remains is to produce a converging cylindrical shock in a facility without disturbances. Shock tubes are hard to use to accomplish this because there will be disturbances from the equipment itself. A first step would be to use a setup like the one in the present study and then add lots of tiny cylinders to create a polygonal shape with a large number of sides. This will create a shape very close to cylindrical. The present experimental setup could be improved by a redesign of the sharp 90° corner of the shock tube, where the gas enters the test section. Several examples of more effective corner designs are available in the literature, see for example Wu *et al.* (1980); Takayama (1978). An improvement in the corner design would enhance the performance of the experiment; an increased amount of gas would reach the test section and the transmitted shock would stabilize faster. We strongly

suggest performing a numerical study of the flow before finalizing the design of the new corner. Another improvement would be to increase the sensitivity of the schlieren optics system to visualize finer details of the converging shock. It would be interesting to compare the amount of light emission produced by different shapes of shock waves that focus with the same amount of energy at the center. For example, a cylindrical shock could be compared to an octagonal shock with an equal amount of flow reaching the focal point. Also, a spectra of the light emission that occurs during the focusing should be investigated. The spectra could then be compared to the spectra from other fluid mechanics applications where light emission occurs, for example sonoluminescence. Furthermore, an estimation of temperatures during the focusing process could be obtained via the spectral measurements. The optimal gas mixture for light emission should be found. In sonoluminescence, a small percentage of the test gas is argon, compared to our experiments where most of the test gas is argon.

8.2. Simulations of shock wave focusing

- The numerical schlieren plots are in good agreement with experimental results.
- The shock speeds of the converging and reflecting shocks are in good agreement with experimental results.
- Regular reflection was observed for the triangular case and Mach reflection was observed for the cases with 4–16 cylinders.
- The Euler equations with an ideal gas assumption constitutes a good model, except when the shock is very close to the focal point and real gas effects are important.
- The self similar stage for the polygonal converging shocks is only reached during the last stages of the focusing process. For the triangle, the self-similar exponent depends on the direction in which the location of the shock front is measured. For the two directions measured here, the exponents were $\alpha = 0.977$ and $\alpha = 1.155$, compared to the expected value of one. The square-shaped shock undergoes Mach reflection, and the self-similar exponent was found to be $\alpha = 0.835$ in agreement with earlier published results.
- The highest maximum pressure and temperature measured near the focal point occurred for the case with no obstacles. With a small number of obstacles, 1–6, the maximum pressure and temperature were lower than with a large number of obstacles, 7–16.

8.2.1. *Outlook*

It is still an open question of what model should be used near the vicinity of the focal point where real gas effects are important and ionization occurs. A first step would be to change the equation of state from the ideal gas law to something more appropriate. Studies by Britan *et al.* (2004) on plane shock

waves perturbed by various shaped barriers (with the same porosity) showed no effect on the pressure behind the barrier. It would be interesting to study the effect of the porosity in this setup to see if the shape and blockage ratio effect the maximum pressure and temperature obtained at the focal point.

8.3. Simulations of weak shock wave focusing in a lithotriptor

- The Euler equations with Tait's equation as equation of state serves as a good model.
- The shape of the reflector has a large impact on the maximum bubble radius.
- The material of the reflector does not have a large influence on the maximum bubble radius.

8.3.1. *Outlook*

There is a need to implement adaptive mesh refinement to reduce the computation time. The same problem will be implemented and simulated by the Overture suite, where AMR and overlapping grids can be used.

CHAPTER 9

Papers and authors contributions

Paper 1

Focusing of strong shocks in an annular shock tube.
V. Eliasson (VE), N. Apazidis (NA), N. Tillmark (NT) & M. B. Lesser, *Shock Waves*, **15**, 205–217 (2006).

The experimental work and the evaluation were performed by VE. NT assisted during the experiments. The numerical simulations were performed by NA. The paper was written by the three authors jointly.

Paper 2

Controlling the form of strong converging shocks by means of disturbances.
V. Eliasson, N. Apazidis & N. Tillmark, *Shock Waves*, **17**, 29–42 (2007).

The experiments and the evaluation of data were performed by VE. NT supervised the experiments. The numerical simulations were performed by NA. The paper was written by VE and NA jointly.

Paper 3

The production of converging polygonal shock waves by means of reflectors and cylindrical obstacles.
V. Eliasson, *AIP Conference Proceedings*, **832**, 445–449 (2006).

Paper 4

Regular versus Mach reflection for converging polygonal shocks.
V. Eliasson, M. Kjellander (MK) & N. Apazidis, *Shock Waves*, **17**, 43–50 (2007).

The experiments where performed by VE. MK provided supplementary experimental results. The paper was written by VE with feedback from NA.

Paper 5

Light emission during shock wave focusing in air and argon.
V. Eliasson, N. Tillmark, A. J. Szeri (AJS) & N. Apazidis, *submitted to Physics*

of Fluids, (2007).

The experiments and the numerical simulations where performed by VE. NT helped during the setup of the experiment. AJS provided ideas for the numerical simulations. The paper was written mainly by VE with feedback from AJS. NT and NA provided comments on the paper.

Paper 6

An experimental and numerical investigation of polygonal converging shock waves.
V. Eliasson, W.D. Henshaw & D. Appelö, *submitted to EE250 Proceedings* (2007).

The work and the writing of the paper was done by the three authors jointly.

Acknowledgements

The Swedish Research Council (VR) and KTH Mechanics are acknowledged for the financial support. The funding from Göran Gustafsson Foundation provided means for the construction of the shock tube and for acquisition of the experimental equipment. Stiftelsen Lars Hiertas Minne, 21st Century COE of Flow Dynamics, Fonden för Erik Petersohns Minne, and NSF provided funding for international conference visits. Bengt Ingeströms Stipendiefond and Helge Ax:son Johnsons Stiftelse financially supported the visit at UC Berkeley and are greatly acknowledged.

First of all I would like to thank my supervisor Dr. Nicholas Apazidis, and my co-supervisor Dr. Nils Tillmark for accepting me as their student and their help and support in every part of this work. I would also like to thank Prof. Henrik Alfredsson for enthusiastically sharing his knowledge in compressible flows. Prof. Emeritus Martin B. Lesser is acknowledged for initiating the project.

Many thanks to Prof. Andrew J. Szeri for the warm welcome to his lab group at UC Berkeley, and for providing computer resources at both UCB and SDSC. The year I spent in your lab at UCB was great.

I would like to express my gratitude to Dr. William D. Henshaw from who I have learnt many things, and for all those hours of both Overture and cycling adventures. I also want to thank Prof. D.W. Schwendeman for valuable discussions and for making the first overlapping grids in Overture for me. Further, I wish to thank Prof. Gunilla Kreiss for much useful advice throughout the course of this work, and many pleasant days at Träskö-Storö. I would also like to thank Ulf Landén and Marcus Gällstedt for the skillful manufacturing of the experimental equipment. Jonathan Iloreta, you taught me many things, from the working principles of SWL to how to handle parallel codes and I really appreciate it. Beth Lopour, not only did you read and comment the whole thesis, also, you always had time for discussions whether it concerned Bessel functions or chili recipes. I would like to thank all my friends and colleagues, especially Allan, Bengt, Calle, Fredrik, Gabriele, Jens, Jun, Kim, Luca F, Nicola, Ramis, Thomas H, Thomas K, and Timmy.

Thanks to my family for their support and encouragement during my studies.

Finally, I would like to thank Daniel for your love and support. Everything is so much funnier when you are around.

References

Aki, T. & Higashino, F. 1990 A numerical study on implosion of polygonally interacting shocks and consecutive explosion in a box. *Current topics in shock waves; Proc. of the Int. Symp. on Shock Waves and Shock Tubes, 17th, Bethlehem, PA, July 17-21, 1989 (A91-40576 17-34). New York, AIP* pp. 167–172.

Anderson, J. D. 1990 *Modern Compressible Flow*. New York, McGraw-Hill Publishing Company.

Apazidis, N. & Lesser, M. B. 1996 On generation and convergence of polygonal-shaped shock waves. *J. Fluid Mech.* **309**, 301–319.

Apazidis, N., Lesser, M. B., Tillmark, N. & Johansson, B. 2002 An experimental and theoretical study of converging polygonal shock waves. *Shock waves* **12**, 39–58.

Bailey, M. R., Crum, L. A., Evan, A. P., McAteer, J. A., Jr., J. C. W., Sapozhnikov, O. A., Cleveland, R. O. & Colonius, T. 2003 Cavitation in shock wave lithotripsy. *Fifth international symposium on cavitation, Osaka, Japan* Paper OS-2-1-006.

Barbosa, F. J. & Skews, B. W. 2002 Experimental confirmation of the von neumann theory of shock wave reflection transition. *J. Fluid Mech.* **472**, 263–282.

Ben-Dor, G. 1981 Relation between the first and the second triple-point trajectory angles in double mach reflection. *AIAA J.* **19**, 531–533.

Ben-Dor, G. 1992 *Shock wave reflection phenomena*. Springer-Verlag New York Inc.

Ben-Dor, G. 2006 A state-of-the-knowledge review on pseudo-steady shock-wave reflections and their transition criteria. *Shock waves* **15**, 277–294.

Betelu, S. I. & Aronson, D. G. 2001 Focusing of noncircular self-similar shock waves. *Phys. Rev. Lett.* **87** (7), 074501.

Blackstock, D. T. 2000 *Fundamentals of physical acoustics*. John Wiley & Sons.

Book, D. L. & Löhner, R. 1990 Simulation and theory of the quatrefoil instability of a converging cylindrical shock. *Current topics in shock waves; Proc. of the Int. Symp. on Shock Waves and Shock Tubes, 17th, Bethlehem, PA, July 17-21, 1989 (A91-40576 17-34). New York, AIP* pp. 149–154.

Brekhovskikh, L. M. 1960 *Waves in layered media*. Academic Press, New York.

Britan, A., Karpov, A. V., Vasilev, E. I., Igra, O., Ben-Dor, G. & Shapiro, E. 2004 Experimental and numerical study of shock wave interaction with perforated plates. *J. of Fluids Eng.* **126** (3), 399–409.

Bryson, A. E. & Gross, R. W. F. 1961 Diffraction of strong shocks by cones, cylinders, and spheres. *J. Fluid Mech.* **10**, 1–16.

Chesshire, G. & Henshaw, W. 1990 Composite overlapping meshes for the solution of partial differential equations. *J. Comp. Phys.* **1**, 1–64.

Courant, R. & Friedrichs, K. O. 1948 *Supersonic Flow and Shock Waves*. Intersciences publishers Inc. New-York.

Demmig, F. & Hehmsoth, H.-H. 1990 Model computation of converging cylindrical shock waves - initial configurations, propagation, and reflection. *Current topics in shock waves; Proc. of the Int. Symp. on Shock Waves and Shock Tubes, 17th, Bethlehem, PA, July 17-21, 1989 (A91-40576 17-34). New York, AIP* pp. 155–160.

Edwards, D. H., Fearnley, P. & Nettleton, M. A. 1983 Shock diffraction in channels with 90° bends. *J. Fluid Mech.* **132**, 257–270.

Eliasson, V. 2006 The production of converging polygonal shock waves by means of reflectors and cylindrical obstacles. *AIP Conference Proceedings* **832**, 445–449.

Eliasson, V., Apazidis, N. & Tillmark, N. 2007 Controlling the form of strong converging shocks by means of disturbances. *Shock waves* **17**, 29–42.

Eliasson, V., Apazidis, N., Tillmark, N. & Lesser, M. B. 2006 Focusing of strong shocks in an annular shock tube. *Shock waves* **15**, 205–217.

Fong, K. & Ahlborn, B. 1979 Stability of converging shock waves. *Phys. Fluids* **22**, 416–421.

Gompf, B., Günther, R., Nick, G., Pecha, R. & Eisenmenger, W. 1997 Resolving sonoluminescence pulse width with time-correlated single photon counting. *Phys. Rev. Lett.* **79**, 1405–1408.

Guderley, G. 1942 Starke kugelige und zylindrische verdichtungsstöße in der nähe des kugelmittelpunktes bzw. der zylinderachse. *Luftfahrt Forsch* **19**, 302–312.

Henshaw, W. D. 2003 Overblown: A fluid solver for overlapping grids, reference guide, version 1.0. Lawrence Livermore National Laboratory.

Henshaw, W. D. & Schwendeman, D. W. 2003 An adaptive numerical scheme for high-speed reactive flow on overlapping grids. *J. Comput. Phys.* **191**, 420–447.

Henshaw, W. D. & Schwendeman, D. W. 2006 Moving overlapping grids with adaptive mesh refinement for high-speed reactive and non-reactive flow. *J. Comput. Phys.* **216** (2), 744–779.

Henshaw, W. D., Smyth, N. F. & Schwendeman, D. W. 1986 Numerical shock propagation using geometrical shock dynamics. *J. Fluid Mech.* **171**, 519–545.

Hilgenfeldt, S., Brenner, M. P., Grossman, S. & Lohse, D. 1998 Analysis of rayleigh-plesset dynamics for sonoluminescing bubbles. *J. Fluid Mech.* **365**, 171–204.

Hiller, R., Weninger, K., Putterman, S. J. & Barber, B. P. 1994 Effect of noble gas doping in single-bubble sonoluminescence. *Science* **266**, 248–250.

Hornung, H. 1986 Regular and Mach reflection of shock waves. *Annu. Rev. Fluid Mech.* **18**, 33–58.

Hornung, H. G., Oertal, H. J. & Sandeman, R. J. 1979 Transitions to Mach reflection of shock waves in steady and pseudo steady flow with and without relaxation. *J. Fluid Mech.* **90**, 541–560.

Hosseini, S. H. R. & Takayama, K. 2005 Implosion from a spherical shock wave reflected from a spherical wall. *J. Fluid Mech.* **530**, 223–239.

Howle, L., Schaeffer, D. G., Shearer, M. & Zhong, P. 1998 Lithotripsy: The treatment of kidney stones with shock waves. *SIAM Rev.* **40**, 356–371.

Iloreta, J., Szeri, A., Zhou, Y., Sankin, G. & Zhong, P. 2007 Assessment of shock wave lithotripters via cavitation potential. *Phys. Fluids* (In press).

Johansson, B. 2000 Experimental study of shock wave focusing in a confined reflector. Licentiate Thesis, TRITA-MEK Tech. Rep. 2000:04.

Knystautas, R., Lee, B. H. K. & Lee, J. H. S. 1969 Diagnostic experiments on converging detonations. *Phys. Fluids. Suppl.* **1**, 165–168.

Knystautas, R. & Lee, J. H. 1967 Spark initiation of converging detonation waves. *AIAA J.* **5**, 1209–1211.

Knystautas, R. & Lee, J. H. 1971 Experiments on the stability of converging cylindrical detonations. *Combust. and Flame* **16**, 61–73.

Leveque, R. J. 2002 *Finite volume methods for hyperbolic problems*. Camebridge university press.

Liepmann, H. W. & Roshko, A. 1957 *Elements of gas dynamics*. John Wiley & Sons, Inc. New York.

Lingeman, J. E., Kim, C. S., Kuo, R. L., McAteer, J. A. & Evan, A. P. 2003 Shockwave lithotripsy: Anecdotes and insights. *J. Enduorol* **17**, 687–693.

Matsuo, H., Ebihara, K. & Ohya, Y. 1985 Spectroscopic study of cylindrically converging shock waves. *J. Appl. Phys.* **58** (7), 2487–2491.

Mouton, C. A. 2006 Transition between regular reflection and Mach reflection in the dual-solution domain. PhD thesis, California Institute of Technology.

Neemeh, R. A. & Ahmad, Z. 1986 Stability and collapsing mechanism of strong and weak converging cylindrical shock waves subjected to external perturbation. *Shock waves and shock tubes; Proc. of the 15th Int. Symp., Berkeley, CA, July 28-August 2, (A87-12576 02-34). Stanford, CA, Stanford Univ. Press* pp. 423–430.

von Neumann, J. 1943 *Collected Works VI*. Pergamon, New York.

Oppenheim, A. K., Urtiew, P. A. & Weinberg, F. J. 1966 On the use of laser light sources in schlieren-interferometer systems. *Proc. of the Royal Society of London. Series A, Mathematical and Physical Sciences* **291**, 279–290.

Perry, R. W. & Kantrowitz, A. 1951 The production and stability of converging shock waves. *J. Appl. Phys* **22**, 878–886.

Pishchalnikov, A., McAteer, J. A. Jr., J. C. W., Pishchalnikova, I. V. & Vonderhaar, R. J. 2006 Why stones break better at slow shockwave rates than at fast rates: In vitro study with a research electrohydraulic lithotripter. *J. Endourol.* **20**, 537–541.

Roig, R. A. & Glass, I. I. 1977 Spectroscopic study of combustion-driven implosions. *Phys. Fluids.* **20**, 1651–1656.

Saito, T. & Glass, I. I. 1982 Temperature measurements at an implosion focus. *Proc. R. Soc. Lond.* **A 384**, 217–231.

Schwendeman, D. W. & Whitham, G. B. 1987 On converging shock waves. *Proc. R. Soc. Lond.* **A413**, 297–311.

Settles, G. S. 2000 Airflow visualization in a model greenhouse. *Proc. 15th Intl. Congr. for plastics in agriculture, Hershey, PA* pp. 88–98.

Settles, G. S. 2001 *Schlieren and shadowgraph techniques, Visualizing phenomena in transparent media*. Springer Berlin.

Sommerfeld, M. & Miller, H. M. 1988 Experimental and numerical studies of shock wave focusing in water. *Exp. Fluids* **6**, 209–216.

Ames Research Staff 1953 Equations, tables, and charts for compressible flow. *Tech. Rep.* 1135. Ames Aeronautical Laboratory.

Sturtevant, B. & Kulkarny, V. A. 1976 The focusing of weak shock waves. *J. Fluid Mech.* **73**, 651–671.

Sun, M. & Takayama, K. 2003 An artificially upstream flux vector splitting scheme for the Euler equations. *J. Comput. Phys.* **189**, 305–329.

Takayama, K. 1978 Shock propagation along 90 degree bends. *Shock tube and shock wave research; Proc. of the 11th Int. Symp., Seattle, Wash., July 11-14, 1977. (A79-15207 04-34) Seattle, Wash., University of Washington Press* pp. 74–81.

Takayama, K., Kleine, H. & Grönig, H. 1987 An experimental investigation of the stability of converging cylindrical shock waves in air. *Exp. Fluids* **5**, 315–322.

Takayama, K., Onodera, O. & Hoshizawa, Y. 1984 Experiments on the stability of converging cylindrical shock waves. *Theor. Appl. Mech.* **32**, 305–329.

Vasil'ev, L. A. 1971 *Schlieren methods*. Israel program for scientific translations, New York.

Vuong, V. Q. & Szeri, A. J. 1996 Sonoluminescence and diffusive transport. *Phys. Fluids.* **8**, 2354–2364.

Watanabe, M., Onodera, O. & Takayama, K. 1995 Shock wave focusing in a vertical annular shock tube. *Shock Waves @ Marseille IV* .

Whitham, G. 1957 A new approach to problems of shock dynamics. Part 1. Two-dimensional problems. *J. Fluid Mech.* **2**, 145–171.

Whitham, G. 1958 On the propagation of shock waves through regions of non-uniform area or flow. *J. Fluid Mech.* **4**, 337–360.

Whitham, G. 1959 A new approach to problems of shock dynamics. Part 2. Three-dimensional problems. *J. Fluid Mech.* **5**, 369–386.

Whitham, G. B. 1974 *Linear and nonlinear waves*. John Wiley & Sons.

Wu, J. H. T., Neemeh, R. A. & Ostrowski, P. P. 1980 Experimental studies of the production of converging cylindrical shock waves. *AIAA J.* **18**, 47–48.

Wu, J. T., Neemeh, R. A. & Ostrowski, P. P. 1981 Experiments on the stability of converging cylindrical shock waves. *AIAA J.* **19**, 257–258.

Zel'dovich, Y. B. & Raizer, Y. P. 1966 *Physics of shock waves and high-temperature hydrodynamic phenomena*. Dover Publications, Mineola, New York.

Part II

Papers

1

Paper 1

Shock Waves (2006) 15:205–217
DOI 10.1007/s00193-006-0035-0

ORIGINAL ARTICLE

Focusing of strong shocks in an annular shock tube

V. Eliasson · N. Apazidis · N. Tillmark · M. B. Lesser

Received: 30 March 2005 / Accepted: 21 September 2005 / Published online: 15 June 2006
© Springer-Verlag 2006

Abstract Focusing of strong shock waves in a gas-filled thin convergence chamber with various forms of the reflector boundary is investigated experimentally and numerically. The convergence chamber is mounted at the end of the horizontal co-axial shock tube. The construction of the convergence chamber allows the assembly of the outer chamber boundaries of various shapes. Boundaries with three different shapes have been used in the present investigation — a circle, an octagon and a smooth pentagon. The shock tube in the current study was able to produce annular shocks with the initial Mach number in the range $M_s = 2.3 - 3.6$. The influence of the shape of the boundary on the shape and properties of the converging and reflected shock waves in the chamber has then been investigated both experimentally and numerically. It was found that the form of the converging shock is initially governed by the shape of the reflector and the nonlinear interaction between the shape of the shock and velocity of shock propagation. Very close to the center of convergence the shock obtains a square-like form in case of a circular and octagonal reflector boundary. This is believed to stem from the instability of the converging shock front triggered by the disturbances in the flow field. The outgoing, reflected shocks were also observed to be influenced by the shape of the boundary through the flow ahead as created by the converging shocks.

Communicated by K. Takayama.

V. Eliasson · N. Apazidis (✉) · N. Tillmark · M. B. Lesser
Department of Mechanics, Royal Institute of Technology,
100 44 Stockholm, Sweden
e-mail: nap@mech.kth.se

Keywords Shock focusing · Annular shock tube · Converging shock · Reflected shock · AUFS vector splitting scheme

PACS 47.40.Nm

1 Introduction

High pressures, temperatures and densities may be achieved in a region of gas compressed by means of a converging shock wave. This feature in connection with various technological applications is one of the main reasons for continuing interest in the problem of shock focusing. The highly nonlinear nature of the process presents a major challenge to its study. At the same time it serves as a source of the non-triviality of this phenomenon.

Two aspects of a converging shock are of special interest. The first one being the connection between the local strength of the shock and the shape evolution of the converging shockfront. The second issue, which is however closely related to the first one, is the question of the stability of converging shocks.

Guderley [1] was first to investigate theoretically the convergence of an initially cylindrical shock wave. Guderley used a similarity power law assumption for the radius of the converging shock as function of time. He was thus able to transform the governing equations to an ordinary differential equation which was integrated numerically. For a cylindrical shock the power law exponent was found to be $\alpha = 0.834$. Over the years, a large number of mainly theoretical and numerical investigations were dedicated to similar problems.

Perry and Kantrowitz [2] were the first to produce experimentally a converging cylindrical shock. The cylindrical shock in their experiment was generated in a shock tube with a tear-drop inserted in the test section. The behavior of the converging cylindrical shock was studied in detail in this pioneering investigation. It was observed that for a shock strength exceeding $M = 2.4$ the cylindrical form of the shock was distorted as the shockfront approached the center of the cavity. This was attributed to the instability of the converging shock resulting from a growth of small perturbations of the cylindrical shape. Another important observation of this study was the luminescence observed in the center of the cavity at the final stages of the shock collapse.

In a later investigation, Sturtevant and Kulkarny [3] used a parabolic reflector to study the complex behavior of shock waves in a focal region. In this extensive experimental study, shocks were brought to a focal region by reflecting an initially plane shock from a surface of the reflector. One of the important results of this study was that it showed a tendency of curved shocks to build planar sections. This tendency to planarity as a result of the nonlinear interaction between the form and the local strength of the shock was later investigated and confirmed in a series of experimental, theoretical and numerical investigations, see e.g. Schwendeman and Whitham [4], Apazidis and Lesser [5], Apazidis et al. [6].

Takayama et al. [7,8] and Watanabe and Takayama [9] studied the convergence of initially cylindrical shock waves in shock tubes with an annular section. One of the interesting observations of these studies was the formation of square-formed shocks in the final stages of the convergence process. This was attributed to four symmetrical perturbations introduced in the flow by the supports holding the annular section of the shock tube. This tendency of the converging shock to build n-gonal structures corresponding to the same number of perturbations in the flow was further confirmed by an introduction of artificial perturbations in the flow field. Takayama et al. [8] referred to this as the mode-n instability. An alternative way would be to describe this as an inherent dynamic stability of the shock in the sense that the curved sections tend to transform to planar ones. In other words, the form of the shock may be considered as unstable since it diverges from the original circular form and at the same time stable since it tends to build a natural for the shock dynamics n-gonal form with plane sides and sharp corners. Once the the n-gonal shape is formed, it will be periodically transforming, repeating itself during the convergence process, see e.g. Schwendeman and Whitham [4], Apazidis and Lesser [5], Apazidis et al. [6]. The condition for such stable periodic behavior is that the perturbations in the flow influencing the shock form are symmetric. This results in a symmetric polygonal form, periodically repeating itself. If, on the other hand, the perturbations lack symmetry the formed polygon will reflect this and the periodicity would therefore be lost.

The influence of the disturbances on the convergence of a cylindrical shock was investigated in an experimental study by Watanabe et al. [10]. This study was performed in a vertical co-axial annular shock tube. Special care was taken in the design of this shock tube to minimize the possible disturbances in the flow. Thus, this facility lacked the supports for the inner tube known to introduce disturbances in the flow. The results of this study showed that the cylindrical shock wave converge more uniformly towards the center than in a similar co-axial shock tube with supports.

In the previous paper by Apazidis et al. [6], a 2D chamber was used to study the convergence of a reflected shock wave. Shock waves were created in a plane chamber which had a specific geometric boundary, in the form of a pentagon with "smooth" corners. The shocks were produced by two different methods, by means of an igniting spark as well as an exploding wire, placed at the center of the chamber. Thus an outgoing cylindrical shock was created. After reflection from the chamber boundary the shock was transformed to a converging pentagonal shock. The Mach number range for the converging reflected shock was 1.1–2.0, producing weak to moderately strong shock waves. The above experimental method was able to produce highly symmetrical converging pentagonal shock waves. One of the disadvantages of the method was the creation of a disturbance zone in the center of the chamber due to the initial spark creation. It was therefore not feasible to continue the study of the converging shock as it approached the center of the chamber. This was unsatisfactory since the main nonlinear focusing effects become more pronounced as the strength of the shock increases in the vicinity of the center.

To be able to study this process in full, a new experimental setup was built at KTH Mechanics. This setup consists of a horizontal annular shock tube similar to those used in the earlier mentioned experiments. Compared to the chamber used in Apazidis et al. [6] there are no disturbances ahead of the shock wave and hence the whole convergence-reflection process is visible.

Another improvement of the new shock tube facility is that it can produce converging shock waves of various shapes. The present shock tube differs from the previous annular shock tubes by the construction of the thin convergence chamber, perpendicular to the tube. The construction of the chamber allows the mounting of the outer boundaries of various shapes. Three different

shapes of the outer boundary have been tested in the present experiment including a circular boundary, an octagonal boundary and a boundary with a smooth pentagonal shape. The purpose of the present work is therefore to study the influence of the form of the shock on the process of shock convergence and reflection. This influence of the shape of the boundary on the form and properties of the resulting shocks have been investigated both experimentally and numerically.

2 Experimental apparatus

The experimental apparatus consists of a 2.4-m-long shock tube where the shock is generated, focused and reflected. The focusing and reflection process is visualized by means of a schlieren system with a camera. The shock speed is measured before the shock converges by sensors placed on the annular part of the shock tube. The experimental setup is shown in Fig. 1.

2.1 The shock tube

The horizontal shock tube consists of two main parts, the high-pressure part or the driver and the driven or low-pressure part. The low-pressure part is divided into three sections: the inlet section with a constant cross-section area where a plane shock is formed, the shock transforming section where the shock becomes annular and finally the plane test section in the rear end of the shock tube. The shock tube has a circular cross-section. In the experiments, the test gas is air and the pressure in the low-pressure part ranges from 0.133 to 13.3 kPa, while the pressure in the high-pressure part is kept almost constant at 1,500 kPa. This yields shock Mach numbers between 2.3 and 3.1 in the annular section of the tube.

The high- and low-pressure parts are separated by an aluminum membrane with a thickness of 0.5 mm. As the pressure is increased in the high-pressure part, the membrane is forced against a knife-cross placed in the inlet of the low-pressure part. When the membrane bursts, a shock is formed and starts to propagate down the 80-mm-wide and 1,300-mm-long inlet section. The inlet section of the low-pressure part is sufficiently long to establish a plane shock. The plane shock is transformed into an annular shape in the transforming section which consists of a conically diverging section where the inner diameter increases from 80 to 160 mm. A 490-mm-long cylindrical inner body (ϕ=140 mm) is mounted coaxially in the interior of the outer tube thus forming an annular channel. The cross-sectional area is maintained constant from the inlet section, through the transformation section. The inner body is mounted by means of two sets of four supports. To minimize the disturbance from the supports, they are shaped as wing profiles. Also, the second set of supports is rotated in the plane of the shock 45° with respect to the first set, see Fig. 2. The speed of the shock, U_s, that impacts upon the test section is determined by two sensors mounted in the wall of the outer tube along the axis of the transforming section. The temperature jump from the shock wave passage triggers the sensors and gives a measure of the shock speed with an accuracy within 0.5%.

At the end of the shock tube the flow turns at a sharp 90° bend and enters radially into the plane test section, see Fig. 3. The inner edge of the reflector plate, marked by 2 in Fig. 3 is at the same radial distance from the center point of the test section as the inner wall of the outer tube, marked by 1 in Fig. 3 for the circular reflector plate. For the other forms of the reflector plate the radial distance to the center will vary along the circumference. The gap between the two facing surfaces is 5 mm and the cross-section area is decreased by a factor of 2 as compared to the annular section. The outer boundary of the test section is exchangeable and three reflector plates of different shapes are used in the experiments, a circular, a pentagonal and an octagonal plate, see Fig. 4. The radius for the circular reflector plate is 80 mm.

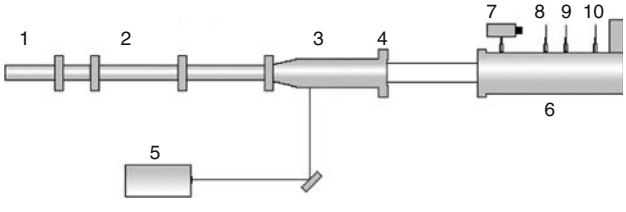

Fig. 1 Schematic overview of the experimental setup: *1* high-pressure part, *2* low-pressure part: inlet section, *3* low-pressure part: transformation section, *4* low-pressure part: test section, *5* pulse laser, *6* schlieren optics, *7* PCO CCD camera, *8* damping filter, *9* lens, *10* schlieren edge

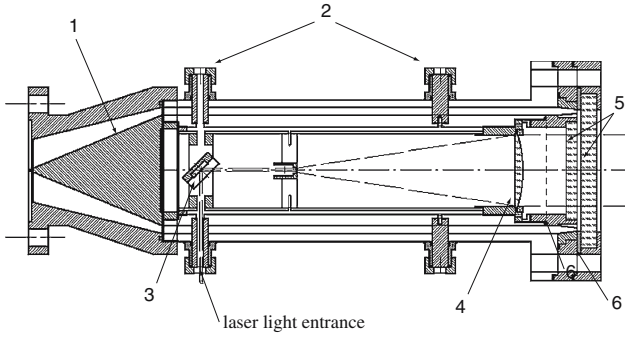

Fig. 2 The annular part of the shock tube: *1* inner body with a cone, *2* supports, *3* mirror, *4* lens, *5* glass windows for visualization, *6* convergence chamber with replaceable reflector plates

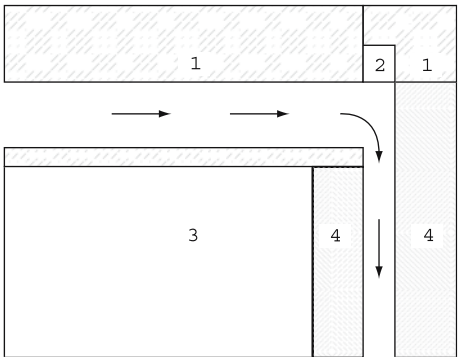

Fig. 3 A simplified sketch of the 90° corner, showing the position of the reflector plate: *1* outer tube, *2* reflector plate, *3* inner body containing optical equipment, *4* glass windows

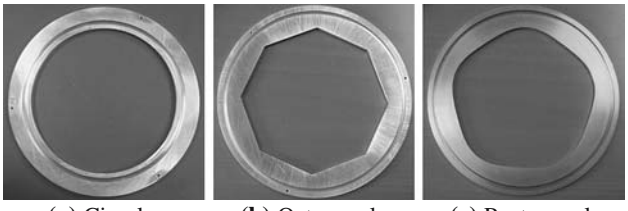

(a) Circular **(b)** Octagonal **(c)** Pentagonal

Fig. 4 The three reflector plates used in the experiments

The shape for the pentagonal boundary is given by

$$r = \frac{r_0}{1 + \varepsilon \cos(5\theta)}, \tag{1}$$

where $\varepsilon = 0.035$ and $r_0 = 77$ mm and r is the radius. Focusing of pentagonal shock waves, given by (1), has previously been studied by Apazidis et al. [6]. The octagonal plate has $R = 80$ mm, which is the radius of the outer circumscribed circle.

2.2 The shock visualization

The facing surfaces in the test section have glass windows and the flow is visualized by schlieren technique. The inner body contains an adjustable beam expander to provide axial parallel light through the test section. An Nd:Yag (NewWave Orion) laser that provides single shot operation, with 5-ns-long light pulses, is used as light source for the schlieren optics. It is mounted outside the shock tube and the light beam from the laser is reflected by a mirror before entering the shock tube. As the laser beam enters the tube through an orifice in one of the inner body supports, it is deflected in the axial direction, see Fig. 1. The parallel light obtained by means of the beam expander passes the test section and leaves the shock tube via the rear end glass window. The light is then focused by schlieren optics. A schlieren edge, a pinhead with r = 1 mm, is placed in the focal plane of the source and intercepts parts of the light before it reaches the camera. The camera, (PCO SensiCam, 12 bits, 1280 $\times$ 1024 pixels, pixel size: 6.7 $\times$ 6.7 μm, CCD) is placed in the focal plane of the test section. The camera is triggered by the same signal as the laser. A time delay unit (Stanford Research System, DG 535) is used to control the laser and the camera to enable exposure of the shock wave at predetermined positions in the test section.

3 Experimental Results

The present light source system allows one exposure at each run. To resolve the process of shock focusing and reflection in time, single exposures are taken with different time delays. For each run the time instants t_1 and t_2 when the shock wave passes the sensors are recorded. From these, the shock speed, U_s, can be determined. These measurements have a high repeatability giving low error level. For a typical shock speed around 800 m/s the average of the passage time $t_2 - t_1$ and the rms-value are 312 μs and 1.32 μs respectively, i.e. the error is less than 0.5%. In Fig. 5 a typical time history of signals recorded by the two sensors is shown. The upper curve is the signal from the first sensor. The first peak corresponds to the time t_1 and the second peak is the reflected shock wave. The lower curve is the signal from the second sensor. The resolution used in the measurements of the time signals is 2 μs.

Typical sets of pictures are shown in Figs. 6, 7 and 8. The size of the visualized area is 70 mm in diameter, that is ca 50% of the test section. In Fig. 6, where the circular reflector plate is used, the shock wave is seen to maintain a slightly perturbed circular form during the main

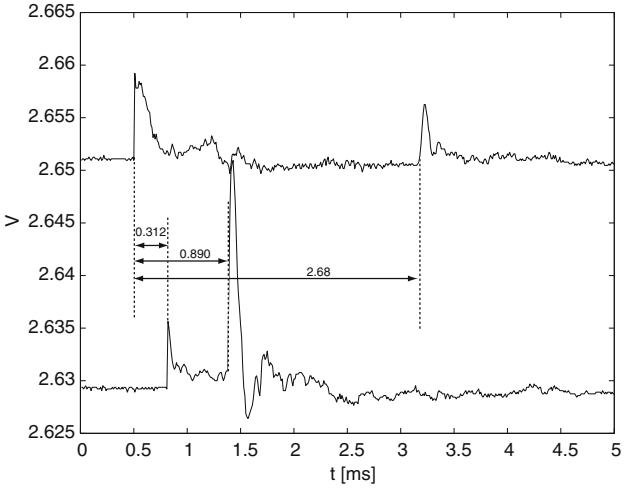

Fig. 5 The signal from the two sensors showing the shock wave passage and reflection, $M_s = 2.3$, octagonal reflector

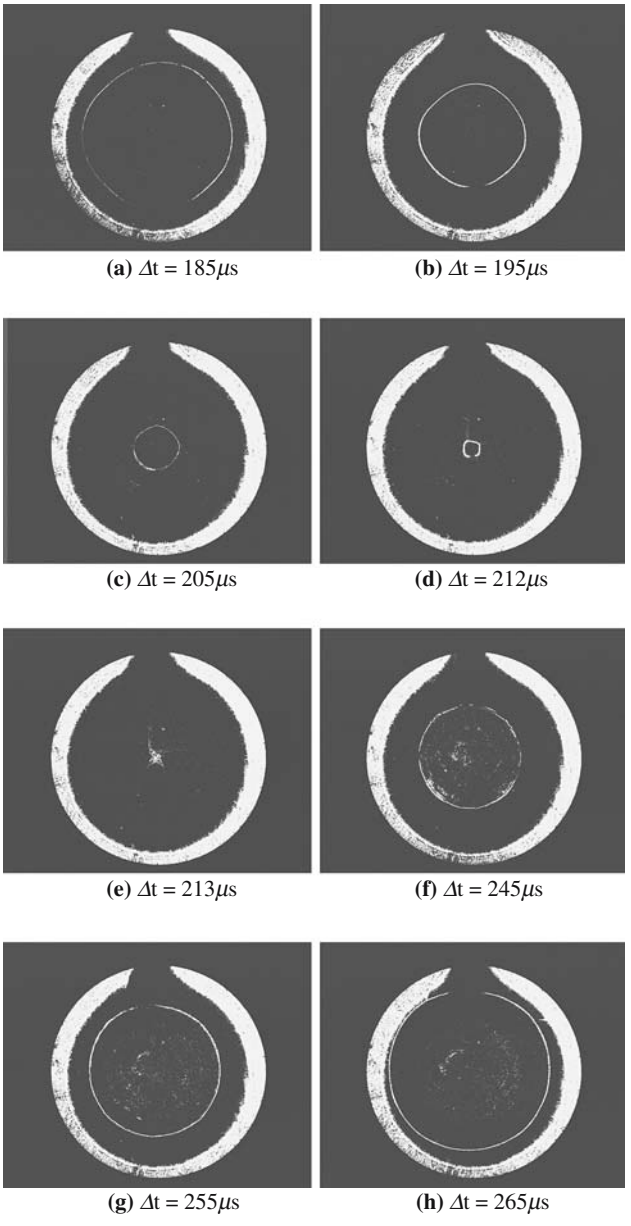

Fig. 6 The shock wave for the annular Mach number $M_s = 2.3$ at different instants for the circular reflector plate

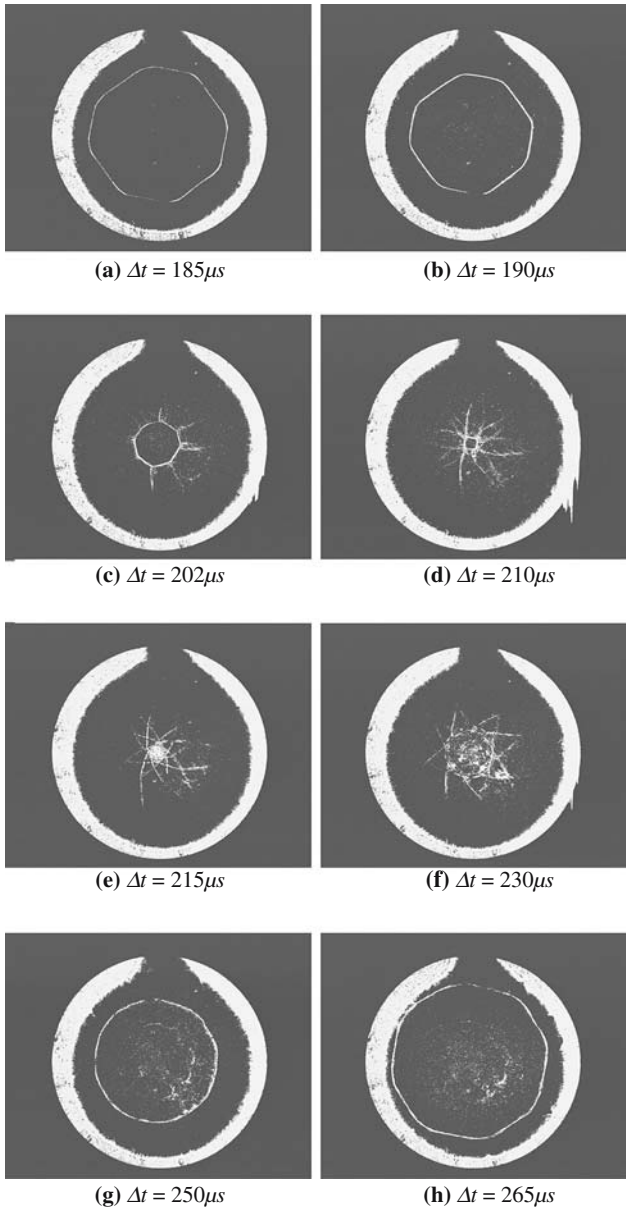

Fig. 7 The shock wave for the annular Mach number $M_s = 2.3$ at different instants for the octagonal reflector plate

part of the focusing process. Very close to the center the shock wave loses its circular shape and becomes square-shaped, see Fig. 6d. The reflected shock propagates into a flow field created by the converging shock. Although the final form of the converging shock is square-like the reflected shock wave regains its circular symmetry after focusing. The circular symmetry of the outgoing shock is then maintained through the rest of the reflection process, see Fig. 6e–h.

In Fig. 7 the shock focusing and reflection using an octagonal reflector plate is shown. Initially the shape of the shock wave is octagonal and has the same orientation as the reflector boundary, see Fig. 7a. During the focusing process the octagonal-shaped shock wave transforms first into a double octagon and then obtains again an octagonal form, see Fig. 7c. This time, however the orientation of the shock front differs from that of the boundary in the sense that corners of the shock are now positioned against the plane sides of the reflector and vice versa. That is the octagonal shape is now reoriented as compared to the initial shape, compare Fig. 7b and 7c. This behavior was predicted earlier in the numerical studies of polygonal shock convergence, see e.g. Schwendeman and Whitham [4] and Apazidis

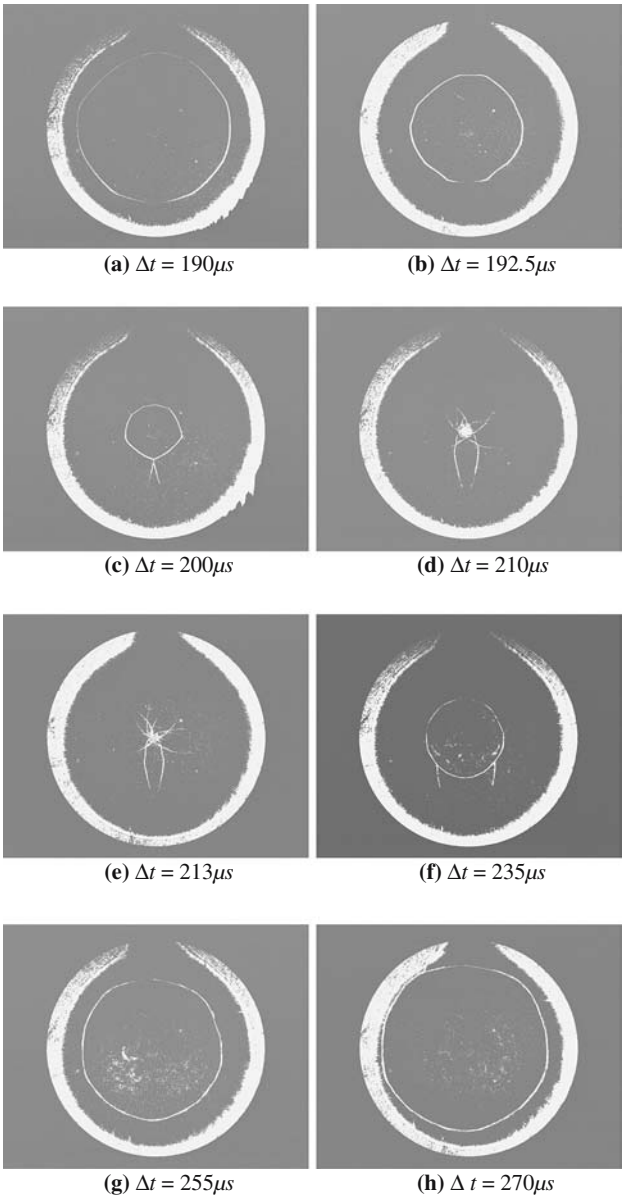

(a) $\Delta t = 190\mu s$ **(b)** $\Delta t = 192.5\mu s$

(c) $\Delta t = 200\mu s$ **(d)** $\Delta t = 210\mu s$

(e) $\Delta t = 213\mu s$ **(f)** $\Delta t = 235\mu s$

(g) $\Delta t = 255\mu s$ **(h)** $\Delta\, t = 270\mu s$

Fig. 8 The shock wave for the annular Mach number $M_s = 2.3$ at different instants for the pentagonal reflector plate

and Lesser [5]. The above phenomenon originates from the nonlinear coupling between the shape of the shock and the velocity of the shock propagation. Due to the high curvature in the vicinity of the corner areas, these propagate with higher velocities than the plane parts of the shock front. This leads to a transformation and reorientation of the shock front shape with new plane portions replacing the corners and new corners being built at the middle positions of the previous plane sides. To our knowledge this feature has not been observed experimentally earlier. Numerical studies indicate that this process would repeat itself through several cycles.

The present experimental observations show however that close to the center of convergence the shock obtains a square-like form, see Fig. 7d. We believe that this is attributed to the disturbances in the flow introduced by the supports holding the inner body of the shock tube. It seems that the 4-mode instability mentioned earlier in Takayama et al. [7,8] plays an important role here.

Although the final form of the converging shock is square-like just before the focusing the reflected shock obtains a circular form in the beginning of the reflection process just as in the case of a circular reflector, see Figs. 7f, g. The difference as compared to the circular case is a more complicated structure of the flow field created by the converging shock seen in these figures. In the later stages of the reflection process, the outgoing shock transforms from a circular to an octagonal form, now as the result of the interaction with the flow ahead of the shock, see Fig. 7h.

Finally, Fig. 8 shows the focusing and reflection process for the pentagonal reflector plate. The shock behavior in this case is similar to that of the octagonal case. The shape of the converging shock initially resembles the form of the reflector boundary, see Fig. 8a. As the converging shock approaches the center of the test section, its form is transformed to that of an reoriented smooth pentagon as in Fig. 8c. The reflected shock is influenced by the flow ahead of it, as created by the converging shock. This influence transforms the shock from a more circular-like form at the beginning of the reflection to a pentagon-like form at the later stages of the process, as seen in Fig. 8h. The orientation here is the same as in Fig. 8c, that is opposite to the orientation of the reflector boundary.

Near the center of convergence the shock wave is observed to attain a square shape, for the circular and octagonal reflector case. It is likely that this is caused by the disturbances in the flow introduced by the second set of supports to the inner body. The corners of the square-shaped shock wave correspond to the location of the second set of supports. As mentioned earlier this phenomenon was observed in the experiments performed by Takayama et al. [7,8].

The present experimental study shows that the flow field behind the shock influences not only the converging shock but is equally important for the shape of the the reflected shock.

Figure 9 shows a blow up of the center of convergence for different reflector forms and Mach numbers, all showing the square shape of the shock wave. In Fig. 9d the initial Mach number was increased to $M_s = 3.68$ by using helium as the driver gas instead of air.

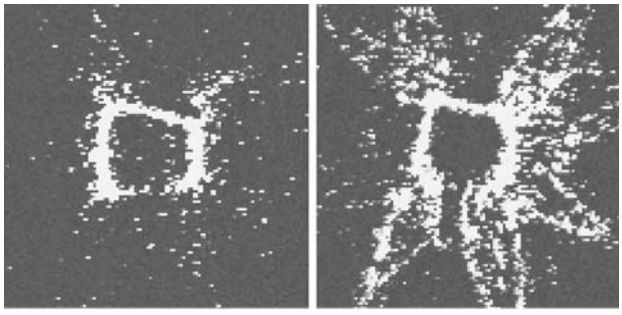

(a) $M_s = 2.51$, circular reflector

(b) $M_s = 2.35$, octagonal reflector

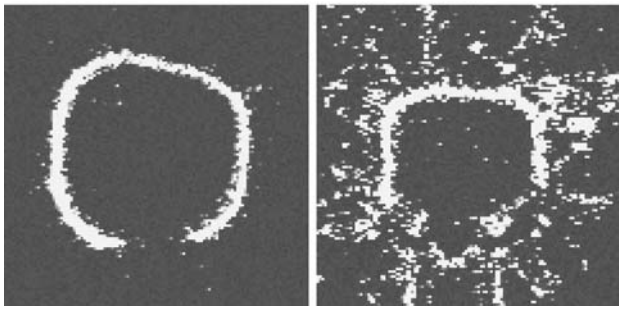

(c) $M_s = 2.35$, circular reflector

(d) $M_s = 3.68$, octagonal reflector

Fig. 9 Square-shaped shock waves near the center of convergence for circular and octagonal reflectors for various values of the annular Mach number M_s

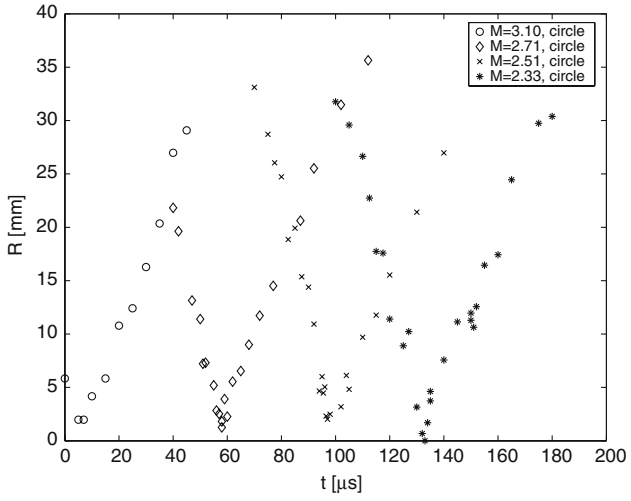

Fig. 10 Radius as function of the delay time for the circular reflector plate and four various values of the annular Mach number

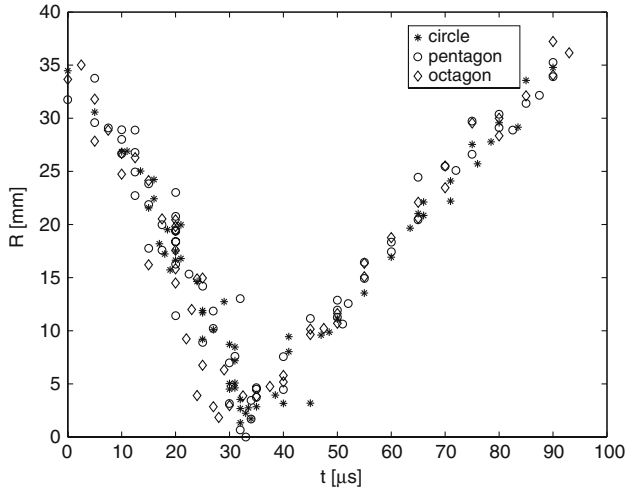

Fig. 11 Comparison between octagonal, pentagonal and circular reflector plates for the annular Mach number $M_s = 2.3$

To be able to make comparisons of the shock speed of the three different shaped shock waves, a concept of equivalent radius is introduced. This radius is defined as the mean value of the smallest circle surrounding the shock and largest contained inside the shock wave. The equivalent radius for four different pressure ratios corresponding to Mach numbers (measured in the annular section), $M_{s1} = 3.10$, $M_{s2} = 2.71$, $M_{s3} = 2.51$ and $M_{s4} = 2.36$ are plotted in Fig. 10. The visualization technique is not satisfactory when using low-pressures in the low-pressure part, (< 4 kPa), which explains the reduction of points for the converging shock with $M_s = 3.10$ in Fig. 10.

In Fig. 11 the radius of the shock wave is plotted versus the delay time for the three reflector plates at the same annular Mach number, $M_s = 2.3$.

In Figs. 12, 13 and 14 the radius of the shock wave is plotted versus the time delay for the circular, pentagonal and octagonal reflectors, respectively.

To estimate the error in the shock wave position the time delay was set to $\Delta t = 200$ μs and a series of 5–9 runs were performed for the three different reflectors. The rms values and the equivalent radius are presented in Table 1. As seen from Table 1, the errors are about 10% for the pentagonal and the octagonal reflectors and about 5% for the circular reflector. Possible sources of errors are fluctuations in temperature and variations in the light pulse emission in the laser. These errors could be effectively reduced if equipment allowing several exposures per run were used, as in Takayama et al. [7].

An attempt was made to compare the experimental data for the converging shock wave radius with the similarity solution obtained by Guderley [1],

$$\frac{R}{R_c} = \left(1 - \frac{t}{t_c}\right)^{\alpha}, \tag{2}$$

where R_c is the outer radius of the test section and t_c is the time when the converging shock wave arrives

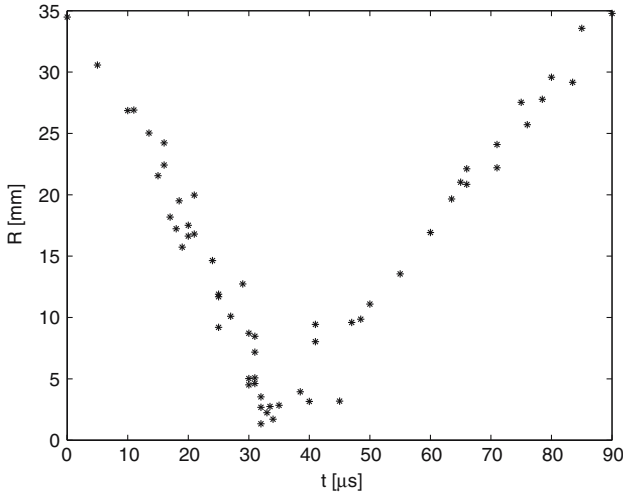

Fig. 12 Radius of the converging and reflected shock wave for the circular reflector for the annular Mach number $M_s = 2.3$

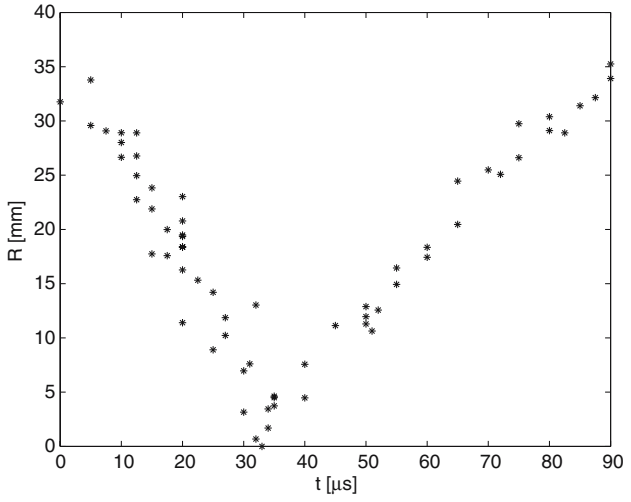

Fig. 13 Radius of the converging and reflected shock wave for the pentagonal reflector for the annular Mach number $M_s = 2.3$

at the center. By a nonlinear least square fit to the experimental data, R_c, t_c and α are found. The single-run procedure used in the estimation of the shock position makes the determination of the R_c, t_c and α difficult. Despite the low level of variation of the Mach number value between various runs it was not possible to determine an accurate value based on the present experimental results. This is due to the sensitivity of the α-value on even small variations in the experimental data between the runs, especially in the vicinity of the convergence center. In the next section we give a comparison of the present numerical results with the similarity power law assumption (2) for both numerical and experimental data obtained by previous investigators.

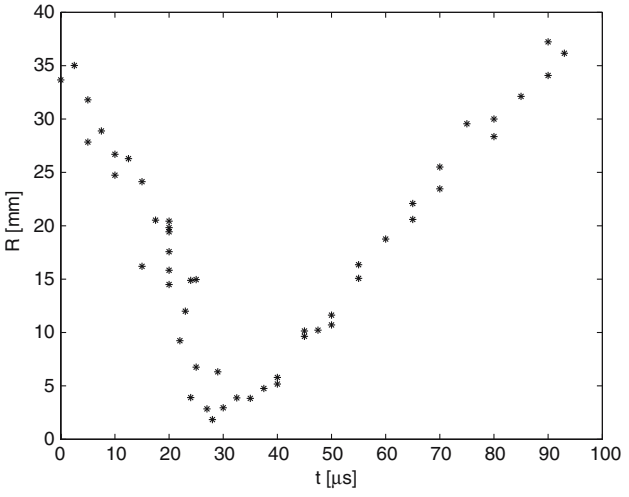

Fig. 14 Radius of the converging and reflected wave for the octagonal reflector for the annular Mach number $M_s = 2.3$

Table 1 Error estimation for $\Delta t = 200\mu s$ for all three reflectors, $p_1 = 13.3$ kPa

Reflector	rms	mean radius (mm)
Circle	$\sigma = 1.20$	$\bar{R} = 22.9$
Pentagon	$\sigma = 2.12$	$\bar{R} = 19.4$
Octagon	$\sigma = 1.89$	$\bar{R} = 18.6$

4 Numerical simulation and comparison with the experimental results

The numerical calculations were based on the artificially upstream flux vector splitting scheme (AUFS) for Euler equations, introduced by Sun and Takayama [11]. The scheme proved to be highly accurate, stable and robust in the considered configurations. In the following, we describe the initial and boundary value problem investigated in the present numerical study.

We will consider propagation of strong shocks in a gas-filled thin chamber with various shapes of the outer boundary. The shock is assumed to be initiated by an impulsive high pressure in a thin annular zone adjacent to the outer boundary of the test section. The outer boundary of this zone is the reflector plate and the inner boundary is a circle defined by the inner body of the shock tube. The inner of the chamber is initially kept at lower pressure. The complete two-dimensional flow in the chamber is then computed. This is certainly an approximation which disregards the details of the complex flow situation in the shock tube as the flow turns 90° from the annular section and enters test section. The validity of this approach was tested by comparison of the computational results with the experimental observations in the present study which proved to be good. The

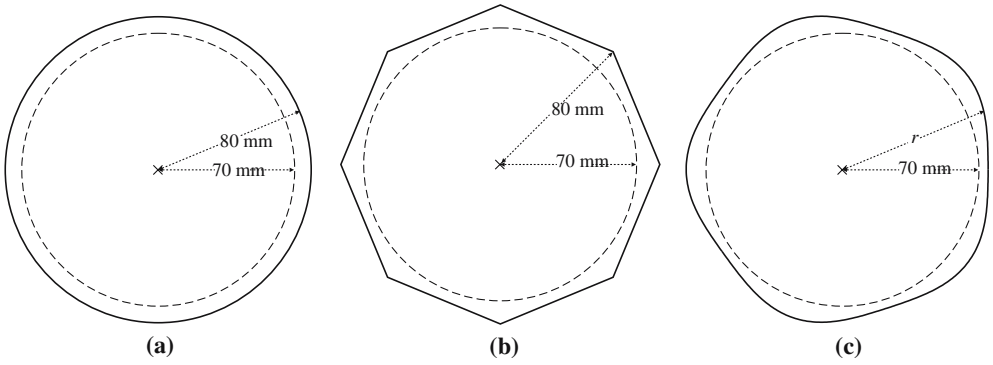

Fig. 15 Initial high-pressure zone adjacent to the chamber boundary. **a** circular boundary, **b** octagonal boundary **c** smooth pentagon defined by $r = r_0/\left(1 + \varepsilon \cos\left(5\theta\right)\right)$ where $r_0 = 77$ mm and $\varepsilon = 0.035$

numerical model correlates well with the major features of the flow in various investigated configurations.

The process of convergence of the initial shock toward the center of the boundary as well as the following propagation of the outgoing reflected shock from the center of the chamber was studied in detail and the results compared to the experimental observations. The shape of the chamber together with the thin high-pressure zone adjacent to the chamber boundary are shown schematically in Fig. 15.

The comparison with the experimental results has been carried out for the three cases shown in Fig. 15. In the first case (Fig. 15a) the shock is generated by means of an initially high pressure between the inner and outer circular boundary, corresponding to the annular end of the inner body. In the second case (Fig. 15b) the outer boundary of the test section is formed as an octagon and in the third case (Fig. 15c) as a "smooth" pentagon.

In all three cases the pressure in the inner cylindrical part of the chamber was set to $p_1 = 13.3$ kPa. This value was chosen to be the same as the one used in the experiment. The pressure in the driver section in the experiment was $p_4 = 112\, p_1$. In our case the losses in the straight portion of the tube are minimized, however we should expect greater losses due to the sharp 90° bend. The flow in the sharp 90° has been simulated numerically and the results indicate a significant drop on the Mach number after the turn. Calculations of the converging shock for various values of the initial pressure ratio in the chamber have been performed. One of the measured and calculated parameters of the complete flow is the average radius of the converging and reflected shock in the chamber as function of time. These curves were calculated for various initial pressure ratios at the boundary of the chamber starting from the maximum theoretical ratio $p_4/p_1 = 112$ and gradually decreasing this value in order to account for the pressure losses in the tube. The pressure ratio value that compared best with the experimental curves turned out to be about 30% of the maximum value, giving $p_4/p_1 = 33.6$. This value was used in the calculations. Comparison of the calculated and experimental curves showing the shock radius as function of time for various initial configurations are shown in Fig. 16.

In case of a pentagonal and octagonal boundary the value of the radius in the experimental measurements as well as in calculations is chosen as the average shock radius at each time instant, that is $r = \left(r_{\max} + r_{\min}\right)/2$. Shock positions of the converging shock at different locations in the chamber with an octagonal boundary are displayed in Fig. 17a. Figure 17b shows the corresponding density profiles in the chamber at a certain instant of the process.

Figure 18 shows comparison of the calculated shock profiles with the schlieren images at the corresponding time instants in the test section.

The calculated density contours for the outgoing shock in the case of an octagonal reflector are compared with the schlieren image in Fig. 19. The complicated flow situation with a circular shock front and an eight-point star-like profile is seen to be clearly reproduced in the numerical simulation.

As we can see from Fig. 16 the calculated and experimentally obtained values of the radii of the converging and diverging shock fronts compare well in all three geometrical configurations. It was mentioned in Sect. 3 that values of the radius as function of time for the converging shock have been compared with the similarity power law assumption both for the calculated and experimental values. Due to the single-run procedure for each shock position it was not possible to make an accurate estimate of the power law exponent from the experimental data. The α value was however obtained from the numerical computations. The results are given in Table 2.

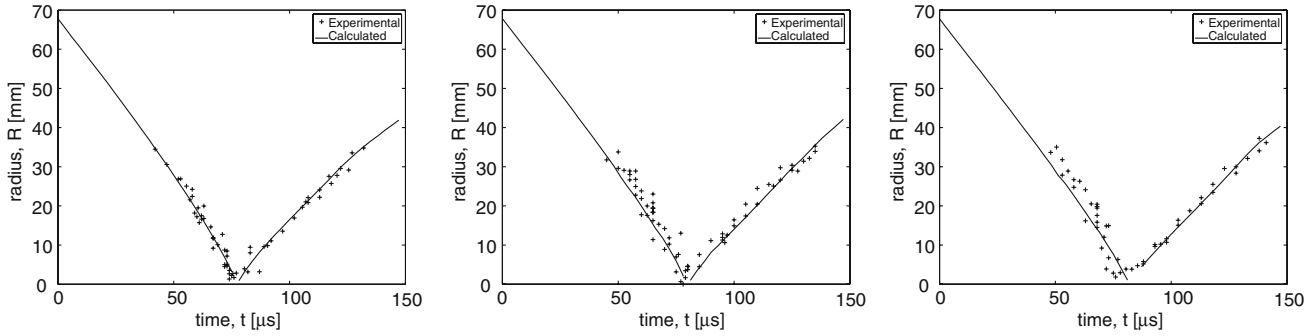

(a) Circular boundary **(b)** Octagonal boundary **(c)** Smooth pentagon

Fig. 16 Calculated and measured values of the average shock radius in the chamber for $p_4/p_1 = 33.6$. **a** Circular boundary, **b** octagonal boundary **c** smooth pentagon

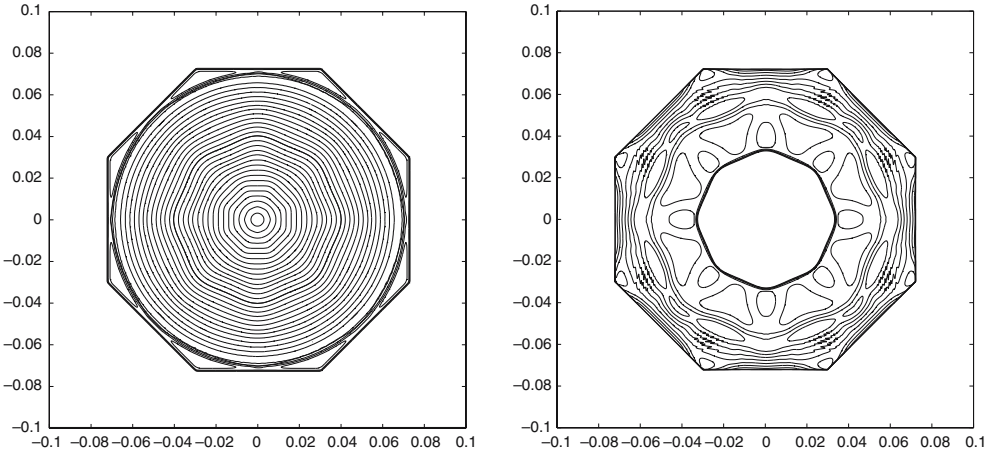

(a) Converging shock fronts **(b)** Density contours at certain instant

Fig. 17 Calculated converging shock in an octagonal chamber for $p_4/p_1 = 33.6$

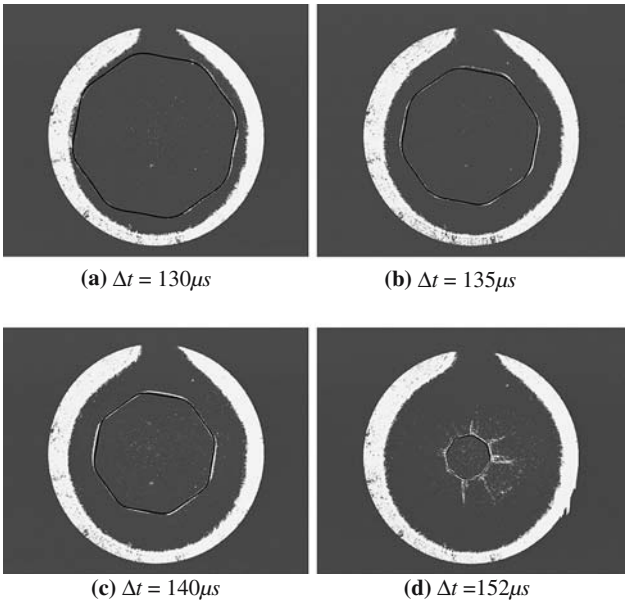

(a) $\Delta t = 130\mu s$ **(b)** $\Delta t = 135\mu s$

(c) $\Delta t = 140\mu s$ **(d)** $\Delta t = 152\mu s$

Fig. 18 Comparison of the calculated shockwave profiles with the experimental schlieren images in the chamber with an octagonal boundary for $p_4/p_1 = 33.6$

Table 2 Numerical computation of α-values

Shape	Pressure ratio	α
Circle	no counter pressure	0.832
Circle	$p_4/p_1 = 33.6$	0.857
Smooth pentagon	$p_4/p_1 = 33.6$	0.879
Octagon	$p_4/p_1 = 33.6$	0.883

The α value for the case of a circular reflector with no counter pressure compares well with previous numerical results, see e.g. Takayama et al. [7], Mishkin and Fujiumoto [12] and experimental results of Takayma et al. [7]. The lower values of the similarity exponent give higher values of the shock acceleration and thus higher velocity as the shock approaches the center of convergence. The calculated values indicate that the most favorable shape in terms of shock velocity and acceleration is the circular one.

There is however another parameter here which influences the converging shock velocity and thus the value of the similarity constant. This parameter is the distance

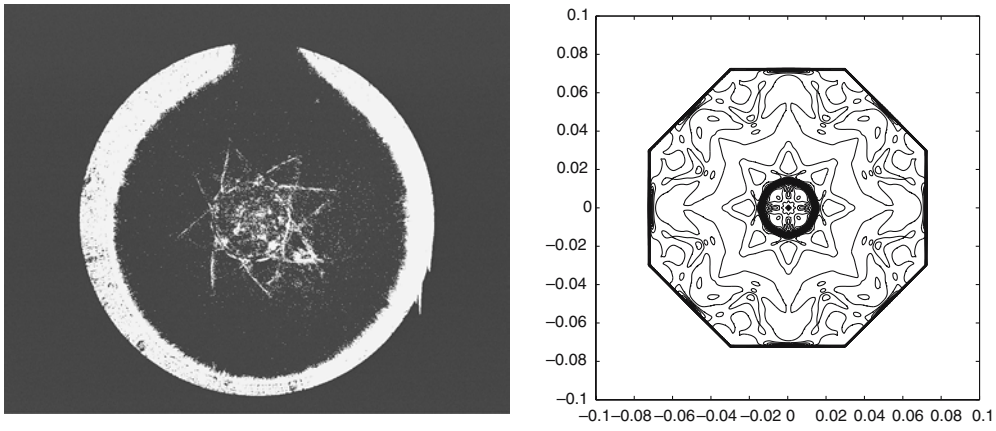

(a) Schlieren photograph of the flow for an outgoing shock

(b) Calculated density gradient contours for at outgoing shock

Fig. 19 Comparison of the experimental and calculated density gradient profiles for an outgoing shock for $p_4/p_1 = 33.6$ in an octagonal chamber at $\Delta t = 230\,\mu$s

from the inner circular end of the shock tube to the outer boundary of the chamber. For the pentagonal and octagonal case this distance will of course vary around the perimeter. If the distance is small the expansion wave, reflected from the chamber boundary will catch up with the converging shock and decrease its strength. This property is investigated numerically for the case of a circular boundary and the results are shown in Fig. 20.

This figure shows the Mach number of the cylindrical shock as it is approaches the center of the chamber and then transforms to a reflected wave expanding from the center of convergence. The inner circular boundary of the high-pressure zone has a fixed radius $r_{\text{in}} = 0.07$ m corresponding to the present experimental setup. The Mach number distribution is then calculated for various outer radii starting from $r_{\text{out}} = 0.072$ m and up to $r_{\text{out}} = 0.2$ m. As we can see from the figure, in case of a thinnest zone the strength of the converging shock wave is severely decreased by the reflected expansion wave. This influence, however, decreases rapidly as the thickness of the zone is increased. For $r_{\text{out}} = 0.09$ m there is no influence of the reflected expansion wave on the converging shock.

In order to exclude the influence of the reflected expansion wave we have conducted calculations for a configuration with various outer boundaries but the same circular inner boundary and the same area of the high-pressure zone for all cases. The results are displayed in Fig. 21. As we can see the maximum Mach

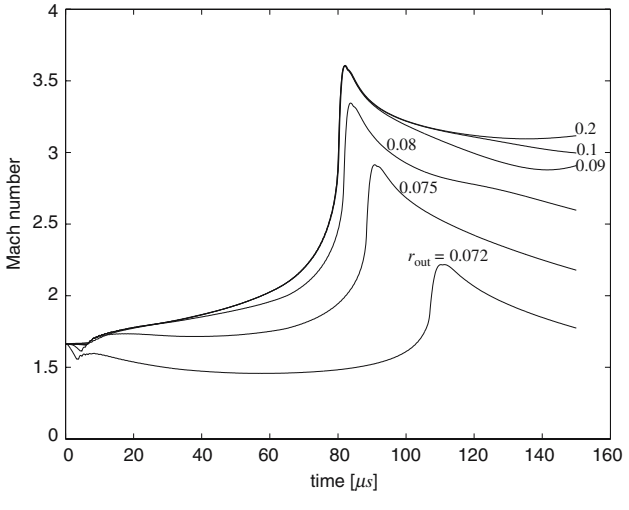

Fig. 20 Influence of the high-pressure zone thickness on the Mach number. The inner radius of the the high-pressure zone is $r_{\text{in}} = 0.07$ m and the value of the outer radius is marked on each curve

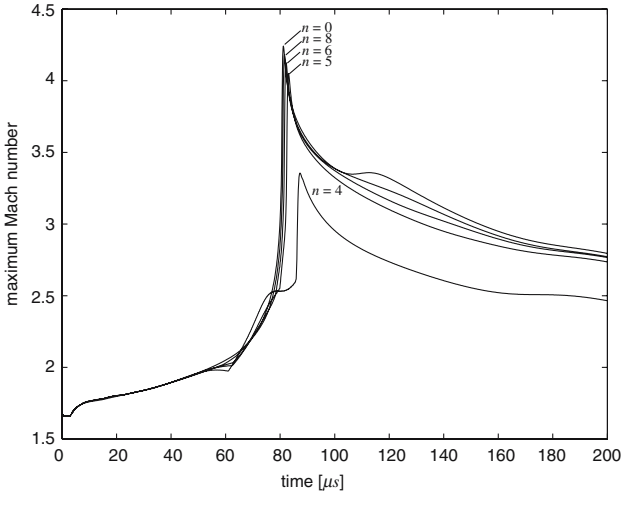

Fig. 21 Influence of the form of the chamber boundary on the Mach number. Each curve is marked by a corresponding number of the polygon sides of the outer boundary. $n = 0$ corresponds to a circular boundary

number is obtained for a circular form, marked by $n = 0$ in the figure. This maximum is followed by an octagon, hexagon, pentagon and finally a square. As seen the deviation from the rest of the curves is largest for a square reflector form giving a maximum mach number of $M_{\max} = 3.35$ as compared with $M_{\max} = 4.24$ for a circular form.

5 Conclusions

A new type of a a horizontal co-axial shock tube was used to investigate the properties of converging and reflected shocks with various initial shapes. The shape of the converging shock was generated by means of the reflector boundary in a thin cylindrical test section mounted at the rear part of the co-axial shock tube. Three various shapes of boundaries have been used in the present study—a circle, an octagon and a smooth pentagon. Numerical calculations have been performed to simulate the three described experimental configurations and the predictions of calculations have been compared with the experimental observations.

We summarize the major results of the present investigation.

(1) The initial form of the converging shock can be tailored by an appropriate choice of the form of the reflector boundary.
(2) The nonlinear dynamics of the shock convergence is observed in the present experimental study. The form of the shock undergoes a transformation from an original octagonal form through a double octagon back to a new octagon with an opposite orientation. This is due to the nonlinear coupling between the form of the shock and the velocity of shock propagation. The above feature, previously shown only in the numerical simulations is thus confirmed experimentally in the present study. The same type of behavior is observed in the case of a pentagonal reflector boundary.
(3) The final form of the converging shock in the immediate vicinity of the convergence center is square-like for circular and octagonal reflector boundaries. This is believed to stem from the perturbations in the flow due to the set of four supports in the annular portion of the shock tube. The shock strength is increasing as it approaches the center of the cavity and the disturbances in the initial flow are amplified. In the immediate vicinity of the center of convergence the form of the shock is mainly determined by the disturbances in the flow field. In the present case the shock was observed to obtain a square-like form very close to the convergence center. This is in agreement with the previous experimental studies.
(4) The reflected shock initially has a circular symmetry for all three reflectors. It retains its circular symmetry in the case of the circular reflector. In the case of the octagonal and pentagonal reflector the form of the outgoing shock is influenced by the flow field created by the converging shock. In the octagonal case the shock is transformed to an octagon-like form while in the case of a pentagon it attains a pentagon-like shape. This shows the influence of the flow ahead of the shock on the shape of the reflected shock.
(5) The numerical simulation of the flow in the convergence chamber was performed by the numerical solution of the full set of Euler equations. The numerical calculations were based on the AUFS, introduced by Sun and Takayama [11]. Several flow parameters obtained from the numerical computations have been compared with the experimental data. The first one is the average radius of the converging and reflected shocks as function of time. The experimental data was obtained from the schlieren images of the shocks. Also the shape of the shock fronts in the test section at various instants of the convergence and reflection processes as well as the density profiles obtained by means of the numerical calculations were compared with the schlieren images. The numerical results were found to be in good agreement with the experimental data and were also able to reproduce the major features of the flow in the chamber. Numerical results indicate further that the maximum Mach number at the center of the chamber is obtained for the circular reflector and is lower for a reflector with a polygonal form, decreasing with the number of sides of a polygon.

Acknowledgment The authors would like to thank Mr Ulf Landén and Mr Marcus Gällstedt at KTH Mechanics for skillful construction of the new shock tube facility. This work has been financially supported by The Swedish Research Council (VR). This is gratefully acknowledged. The funding from the Göran Gustafsson Foundation provided means for the construction of the shock tube and for acquisition of the experimental equipment which is gratefully acknowledged.

References

1. Guderley, G.: Starke kugelige und zylindrische Verdichtungsstöße in der Nähe des Kugelmittelpunktes bzw. der Zylinderachse. Luftfahrt Forsch **19**, 302–312 (1942)

2. Perry, R.W., Kantrowitz, A.: The production and stability of converging shock waves. J. Appl. Phys. **22**, 878–886 (1951)
3. Sturtevant, B., Kulkarny, V.A.: The focusing of weak shock waves. J. Fluid Mech. **73**, 651–671 (1976)
4. Schwendeman, D.W., Whitham, G.B.: On converging shock waves. Proc. R. Soc. Lond. A **413**, 297–311 (1987)
5. Apazidis, N., Lesser, M.B.: On generation and convergence of polygonal-shaped shock waves. J. Fluid Mech. **309**, 301–319 (1996)
6. Apazidis, N., Lesser, M.B., Tillmark, N., Johansson, B.: An experimental and theoretical study of converging polygonal shock waves. Shock waves. **12**, 39–58 (2002)
7. Takayama, K., Onodera, O., Hoshizawa, Y.: Experiments on the stability of converging cylindrical shock waves. Theor. Appl. Mech. **32**, 117–127 (1984)
8. Takayama, K., Kleine, H., Gröning H.: An experimental investigation of the stability of converging cylindrical shock waves in air. Exp. Fluids **5**, 315–322 (1987)
9. Watanabe, M., Takayama, K.: Stability of converging cylindrical shock waves. Shock Waves **1**, 149–160 (1987)
10. Watanabe, M., Onodera, O., Takayama, K.: Shock wave focusing in a vertical annular shock tube. Brun, R., Dimitrescu, L.Z. (eds.) Shock Waves @ Marseille IV. pp 99–104. Springer, Berlin Heidelberg NewYork (1995)
11. Sun,M., Takayama, K.: An artificially upstream flux vector splitting scheme for the Euler equations. J. Comput. Phys. **189**, 305–329 (2003)
12. Mishkin, E., Fujimoto, Y.: Analysis of a cylindrical implodimg shock wave. J. Fluid Mech. **89**, 61–78 (1978)

2

Paper 2

Shock Waves (2007) 17:29–42
DOI 10.1007/s00193-007-0087-9

ORIGINAL ARTICLE

Controlling the form of strong converging shocks by means of disturbances

V. Eliasson · N. Apazidis · N. Tillmark

Received: 19 May 2006 / Accepted: 18 October 2006 / Published online: 20 June 2007
© Springer-Verlag 2007

Abstract The influence of artificial disturbances on the behavior of strong converging cylindrical shocks is investigated experimentally and numerically. Ring-shaped shocks, generated in an annular cross sectional shock tube are transformed to converging cylindrical shocks in a thin cylindrical test section, mounted at the rear end of the shock tube. The converging cylindrical shocks are perturbed by small cylinders placed at different locations and in various patterns in the test section. Their influence on the shock convergence and reflection process is investigated. It is found that disturbances arranged in a symmetrical pattern will produce a symmetrical deformation of the converging shockfront. For example, a square formation produces a square-like shock and an octagon formation a shock with an octagonal front. This introduces an alternative way of tailoring the form of a converging shock, instead of using a specific form of a reflector boundary. The influence of disturbances arranged in non-symmetric patterns on the shape of the shockfront is also investigated.

Keywords Shock focusing · Annular shock tube · Imploding shock

PACS 47.10.ab · 47.40.Nm

1 Introduction

Focusing of shock waves can be used to generate high temperatures and pressures. This, together with many technological applications is one of the main reasons for continuing research in this area. A challenging problem is to generate imploding cylindrical shock waves preserving their original shape. It is known, however, that a converging cylindrical shock wave is very sensitive to perturbations and will change its form when encountering a disturbance. It is, therefore, important to clarify the influence of disturbances on the process of shock convergence and reflection. The influence of obstacles on the flow is closely related to two interesting problems. The first one being the relation between the shape and the local strength and thus speed of the shockfront propagation. This means that a highly curved part of the shock wave propagates faster than the adjacent planar part, which leads to a transformation and reorientation of the shock shape. The second problem concerns with the stability of the converging shock.

Shock diffraction is a classic example of shock wave propagation over obstacles. Bryson and Gross [4] investigated plane strong shock diffractions over cones, a cylinder and a sphere. Detailed schlieren photographs of the diffraction show the regular reflection, Mach reflections generating vortexes, triple points and their interaction. Their results were shown to be in good agreement with Whitham's theory [12–14].

A study of shock wave focusing, by Takayama et al. [10], was conducted in a horizontal coaxial annular shock tube. They introduced disturbances in the flow by thin cylindrical rods with three different diameters. Experiments showed that the disturbance behind the shockfront was more significant for rods with larger diameter. The inner body of the shock tube was suspended by four pieces of relatively large diameter cylindrical rods and hence a mode-4 instability was observed, even when larger diameter disturbances were introduced in the flow.

In 1987, Takayama et al. [9] used two different annular horizontal shock tubes, both of which were equipped with n

Communicated by K. Takayama.

V. Eliasson · N. Apazidis (✉) · N. Tillmark
KTH Mechanics, Royal Institute of Technology,
10044 Stockholm, Sweden
e-mail: nap@mech.kth.se

supports for the inner body, and observed an n-mode instability. To test the influence of an initial disturbance on the shock convergence, 12 cylindrical rods were placed in the test section of the shock tube having four supports. At first, the shock wave was deformed by the 12 rods, but when it approached the center of convergence the mode-4 pattern appeared again. It was concluded that it was not possible to completely suppress the disturbances caused by the presence of supports.

Watanabe et al. [11] studied converging cylindrical shocks in a vertical annular shock tube having a self-sustained structure, lacking supports. They were able to produce converging shock waves more uniformly than in a similar horizontal coaxial shock tube with supports. Even in the absence of supports, small disturbances were observed in the flow, presumably caused by small area variations in the coaxial channel. Watanabe et al. [3] distributed cylindrical rods at a certain distance upstream of the test section. Using both 2, 12 and combinations of 4 and 6 rods, they observed that disturbances created by a smaller mode number were stronger than those with higher mode number.

There is a close connection between the original shock shape and its preservation of symmetry during the focusing process. Schwendeman and Whitham [7] showed analytically that for shocks with regular polygonal shape the original shape was periodically repeated during convergence. Apazidis and Lesser [2] showed this feature numerically in the case of a smooth pentagonal converging shock wave. In an experimental study of a reflection and convergence process in a chamber with a smooth pentagonal reflector, Apazidis et al. [1], confirmed the previous analytical and numerical results in this area. Due to limitations in the experimental setup it was not possible to see the complete cycle of the shock reorientation during the focusing procedure.

The complete shock reorientation cycle was first observed experimentally in Eliasson et al. [5]. In this study, strong shock waves of various forms were produced by changing the shape of the outer boundary of the test section placed at the rear end of the horizontal shock tube. It was verified, for the first time, that octagonal and pentagonal converging shocks successively reorient and repeat the original shape during the focusing process. This is caused by the nonlinear dynamics of the shock propagation and stems from the fact that corners of the shock with high curvature move faster than the adjacent plane sides. The shock wave changes its shape as corners undergo Mach reflection and transform to plane sides. Unlike predictions provided by linear perturbation theories, slightly perturbed shock shapes never grow to catastrophic deformation but will obey the nonlinear deterministic system, which simply means the onset of Mach reflection.

In the present paper, we show a new way of producing converging shock waves of various shapes. Using the same shock tube as in [5] but instead of changing the shape of the outer boundary of the test section, we distribute cylindrical rods inside the test section. The rods are arranged in various positions and patterns and hence can create any disturbance shapes as desired. In the present experiment we study how the shock focusing and reflection is influenced by artificial disturbances. The present numerical work is based on the artificially upstream vector splitting scheme (AUFS) for solving the Euler equations introduced by Sun and Takayama [8]. Good agreement is found between the numerical simulations and the experimental results.

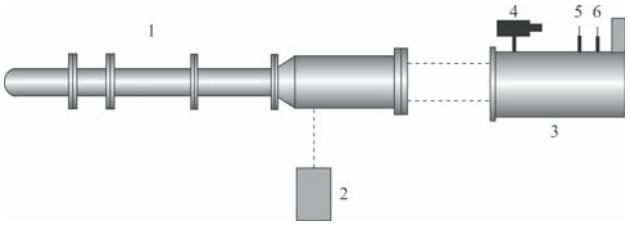

Fig. 1 Schematic overview of the experimental setup: *1* shock tube, *2* pulse laser, *3* schlieren optics, *4* PCO CCD camera, *5* lens and *6* schlieren edge

In Sect. 2 we describe the experimental setup in detail: the shock tube, the visualization technique and artificial disturbances. Section 3 presents experimental results. In Sect. 4 the numerical results are showed and compared with experiments. In Sect. 5, we conclude and summarize the present study.

2 Experimental setup

The experimental setup is shown in Fig. 1 and consists of a horizontal shock tube, schlieren optics and a laser as light source. The shock tube has a test section consisting of a thin cylindrical chamber, in which cylindrical shock waves converge and reflect. The shock wave is visualized using schlieren optics. Schlieren images are recorded by a CCD camera.

2.1 The shock tube

Figure 2 shows the 2.4 m long and 80 mm diameter shock tube, which consists of a high pressure chamber and a low-pressure channel separated by a 0.5 mm thick aluminum diaphragm. To create a shock wave, first the low pressure driven section is evacuated and then the driver section is filled with high pressure gas. The pressure difference across the diaphragm causes it to rupture, driving a shock wave. To achieve a controlled diaphragm opening, we use a cross-arranged knife at the low pressure channel entrance. The knife helps to evenly burst the diaphragm. The shock wave becomes planar while propagating along the low pressure

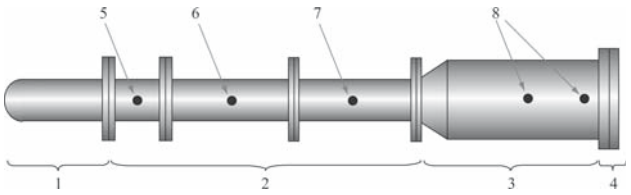

Fig. 2 Schematic overview of the shock tube setup: *1* high pressure part, *2* low pressure part: inlet section, *3* low pressure part: transformation section, *4* low pressure part: test section, *5* low pressure sensor, *6* vacuum valve, *7* vacuum pump, and *8* shock sensors

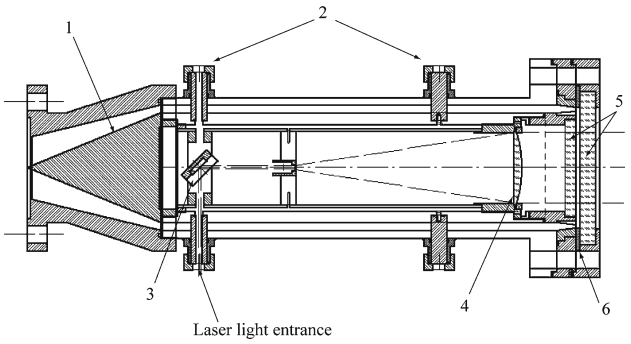

Fig. 3 The annular part of the shock tube:*1* inner body with a cone, *2* supports, *3* mirror, *4* lens, *5* glass windows for visualization, and *6* test section where the obstacles are positioned

channel, then enters the transformation section where it obtains annular cylindrical shape.

The transformation section consists of a conically diverging section, along which the diameter increases from 80 to 160 mm as seen in Fig. 3. The cross-section area is kept constant from the inlet section through the transformation section. An inner body is mounted coaxially in the outer larger diameter tube, which forms the annular section. The 490 mm long and 140 mm diameter inner body is suspended by two sets of four supports. The supports are shaped as wing profiles in order to minimize the disturbances in the flow. The second set of supports is angularly displaced by 45° relative to the first set. The plane test section is mounted directly at the end of the annular section. Hence, the shock wave can enter into the test section via a sharp 90° bend eventually to focus and reflect. The gap width of the cylindrical parallel test section between the two facing glass windows is 5 mm and, therefore, the cross section area is one half of that of the annular part. The outer boundary of the test section is circular. The test gas in the present experiments is air at 13.3 kPa at room temperature and the driver gas is also air at about 1,500 kPa at room temperature. This pressure ratio produces strong shock waves at Mach number 2.3.

The shock speed, U_s, is measured by thin-film heat transfer gauges placed along the annular section, with which the temperature jump across the shock waves is detected and the shock speed estimated within the accuracy of 0.5%.

2.2 The shock visualization

An Nd:Yag laser (NewWave Orion) emitting a 5 ns light pulse is used as light source for the schlieren optics. As shown in Fig. 3, the light beam is introduced into the shock tube perpendicularly to the tube axis and then deflected in the axial direction by a mirror placed inside the inner tube. To minimize spurious reflections from the inner side of the inner tube the walls are coated with non-reflective material. To form a parallel light beam for the schlieren optics, an adjustable beam expander is mounted inside the inner tube. The parallel light beam passing through the test section is then forming the schlieren images in the receiving optics. A 1.0 mm diameter pin head is placed at the focal plane of the image lens as schlieren knife-edge. It intercepts parts of the light beam to exhibit schlieren effects before reaching an image plane of a CCD camera (SensiCam, 12 bits, 1,280 × 1,024 pixels, pixel size 6.7 × 6.7 μm, CCD). The CCD camera and the light source laser are triggered by an output signal from the shock sensors via a properly adjusted time-delay unit. The delay unit (Stanford Research System, DG535) retards the output signal with a properly preset value to synchronize schlieren images at expected positions in the test section.

2.3 Artificial disturbances

Artificial disturbances are introduced in the flow by 1–16 cylinders with three different diameters (7.5, 10 and 15 mm). The cylinders are placed at two radial positions, $r_1 = 46.25$ mm and $r_2 = 66.25$ mm, in both regular and irregular patterns using a template with holes as shown in Fig. 4 a. Figure. 4b shows an example of 16 cylinders of 10 and 15 mm diameters placed at $r = r_1$.

3 Experimental results

Gas temperature is an important parameter in determining the speed of sound and thus the Mach number. We therefore checked, using a cold wire, the temperature variation during the pressure adjustment in the low pressure section of the shock tube. We found that the temperature reached a constant value 1 min after final adjustment of the pressure. Figure 5 shows the temperature variation during the pressure adjustment. Before time instant (I), the gas is at low pressure and in thermal equilibrium with its confinement. Between (I) and (II) the gas is supplied to the driven section and the temperature rises. Between (II) and (III) the gas is cooled by the surrounding walls. The vacuum pump is started at (III) to decrease the pressure to 13.33 kPa and stopped at (IV). The temperature first falls due to the gas expansion and then rises to ambient value within approximately 1 min.

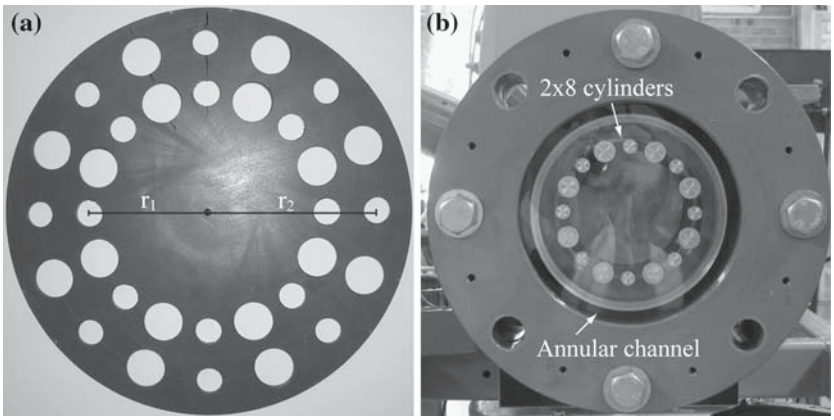

Fig. 4 **a** Template for cylinder positioning, $r_1 = 46.25$ mm and $r_2 = 66.25$ mm. **b** Rear part of the shock tube with 2×8 cylinders placed in the test section at $r = r_1$

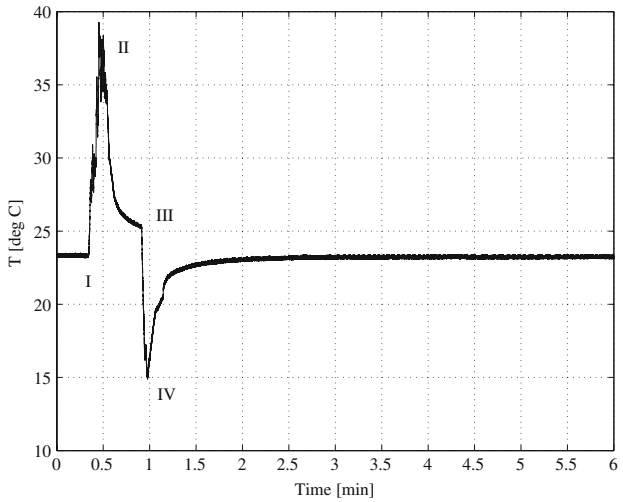

Fig. 5 The temperature in the low pressure part during evacuation

An initially cylindrical shock wave is disturbed by interacting with cylindrical obstacles placed in the test section. The shock wave diffracted over the cylindrical obstacles eventually produces series of Mach reflections which move toward the center of convergence. Present results show that a symmetric pattern of obstacles eventually produces a regular shock wave with plane sides and corners which will repeat its shape in successive intervals. It is thus possible to create shock waves of various polygonal shapes, for example octagons, by introducing corresponding polygonally distributed obstacles. The present study agrees with earlier analytical, numerical and experimental results obtained by Schwendeman and Whitham [7], Apazidis and Lesser [1] and Eliasson et al. [5], which also show that polygonal shock shapes are successively repeated. Unlike our previous experiment, in this case the polygonal shock shape is obtained not by the reflection from the polygonal reflector, but by the interaction with distributed cylindrical obstacles placed in the test section. Their influence on the shock form depends on the diameter of obstacles. Cylinders with larger diameters generate more significant disturbances. This agrees with the results of Takayama et al. [9].

First, a single 15 mm diameter cylinder was placed at $r_1 = 46.25$ mm in the test section. In Fig. 6, a schlieren photograph shows the converging shock shape after passing over the cylinder. A reflected shock wave (RC) is created upon the converging shock's impingement on the cylinder. After diffraction over the rear side of the cylinder, a three-shock system consisting of a Mach shock (MS), a converging or incident shock (CS), and a reflected shock (RS) forms a

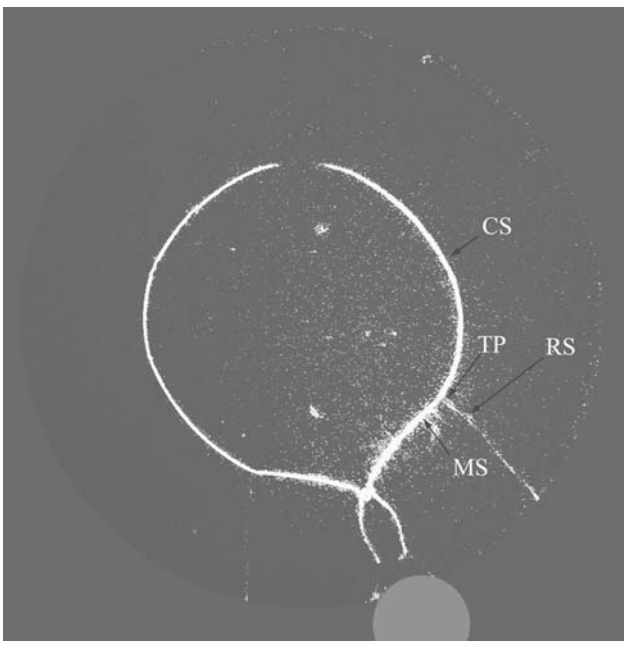

Fig. 6 Schlieren photograph of a shock wave passing a single 15 mm diameter cylinder. $M_S = 3.2$. CS converging cylindrical shock, RS reflected shock from the cylinder, MS Mach shock and TP triple point. The *grey filled circle* shows the position of the cylindrical obstacle

triple point (TP) as seen in Fig. 6. Photographs taken at different time instants are displayed in superposition in Fig. 7. We can readily compare the evolution of shock shapes and wave interactions. Comparing our results with Bryson and Gross [4], we can see similar behavior in planar shock diffraction over a cylinder. The difference is in the shape of the incoming, reflected and converging shocks.

Second, two 15 mm diameter cylindrical obstacles were placed at $r_1 = 46.25$ mm opposite each other. Sequential images are shown in Fig. 8 which is similar to Fig. 7. Here it is clearly observed that parts of the shock wave are delayed when passing over an obstacle.

To compare the effect of the diameter size on the shock shape, we replaced one of the two cylinders by a smaller one with a diameter of 7.5 mm. Four sequential images are presented in Fig. 9. It is now possible to see the influence of the diameter on the shock shape and propagation. We can see a clear asymmetry in the shock shape due to the difference in the diameters. On the rear side of the smaller cylinder, a second Mach shock and a triple point are visible. This was also observed in schlieren photographs of planar shock diffraction over a cylinder [4] when the incident shock wave passed about 0.5– 1.0 diameter past the rear stagnation point of the cylinder. The secondary Mach shock appears due to collision of the two initial Mach shocks.

Third, we performed a series of experiments with three 15 mm diameter cylinders placed at $r_1 = 46.25$ mm in a right isosceles triangle formation. The result of sequential visualization of converging shocks is shown in Fig. 10 in a similar way as in the previous displays. Plane Mach shocks develop after the shock diffraction over the cylindrical obstacles. The original circular shock shape tends to build plane sides with

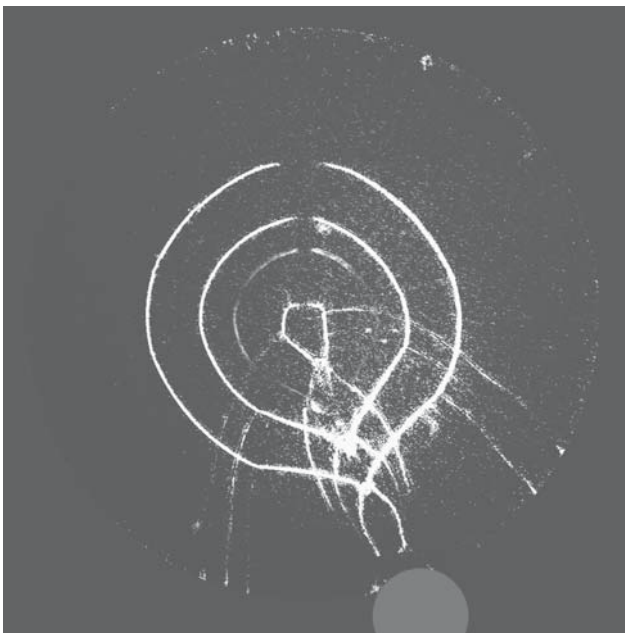

Fig. 7 Schlieren photograph of four shock waves at different time instants passing a single 15 mm diameter cylinder. $M_S = 3.2$. The *grey filled circle* shows the position of the cylindrical obstacle

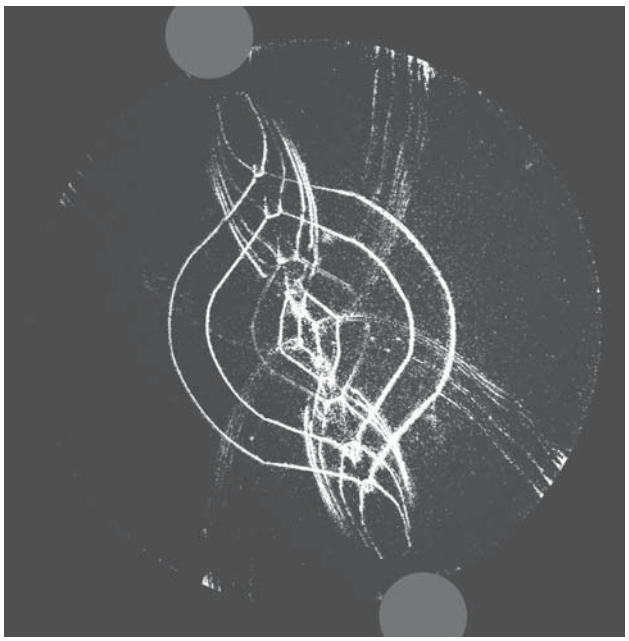

Fig. 8 Schlieren photograph of converging shock waves at five different instants. Two 15 mm diameter cylindrical obstacles are placed opposite each other. The *grey filled circles* show the positions of the cylindrical obstacles

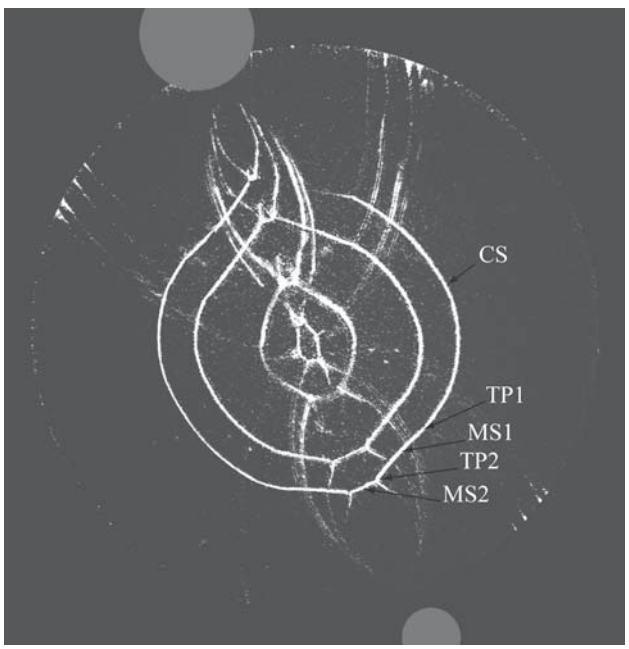

Fig. 9 Schlieren photograph of four shock waves at different time instants passing a 15 and 7.5 mm diameter cylinders. $M_S = 3.2$. CS converging cylindrical shock, RS reflected shock from the cylinder, MS, Mach shock and TP, triple point. The *grey filled circles* show the positions of the cylindrical obstacles

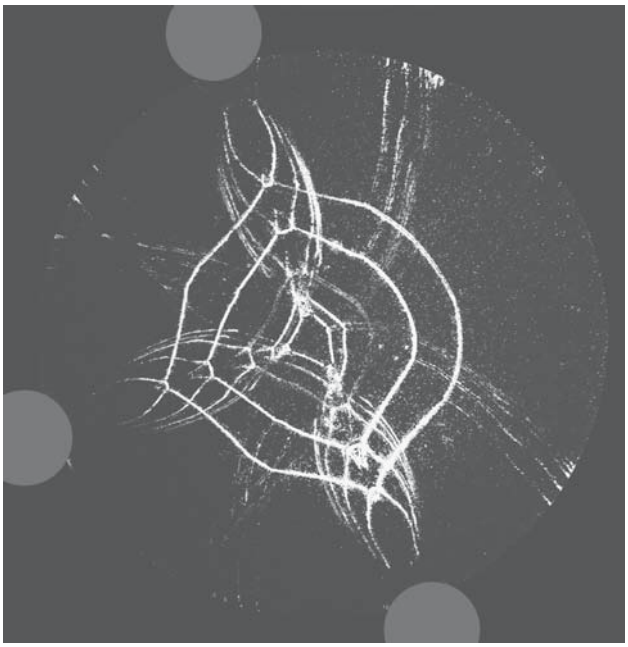

Fig. 10 Schlieren photographs of five shock waves at different time instants passing three 15 mm diameter cylinders. The grey filled circles show the positions of the cylindrical obstacles

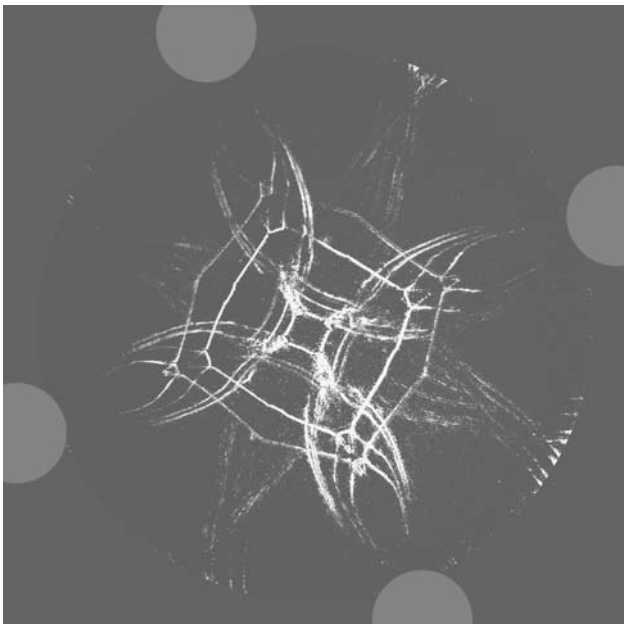

Fig. 11 Schlieren photographs of a shock wave at five different time instants passing four 15 mm diameter cylinders. The *grey filled circles* represent the cylindrical obstacles

sharp corners even in the undisturbed part of the shock as the shock approaches the center. The undisturbed part also travels faster than the disturbed part of the shock.

To create a square-like shock shape, we placed four 15 mm diameter cylinders at $r_1 = 46.25$ mm in a square formation. Corresponding sequential schlieren images are shown in Fig. 11. At first, eight sides, which are convex, form an octagon with square-like shape. As the shock wave approaches the center the sides become plane and the octagon is replaced by a square.

Figure 12 shows the deviation of shock wave radii normalized by the mean radius at $\Delta t = 200$ μs, $\Delta t = 205$ μs, $\Delta t = 210$ μs and $\Delta t = 215$ μs in the case of four cylindrical obstacles. The time delay, Δt, is defined to be the time interval between the instant when the shock passes the second sensor and that when the photograph is taken. In the first frame, $\Delta t = 200$ μs, a slightly perturbed octagonal shape is observable. At later time, the Mach shock parts forming the sides, become more planar.

Next we placed eight 15 mm diameter cylinders at $r_1 = 46.25$ mm in an octagonal formation. After interaction with the obstacles, the shock shape becomes that of an octagon with curved concave sides as seen in Fig. 13a and b and then transforms into a polygon with 16 sides as shown in Fig. 13c. At a later instant, the shock wave transforms to an octagonal shape again as seen in Fig. 13d. The second octagonal shock shape is rotated by 45° with respect to the initial shape. This is an experimental confirmation of the polygonal shock

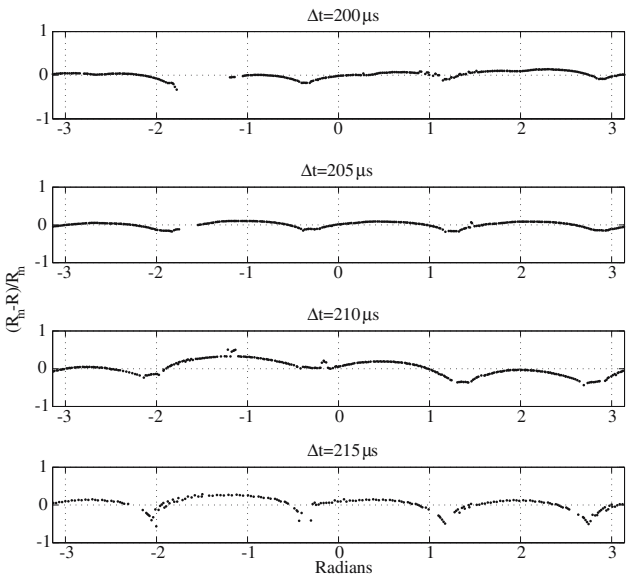

Fig. 12 The deviation from the mean radius normalized with the mean radius for the case with four cylinders placed at the corners of a square. The time delay, Δt, for the individual shock waves are 200, 205, 210 and 215 μs, respectively

dynamics predicted earlier analytically [7], and numerically [2]. Eliasson et al. [5] confirmed experimentally this trend by using a different approach for shock formation.

The reflected shock wave displayed in Fig. 13f and g shows that a circular shape is obtained at the early stage of shock reflection. Eliasson et al. [5] found that the shock was later

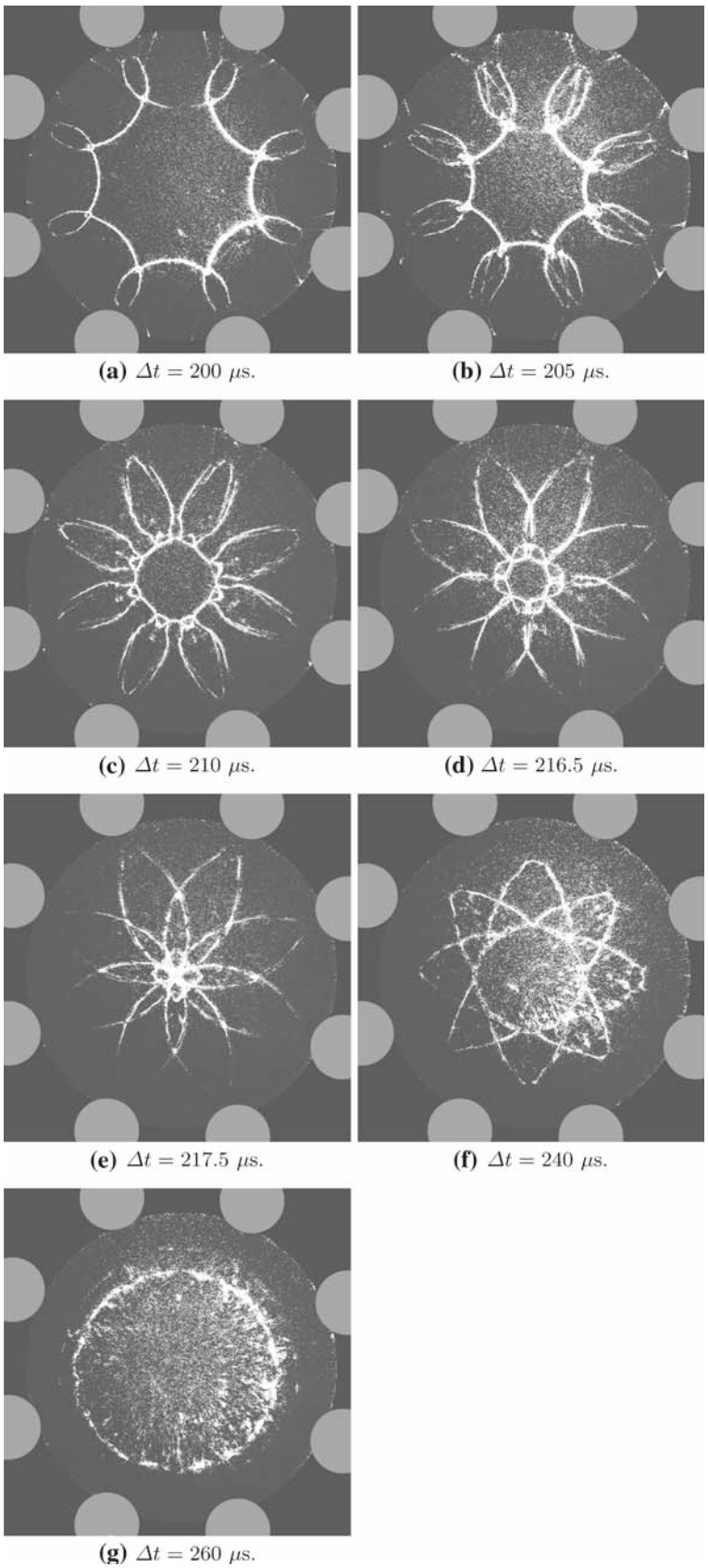

(a) $\Delta t = 200\ \mu$s. **(b)** $\Delta t = 205\ \mu$s.

(c) $\Delta t = 210\ \mu$s. **(d)** $\Delta t = 216.5\ \mu$s.

(e) $\Delta t = 217.5\ \mu$s. **(f)** $\Delta t = 240\ \mu$s.

(g) $\Delta t = 260\ \mu$s.

Fig. 13 Schlieren photographs of shock waves at different time instants passing eight 15 mm diameter cylinders. The *grey circles* represent the cylindrical obstacles

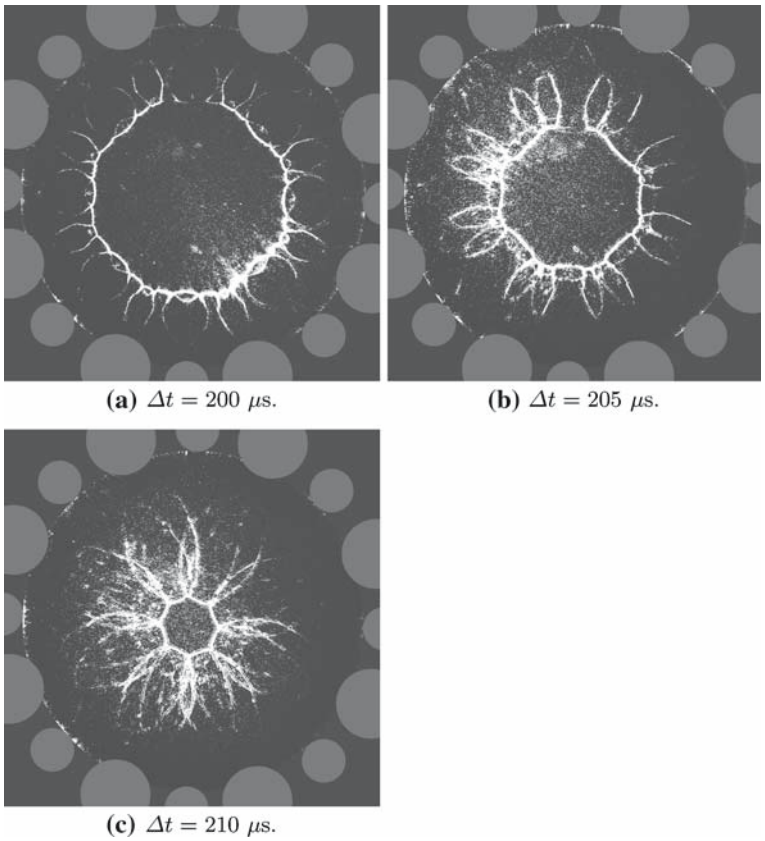

(a) $\Delta t = 200\ \mu$s. **(b)** $\Delta t = 205\ \mu$s.

(c) $\Delta t = 210\ \mu$s.

Fig. 14 Schlieren photographs of shock waves at three different time instants passing sixteen 15 and 10 mm diameter cylinders. The *grey filled circles* show the positions of the cylindrical obstacles

affected by waves and flow behind the converging shock, which eventually resulted in an octagonal shape.

To further investigate the effect of the size of cylindrical objects, we studied shock interaction with more complex obstacle formations. The first formation we looked at was a combination of eight 15 mm diameter cylinders and eight 10 mm diameter cylinders distributed in two symmetric octagonal formations as shown in Fig. 14. Initially the influence of all 16 cylinders is present. The shock shape appears to contain 16 concave fronts but has still an octagon form. Disturbances generated by the interaction with larger diameter cylinders overtake those created by the smaller ones as the shock wave is approaching the center of convergence, and again a shock with an octagonal shape is formed.

To examine the effect of asymmetrical blockage, we placed several cylindrical objects in a dense formation at a certain angular position leaving the rest of the chamber free. Three 15 mm diameter and two 10 mm diameter cylinders where placed at $r_1 = 46.25$ mm while three 7.5 mm diameter cylinders at $r_2 = 66.25$ mm, at the same angular position as 15 mm diameter cylinders, as shown in Fig. 15. At such high blockage ratio, the disturbed part of the shock was attenuated and delayed.

From the schlieren images in Fig. 16, we observed that the center of individual shockfronts shifted as a result of the asymmetrical blockage. The schlieren images of the shockfronts are used to calculate the radial distance and the center point. The calculated curves are then centered at a common origin and displayed together with the schlieren images in Fig. 16. If the center of the individual shock waves did not shift, the calculated and the visualized shockfronts would overlap exactly. The calculated fronts of the largest two shock waves at 200 and 210 μs overlap with the schlieren images. However, the calculated front of the third shock wave at 215 μs does not overlap. Hence, we can conclude that the center of the shockfront is shifted toward the obstacles. This agrees with previous observations made by Perry and Kantrowitz [6]. However, the influence of the disturbances on the shock shape is more significant than that on the deviation of its center. Thus the deviation of the convergence center is small as compared to the shockfront deformation.

4 Numerical results

In our previous work [5], we used the artificially upstream flux vector splitting scheme (AUFS) for solving the two-dimensional Euler equations, introduced by Sun and Takayama [8]. In the present work this scheme once again was able to accurately predict and reproduce the major features of the shock propagation process.

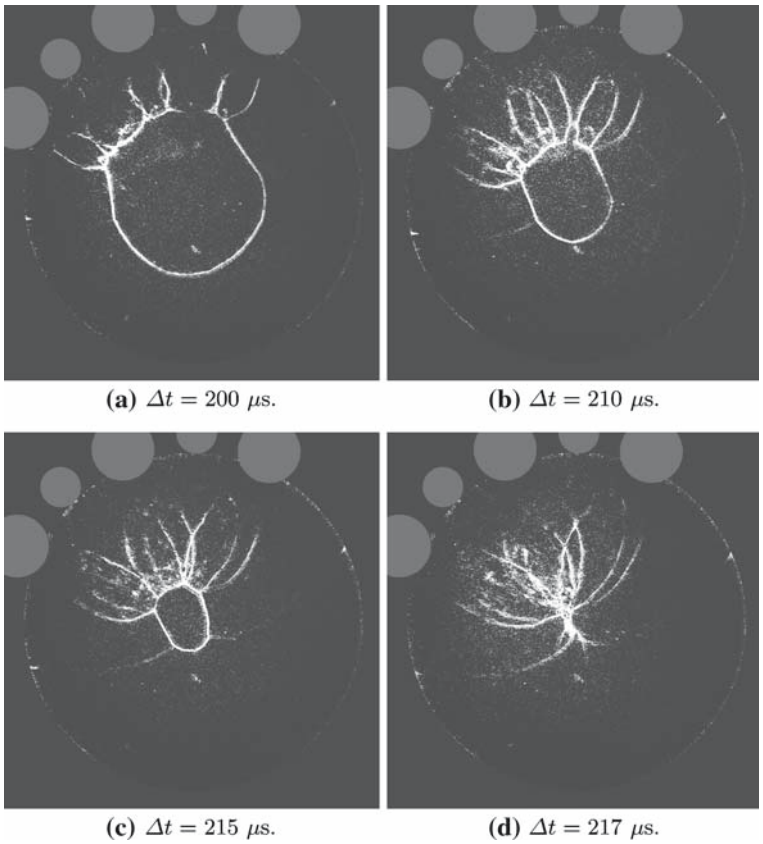

Fig. 15 The shock wave at different instants, $M_s = 2.3$. The *grey filled circles* show the positions of the cylindrical obstacles. Three additional 7.5 mm diameter cylinders are not seen in the figure, placed outside the 15 mm diameter cylinders

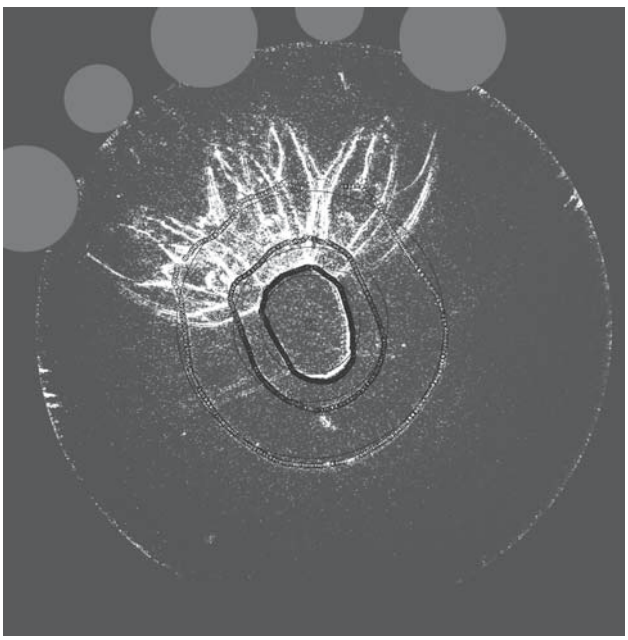

Fig. 16 Schlieren photographs of three converging shock waves, (same as the first three photographs in Fig. 15), a calculated front of the shock wave and a calculated center point

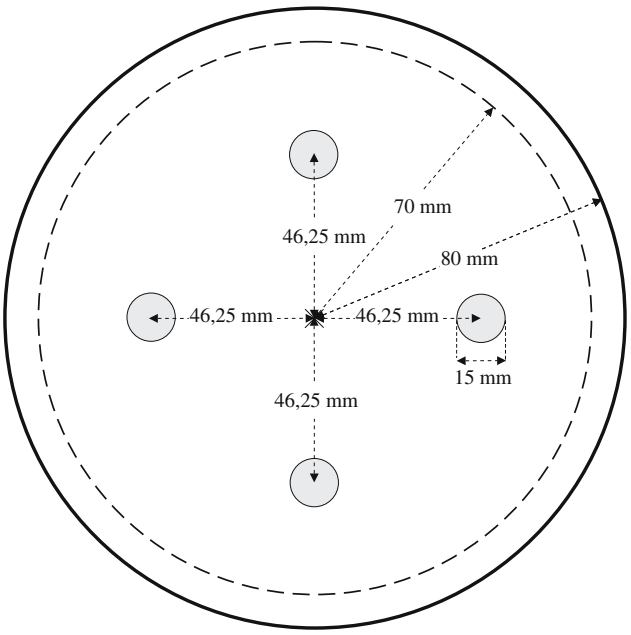

Fig. 17 The outer cylindrical computational domain boundary with the thin adjacent initial high pressure zone and four cylindrical obstacles

We consider the propagation of a strong shock in the computational domain representing the shock tube test section. As explained earlier, the test section is a thin cylindrical chamber mounted at the rear end of the shock tube. Shocks are created upon the release of a high pressure in a thin annular outer boundary and propagate into the inner part of the test

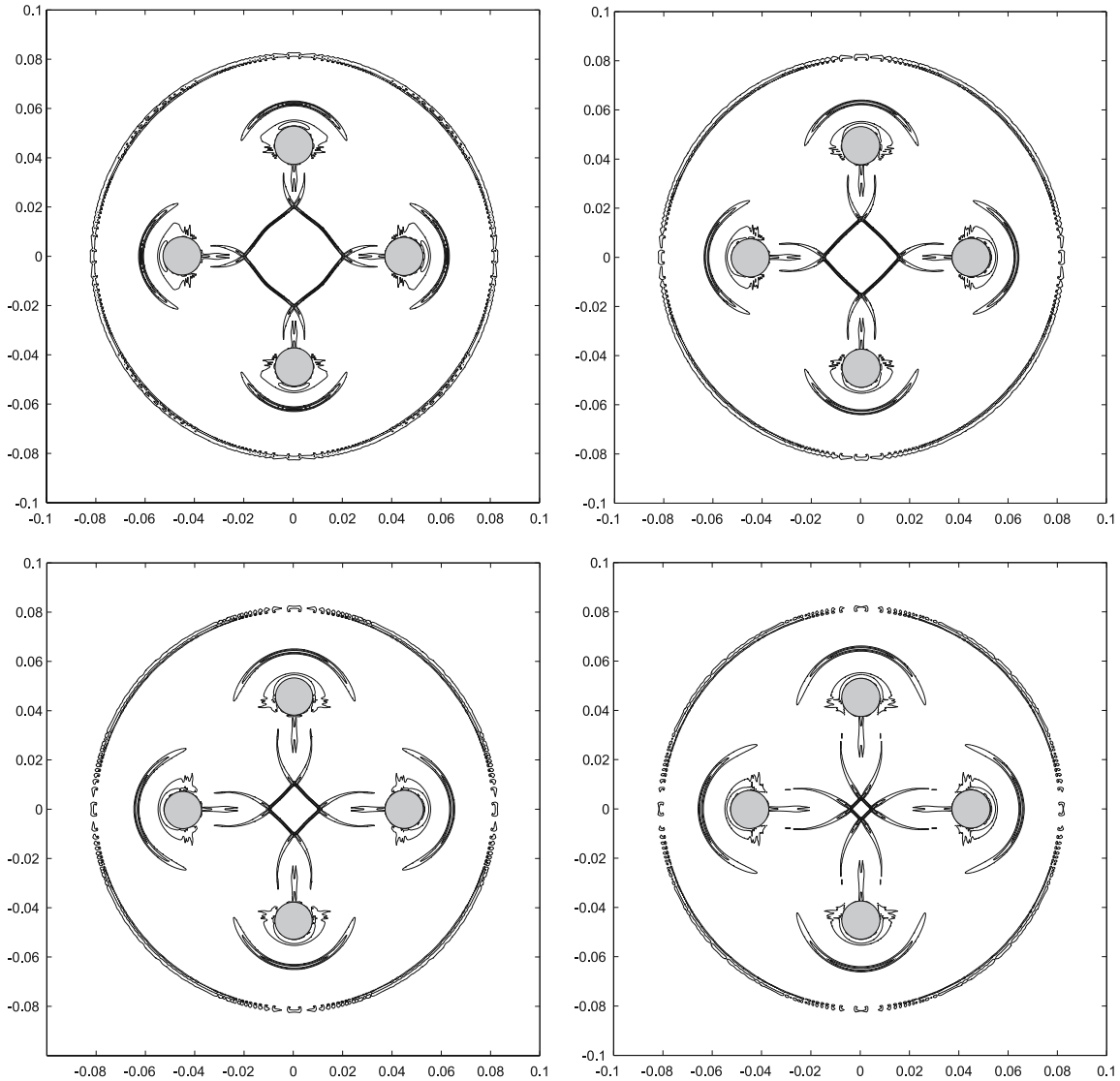

Fig. 18 Density gradient profiles at various positions for the case of four cylindrical disturbances

section, initially kept at lower pressure. Cylindrical obstacles of various radii are placed in various formation patterns in this domain.

The pressure in the inner of the test section is set to 13.3 kPa, in all considered cases, the same value as in the experiment.

The pressure loss for a shock propagating along the straight shock tube is small; however, it may be significant at the sharp 90° bend. Eliasson et al. [5] numerically simulated shock attenuation and losses at the sharp 90° bend and indicated a significant decrease in Mach number after the bend. One of the measured and calculated parameters of the complete flow was the average radius of the converging and reflected shock in the computational domain as a function of time. These curves were calculated for various initial pressure ratios starting from the maximum theoretical ratio of 112 and gradually decreasing this value in order to account for the pressure losses in the tube. The pressure ratio value that compared best with the experimental curves was found to be about 30% of the maximum value, giving $p_4/p_1 = 33.6$. This value was used in the present calculations as well.

The convergence of the initial cylindrical shock, its interaction with cylindrical obstacles placed in various formation patterns, and the following reflection process from the center are studied in detail and results are compared with the experimental observations. The computational domain including a thin high-pressure zone adjacent to the domain boundary and a typical configuration of cylindrical obstacles are schematically shown in Fig. 17.

The density gradient profile at various positions is shown in Fig. 18 for the four cylindrical obstacles in a square

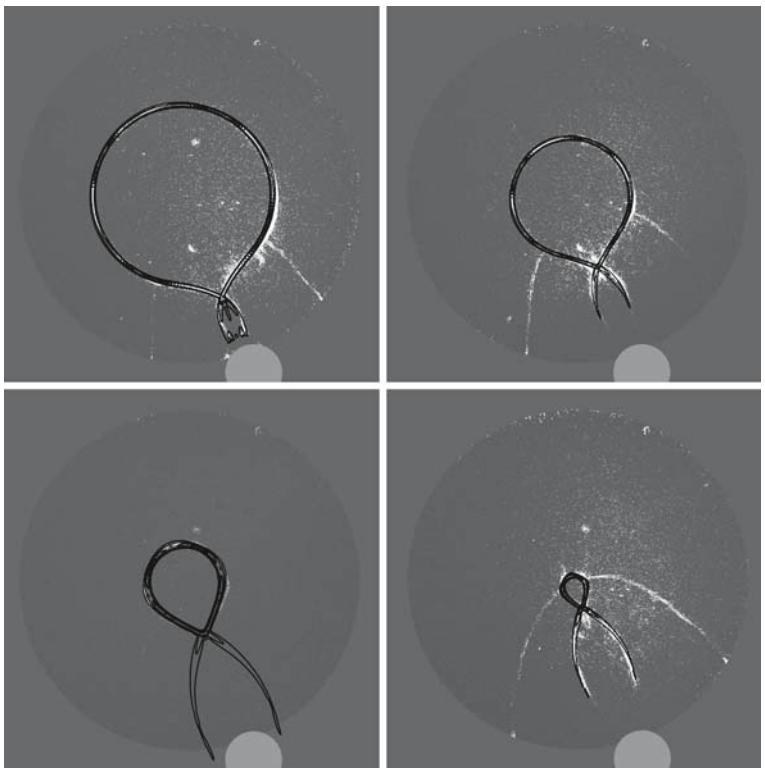

Fig. 19 Comparison of the calculated shockwave profiles with the experimental schlieren images with one cylindrical disturbance for $p_4/p_1 = 33.6$

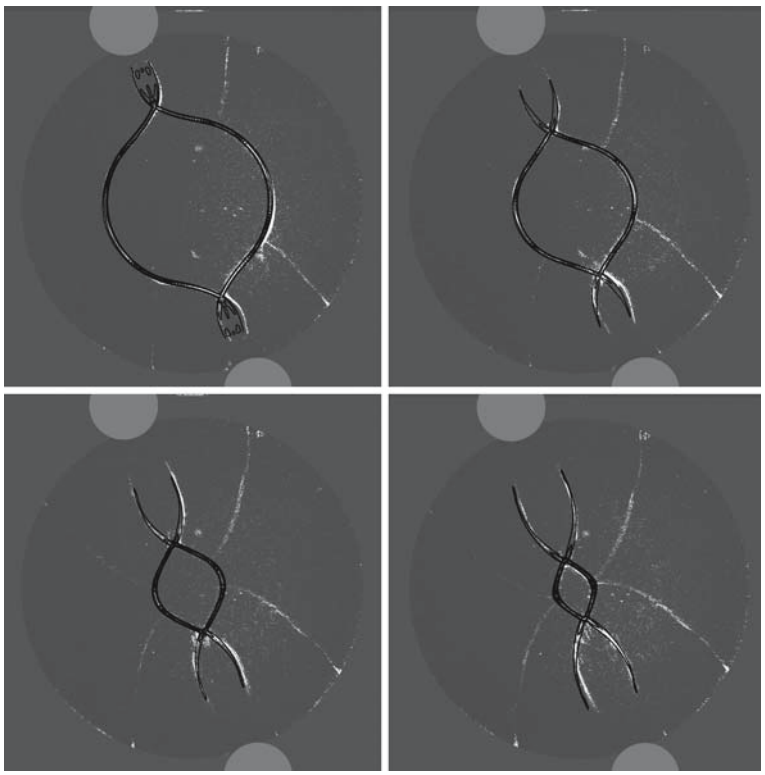

Fig. 20 Comparison of the calculated shockwave profiles with the experimental schlieren images at various positions with two cylindrical disturbances for $p_4/p_1 = 33.6$

formation. In the beginning, the diffracted shock wave appears to be convex similar to experimental observations. A square-like shock shape is formed at a later stage as the shock propagates toward the center. Similar to experimental observations, the sides of the shockfront become plane as shown in Fig. 11.

A comparison of the numerical and experimental results for one, two, four and eight cylindrical obstacle cases are

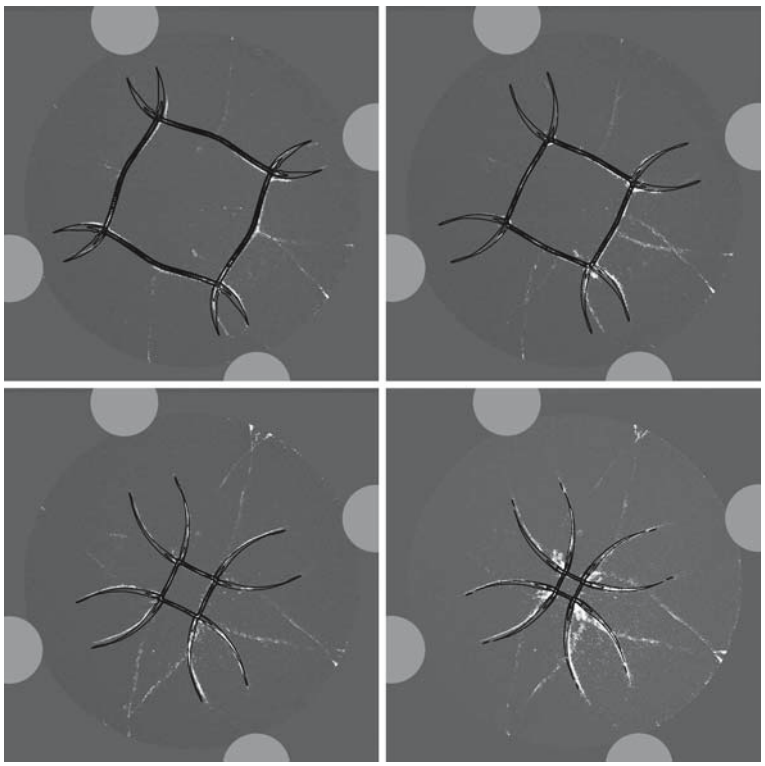

Fig. 21 Comparison of the calculated shockwave profiles with the experimental schlieren images at various positions with four cylindrical disturbances for $p_4/p_1 = 33.6$

shown in Figs. 19, 20, 21 and 22. As we can see the AUSF scheme reproduces the main features of the shock propagation. The simulated converging shock shapes agree well with experimental ones. The numerical shockfronts are displayed as black curves overlapping the white experimental shock shapes.

Figures 21 and 22 show that it is possible to obtain converging shocks with polygonal form by means of cylindrical obstacles placed in the computational domain. In Fig. 21 four cylindrical obstacles are placed symmetrically resulting in a square shock shape, while in Fig. 22 an octagonal shock shape is produced with eight cylindrical obstacles. Alternatively, various converging shock shapes may be produced by adopting an appropriate form of the reflector boundary as reported earlier in [5]. The present method is simpler in terms of practical applications. However, losses due to disturbances in the flow is one of the topics for further discussion. In other words, one would like to compare numerically the development of the maximum shock Mach number during the convergence process in both cases. Figure 23 shows that the maximum Mach number (at a certain time over the whole computational domain) is higher in the case of an octagonal reflector as compared to eight 15 mm diameter cylindrical obstacles. The dashed line represents the maximum shock Mach number for the eight cylindrical obstacles. The first sharp increase in shock Mach number at $t = 20$ μs is due to the area contraction in the flow introduced by the obstacles. The second sharp increase is created at the center of convergence and a gradual decrease of the shock strength follows during the reflection.

5 Conclusions

A horizontal coaxial shock tube was used to study the convergence and reflection of strong shock waves. The interaction of converging shock waves with cylindrical obstacles with three different cylinder diameters was visualized. The cylindrical obstacles were distributed in various patterns. A numerical study was performed and the results were compared with the visualization. The main results are summarized as follows:

(1) We succeeded in generating various polygonal shock shapes by introducing cylindrical obstacles in polygonal formation patterns. The method proposed herein is easier to implement than the one in which the shock is formed by the test section boundary [5]. Since a converging cylindrical shock wave is unstable, it is easy to disturb it and transform the shape of the shock.
(2) The nonlinear, shock-dynamic effect of the evolution of converging polygonally shaped shocks is well demonstrated in the present experiments. An octagonal shockfront transforms into a double octagon and then reconfigures to an octagonal shape although the phase

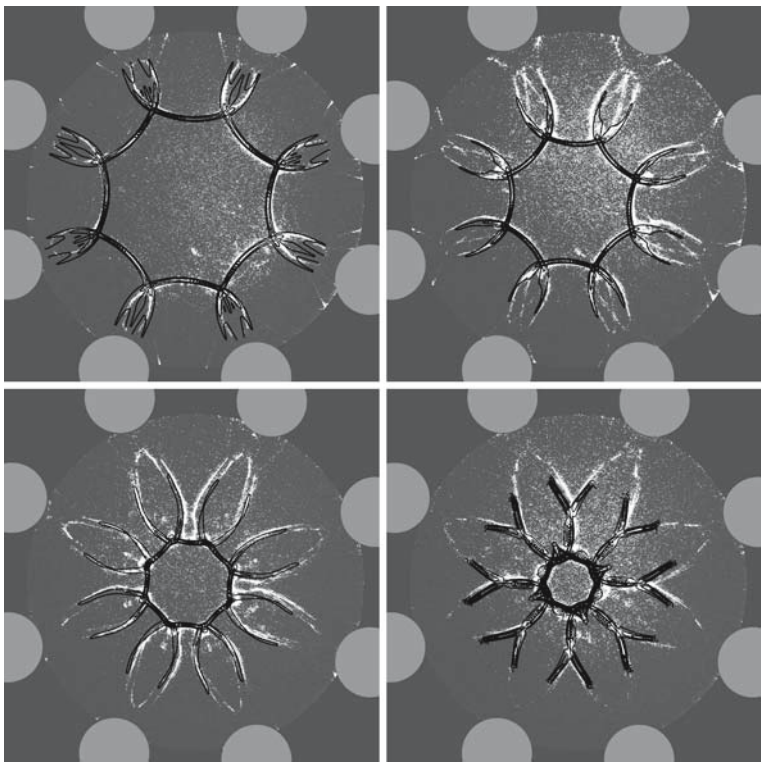

Fig. 22 Comparison of the calculated shockwave profiles with the experimental schlieren images at various positions with eight cylindrical disturbances for $p_4/p_1 = 33.6$

of its orientation is shifted. We thus confirmed experimentally the coupling between the local form of the shock and its local propagation velocity.

(3) Artificial disturbances placed in the test section are more prominent than the disturbances inherited from four supports of the shock tube inner body. The later are suppressed and not observable here as the supports were shaped to minimize initial disturbances.

(4) The diverging reflected shock propagating from the center of convergence is stable and initially of circular shape regardless of the degree of converging shock wave deformation. The form of the shock at farther distances from the center was not visualized here. It is known however that the shock form will be affected by the non-uniform flow created by the converging shock as reported by Eliasson et al. [5].

(5) Diffracted shock waves over cylindrical obstacles are delayed. The center of the converging shock wave is slightly deviated toward the disturbed side. However, the presence of the cylindrical obstacles more significantly affects the shock shape than the shift of the shock center.

(6) Numerical simulations based on the AUFS scheme successfully reproduced the major features of the shock propagation process. The numerical shock motion and flow patterns agreed well with experimental observations. This numerical scheme may therefore serve for a future extension of experimental works.

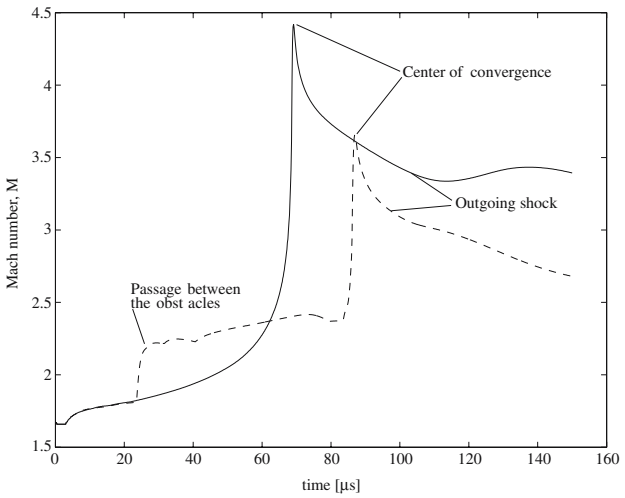

Fig. 23 Comparison of the maximum Mach number in the computational domain for a shock produced by an octagonal boundary, *solid line*, Versus eight cylindrical disturbances, *dashed line*

Acknowledgments This research was initiated in collaboration with Prof. Martin Lesser and his ideas and suggestions are gratefully acknowledged. The authors would like to thank Mr Ulf Landén at KTH Mechanics for careful construction of the cylindrical obstacles. We also would like to thank Dipl. Ing. Ramis Örlü for helping with the cold wire temperature measurements. This work has been financially supported by The Swedish Research Council (VR). This is gratefully acknowledged. The funding from the Göran Gustafsson Foundation provided means for the construction of the shock tube and for acquisition of the experimental equipment which is gratefully acknowledged. We also wish to

express our thanks to Prof. Takayama for his perusal of the manuscript and for the valuable suggestions.

References

1. Apazidis, N., Lesser, M., Tillmark, N., Johansson, B.: An experimental and theoretical study of converging polygonal shock waves. Shock Waves **12**, 39–58 (2002)
2. Apazidis, N., Lesser, M.: On generation and convergence of polygonal-shaped shock waves. J. Fluid Mech. **309**, 301–319 (1996)
3. Watanabe, M., Onodera, O., Takayama, K.: Shock wave focusing in a vertical annular shock tube. In: Brun, R., Dimitrescu, L.Z. (eds.) Shock Waves@Marseille vol. 4, pp. 99–104. Springer, Berlin (1995)
4. Bryson, A.E., Gross, R.W.F.: Diffraction of strong shocks by cones, cylinders, and spheres. J. Fluid Mech. **10**, 1–16 (1961)
5. Eliasson, V., Apazidis, N., Tillmark, N., Lesser, M.B.: Focusing of strong shocks in an annular shock tube. Shock Waves **15**, 205–217 (2006)
6. Perry, R.W., Kantrowitz, A.: The production and stability of converging shock waves. J. Appl. Phys. **22**, 878–886 (1951)
7. Schwendeman, D., Whitham, G.: On converging shock waves. Proc. R. Soc. Lond. A **A413**, 297–311 (1987)
8. Sun, M., Takayama, K.: An artificially upstream flux vector splitting scheme for the euler equations. J. Comput. Phys. **189**, 305–329 (2003)
9. Takayama, K., Onodera, O., Hoshizawa, Y.: Experiments on the stability of converging cylindrical shock waves. Theor. Appl. Mech. **32**, 305–329 (1984)
10. Takayama, K., Kleine, H., Gröning, H.: An experimental investigation of the stability of converging cylindrical shock waves in air. Exp. Fluids **5**, 315–322 (1987)
11. Watanabe, M., Takayama, K.: Stability of converging cylindrical shock waves. Shock Waves **5**, 149–160 (1991)
12. Whitham, G.: A new apporach to problems of shock dynamics. Part 1. Two-dimensional problems. J. Fluid Mech. **2**, 145–171 (1957)
13. Whitham, G.: On the propagation of shock waves through regions of non-uniform area or flow. J. Fluid Mech. **4**, 337–360 (1958)
14. Whitham, G.: A new approach to problems of shock dynamics. Part 2. Three-dimensional problems. J. Fluid Mech. **5**, 369–386 (1959)

Paper 3

3

The Production of Converging Polygonal Shock Waves by Means of Reflectors and Cylindrical Obstacles

Veronica Eliasson

KTH Mechanics, Royal Institute of Technology, SE-100 44 Stockholm, Sweden

Abstract. Converging and reflecting strong shock waves are investigated experimentally in a horizontal co-axial shock tube. The shock tube has a test section mounted at the end of the tube. Two different methods to produce various geometrical shapes of shock waves are tested. In the first method the reflector boundary of the test section is exchangeable and four different reflectors are used: a circle, a smooth pentagon, a heptagon and an octagon. It is shown that the form of the converging shock wave is influenced both by the shape of the reflector boundary and by the nonlinear dynamics between the shape of the shock and the velocity of the shock front. Further, the reflected outgoing shock wave is affected by the shape of the reflector through the flow ahead of the shock front. In the second method we use cylindrical obstacles, placed in the test section at various positions and patterns, to create disturbances in the flow that will shape the shock wave. It is shown that it is possible to shape the shock wave in a desired way with these obstacles. The influence of the supports of the inner body of the co-axial shock tube is also investigated. A square shaped shock wave is observed close to the center of convergence for the circular and octagonal reflectors but not in any other setups. This square-like shape is believed to be caused by the supports for the inner body.

INTRODUCTION

Shock wave focusing has been investigated experimentally since the beginning of the 1950's. Still, it's an interesting research area with unsolved questions. High pressures and temperatures may be achieved in a region of gas compressed by a converging shock wave. This feature in connection with various technological applications, ranging from investigation of cavitation damage near material surfaces to applications in medicine and drug industry, is one of the main reasons for continuing interest in the problem of shock focusing. The highly nonlinear nature of the process presents a major challenge to its study. At the same time it serves as a source of the non-triviality of this phenomenon. Two aspects of a converging shock are of special interest. The first one being the connection between the local strength of the shock and the shape evolution of the converging shock front. The second issue, which is however closely related to the first one is the question of the stability of converging shocks.

Further, a cylindrical shock wave is very sensitive to disturbances and will change its form when encountering a disturbance. [1], [2] and [3] studied cylindrical shock wave focusing in horizontal annular shock tubes. An interesting discovery was the formation of triangular or square formed shocks when the shock reached the final stage of focusing. This disturbance was found to be introduced by the number of supports (3 or 4) for the annular part of the shock tube. To create shock waves without disturbances [4] used a vertical co-axial shock tube without supports. The results showed that cylindrical shocks converged more uniformly than in horizontal shock tubes, used in previous studies.

Analytical and numerical results from [5] showed that if an n-gonal shaped shock wave is formed it will repeat itself during the focusing process. This was confirmed numerically by [6] and [7] for a smooth pentagonal converging shock wave.

In the present study we investigate experimentally the focusing and reflection of strong shocks. The experiments were performed in a new shock tube facility at the department of Mechanics, KTH. The shock tube is a horizontal co-axial tube. A plane shock wave transforms into an annular shape and is then focused and reflected in the test section mounted at the end of the tube. The outer boundary of the test section is exchangeable and various geometrical shapes of the reflector can be chosen.

We apply two different methods to create various geometrical shapes of shock waves. In the first method we choose a specific shape of the outer boundary of the test section. Four boundaries with various shapes have been tested in these experiments: a circular, a smooth pentagonal, a heptagonal and an octagonal boundary. In the second method cylindrical obstacles are placed in the test section. We use cylinders of different sizes, placed at various positions and patterns. These cylinders create disturbances in the flow and make it possible to shape the

CP832, *Flow Dynamics, The Second International Conference on Flow Dynamics*
edited by M. Tokuyama and S. Maruyama
© 2006 American Institute of Physics 0-7354-0324-4/06/$23.00

Downloaded 12 Jul 2007 to 128.32.164.115. Redistribution subject to AIP license or copyright, see http://proceedings.aip.org/proceedings/cpcr.jsp

shock wave in a desired way.

EXPERIMENTAL SETUP

The experimental setup consists of a laser (the light source), a horizontal shock tube and a schlieren optics system. The shock tube has a test section where shock waves are focused and reflected. The process is visualized by the schlieren system with a camera. The experimental setup is shown in Fig. 1.

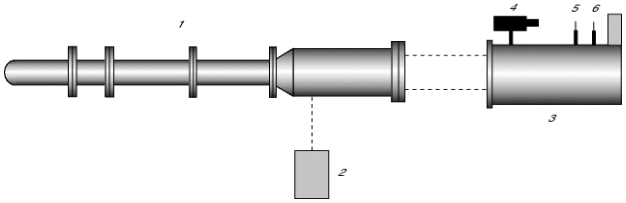

FIGURE 1. Schematic overview of the experimental setup: 1. Shock tube, 2. Pulse laser, 3. Schlieren optics, 4. PCO CCD camera, 5. Lens, 6. Schlieren edge.

The shock tube

The 2.4 m long circular shock tube with a diameter of 80 mm consists of a high pressure part and a low pressure part separated by a 0.5 mm thick aluminum membrane. A schematic illustration of the shock tube and its main parts is shown in Fig. 2. The first step to create a shock wave is to evacuate the low pressure part of gas. Then the high pressure part is filled with gas and at a certain pressure difference between the two parts the membrane bursts and a shock wave is formed. To control the membrane opening, a knife cross is placed at the inlet of the low pressure part. The knife-cross helps the membrane to open evenly. The shock wave becomes planar in the inlet section of the low pressure part, then enters the transformation section and becomes annular. This is

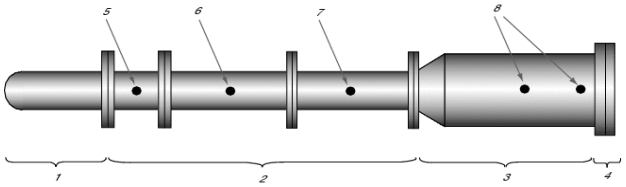

FIGURE 2. Schematic overview of the shock tube setup: 1. High pressure part, 2. Low pressure part: inlet section, 3. Low pressure part: transformation section, 4. Low pressure part: test section, 5. Pressure sensor, 6. Vacuum valve, 7. Vacuum pump, 8. Shock speed sensors.

done by a conically diverging section where the diameter increases from 80 mm to 160 mm. The cross-section area is constant from the inlet section through the transformation section. An inner body is mounted coaxially in the interior of the outer tube, forming the annular section. The 490 mm long inner body with a diameter of 140 mm is mounted with two sets of four supports. The supports are shaped as wing profiles in order to minimize the disturbances in the flow. The second set of supports is rotated 45° relative to the first set. The plane test section is mounted directly at the end of the annular section. Hence, the shock wave enters the test section via a sharp 90° bend and the focusing and reflection process begins. The outer boundary of the test section is exchangeable and various geometrical shapes of the reflector can be chosen. In the present study four reflectors have been used: a circle, a pentagon, a heptagon and an octagon.

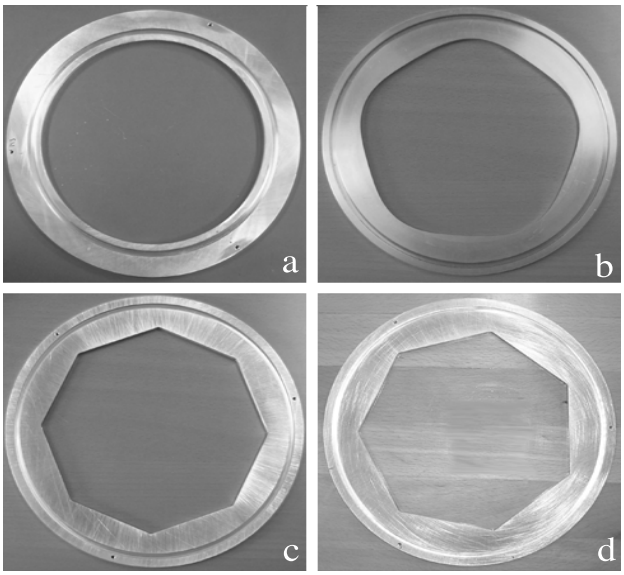

FIGURE 3. The four reflectors used in the present experiment.

The present experiments uses air as gas in both the high and low pressure part of the tube. The pressure in the low pressure part, p_1, is 13.3 kPa and in the high pressure part, p_4, about 1500 kPa. This produces strong shocks at Mach number 2.3.

EXPERIMENTAL RESULTS

The present experimental setup allows only one photograph per run in the shock tube. The visualization process is made by a schlieren system with a CCD camera (SensiCam, 12 bits, 1280 x 1024 pixels, pixel size 6.7 x 6.7 $\cdot 10^{-6}$m, CCD). The light source consists of an Nd:Yag (NewWave Orion) laser with single shot operation. The focusing and reflection process is resolved in time by single exposures taken at different time delays.

Downloaded 12 Jul 2007 to 128.32.164.115. Redistribution subject to AIP license or copyright, see http://proceedings.aip.org/proceedings/cpcr.jsp

The camera and the light source are triggered by sensors placed at the annular part of the shock tube and a time delay unit (Stanford Research System, DG 535) is used to take the photo at the predetermined position.

Typical sets of images of the converging and reflection process are seen in Fig. 4 and Fig. 5.

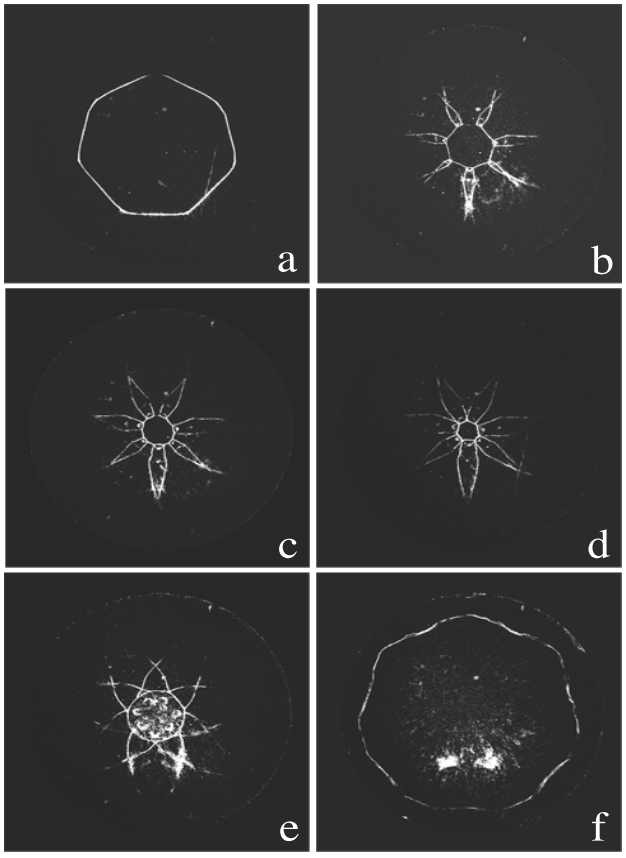

FIGURE 4. Shock waves created with the heptagonal reflector boundary. The time difference between the first and the last schlieren photograph is $75 \cdot 10^{-6}$s.

A series of schlieren photographs with the heptagonal reflector boundary is shown in Fig. 4. At first a heptagonal shock wave, oriented in the same direction as the reflector boundary, is created, see Fig. 4(a). Then it transforms into a double-heptagon and back to a heptagonal shock wave but oriented opposite to the former one, i.e. the corners have developed into plane sides and the plane sides into corners, see Fig. 4(b). This procedure continues during the whole convergence process. When the shock wave starts to reflect it first has a circular shape. After a while it transforms into a heptagonal shape since it is influenced by the flow ahead of the shock front.

In Fig. 5 the octagonal reflector is used. At first an octagonal shaped shock wave is created, Fig. 5(a). It then transforms into a double-octagon and then back again to an octagon. This time it is oriented opposite to the initial shape, see Fig. 5(b). This was earlier predicted by [6] and [5] using numerical analysis. It is due to the nonlinear coupling between the shape of the shock wave and the velocity of the shock propagation that causes this behavior. Regions with high curvature travel faster than the plane parts of the shock which leads to the reconfiguring and reorientation process. The reflected shock wave is at first circular, Fig. 5(c), but after some time it is influenced by the flow ahead of it and transforms into an octagonal shape again.

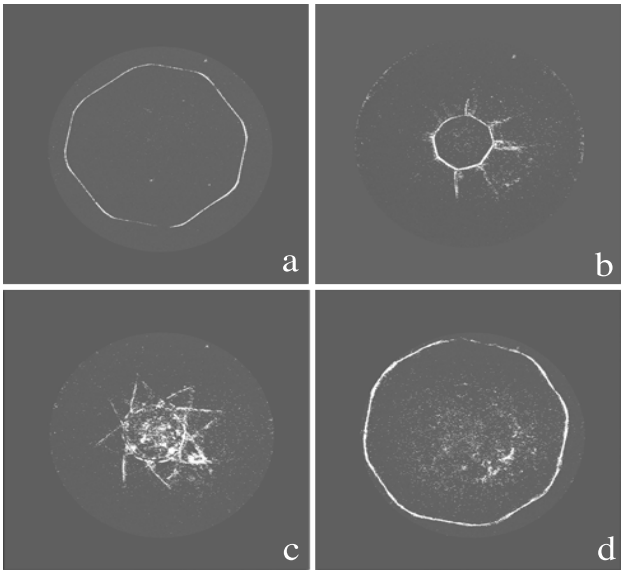

FIGURE 5. Shock waves created with the octagonal reflector boundary, (a)-(b) are converging and (c)-(d) are diverging. The time difference between (a) and (d) is $85 \cdot 10^{-6}$s.

The second method to shape the shock wave is to place cylindrical obstacles in a specific pattern in the test section. The cylinders create disturbances in the flow and hence it is possible to shape the shock wave in a desired way. A circular reflector boundary is used in this case. In Fig. 6 we show the result when 8 cylinders, with diameters of 15 mm, are placed in an octagonal pattern at radial position $r = 46$ mm. At first the shock wave obtains an octagonal shape with sides that are convex forward, Fig. 6(a). Then the sides get plane and the shock transforms into a double-octagon Fig. 6(b) and back to an octagonal shape which is reoriented, Fig. 6(c). In Fig. 6(d) the shape of the reflected shock wave is circular.

The influence of the supports for the inner body is investigated. At first two of the downstream supports where tilted so that they occupied a larger cross-section area. This resulted in a non-symmetrical square shaped shock wave close to the vicinity of the center of convergence. Then the supports where tilted back in their original position to minimize the disturbances in the

Downloaded 12 Jul 2007 to 128.32.164.115. Redistribution subject to AIP license or copyright, see http://proceedings.aip.org/proceedings/cpcr.jsp

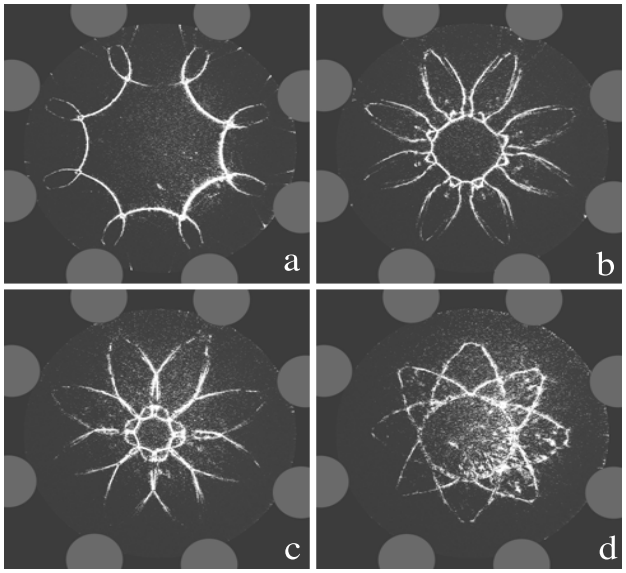

FIGURE 6. Schlieren photographs of shock waves at different time instants passing eight cylinders, with diameters of 15 mm. The grey circles show the positions for the cylindrical obstacles. (a)-(b) are converging and (c)-(d) are diverging. The time difference between (a) and (d) is $60 \cdot 10^{-6}$s.

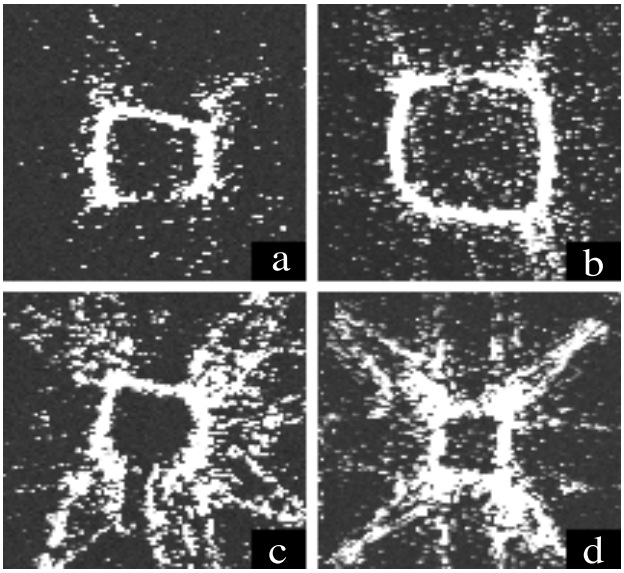

FIGURE 7. Square shaped shock waves close to the vicinity of the center of convergence. The square shaped shock is due to the supports for the inner body. The circular reflector is used for (a) and (b) and an octagonal reflector for (c) and (d).

flow field. The square shaped shock was still present but this time its form was more symmetrical than before. Schlieren photographs of the square shaped shock waves are shown in Fig. 7. In Fig. 7(a) and (b) the circular reflector boundary is used and in Fig. 7(c) and (d) the octagonal reflector boundary is used. In (a) and (c) the supports are tilted and in (b) and (d) they are in original position. The square shaped shock wave is only observed for the circular and octagonal reflectors and not for the pentagonal and the heptagonal reflectors. For the pentagonal and the heptagonal reflectors the shock wave follows the procedure of transforming and reconfiguring as long as we can see it.

NUMERICAL RESULTS

An artificially upstream flux vector splitting scheme (AUFS) for the Euler equations, introduced by [8], was used to conduct a numerical study of the focusing process. In the numerical study most of the features of the shock focusing process could be predicted and reproduced.

In a two-dimensional numerical study of the shock focusing, the initial conditions were chosen as an annular high pressure zone outside a circular low pressure zone. The outer boundary of the high pressure zone was placed at the outer boundary of the test section. The inner boundary corresponded to the inner circular end of the inner body of the shock tube. In all simulations the pressure in the inner circular part was chosen to the same pressure as in the experiments, $p_1 = 13.3$ kPa. In the numerical study the high pressure, p_4, was reduced to 30% of that in the experiment, giving $p_4/p_1 = 33.6$. This reduction can be motivated by pressure losses in to the sharp 90° bend just before the shock wave enters the test section.

In Fig. 8 a comparison between the experiments and numerical results are shown for the case with eight cylindrical obstacles and the circular reflector. As seen from this figure the form of converging shocks compares well with the calculated shock fronts.

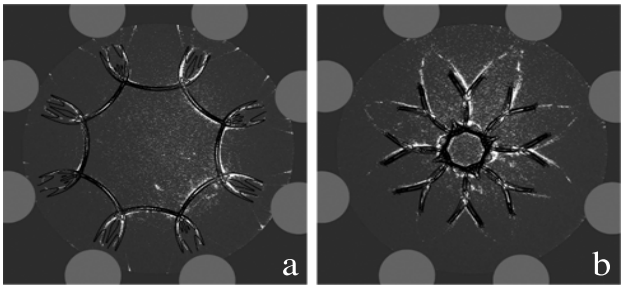

FIGURE 8. Comparison of the computed shock wave profiles with the experimental schlieren photographs at various positions in the test section with eight cylindrical disturbances for $p_4/p_1 = 33.6$.

Downloaded 12 Jul 2007 to 128.32.164.115. Redistribution subject to AIP license or copyright, see http://proceedings.aip.org/proceedings/cpcr.jsp

CONCLUSIONS

We summarize the major results as follows:

(1) The initial form of the converging shock can be tailored by an appropriate choice of the form of the reflector boundary or by introducing obstacles in a specific pattern in the flow.

(2) The nonlinear dynamics of the shock convergence is observed in the present experimental study. The form of the shock undergoes a transformation from an original heptagonal form through a double-heptagon back to a new heptagon with an opposite orientation. This behavior is also observed when the outer boundary is octagonal and pentagonal and also for the case when 8 cylindrical obstacles are introduced in the flow.

(3) The final form of the converging shock is square-like for the case when a circular and octagonal reflector is used. The square like shape is believed to be caused by the supports for the inner body of the co-axial shock tube. It is not observed for the pentagonal or heptagonal reflectors. The artificially introduced disturbances are stronger than the disturbances caused by the four supports for the inner body since the previously observed square-like shape no longer exists, i.e. the octagonal shaped shock wave, created by the eight obstacles, is visible until the shock wave converges.

(4) The reflected shock initially has a circular symmetry for all four reflectors. It retains its circular symmetry in the case of the circular reflector. For the three other reflectors (pentagonal, heptagonal and octagonal) the form of the outgoing shock is influenced by the flow field created by the converging shock. This shows the influence of the flow ahead of the shock on the shape of the reflected shock. This behavior is observed when different reflector boundaries are used and not when obstacles are present in the flow. The reason for this is that no photographs where taken with a large time delay for the case with obstacles.

(5) In a numerical study the major features of the shock wave focusing process in the test section were reproduced. The flow patterns obtained in the numerical computations compare well with the experimental observations.

ACKNOWLEDGMENTS

The author would like to thank Dr. Nicholas Apazidis for providing the numerical simulations and for valuable comments on the manuscript. Dr. Nils Tillmark is acknowledged for many useful suggestions and ideas during the work. Prof. Martin Lesser is acknowledged for initiating this project. 21st Century COE of Flow Dynamics is acknowledged for the invitation and financial support to ICFD2005.

REFERENCES

1. K. Takayama, O. Onodera and Y. Hoshizawa, *Theor. Appl. Mech.*, **32**, 117–127 (1984).
2. K. Takayama, H. Kleine and H. Gröning, *Exp. Fluids*, **5**, 315–322 (1987).
3. M. Watanabe and K. Takayama, *Shock Waves*, **1**, 149–160 (1991).
4. M. Watanabe, O. Onodera and K. Takayama, "Shock Wave Focusing in a Vertical Annular Shock Tube" in *Shock Waves @ Marseille IV.*, edited by R. Brun and L. Z. Dimitrescu, Berlin Heidelberg: Springer-Verlag, 1995, pp. 99–104.
5. D. W. Schwendeman and G. B. Whitham, *Proc. R. Soc. Lond. A*, **413**, 297–311 (1987).
6. N. Apazidis and M. B. Lesser. *J. Fluid Mech.*, **309**, 301–319 (1996).
7. N. Apazidis, M. B. Lesser, N. Tillmark and B. Johansson, *Shock Waves*, **12**, 39–58 (2002).
8. M. Sun and K. Takayama, *J. Comput. Phys.*, **189**, 305–329 (2003).

Downloaded 12 Jul 2007 to 128.32.164.115. Redistribution subject to AIP license or copyright, see http://proceedings.aip.org/proceedings/cpcr.jsp

Paper 4

4

Shock Waves (2007) 17:43–50
DOI 10.1007/s00193-007-0091-0

ORIGINAL ARTICLE

Regular versus Mach reflection for converging polygonal shocks

V. Eliasson · M. Kjellander · N. Apazidis

Received: 27 January 2007 / Revised: 1 May 2007 / Accepted: 11 May 2007 / Published online: 12 June 2007
© Springer-Verlag 2007

Abstract The onset of Mach reflection or regular reflection at the vertices of a converging polygonal shock wave was investigated experimentally in a horizontal annular shock tube. The converging shock waves were visualized by schlieren optics. Two different types of polygonal shock convergence patterns were observed. We compared the behavior during the focusing process for triangular and square-shaped shocks. It is shown that once a triangular shaped shock is formed, the corners in the converging shock will undergo regular reflection and consequently the shape will remain unaltered during the focusing process. A square-shaped shock suffers Mach reflections at the corners and hence a reconfiguring process takes place; the converging shock wave alternates between a square and an octagon formation during the focusing process.

Keywords Shock focusing · Annular shock tube · Imploding shock · Shock reflection

PACS 47.10.ab · 47.40.Nm

1 Introduction

Shock wave focusing has been studied in several research communities since the beginning of the 1940s when a similarity solution was presented for a converging cylindrical shock wave in [9]. Analytical, numerical and experimental investigations have been performed since then; for example, see [13] and [15]. It is well known that a converging cylindrical shock wave is unstable. It is unstable in the sense that it loses its original shape if it is perturbed by disturbances in the flow. The disturbed shape tends to produce a polygonal structure with plane sides and sharp corners. The polygonal shape will lack symmetry if the perturbations in the flow are not symmetric or strong enough. It is, however, possible to generate converging shocks with polygonal symmetric shapes that are stable, i.e. shapes that evolve during the focusing process in a predictable way. Such stable shapes were generated analytically and numerically in [13], numerically in [1], experimentally and numerically in [2,8] and [7]. Depending on the type of reflection that occurs at the vertices of the polygonal shapes, some of these shapes will transform continuously during the focusing process, changing from an n-corner shape into a $2n$-corner shape and then back again; see an example in Fig. 1. The new plane segments emerging from corners as a result of Mach reflection have higher Mach number than the adjacent sides. Hence they travel faster and absorb the adjacent sides. When such two segments meet, they build a new corner. The new polygon has the same number of sides at the end of each cycle but is rotated with respect to the old polygon so that the corners are opposite to the midpoints of the old sides. This reorientation process is due to the nonlinear interaction between the local velocity and the shape of the shock front. For example, a square shaped shock wave will transform into an octagon and then back to a square again, with the second square oriented opposite to the first square. The above reconfiguration process stems from the Mach reflection at the corners and constitutes, in fact, the basis for the Mach number increase on the shock front; each time the reconfiguration cycle is completed, the Mach number over the shock front is increased stepwise; see [13] and [1]. Some elements of this 2D process (i.e. the tendency to form planar pieces) is also visible for converging spherical shocks; see [12].

Communicated by B.W. Skews.

V. Eliasson (✉) · M. Kjellander · N. Apazidis
KTH Mechanics, Royal Institute of Technology,
100 44 Stockholm, Sweden
e-mail: veronica@mech.kth.se

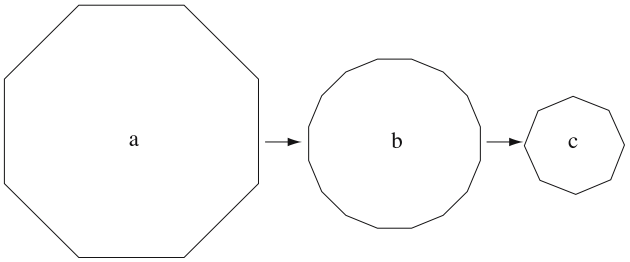

Fig. 1 An example of a polygonal converging shock wave with eight sides that suffers Mach reflection. It will continuously transform from **a** an octagon to **b** a double octagon and then back to **c** an octagon again, oriented opposite to the one in **a**

There exists, however, another mechanism of symmetric polygonal shock focusing in which the Mach number remains bounded. A self similar solution for the focusing process of 2D equilateral triangular shock waves was investigated in [6]. This solution shows that the corners of the triangular shock wave undergo regular reflections and preserve the triangular shape during the whole focusing process for certain values of Mach numbers and initial conditions. The energy density is bounded for this solution which means that the Mach number will approach a constant value at the focus. This is in contrast to symmetric polygonal shocks (with number of sides greater than three) that suffer Mach reflection at the vertices, and where the Mach number increases as the shock approaches the focus. However, if the stability criteria for the triangular shock wave are violated, then a reconfiguring process takes place in which the corners develop into plane sides and the plane sides into corners as mentioned earlier.

There are several criteria for transition from a regular reflection (RR) to a Mach reflection (MR). Three of these were proposed in [11] and since then many more have been suggested; see [4,5]. The length scale concept was introduced in [10] and is the criterion that agrees best with pseudo steady flow in experimental shock tube facilities. The ongoing research on transition conditions for RR↔MR is motivated by difficulties in matching theoretical and experimental results. One problem is the persistence of regular reflections well past the theoretical maximum limit and many publications address this problem; see [3].

Following the ideas in [6], we investigated two different types of reflection, RR or MR, that can occur at the vertices of a converging polygonal shock wave. The polygonal shock waves were generated in the same shock tube and with the same method as in [7]. In the present study we generated triangular and square shaped shocks. Their focusing behavior was compared and it was found that while the triangular shock preserves its form and orientation, the square shock transforms to an octagon and then back to a square shape which is rotated 45° with respect to the initial configuration. According to the previous numerical work in [13] and [1], this reconfiguration process continues until the shock wave reaches the focusing center. The long term objective for this research is to gain knowledge of how to create a stable converging shock wave that will produce the highest temperatures and pressures possible at the center of convergence. At first glance the circular shock would be the most obvious and suitable form to achieve this objective, but, since it is unstable the focusing process is not repeatable. A polygonal shock is stable and as the shock converges the Mach number increases according to exactly the same formula as for a cylindrical shock, [13]. Thus, we have investigated experimentally how to create various geometrical shapes of converging shocks that undergo either Mach reflection or regular reflection.

We start by describing the experimental setup and the method used to create the polygonal shock waves. This is followed by the experimental results. Finally we conclude and summarize the results.

2 Experimental setup

The experimental setup consists of a 2.4 m long horizontal annular shock tube where the shock wave is generated and focused. A laser (an air-cooled Nd:Yag, NewWave Orion) is used as a light source for the visualization equipment that consists of a schlieren system with a CCD camera (PCO SensiCam, 12 bits, 1,280×1,024 pixels, pixel size: 6.7×6.7 μm). See Fig. 2 for a schematic overview of the experimental setup. The shock tube consists of two main parts, a high pressure chamber and a low pressure channel. The two parts are separated by a 0.5 mm thick aluminum membrane. The experiment is initiated by filling the high pressure chamber with gas. At a certain pressure difference the membrane will break. After the membrane breaks, a plane shock wave is formed and starts to travel downstream in the shock tube through the low pressure channel. The low pressure channel is divided into three sections; an inlet section where the plane shock wave is formed, a transformation section where the plane shock wave becomes annular and the test section which is located at the rear end of the shock tube where the shock

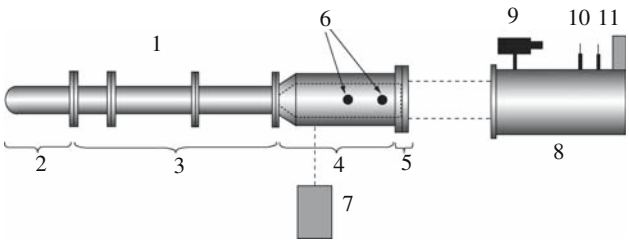

Fig. 2 Schematic overview of the experimental setup: *1* shock tube, *2* high pressure chamber, *3* low pressure channel: inlet section, *4* low pressure channel: transformation section, *5* low pressure channel: test section, *6* shock speed sensors, *7* laser, *8* schlieren system, *9* CCD camera, *10* lens, *11* schlieren edge

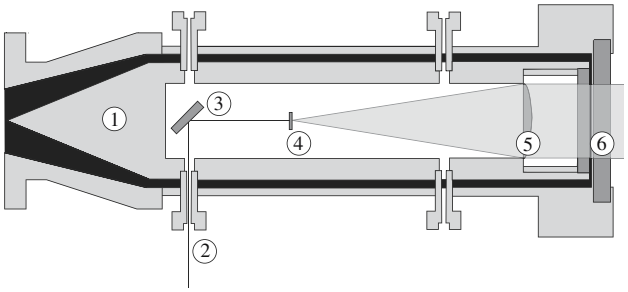

Fig. 3 Schematic overview of the rear part of the shock tube: *1* the inner body consisting of a cone followed by a cylindrical tube, *2* laser light entrance through one of the supports, *3* mirror to deflect the laser light in the axial direction, *4–5* beam expander, *6* glass windows. The shock wave travels in the *black* region between the outer tube and the inner body

wave is focused and reflected. The annular part of the shock tube is composed of an inner body mounted coaxially inside the wider diameter outer tube. The inner body is represented by the dotted line in the low pressure channel shown in Fig. 2 and a simplified drawing of its various parts is shown in Fig. 3. The inner body consists of a cone followed by a cylindrical tube and is suspended by two sets of four supports. The two sets are placed 30.75 cm apart and the supports are shaped as wing profiles to minimize the disturbances on the flow. The second set of supports is rotated 45° relative to the first set. The cross-section area of the shock tube is held constant through the inlet section and into the transformation section and is then reduced by 50% in the test section.

The shock wave enters the test section radially through a sharp 90° bend. It is after the bend that the focusing and reflection process takes place. The test section has glass windows to enable visualization of the focusing and reflection process. The outer boundary of the test section is circular with a radius of 80 mm. The width of the air gap in the test section, between the two facing glass windows, is 5 mm.

The present experimental study uses air as gas in both the high and low pressure part of the tube. The pressure in the low pressure channel is 13.3 kPa and in the high pressure chamber about 1,500 kPa. This pressure difference produces strong shocks at Mach number $M_s = 2.3$, measured in the annular part of the shock tube before the shock wave enters the test section. Further details of the experimental setup can be found in [8].

2.1 Method to create polygonally shaped converging shock waves

A polygonally shaped converging shock wave was created by disturbing the shape of the initially cylindrical converging shock wave. The disturbances were produced by small metal cylinders placed inside the test section. Depending on the size and the positions of the cylindrical obstacles, it was possible to tailor the shape of the cylindrical converging shock wave into a desirable polygonal shape, as shown in [7]. Two different diameters of cylinders, 10 and 15 mm, were used in this experiment; see Fig. 4a. They were placed at two radial positions, $r_1 = 46.5$ mm and $r_2 = 61.5$ mm. Two different geometrical setups were used, an equilateral triangular and a square pattern; see Fig. 4b and c.

3 Experimental results

Two different geometrical shapes of shock waves were generated: triangular and square shaped shocks. To visualize the focusing process, the schlieren system together with the CCD camera was used to take single exposures at various time delays for each run in the shock tube. The reason for taking only one exposure during each run in the shock tube was due to limitations in the light source equipment and the CCD camera. The time delay unit, a Stanford Research System DG535, enabled schlieren exposures of the converging and reflecting shock at different time instants inside the test section. The size of the visualized area was 75 mm in diameter. The repeatability was good and the error in the shock speed, U_s, between consequent runs in the shock tube was about 0.5%. The results from the various setups are presented and discussed in the following two sections.

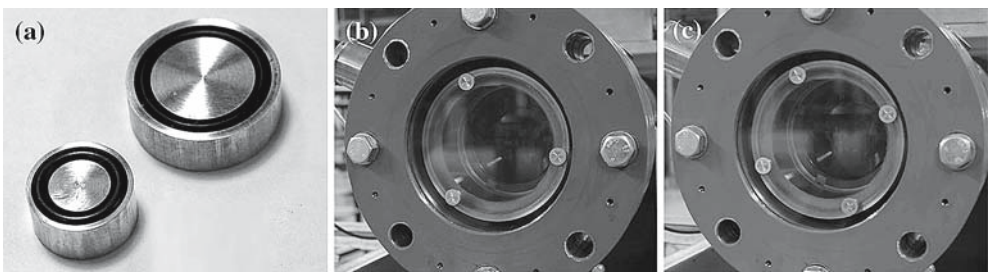

Fig. 4 **a** Two sizes of cylinders were used, 10 and 15 mm in diameter. **b** The equilateral triangular pattern and in **c** the square pattern of cylindrical obstacles

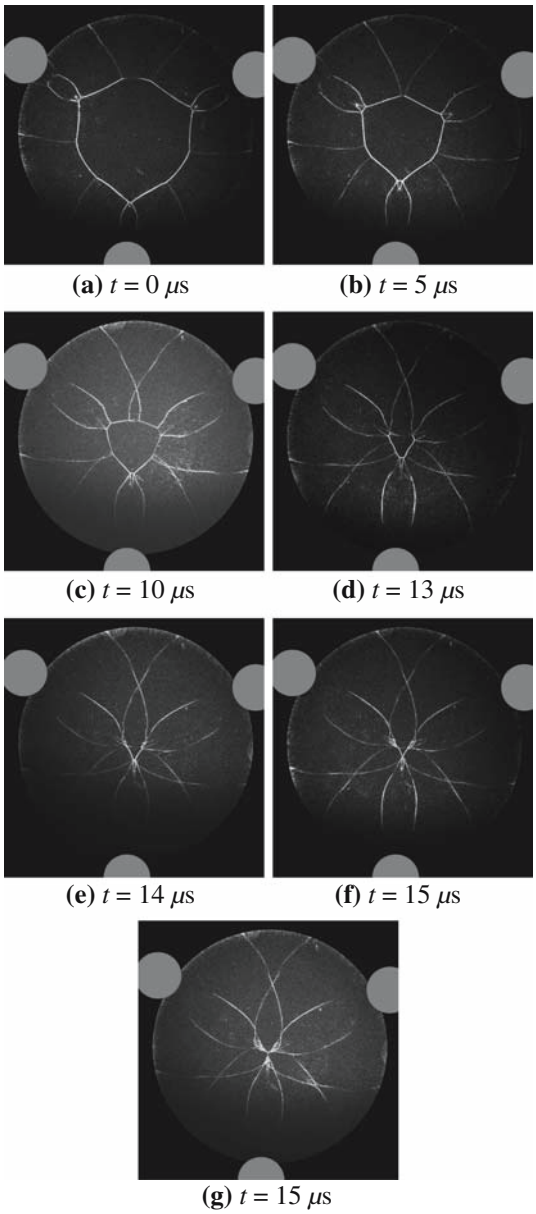

Fig. 5 Schlieren photographs at different time instants. Each photograph is from an individual run in the shock tube. The cylindrical shock wave is diffracted over three cylinders with diameters of 15 mm placed at $r = 46.5$ mm from the convergence center. The *grey circles* represent the cylinders

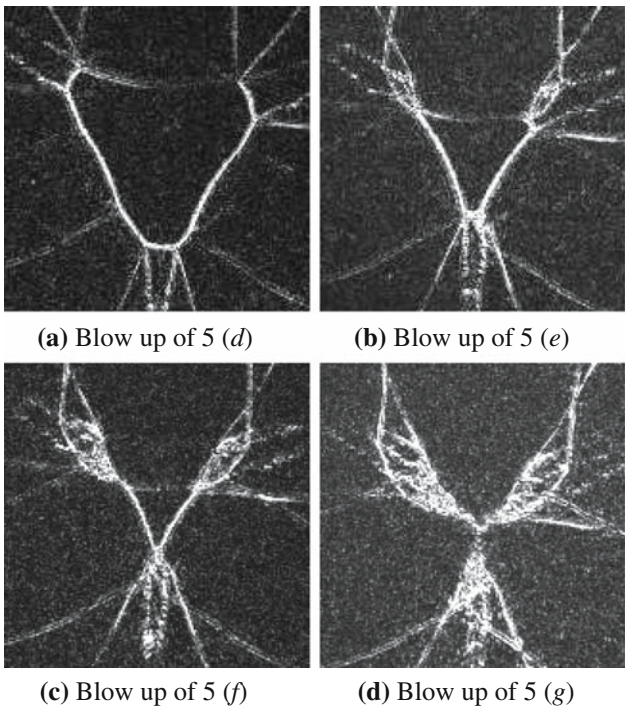

Fig. 6 Enlargements of schlieren photographs in Fig. 5d–g

3.1 Diffraction of a cylindrical shock wave from three cylinders

Three cylinders with diameters of 15 mm were placed inside the test section in an equilateral triangular pattern (Fig. 4b), at a radial position of $r_1 = 46.5$ mm. Schlieren photographs showing the convergence process of the diffracted shock wave are shown in Fig. 5. Each photograph is from an individual run in the shock tube and M_s was 2.3. In the beginning, the shock wave has a hexagonal shape (Fig. 5a–c), consisting of the disturbed plane parts and undisturbed convex parts. The plane parts are Mach shocks, formed after the shock is diffracted over the cylindrical obstacle. The undisturbed parts will decrease and finally disappear as the focusing process continues. Hence the shape of the shock wave becomes triangular; see Fig. 5d. In this frame the sides of the triangle are not planar but slightly curved. As the shock wave approaches the center of convergence, the sides eventually become planar; see Fig. 5d–f, or enlargements in Fig. 6a–c. Due to the angle between the reflected sides, the incident angle, and the shock Mach number, a regular reflection occurs at the corners of the triangle and the triangular shape remains unaltered until it has focused completely; see Fig. 5g and a blow up in Fig. 6d. There is one pair of photographs, Fig. 5f and g, that are taken at the same time instant but are slightly different in position. This is due to the fact that each shock is from an individual run in the shock tube and that will produce small variations in the conditions. Thus, the shocks are at slightly different positions at the same time instant. This is more pronounced closer to the center of focusing since the shock waves move faster there.

In the next experimental setup, the three cylinders were moved to the second radial position, $r_2 = 61.5$ mm, outside the frame of the visualized area. Then the above described experiment was repeated. Schlieren images are shown in Figs. 7 and 8. The converging shock wave behavior is similar to the previous case. In addition, two photographs of the reflected shock wave are shown in Fig. 7h and i. In Fig. 7h,

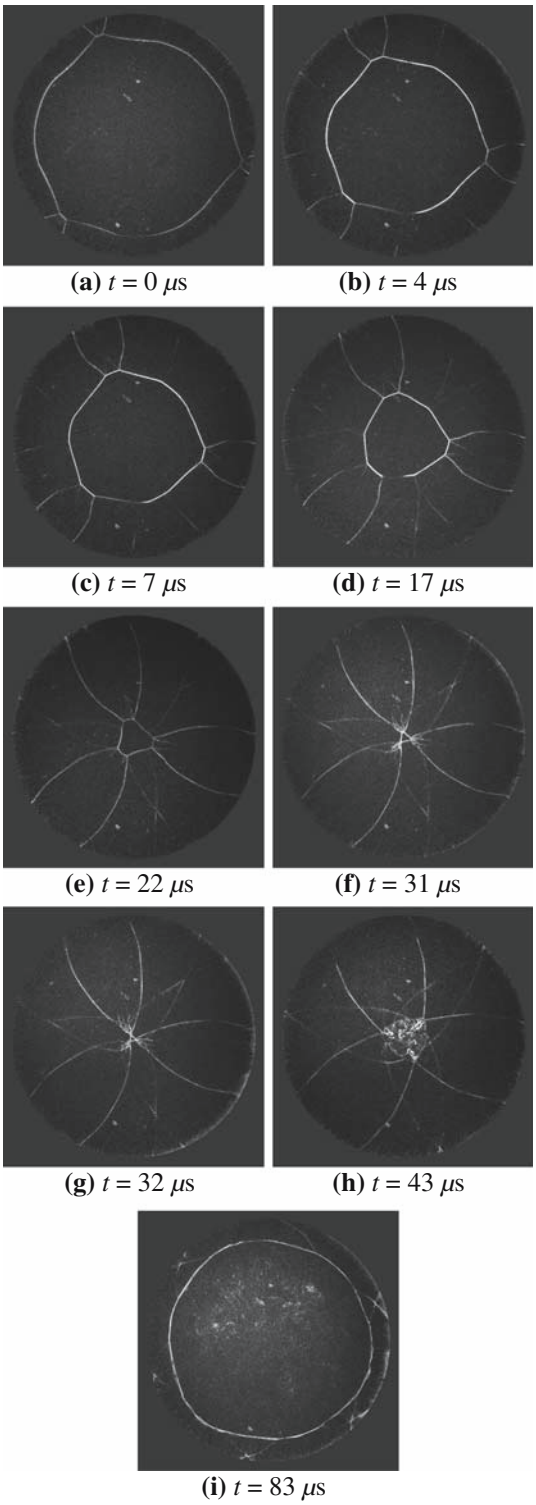

Fig. 7 Schlieren photographs at different time instants. Each photograph is from an individual run in the shock tube. The cylindrical shock wave is diffracted over three cylinders with diameters of 15 mm placed at $r = 61.5$ mm from the convergence center

the outgoing shock wave has a somewhat disturbed triangular shape. Later, the reflected shock wave becomes influenced by the still incoming flow, and the shape changes into a shape

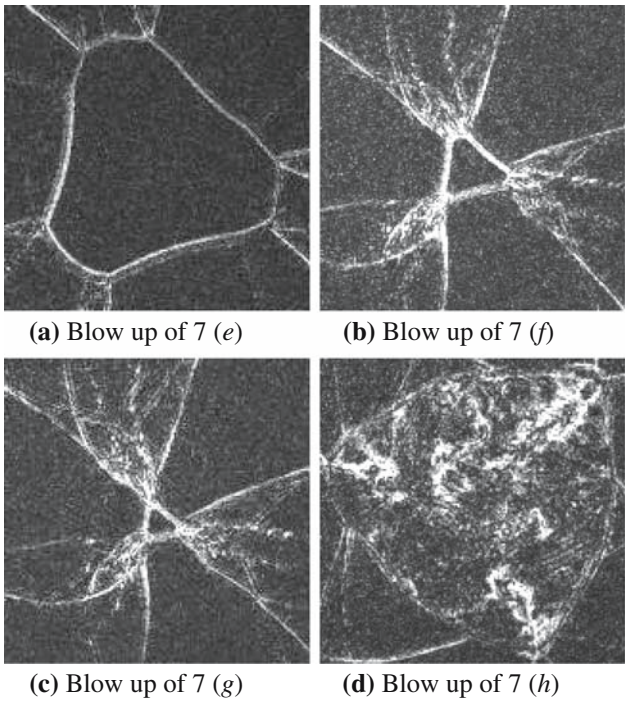

Fig. 8 Enlargements of schlieren photographs in Fig. 7e–h

that resembles the shape of the in-going shock wave in an early stage, as the one shown in Fig. 7a. The shock shape in Fig. 7i is less hexagonal and more cylindrical than the shock wave in Fig. 7a. This was also seen in [8], in wich the reflected shock wave first had a cylindrical shape that later became influenced by the incoming flow and changed into a shape that was similar to the shape of the converging shock wave in an early stage.

In the third experiment, the 15-mm diameter cylinders in the previously mentioned setup were replaced by 10-mm diameter cylinders. Schlieren photographs are shown in Figs. 9 and 10. Compared to the previous case, it is seen that the Mach stem is more pronounced in an earlier stage for this setup. The overall shape of the shock wave is less disturbed than in the previous case; it is more cylindrical than hexagonal. Still, as the shock wave converges it attains a triangular shape and when that shape is reached, it does not change. Rather, it decreases until it has reached the center of focus.

3.2 Diffraction of a cylindrical shock wave from four cylinders

For a square-shaped shock in air, the angle of incidence is $\pi/4$ and according to the detachment criterion, see [6], a regular reflection will be possible only for $M_s \leq 1.24$. An increase in Mach number will always end with Mach reflection at the corners of the polygonal shock wave and hence the previously mentioned reconfiguring process will take place.

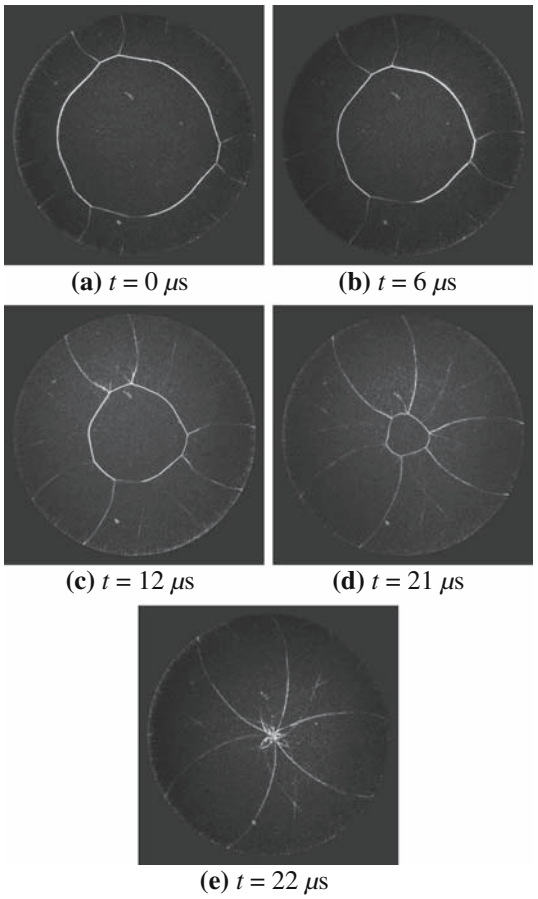

Fig. 9 Schlieren photographs at different time instants. Each photograph is from an individual run in the shock tube. The cylindrical shock wave is diffracted over three cylinders with diameters of 10 mm placed at $r = 61.5$ mm from the convergence center

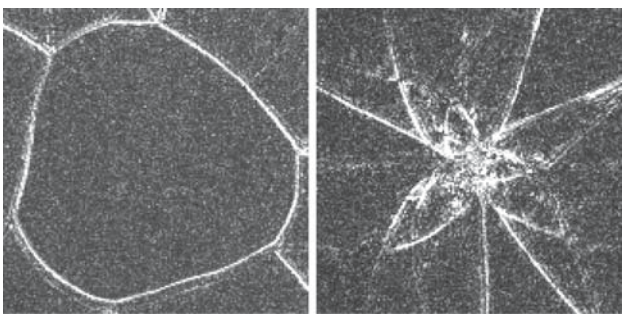

Fig. 10 Enlargements of schlieren photographs in Fig. 9d and e

Four cylinders were positioned as the corners in a square, at a radial position of $r_2 = 61.5$ mm, and then the above mentioned experiments were repeated. The Mach number used in the present study, $M_s = 2.3$, is higher than the limiting value for a regular reflection, resulting in a Mach reflection at the corners of the square shaped shock wave during the focusing process. Earlier results ([7]), also using Mach numbers higher than the limiting value for a regular reflection,

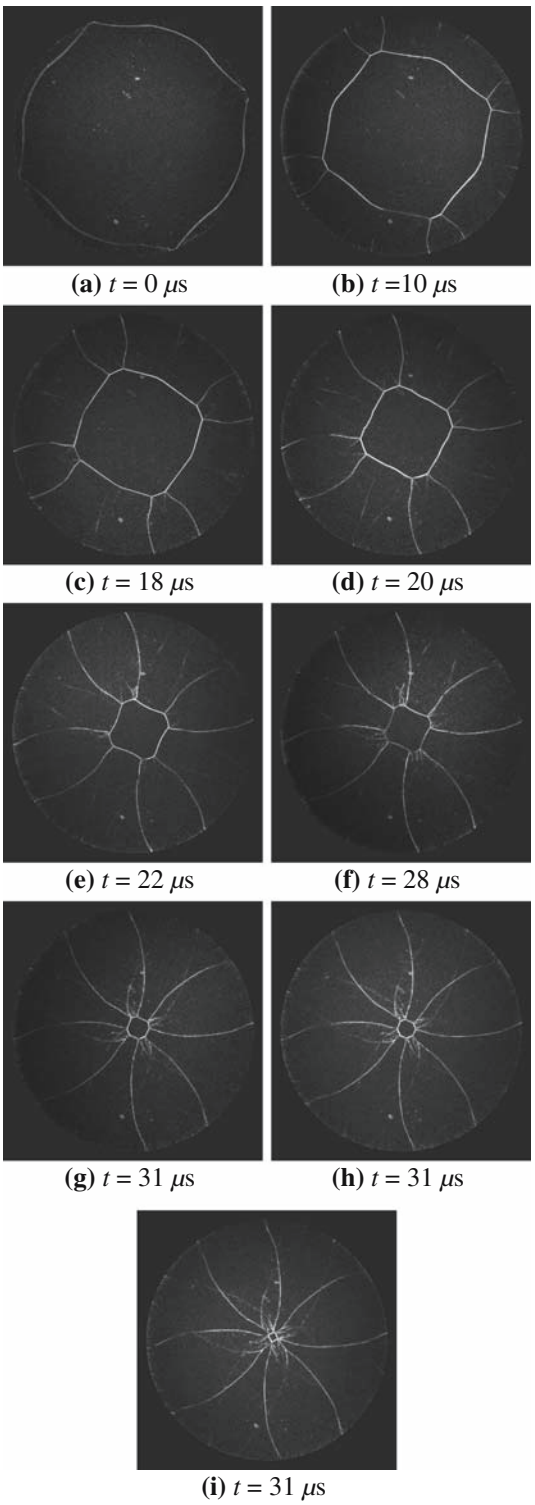

Fig. 11 Schlieren photographs at different time instants. Each photograph is from an individual run in the shock tube. The cylindrical shock wave is diffracted over four cylinders with diameters of 15 mm placed at $r = 61.5$ mm from the convergence center

show that when a converging shock wave obtains a square-like shape it will reconfigure between a square and an octagon during the focusing process. In Fig. 11, schlieren photographs

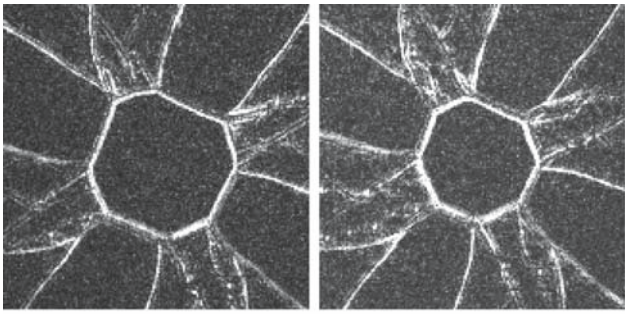

(a) Blow up of 11 (*g*) **(b)** Blow up of 11 (*h*)

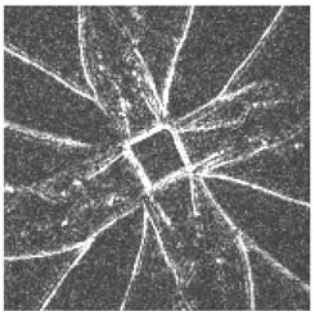

(c) Blow up of 11 (*i*)

Fig. 12 Enlargements of schlieren photographs in Fig. 11g–i

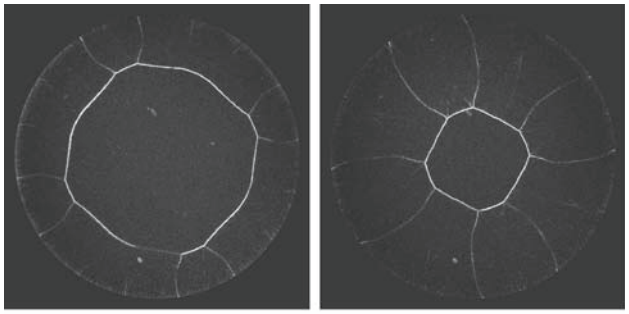

(a) $t = 0\ \mu$s **(b)** $t = 10\ \mu$s

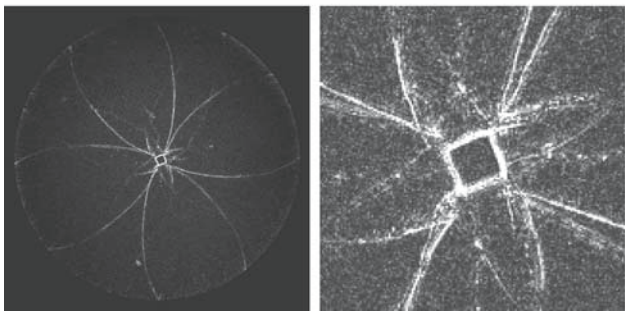

(c) $t = 20\ \mu$s **(d)** Blow up of (*c*)

Fig. 13 Schlieren photographs at different time instants. Each photograph is from an individual run in the shock tube. The cylindrical shock wave is diffracted over four cylinders with diameters of 10 mm placed at $r = 61.5$ mm from the convergence center

are shown for the setup with 15 mm diameter cylinders. In Fig. 11a, the shock wave has just reached the visualization area and the undisturbed parts still remain cylindrical. Thereafter the shock wave approaches a square-like shape, shown in Fig. 11b,c. The sides of the square are divided into several shorter pieces, that together produce an almost planar side, see Fig. 11c. The individual pieces constructing one side originate from the undisturbed part of the shock wave in between two Mach stems emanating from the diffraction over the cylindrical obstacle. As the convergence process continues, the sides of the square blend into one slightly curved smooth part. Later, the slightly curved sides become planar and Mach stems are formed at the corners. At this time the reconfiguring process starts. The Mach stems at the corners can be seen in Fig. 11g and an octagonal shape is seen in Fig. 11h. The first cycle of the reconfiguration process is ended when a square shaped shock wave with an orientation opposite to Fig. 11d–g is formed as shown in Fig. 11i. Enlargements of Figs. 11g–i are shown in Figs. 12a–c.

In Fig. 13 three images from the case with 10 mm diameter cylinders are shown. The behavior is similar to the previous case in a sense that the shock wave will first develop planar sides and then start to reconfigure and change orientation. The last image, Fig. 13c, shows the first reoriented shock wave, enlarged in Fig. 13d.

Finally, we investigated whether the last visible shock wave originates from the disturbance caused by the four cylinders or by the four supports located at the rear part of the annular part in the shock tube. To do so the square formation of cylinders was rotated angularly compared to the four supports in order to determine which one was acting as disturbance generator. The orientation of the square-shaped shock wave, visible in the last stage of the focusing process, told us that it was the disturbance from the four cylinders that was responsible for the shape of the shock wave. It has been shown earlier that the supports for the annular parts of horizontal shock tubes cause disturbances that are visible when the shock wave is close to the center of convergence, see [14–16]. In the present setup, the lack of visible disturbances from the supports on the triangular shocks are most likely due to the fact that it would require a larger perturbation to change the shape from a converging shock with an odd number of sides to a converging shock with an even number of sides. For the square-shaped shocks, the disturbances from the supports can not overtake those from the cylindrical obstacles and because of that, the shape of the shock is not influenced by the supports. The conclusion is that the disturbances from the cylindrical obstacles are larger than those from the supports for the inner body.

4 Conclusions

An experimental investigation of converging triangular and square-shaped shock waves was performed in an annular

horizontal shock tube. A schlieren system combined with a CCD camera was used to visualize the focusing process. The system took snapshots of the converging shock wave at different time instants. An initially cylindrical converging shock wave was perturbed by cylindrical obstacles inside the test section. The obstacles were configured in an equilateral triangular or a square formation. As a result two different types of shock convergence behavior were observed. In a triangular case, a triangle-shaped shock was formed and converged with unaltered form and orientation during the rest of the focusing process, thus indicating that the vertices of the triangle undergo regular reflection. A square formation produced a square-like shock. The corners of the shock suffered Mach reflection and a reconfiguring process took place. After one cycle a new square, oriented opposite to the old one was formed. The present experimental results complement previous results, both analytical and numerical; see [6,13] and [1]. An improvement of the present experimental setup would be to use a visualization system that allows several photographs during the same run, e.g. a pulse laser with a high speed camera or a rotating prism camera. It would then be possible to monitor the motion of the shock front which would allow us to investigate the Mach number increase during the focusing process.

Acknowledgments We would like to thank Prof. P. H. Alfredsson for financial support during this work. The authors would also like to thank Mr Ulf Landén at KTH Mechanics for careful construction of the cylindrical obstacles. Our sincere thanks to Dr. Nils Tillmark for help and advice during the setup of the experiment. The funding from the Göran Gustafsson Foundation provided means for the construction of the shock tube and for acquisition of the experimental equipment which is gratefully acknowledged.

References

1. Apazidis, N., Lesser, M.B.: On generation and convergence of polygonal-shaped shock waves. J. Fluid Mech. **309**, 301–319 (1996)
2. Apazidis, N., Lesser, M.B., Tillmark, N., Johansson, B.: An experimental and theoretical study of converging polygonal shock waves. Shock Waves **12**, 39–58 (2002)
3. Barbosa, F.J., Skews, B.W.: Experimental confirmation of the von Neumann theory of shock wave reflection transition. J. Fluid Mech. **472**, 263–282 (2002)
4. Ben-Dor, G.: Shock wave reflection phenomena. Springer, New York (1992)
5. Ben-Dor, G.: A state-of-the-knowledge review on pseudo-steady shock-wave reflections and their transition criteria. Shock Waves **15**, 277–294 (2006)
6. Betelu, S.I., Aronson, D.G.: Focusing of noncircular self-similar shock waves. Phys. Rev. Lett. **87**(7), 074,501 (2001). doi:10.1103/PhysRevLett.87.074501
7. Eliasson, V., Apazidis, N., Tillmark, N.: Controlling the form of strong converging shocks by means of disturbances. Shock Waves (in press) (2006)
8. Eliasson, V., Apazidis, N., Tillmark, N., Lesser, M.B.: Focusing of strong shocks in an annular shock tube. Shock Waves **15**, 205–217 (2006)
9. Guderley, G.: Starke kugelige und zylindrische verdichtungsstöße in der nähe des kugelmittelpunktes bzw. der zylinderachse. Luftfahrt Forsch **19**, 302–312 (1942)
10. Hornung, H.G., Oertal, H.J., Sandeman, R.J.: Transitions to Mach reflection of shock waves in steady and pseudo steady flow with and without relaxation. J. Fluid Mech. **90**, 541–560 (1979)
11. von Neumann, J.: Collected Works VI. Pergamon, New York (1943)
12. Schwendeman, D.W.: On converging shock waves of spherical and polyhedral form. J. Fluid Mech. **454**, 365–386 (2002)
13. Schwendeman, D.W., Whitham, G.B.: On converging shock waves. Proc. R. Soc. Lond. A **A413**, 297–311 (1987)
14. Takayama, K., Kleine, H., Grönig, H.: An experimental investigation of the stability of converging cylindrical shock waves in air. Exp. Fluids **5**, 315–322 (1987)
15. Takayama, K., Onodera, O., Hoshizawa, Y.: Experiments on the stability of converging cylindrical shock waves. Theor. Appl. Mech. **32**, 305–329 (1984)
16. Watanabe, M., Takayama, K.: Stability of converging cylindrical shock waves. Shock Waves **5**, 149–160 (1991)

Paper 5

5

Light emission during shock wave focusing in air and argon

Veronica Eliasson, Nils Tillmark, Andrew J. Szeri & Nicholas Apazidis.

The light emission from a converging shock wave was investigated experimentally. Results show that the shape of the shock wave close to the center of convergence has a large influence on the amount of emitted light. It was found that a symmetrical polygonal shock front produced more light than an asymmetrical shape. The light emission appears as the shock wave collapses. The full width at half maximum of the light pulse is about 200 ns for all geometrical shapes. It was also found that argon as a test gas produces more light than air. Numerical simulations showed good agreement with experimental results regarding the shape of the shock and the flow field behind the shock. The temperature field from the numerical simulations was investigated and shows that the triple points behind the shock front are hot spots that increase the temperature at the center as they arrive there.

1 Introduction

Shock wave focusing appears in a wide range of situations, from supernovae collapse, [1], to shock wave lithotripsy, [7]. A converging shock wave can be used as a method to focus energy because it produces high pressures and temperatures at the center of convergence. As we explore in the present work, a gas compressed at the center of convergence can be hot enough to emit light.

In the first published experimental investigation of converging shock waves [23] cylindrical shock waves were focused in a horizontal shock tube. Plane shock waves were transformed into cylindrical shock waves through a teardrop insert in the rear part of the shock tube. Moderately strong shocks of Mach number M=1.7 were created and focused. The results showed that a cylindrical shock wave is unstable in the sense that it deviated from its original shape while focusing. The authors reported that converging shocks in air produced light emission visible to the naked eye but difficult to photograph, while shocks of the same strength in argon *"produced easily photographable luminosity"*. A rough examination of the electrical conductivity of the argon in the vicinity of the center of convergence indicated ionization.

Imploding detonation waves were generated and investigated in [19]. The authors produced a 2D shock front in the shape of a regular polygon, consisting of 30 sides, and followed the wave structure as the detonation wave converged. It was reported that Mach reflections occurring between the sides of the polygonal wave induced a smoothing effect on the shape and that it finally became cylindrical. A spectroscopic analysis suggested that high temperatures, $1.89 \cdot 10^5$ K, were obtained as the shock reflected from the center, and at the same time, a bright flash was generated at the center of convergence. Imploding shock waves were produced in [24], in a hemispherical chamber. A blast wave was produced at the center of the chamber. It decayed into a detonation wave and travelled outwards and reflected from the walls, resulting in a converging detonation wave. The measured peak temperatures were around 5,000 K. The authors of [24], also indicated that

the temperatures obtained in [19], were overestimated due to the invalid use of Wein's law, and that the actual peak temperature probably lay below 10,000 K. Later works [25, 21] indicated peak temperatures of 10,000-13,000 K and 13,000-34,000 K respectively. The variation in peak temperatures depended on the initiation energy.

Other examples of phenomena where light emission occur include sonoluminescene, mechanoluminescence and shrimpoluminescence. A short explanation of each phenomenon follows.

Sonoluminescence occurs when energy is focused so strongly by imploding bubbles that light is emitted. It is divided into two types, multi and single-bubble sonoluminescence. Single-bubble sonoluminescence (SBSL) was discovered by Felipe Gaitan in 1989, [12]. He found a regime where a single bubble was trapped in an acoustical field, stable in position but oscillating in a radial mode in a stable, repeatable manner. Once, during each period, the bubble collapses violently and a luminous spot appears briefly. The emitted light can be visible to the naked eye, depending on materials and conditions. The width of the light pulse was measured to be of the order of a few hundreds of picoseconds, [13], as suggested by earlier simulations [26], and the spectrum increases toward the ultraviolet, [18]. The light emission is thought to be caused by near-adiabatic compression of the bubble during the collapse. The cavitation collapse is so fast that the heat generated within the bubble is trapped within and can not escape, see [13] and [26]. The light intensity depends on a range of parameters; the amplitude of the forcing pressure, the concentration of gas dissolved in the liquid, the temperature of the liquid, [2], and also the type of gas within the bubble. A small amount of a noble gas, for example argon, helium or xenon, increases the light intensity, [18]. For a comprehensive review on the subject of SBSL, see [6].

Mechanoluminescence, also known as triboluminescence or fractoluminescence, is a phenomena where light emission, sometimes a dim light, is induced by a mechanical action on a solid. For example, light is emitted when one chews on hard opaque candies made of sugar. Compared to mechanical actions as grinding and cleaving, shock waves in acoustic cavitation can be used to generate up to 1000 times brighter luminescence; see [8].

Shrimpoluminescence, caused by a shrimp snapping its claw shut so fast that light emission occurs, was reported in [20]. The shrimp, *Alpheus heterochaelis*, has an oversized claw with which it stuns its prey. The light emission is caused by a cavitation bubble generated in the wake of a high-velocity water jet formed when the claw is shut. The amount of emitted light is one or two orders of magnitude less than for sonoluminiescence and not visible to the naked eye.

In this paper we consider both experimental and numerical results. In the experimental part of this paper we investigate the light emission that occurs during shock wave focusing using the same shock tube as we employed in previous studies [11, 10, 9]. We consider several aspects of the light emission, such as where the shock is positioned when the light appears, how long the light is emitted and how different geometrical shapes of the converging shock wave influence the light emission. Two types of test gases, air and argon, are used and compared. It is shown that argon is associated with more light than air. To explain how the various geometrical shapes of converging shock waves are generated in the experiment, we start by a short review of our earlier work on how to produce and design converging shock waves of various shapes.

In [11] we used a horizontal shock tube to generate annular shock waves that were focused in a thin cylindrical test section mounted at the rear part of the shock tube. Various geometrical shapes of converging shock waves were created by changing the geometry of the outer reflector boundary of the test section. Three different reflector boundaries were tested: circular, smooth pentagonal and octagonal. Results showed that the shape of the converging shock wave was initially influenced by the shape of the reflector boundary and later by the non-linear interaction between

the local strength and the curvature of the shock. Very close to the center of convergence, the shock wave obtained a square-like shape for the octagonal and circular reflectors. This was thought to be caused by disturbances in the flow caused by the supports for the inner body, creating the annular part of the shock tube. The square-like shape was not observed for the case with the smooth pentagonal reflector; it appears that the disturbances from the supports were too weak to transform a shock wave with an odd number of sides into an even number of sides.

A heptagonal outer boundary was used in [9] in the same experimental setup as in [11]. It was shown that the shock wave initially became shaped as a heptagon and then oscillated between that and a double heptagonal shock wave, until the shock wave reached the center of convergence. There were no visible disturbances from the supports of the inner body of the shock tube.

In [10] we continued the research on polygonally shaped shock waves. In these experiments the polygonal shock waves were created through carefully placed artificial disturbance elements inside the test section. The disturbance elements consisted of metal cylinders, with three different diameters; 7.5 mm, 10 mm and 15 mm, placed in various positions and patterns inside the test section. A symmetrical pattern produced a symmetrically deformed shock front, that later developed into a polygonal shape. If n obstacles were placed inside the test section, at first an n-sided polygonal shock wave was created. The corners of the polygonal shock wave propagate faster than the adjacent plane parts, due to the high curvature of the shock front in the corners. This results in new plane sides, emerging from the corners, transforming the shock with n corners into a $2n$ corner shock. This subsequently evolves back to a shape with n corners. If there are no other disturbances present, this reconfiguring process will continue until the shock wave reaches the center of convergence. The results showed that the supports for the inner body of the annular part of the shock tube created significant disturbances so that all even-sided polygonal shapes transformed into square-shaped shocks close to the center of convergence. However, it was not possible to see any square-shaped shocks close to the center for the polygonal shaped shocks with an initially odd number of sides.

The type of reflection that occurs at the vertices of a reconfiguring polygonal shock wave is a Mach reflection. Mach reflections take place when the incident angle between two sides are larger than a critical angle, and in this case, the Mach number will increase during the focusing process. If the incident angle between the two sides is less than the critical angle, a regular reflection will occur, and both the shape and the Mach number will be preserved throughout the convergence process. An extensive review on the subject on Mach reflections and other shock wave reflection phenomena can be found in [3] and [4].

The numerical simulations in this paper are accomplished using the Overture suite, [14]. The use of this tool allows us to examine the shapes of the shock waves close to the center of convergence and investigate the temperature field generated by the converging shocks.

2 Experimental setup

The experimental setup, shown in figure 1, consists of a horizontal annular shock tube where a plane shock wave is generated and transformed into an annular shape. The annular shock is then focused in a thin test section mounted at the rear part of the shock tube. The experimental setup is the same as in [11] and [10] and a detailed description can be found in those two references. A laser serves as a light source for the visualization system consisting of schlieren optics and a CCD camera. Both the CCD camera and the laser are triggered by an output signal from a shock sensor

placed on the annular part of the shock tube. The signal from one of the shock sensors is delayed via a time-delay unit to obtain schlieren images of the converging shock wave at different positions in the test section. A photomultiplier (PM) tube is connected to the rear end of the shock tube. The PM tube (RCA 4526) is a light detector; the time resolved output signal is proportional to the number of photons detected at each moment. The PM tube is placed in a light-sealed plastic cover to ensure that the detected light is originating from the converging shock wave and not from light sources within the laboratory. The PM-tube and the light-cover is shown in figure 2. It is possible to mount the PM-tube in two different positions inside the cover, and one of these will allow the use of schlieren optics and the PM-tube simultaneously.

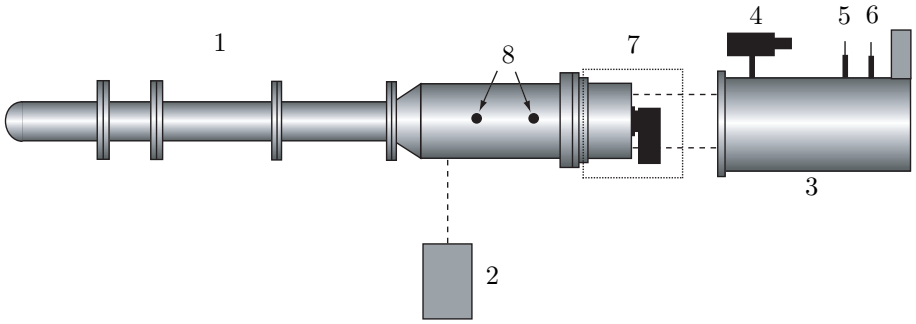

Figure 1: Schematic overview of the experimental setup: 1. Shock tube, 2. Pulse laser, 3. Schlieren optics, 4. PCO CCD camera, 5. Lens, 6. Schlieren edge, 7. PM tube with light cover, 8. Shock sensors.

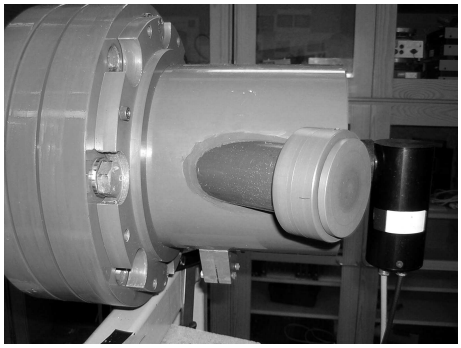

Figure 2: The PM-tube connected to the light cover.

2.1 Shaping the shock waves

Two different methods were used to shape the converging shock waves. The first method, described in [11] uses a circular, a heptagonal and an octagonal outer boundary of the test section. The circular boundary has a radius of 80 mm. Both the heptagonal and octagonal boundaries have a

radius of 80 mm, which is the radius of the outer circumscribed circle. These two reflectors will block parts of the flow from entering the test section, since the open area inside them are smaller than that of the circular boundary.

The second method, see [10], consists of placing cylindrical obstacles in various patterns inside the test section. The cylinders consist of metal rods with a diameter of 15 mm. They are placed at a radial position of 46.25 mm from the focal point, in various patterns. The circular boundary for the test section is used to create an initially converging cylindrical shock that becomes perturbed and shaped by the cylindrical obstacles. The one cylinder case consists of one cylindrical obstacle. In the triangular case, the cylinders are placed in an equilateral triangular shape centered on the convergent spot, with the cylinders placed in the corners of the triangle. In the last case, the cylinders are placed in the corners of a square-formation centered about the convergent spot. Compared to the circular case, the cylinders will influence the flow and partially block it.

3 Experimental results

The results from the present experimental work will be discussed in the four following subsections.

3.1 The shape of the shock wave close to the center of convergence

First, we begin by investigating the shock shape close to the center of convergence for different geometrical shapes of shock waves. The different shapes are generated either by a change of shape in the outer reflector boundary of the test section or by introducing cylindrical obstacles inside the test section. The various geometrical shapes that we investigate and compare to each other are; a cylindrical shock, an initially cylindrical shock that is influenced by one, three or four cylindrical obstacles, a heptagonal and an octagonal shock wave created by changing the outer boundary of the reflector.

A close-up of various geometrical shapes of shock waves, close to the center of convergence, is shown in figure 3. The scale used in all figures is nearly identical. A cylindrical shock wave is unstable and hence it will be influenced even by small disturbances present in the shock tube. Disturbances are generated by the supports for the center body of the shock tube. Although the supports are shaped as wing profiles to minimize disturbances, they still affect the flow. Owing to the inherent instability of converging cylindrical shocks, an initially cylindrical shock wave becomes square-shaped close to the center of convergence; see figure 3 (a). The square-like shape becomes visible close to the focal point. For the case with one cylinder the shape resembles a teardrop; see (b). A triangular shape is formed for the case with three obstacles (c). In (d), four obstacles are used and close to the center of convergence the shock wave is square-shaped. The square in (d) is oriented differently compared to the square in (a), suggesting that the four supports are not the reason for the final shape, but the four cylinders. The shape in (d) is a result of an alternating shock wave, starting with four sides and corners that transforms into eight sides and corners and back again. A heptagonal reflector boundary creates a heptagonal shape close to the center of focusing, while an octagonal reflector boundary creates a square-like shape, see (e) and (f) respectively.

Results show that converging shock waves with an even number of sides, generated by the reflector boundaries, will be influenced by the four supports and become square-shaped close to the center of convergence. However, shock waves with an even number of sides generated by the

cylindrical obstacles will not be influenced by the four supports. All shocks with an odd number of sides will also remain unaffected by the four supports.

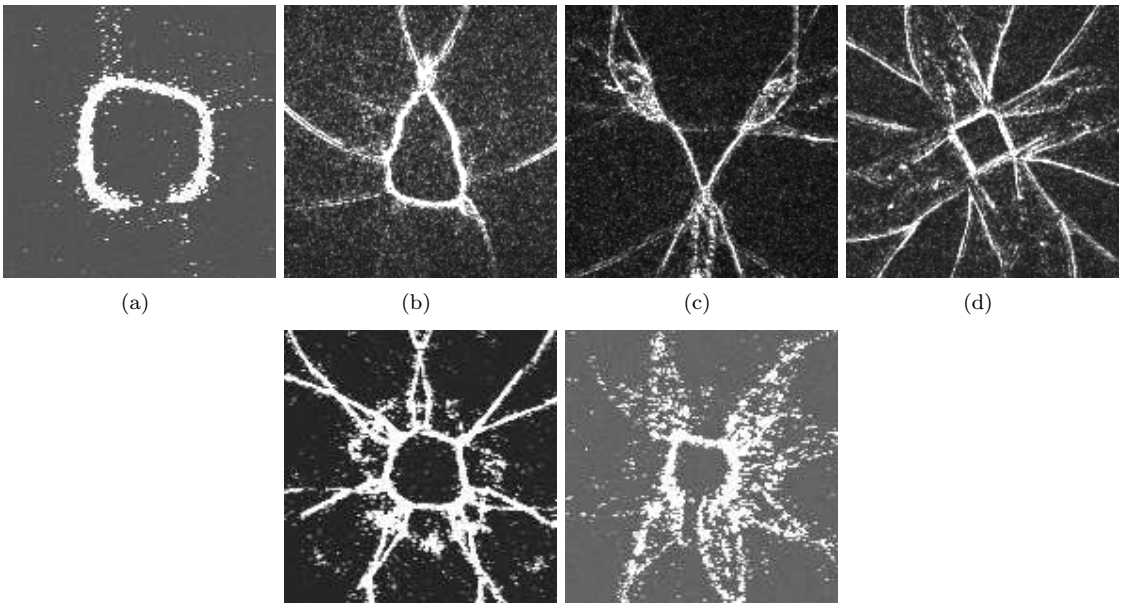

Figure 3: Schlieren photographs of shock waves close to the center of convergence for different shapes (a) Cylinder (b) One cylinder (c) Three cylinders (d) Four cylinders (e) Heptagon (f) Octagon.

3.2 Shock position at the instant of light emission

To determine the shock position when the light emission appears a PM-tube signal was monitored with an oscilloscope together with the signal from the second shock sensor, see figures 1 and 4 (a). The upper curve is the signal from the shock sensor and the lower curve is the signal from the PM-tube. The sharp excursions in the upper and lower curves correspond to the passage of the shock wave and the later instant of light emission. A longer sampling time was used for the same experiment and the result is shown in 4 (b). The upper and lower signals are from the PM tube and the shock sensor respectively. The first indication of light from the PM-tube signal originates from the converging shock and then, after about 3.4 ms, there is more light emission. This originates from small pieces of the aluminum membrane, originally placed between the high and low pressure parts of the shock tube. Both incidents can be seen by the naked eye. However, a change in gas, from air to argon, dramatically increases the light emission from the shock wave and reduces the light from the glowing particles. A comparison between air and argon as test gas in the low pressure part is carried out in section 3.5. Using the PM-tube together with the shock sensors, an approximate location of the shock wave was found. We first tried to take schlieren photographs

using a time delay estimated from the time signal from the PM-tube, (see figure 4 (a)). However, because each run in the shock tube produces slightly different conditions, it was difficult to time the schlieren photo precisely with the instant of the light emission. To ensure simultaneity, both the PM-tube and the schlieren optics were used at the same time. By comparing the time instants for the laser pulse and the light emission in the same run, it was possible to determine the shock position at the instant of light emission. Two typical signals from the PM tube and the laser in this setup are shown in figures 4 (c)-(d). The octagonal outer boundary was used for this test. The first peak in figure 4 (c), labeled A, corresponds to the laser pulse and the second peak, labeled B, corresponds to the light emission from the shock wave. The shock position, corresponding to the instant when the laser pulse is captured by the PM-tube is shown in the lower left corner of figure 4 (c). This photograph is taken just before the light emission caused by the shock occurs. In figure 4 (c), the laser fires when the light emission from the gas compressed by the shock is near its end. The schlieren photo is shown in the lower right corner of the same figure. It is seen that the shock has collapsed and just started to reflect. It could now be concluded that the light emission appears when the shock wave is very close to the center of convergence.

A clarification about the triggering signal for the last two tests, 4 (c)-(d) should be made. The oscilloscope was triggered when the Q-switch on the laser was energized, thus going from 0 V to 5 V. This happened a very short time, about 80 ns, before the laser was fired, see [22].

3.3 Features of the PM-tube signal during the light emission

The PM-tube was connected to an oscilloscope and a typical output signal from the PM-tube is shown in figure 5. The signal from the PM-tube shows the light intensity level as a function of time. At first nothing happens, it is dark. As soon as light is detected, the signal from the PM-tube decreases below zero. The deviation from the reference voltage level, (the reference level is when there is no light), is proportional to the intensity of the detected light and also dependent on the voltage level used to operate the PM-tube itself. The same voltage level (-1100 V) was used for all experiments. When the light intensity was too high and the output signal became saturated a filter was attached to the PM-tube, decreasing the light intercepted by the tube. The filter was a 6BL-filter, reducing the light intensity by 2^6 times. In figure 5, it is possible to see when the maximum intensity of the light is emitted; it corresponds to the minimum level. The full width at half maximum (fwhm) of the light pulse in figure 5 is 200 ns. The slope of the signal gives the measure of the speeds at which the light intensity is increased to the maximum level and then decreased during the relaxation phase.

A test was made to ensure that the PM-tube was fast enough to resolve temporally the light emission from the converging shock wave. We used the laser as light source for the PM-tube. The laser pulse has a duration of 5 ns, which is shorter than the width of the light pulse from the converging shock. The PM-tube was able to resolve the light emission from a laser pulse with a slope of $9.51 \cdot 10^7$ V/s. The slope of the light emission caused by the converging shock is $2.86 \cdot 10^6$ V/s; this is an order of magnitude lower than the laser pulse. Thus the response time of the PM-tube is rapid enough to resolve the signal from the light emission caused by the converging shock wave.

PM-tube signals from a set of runs from each geometrical configuration are shown in figure 6. Because less than 10 runs were made for each setup, we can only report the trends and not true statistical values. The sampling of data started when the voltage level from the PM-tube became less than $-0.05\ V$, this corresponds to the time instant $t = 0$ in the following results. Also, the

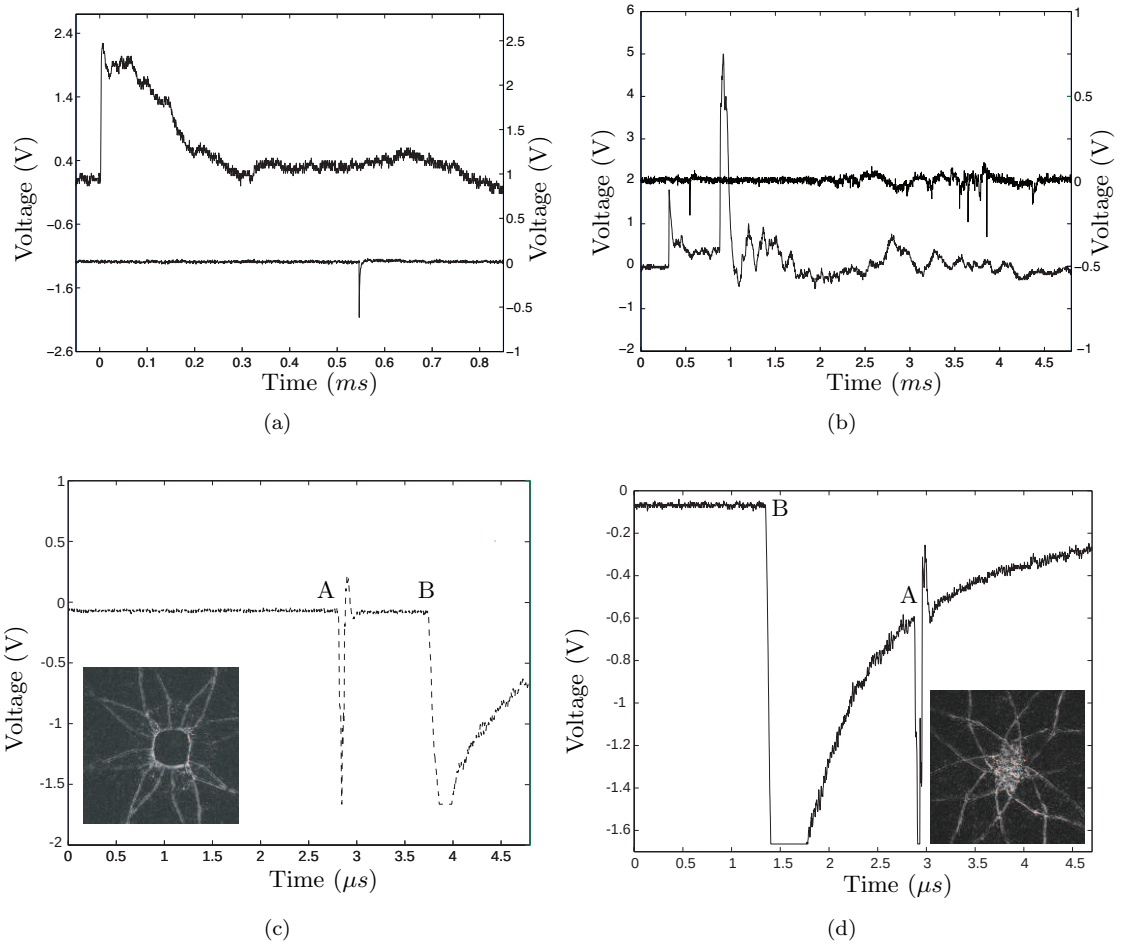

Figure 4: (a) The signal from the second shock sensor (top signal, left y-axis) and the signal from the PM-tube (bottom signal, right y-axis) during the light emission. (b) The same signals are shown for a longer time span. The shock sensor signal (bottom signal, left y-axis) shows both the incoming (0.4 ms) and reflected shock (1 ms). The PM-tube (top signal, right axis) signal shows the light emission from the converging shock wave (0.6 ms) and the glowing particles (3.4 ms). In (c) and (d) the PM-tube signals showing both laser pulse for the schlieren imaging (labeled A) and light emission from the converging shock (labeled B) and the schlieren photograph obtained during the run.

oscilloscope used to capture the signals from the PM-tube was programmed to save data prior to the start instant by 0.1 μs to make sure that the whole light emission process was captured. In figure 6 (a) eight runs from an initially cylindrical shock wave are shown. The maximum light intensity varies by a factor of 10 between consequent runs, using the same initial conditions. This is believed to be caused by the fact that a cylindrical shock wave is unstable. Hence it does not

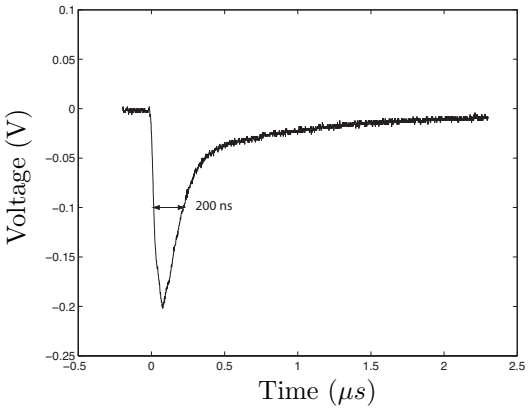

Figure 5: A typical signal from the PM-tube in the case with the cylindrical shock.

focus in exactly the same way during all runs. This signal is the only one that is filtered by the 6BL-filter which reduces the intensity 2^6 times, so to get a correct voltage level on the y-axis, it should be multiplied by 64. In figure 6 (b), the PM-tube signals from five runs with an initially cylindrical shock, perturbed by one cylindrical obstacle, are shown. Compared to (a), this set of signals has less spread and the individual runs have almost the same minimum value. In 6 (c), (d), (e) and (f) cases with 3 obstacles, 4 obstacles, heptagon and octagon shapes are shown. In all of these cases, the minimum value varies less than for the circular case, (see figure 6 (a)). The variation of the signals from one set is small, which probably is related to the fact that the shapes in 6 (b) – (f) are stable and focus similarly every time.

A comparison of the PM-signals between the previously mentioned geometrical configurations is made in figure 7. In figure figure 7 (a) the cylindrical case is compared to the case with one obstacle. As can be seen, the minimum levels and the time when the minimum is reached differ. The cylindrical shock reaches the minimum level before the one cylinder shock. The main reason for this is that while the shape close to the center of convergence is symmetric for the cylindrical shock, it is not symmetrical for the shock disturbed by one cylinder, see figure 3 (a) and (b). Also, the flow is partially blocked by the cylindrical obstacle in (b) as compared to the flow in (a) which means that the same amount of shock front is not converged to the focal point.

In figure 7 (b), the cases with one (solid) and three (dashed) cylinders are compared. Here it is seen that the case with one cylinder yields less light and that the minimum level is reached later than for the triangular shape. A triangular shock evolves with regular reflection at the corners and thus the shape will be unaltered during the focusing process. According to numerical experiments, [5], the Mach number of the shock, reaches a constant value during the focusing process and hence a bound in energy is reached. For the three cylinder case, a larger amount of the shock front is blocked and reflected by the cylinders, so the amount of energy reaching the focal point is decreased compared to the one cylinder case. However, the triangular case produced more light than the one cylinder case. This suggests that the shape of the shock close to the center of convergence has a large impact on the light emission in this case. The shape for the one cylinder case is elongated as a teardrop and far from symmetric.

The case with three cylinders (solid) is compared to the case with four cylinders (dashed) in figure 7 (c). The shape of the signals are similar but the four cylinder minimum is lower than the minimum for the three cylinder case. This could be explained by the shape of the shock wave close to the center of convergence. The three cylinder case results in a triangular shape while the four cylinder case is square-shaped. The triangular shock undergoes regular reflection and the shape remains unaltered during the focusing process. Mach reflection takes place for the square-shaped shock and the Mach number increases as mentioned above. On the contrary, a larger amount of the wave energy is reflected back when it hits the four cylinders than the three cylinders, thus giving a decreased amount of energy arriving at the focal point. However, this seems to be less important than the actual shape of the shock wave.

The octagonal and heptagonal cases are compared to each other in figure 7 (d). The signal from the octagon case reaches the minimum level before the heptagon case and the minimum level for the octagonal case is about -0.8 V while for the heptagon case it is about -0.6 V. In this case, the heptagonal boundary of the test section, reflects back a larger amount of the shock than the octagonal boundary does. Once again, it seems like the shape of the shock wave is more important than the amount of energy reaching the center point.

3.4 Photographs of light emission

Photographs of the emitted light were taken with the CCD camera. The exposure time on the CCD camera was set to 250 μs. Photographs are shown in figure 8 with argon as test gas. The most intense light comes from the case with a circular outer boundary and the shape of the light spot is square-like, as is the shape of the shock wave close to the focus point as mentioned earlier. The cases with one and three cylinders give less light and it is not possible to distinguish the shape of the emitted light. For the four cylinder and the octagonal case, the shape of the light spot can be seen and is again square-like, as the shape of the converging shock, see figure 3 (d) and (f). The size of the glowing spot in (a) is about 1 mm. The same scale is used for all cases. Once again, it is possible to see that a symmetrically shaped shock gives more light emission. The circle, square formation and the octagon produce more light than the single and three cylinder formation.

3.5 Air and argon

Two different test gases were investigated; air and argon. To fill the low pressure channel with argon, the following steps are taken. First, air is evacuated from the channel until the pressure reaches 0.53 kPa (4 torr). Then argon is supplied to the low pressure part until the pressure reaches 13.33 kPa (100 torr) and then the experiment is performed. Two photographs from the CCD camera are shown in figure 9 together with plots of the intensity level along a horizontal line where the maximum value of the light is found. The light emission for air is less than for argon, the maximum levels are 132 for air and 3607 for argon respectively. To get a good accuracy of the maximum levels the CCD photographs were saved as 16-bit grayscale data, where only 12 bits were used for the actual data (because the camera sets the higher four bits to zero) resulting in 4096 shades of gray. The exposure time for the CCD camera was set to 1 ms, very long compared to the actual length of the light pulse. The geometrical shape used for this test was the octagonal outer boundary. The size of the light spot in (b) is approximately 1 mm in diameter.

4 Numerical simulations

As a compliment to the experiments, we have performed numerical simulations of two dimensional converging shocks. The purpose of the simulations was to study the shape of the shock close to the focal point and the temperature field. As mentioned earlier, the experimental results indicate that the shape and symmetry of the shock close to the center are factors for the magnitude of the light production. In the current experimental setup we could not measure the temperature of the compressed gas. Therefore, we use numerical simulations to study the temperature field for the various geometrical setups.

Here we use the two dimensional Euler equations, as a model for the converging shock wave inside the test section. In the computations we assume the gas to obey the ideal gas law with constant specific heats. This assumption is valid away from the center of convergence (were the temperature becomes so high that the gas no longer behaves as a calorically perfect gas). The assumption of constant specific heats is valid up to 1000 K for air, then the vibrational motion of O_2 and N_2 molecules affect the specific heats and these are no longer constant. For argon, the assumption of specific heats is valid up to temperatures where the gas undergoes ionization.

The complex geometry of the experimental setup requires a numerical flow solver that handles such geometries. An intrinsic numerical difficulty of the converging shock wave problem is the continuously changing scales associated with the focusing process. The change in scales justifies the use of adaptive mesh refinement (AMR). The Overture suite, [14], which we used for the numerical simulations, has support for both geometry and AMR and includes various flow solvers. For the experiments presented here we use the OverBlown solver for the Euler equations, based on the second order accurate Godunov method, discussed in [16]. Artificial viscosity is added to the numerical scheme to stabilize the method and to give sharp shocks without overshoots, this is further explained in [15].

4.1 Problem setup

The two dimensional model of the test section consists of two background grids, one Cartesian and one annular grid, and optional cylindrical obstacles described by individual annular grids. The grid spacing of the annular grids are adjusted to conform with the grid spacing, h, of the Cartesian grid.

The following cases were simulated; a circular converging shock wave, a circular converging shock perturbed by one cylinder, three cylinders placed in a equilateral pattern and four cylinders placed in a square formation. All cylinders were placed at a radial distance of 46.25 mm from the focal point and had a diameter, D, of 15 mm. The cylindrical obstacles are perfectly reflecting, which is a simplification compared to the experiments. However, the influence on the flow field from the waves traveling inside the cylinders in the experiments is negligible compared to the shock waves traveling in the gas. The diameter of the computational domain was set to 150 mm for all cases. In all computations considered here, the grid spacing is 0.4959 mm on the Cartesian grid. The errors are small and the second order accuracy is verified where the solution is smooth. An example of the initial grids for the case with four cylinders is shown in figure 10 (a). A fine scale view of the edge of one of the four cylinders is shown in figure 10 (b), where the Cartesian and the annular background grids are visible, together with the annular grid describing one of the cylinders. During the simulation the grid spacing is adaptively reduced (AMR) close to shock fronts and other regions where the solution changes rapidly. Here, two refinement levels are used

with a refinement ratio of four, i.e. the grid spacing on the fine grid is 0.1240 mm. An example where the grid has been adapted is shown in figure 10 (c).

Given the initial conditions in front of the converging shock, the state behind the shock can be parametrized with the Mach number. Here we set the initial conditions in front of the shock to be a gas at rest at room temperature. We then adjust the initial Mach number so that the radius of the converging and reflecting shock for the circular case, as a function of time, match the experimental results. A comparison between the numerical and experimental results are shown in a $r - t$ diagram in figure 11. The best match between the numerical and the experimental results was obtained when setting the initial Mach number to 2.4. The same initial conditions were then used for all simulations in this paper. The boundary conditions on the cylinders are modeled by slip wall conditions. At the perimeter of the computational domain supersonic outflow boundary conditions are imposed, this is one of the simplest models of non reflecting boundary conditions.

Simulations for both air and argon were made. For air, the ratio between the specific heats is $\gamma = 1.4$ and the gas constant is set to $R = 287.06$ J/KgK. These parameters were changed to $\gamma = 1.67$ and $R = 208.1$ J/KgK when simulating argon.

A normal shock in argon, propagating into a gas at $p = 13.33$ kPa (100 torr) at room temperature $T = 294$ K, has a thickness close to the mean free path of the gas, λ, which is approximately 13 μm. The mean free path is given by $\lambda = \mathcal{R}T/(\sqrt{2}\pi d^2 N_A p)$, where $\mathcal{R}$ is the universal gas constant 8.314 J/(mol·K), d is the molecular diameter, 0.71 Å for Argon, and N_A is Avogadro's number $6.022 \cdot 10^{26}$ mol^{-1}. This may be compared with the finest grid scale of 124 μm. The shock itself is not resolved, but we assume that the thickness of the shock front does not influence the results we are interested in.

4.2 Results

'Schlieren' plots, i.e. plots of the density gradients, of the converging shocks close to the center of convergence are shown in figure 12 for the one cylinder, three cylinder and four cylinder case. The diameter of a cylindrical obstacle is indicated in each plot. For the case with one cylinder, the shape of the shock resembles a teardrop, for the triangular case it is shaped as a triangle and the square formation produces a square-like shape close to the center of convergence. The numerical simulations agree well with the experimental results discussed earlier, compare figures 3 and 12. Also, the locations of triple points and shock-shocks match the experimental results. An advantage of the numerical simulations is the increased level of detail and the flexibility to follow the convergence process closely by animations.

The temperature field of the gas, during the time when the converging shock is close to the focal point, has been investigated. A series of temperature plots for the four cylinder case is shown in figure 13. The plotted region is the 2 mm x 2 mm square around the center. The temperature field shows that the triple points, located at the corners of the converging polygonal shock wave, are hot spots that will increase the temperature at the focal point dramatically when they arrive there. The maximum temperature in each plot, T_{max}, is made dimensionless with respect to the dimensionless gas constant γ and the room temperature, in this case 294 K.

The maximum temperature, in a 2 mm x 2 mm region centered at the focal point, for each time step was calculated for the circular, one, three and four cylinder cases for both air and argon, see figure 14. A blow up of the peaks in figures 14 (a) and (c) are shown in figures 14 (b) and (d) respectively. The temperature is the same for all cases in the beginning due to the initial conditions. When the shock front arrives in the monitored region the temperature is increased sharply. As

the shock wave is reflected and travels outward the temperature decreases. The highest maximum temperature is obtained for the circular case, followed by the single, four and finally the three cylinder case. The main difference between the air and argon cases is that the peak temperatures are much higher for argon than for air.

Because the shape of the shock wave seems to be a large influencing factor on the amount of light that is produced, the regions where high temperature exists are investigated. Temperature fields are plotted in figures 15 (a)-(d). The circular case is shown in (a), the one cylinder case in (b), the three cylinder case in (c) and finally the four cylinder case in (d). The time instant for the plot is chosen as the time when the maximum temperature is reached for the respective case. The domain is again the 2 mm x 2 mm region around the focal point. The shapes of the hot regions are similar to the shape of the shock waves close to the focal point, except for the four cylinder case in figure 15 (d) which is circular. The regions with 95% of the maximum temperature are indicated in the figures as contour lines.

4.3 Remarks

We have used a simplified model with an ideal gas assumption where the ionization and real gas effects are ignored. The results from the simulations should be viewed as preliminary and as a first step to take before continuing with more advanced models. The values of maximum temperatures are not the true values, because, as the grid is refined further, the artificial viscosity is reduced and then the values for temperature approach closer to infinity. This would not happen in laboratory experiments, for the reason that viscosity exists and places a physical limit on the maximum temperature during the convergence. However, because the simulations of the different cases are undertaken with the same grid resolution, and therefore suffer the same artificial viscosity, we regard these numerical simulations as having probed the qualitative influence of shape on temperatures developed during the convergence.

5 Conclusions

It has been demonstrated in experiments that a converging shock emits light. In this work we investigated experimentally how the shape of the shock wave influences the amount of emitted light. It is shown that the shape of the shock wave, close to the center of convergence has a large influence on the amount of produced light. For example, a shock wave with a square-like shape close to the center of convergence emits more light than a shock shaped as a teardrop or a triangle. We believe that a stable shape as close as possible to a circle should produce more light. Stability ensures a predictable evolution of the converging shock front while symmetry ensures simultaneity of arrival of different points on the shock front at the focal point.

The time instant when the light appears coincides with the collapse of the shock wave. There is no significant variation of the length of the light pulse for the various cases. The full width at half maximum of the light pulse is about 200 ns, compared to hundreds of picoseconds for single bubble sonoluminescence. The major difference between our experiment and the case with sonoluminescence is that there is no near-adiabatic compression in our experiment as it is in sonoluminescence, induced by the rapid motion of the collapsing bubble walls. Moreover, the length scale is much larger. This suggests that the present process is different from sonoluminescence.

For each geometrical setup a different amount of wave energy is reflected back, due to boundaries or obstacles, and the amount reaching the focal point is not the same. Hence it is difficult to compare directly the various cases with each other. However, we found that the reflection losses had less effect on the amount of emitted light than the shape of the shock close to the center; for example, the square-shaped shock produced more light than the one cylinder case.

Two different gases, argon and air, were tested in the low pressure channel of the shock tube. A considerable increase in light emission was registered for argon. This recalls a similar result for SBSL, where a noble gas increases the light intensity, [18].

The numerical simulations show that both the shape of the shock waves close to the center of focusing and the radius as a function of time are in good agreement with experimental results. The temperature fields show that triple points are hot spots that increase the temperature at the center when they arrive there. The maximum temperatures obtained in a small region close to the focal point show that higher temperatures are obtained for argon than for air, which is likely correlated with more light.

To decide finally what geometrical shape of the converging shock is best for producing light, then the shape should be the only difference between the various cases. In our experiments, the strength of the shocks close to the center of convergence in the various cases differ. This, due to the fact that all runs started with the same initial conditions and for all cases, except the circular configuration, a certain amount of the shock is reflected back before it reaches the center. One solution might be to vary the initial conditions in the shock tube so that the strength of the shock wave close to the focal point is the same for all cases.

It would also be interesting to measure the spectra of the light emission and then compare to those obtained from SBSL, [17]. This could enable further comparison of the two phenomena. Another future undertaking would be to investigate the ratio of argon and air that produces most light. Also, other gas combinations should be tested.

An improvement of the experimental setup would be to use a visualization system that allows several photographs during the same run, for example a high speed camera or a rotating prism camera with a pulse laser as a light source for the schlieren optics system. It would then be possible to follow the shock front during the convergence and get an estimation of the shock speed.

To improve the numerical simulations, another equation of state should be used as the shock converges and the temperatures and pressures rise. It would also be interesting to use a model where the level of ionization for the various geometrical shock waves can be computed. If a better model was used, it would then be possible to investigate whether the stair case increase of the temperature in the numerical simulations, as the shock is very close to the convergence center, is connected to the oscillations in the light emission signals from the experiments. The stair case phenomena is observed in figures 14 (b) and (d) and the oscillations from the light emission experiments are observed in figure 6 (d) in the case of four obstacles.

Acknowledgments

The authors wish to acknowledge Dr. W. D. Henshaw for providing superb help on anything regarding Overture and Prof. D. W. Schwendeman for help with generating the first overlapping grids for this problem. Prof. Emeritus M. B. Lesser is acknowledged for initiating the project. V. E. thanks the Department of Mechanical Engineering at the University of California, Berkeley, for hosting her visit and providing computational resources. The work of V. E. was supported by KTH Mechanics, Stiftelsens Bengt Ingeströms Stipendiefond and Helge Ax:son Johnsons Stiftelse.

The work of A. J. S was supported by a grant from the National Science Foundation Program in Biomedical Engineering and Research to Aid Persons with Disabilities. The funding from the Göran Gustafsson Foundation provided means for the construction of the shock tube and for acquisition of the experimental equipment which is gratefully acknowledged.

References

[1] W. D. Arnett, J. N. Bahcall, R. P. Kirshner, and S. E. Woosley. Supernova 1987a. *Annu. Rev. Astron. Astrphys.*, 27:629 – 700, 1989.

[2] B. P. Barber, C. C. Wu, R. Löfstedt, P. H. Roberts, and S. J. Putterman. Sensitivity of sonoluminescence to experimental parameters. *Physical review letters*, 72:1380–1383, 1994.

[3] G. Ben-Dor. *Shock wave reflection phenomena*. Springer-Verlag New York Inc., 1992.

[4] G. Ben-Dor. A state-of-the-knowledge review on pseudo-steady shock-wave reflections and their transition criteria. *Shock waves*, 15:277–294, 2006.

[5] S. I. Betelu and D. G. Aronson. Focusing of noncircular self-similar shock waves. *Phys. Rev. Lett.*, 87(7):074501, Jul 2001.

[6] M. P. Brenner, S. Hilgenfeldt, and D. Lohse. Single-bubble sonoluminescence. *Reviews of modern physics*, 74:425–484, 2002.

[7] C. Chaussy, E. Schmiedt, W. Brendel, B. Forssmann, and V. Walther. First clinical experience with extracorporeally induced destruction of kidney stones by shock waves. *Journal of Urology*, 127:417–420, 1982.

[8] N. C. Eddingsaas and K. S. Suslick. Light from sonication of crystal slurries. *Nature*, 449:163, 2006.

[9] V. Eliasson. The production of converging polygonal shock waves by means of reflectors and cylindrical obstacles. *AIP Conference Proceedings*, 832:445–449, 2006.

[10] V. Eliasson, N. Apazidis, and N. Tillmark. Controlling the form of strong converging shocks by means of disturbances. *Shock waves*, page In press, 2006.

[11] V. Eliasson, N. Apazidis, N. Tillmark, and M. B. Lesser. Focusing of strong shocks in an annular shock tube. *Shock waves*, 15:205–217, 2006.

[12] D. F. Gaitan, L. A. Crum, C. C. Church, and R. A. Roy. Sonoluminescence and bubble dynamics for a single, stable, cavitation bubble. *J. Acoust. Soc. Am.*, 91(6):3166–3183, June 1992.

[13] B. Gompf, R. Günther, G. Nick, R. Pecha, and W. Eisenmenger. Resolving sonoluminescence pulse width with time-correlated single photon counting. *Phys. Rev. Lett.*, 79:1405–1408, 1997.

[14] W. D. Henshaw. http://www.llnl.gov/casc/overture/.

[15] W. D. Henshaw. Overblown: A fluid solver for overlapping grids, reference guide, version 1.0, 2003.

[16] W. D. Henshaw and D. W. Schwendeman. An adaptive numerical scheme for high-speed reactive flow on overlapping grids. *J. Comput. Phys.*, 191:420–447, 2003.

[17] R. Hiller, S. J. Putterman, and B. P. Barber. Spectrum of syncronous picosecund sonoluminescence. *Phys. Rev. Lett.*, 69:1182–1184, 1992.

[18] R. Hiller, K. Weninger, S. J. Putterman, and B. P. Barber. Effect of noble gas doping in single-bubble sonoluminescence. *Science*, 266(5183):248–250, Oct 1994.

[19] R. Knystautas, B. H. K. Lee, and J. H. S Lee. Diagnostic experiments on converging detonations. *Phys. Fluids. Suppl.*, 1:165–168, 1969.

[20] D. Lohse, B. Schmitz, and M. Versluis. Snapping shrimp make flashing bubbles. *Nature*, 413:477–478, 2001.

[21] H. Matsuo, K. Ebihara, and Y. Ohya. Spectroscopic study of cylindrically converging shock waves. *J. Appl. Phys.*, 58(7):2487–2491, October 1985.

[22] New Wave Research, 47613 Warm Springs Blvd., Fremont, CA 94539. *Operator's Manual New Wave Research Orion Air Cooled Nd:Yag Laser System*, April 2003.

[23] R. W. Perry and A. Kantrowitz. The production and stability of converging shock waves. *J. Appl. Phys*, 22:878–886, 1951.

[24] R. A. Roig and I. I. Glass. Spectroscopic study of combustion-driven implosions. *Phys. Fluids.*, 20(10):1651–1656, October 1977.

[25] T. Saito and I. I. Glass. Temperature measurements at an implosion focus. *Proc. R. Soc. Lond.*, A 384:217–231, 1982.

[26] V. Q. Vuong and A. J. Szeri. Sonoluminescence and diffusive transport. *Phys. Fluids.*, 8(9):2354–2364, September 1996.

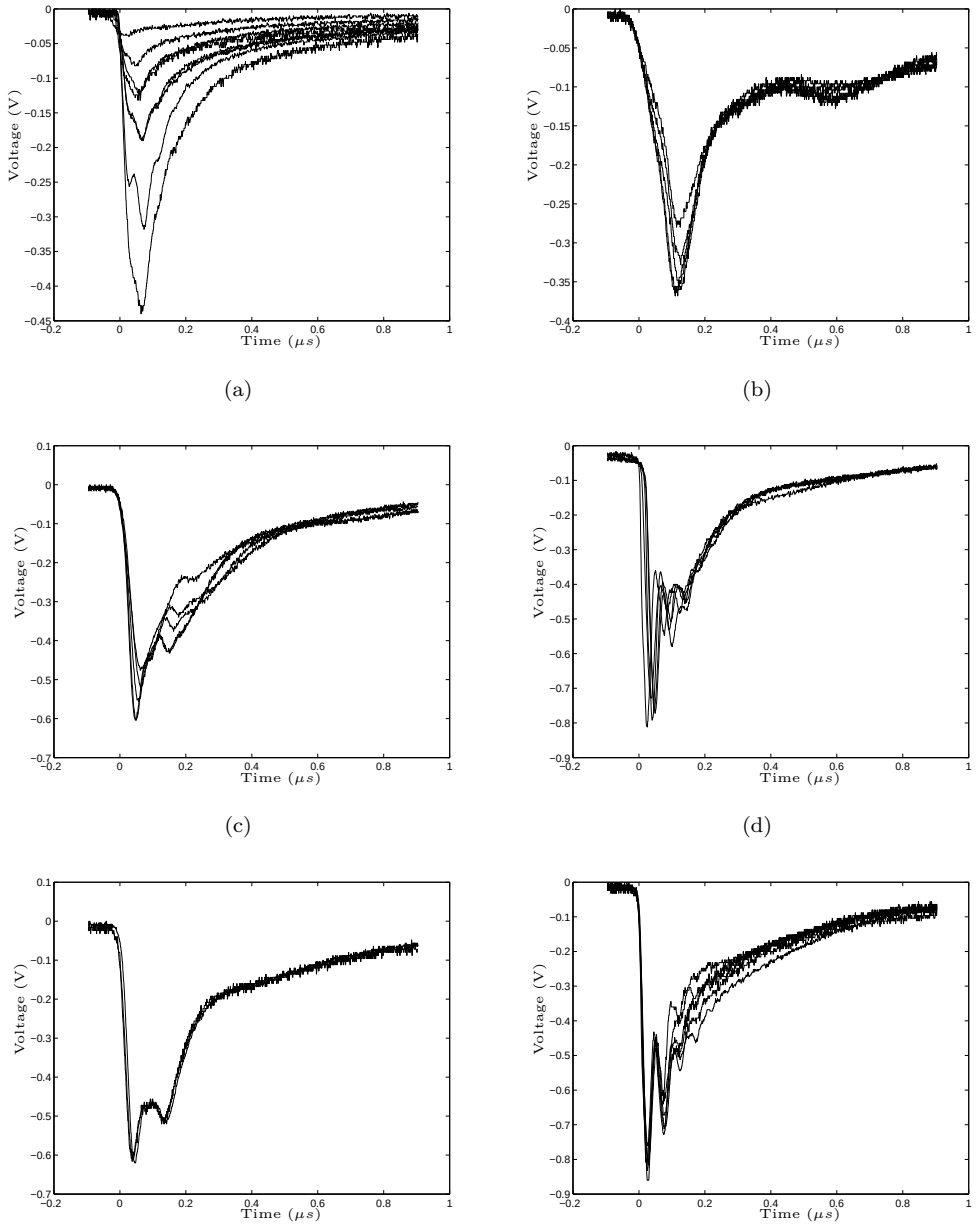

Figure 6: PM-tube signals for the various cases, (a) circle with 6BL-filter, (b) one obstacle, (c) three obstacles, (d) four obstacles, (e) heptagon and in (f) octagon.

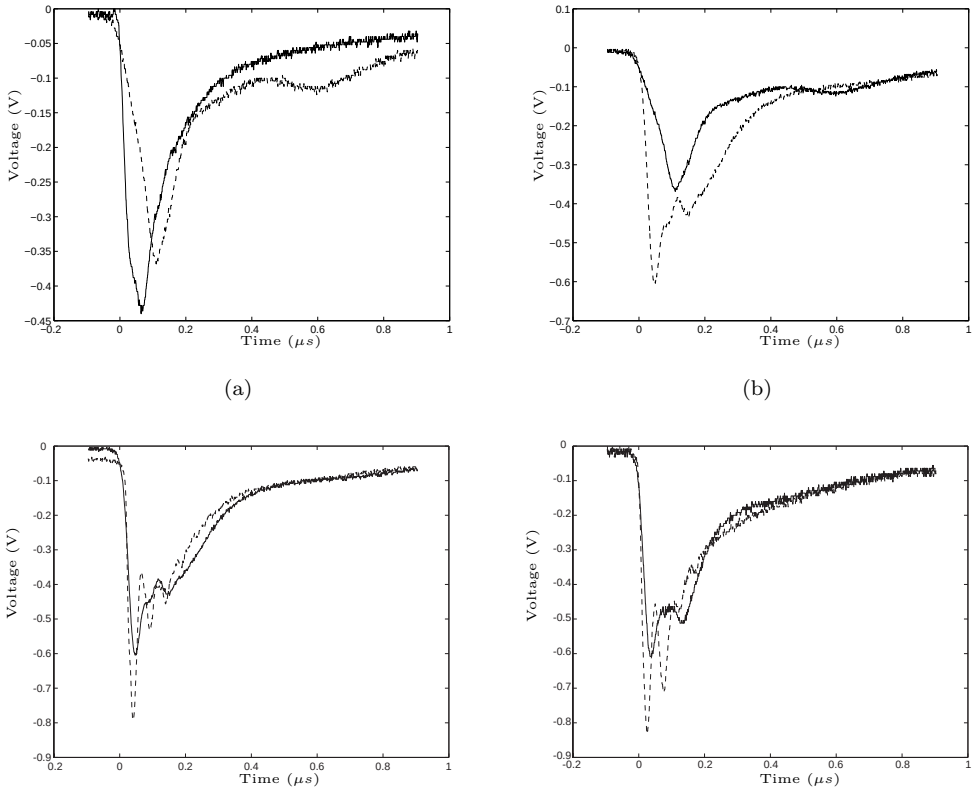

Figure 7: Comparison of PM-tube signals for the various cases, (a) circle with a 6BL-filter (solid) vs one cylinder (dashed), (b) one (solid) vs three cylinders (dashed), (c) three (solid) vs four cylinders (dashed), (d) heptagon (solid) vs octagon (dashed).

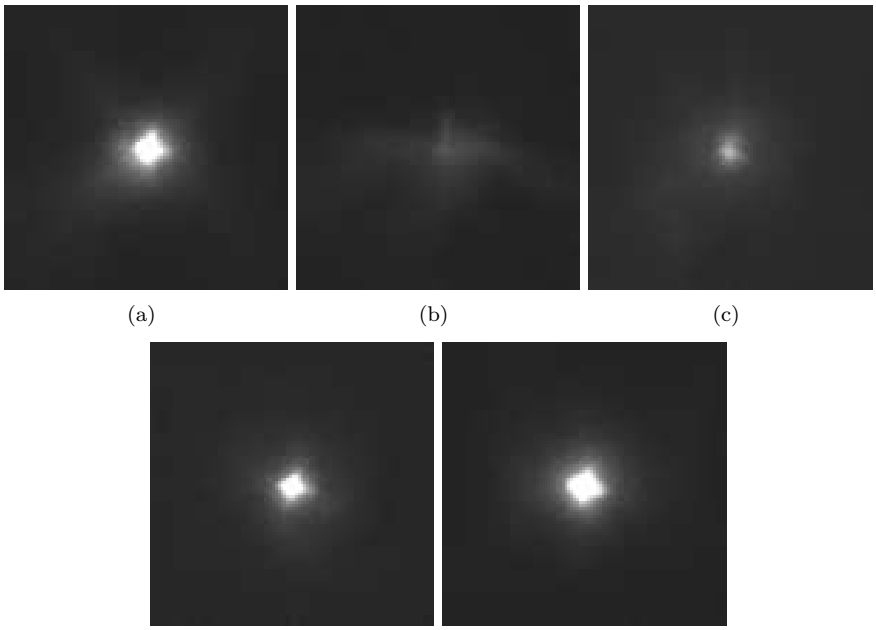

Figure 8: Photographs from the CCD camera showing the light emission for the different cases, (a) circle, (b) one cylinder, (c) three cylinders, (d) four cylinders and in (e) an octagon. The test gas is argon.

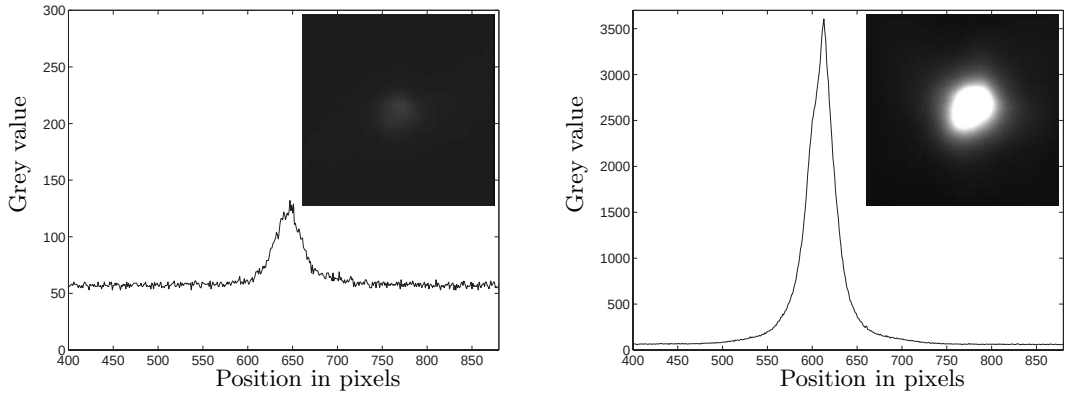

(a) (b)

Figure 9: Comparison between light emission from (a) air and (b) argon in the low pressure channel. The octagonal outer boundary is used. Note that the scaling for the y-axis in (a) and (b) are different.

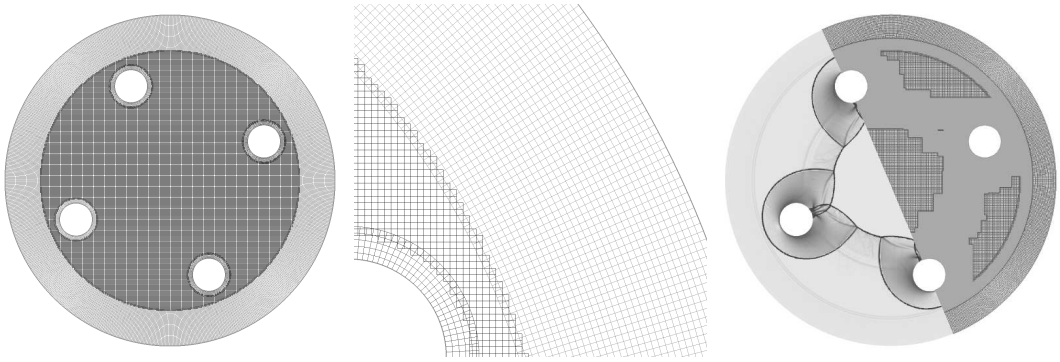

(a) (b) (c)

Figure 10: The initial grid used for the case with four cylinders, (a) the whole grid consisting of six different sub grids and (b) a close-up of an edge of one of the cylinders and the surrounding grids. (c) A plot at a later time showing the AMR grids and the corresponding schlieren plot.

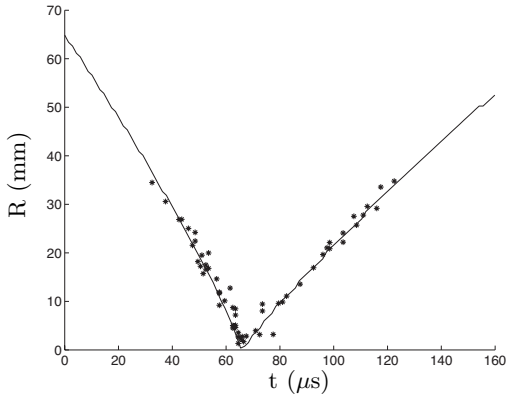

Figure 11: A comparison between experiments and simulations on radius as a function of time for the circular case. The initial Mach number for the simulation is set to 2.4, so as to begin with an initial condition that allows for comparison with the experimental results.

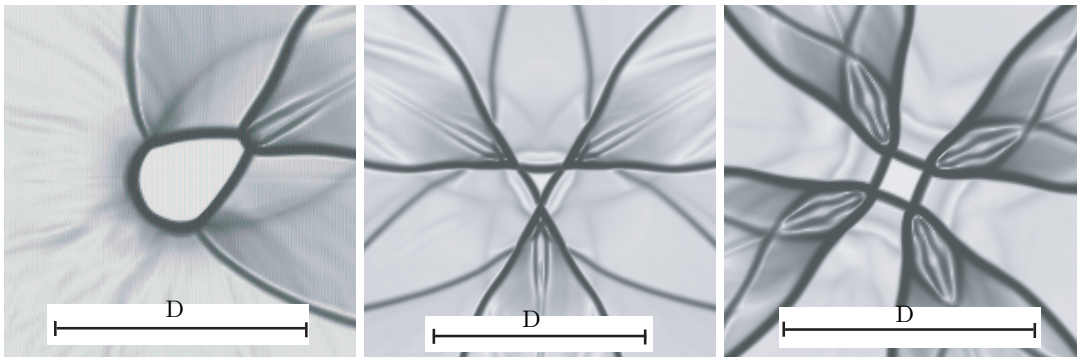

(a) (b) (c)

Figure 12: Schlieren images from simulations in Overture showing shock waves close to the center of convergence for different shapes (a) one cylinder, (c) three cylinders and (d) four cylinders. The diameter, D, of the cylindrical obstacle is indicated in the figures.

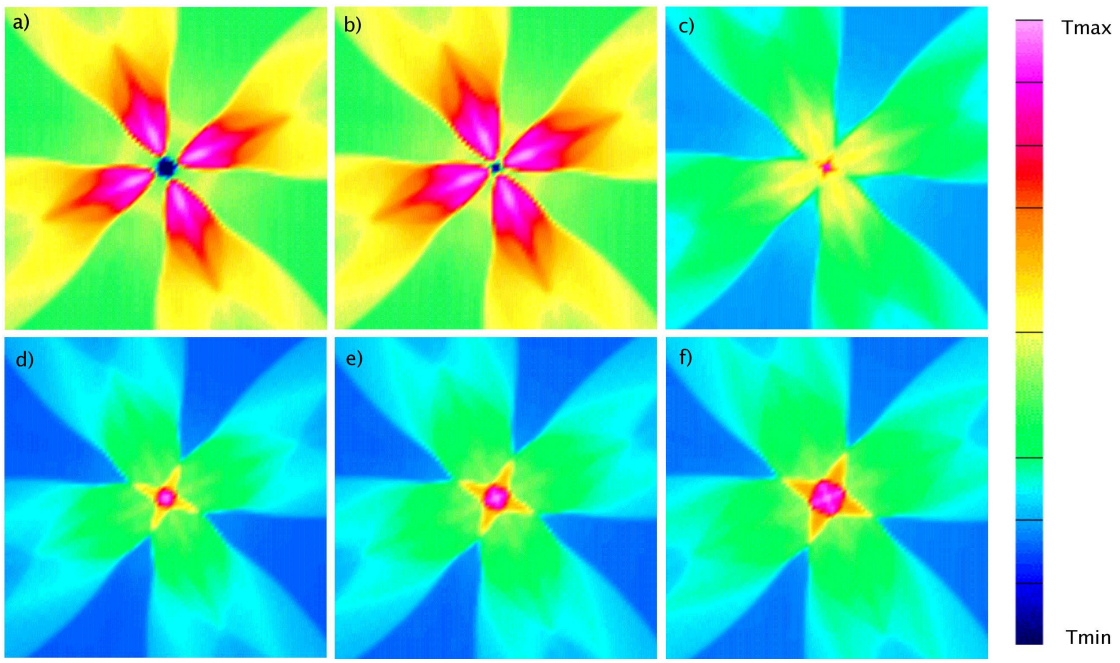

Figure 13: Temperature distribution in a 2 mm x 2 mm square for the four cylinder case during the collapse of the shock wave. The normalized maximum temperatures are (a) $T_{max} = 4.0$, (b) $T_{max} = 3.9$, (c) $T_{max} = 6.5$, (d) $T_{max} = 7.7$, (e) $T_{max} = 7.4$ and (f) $T_{max} = 7.1$.

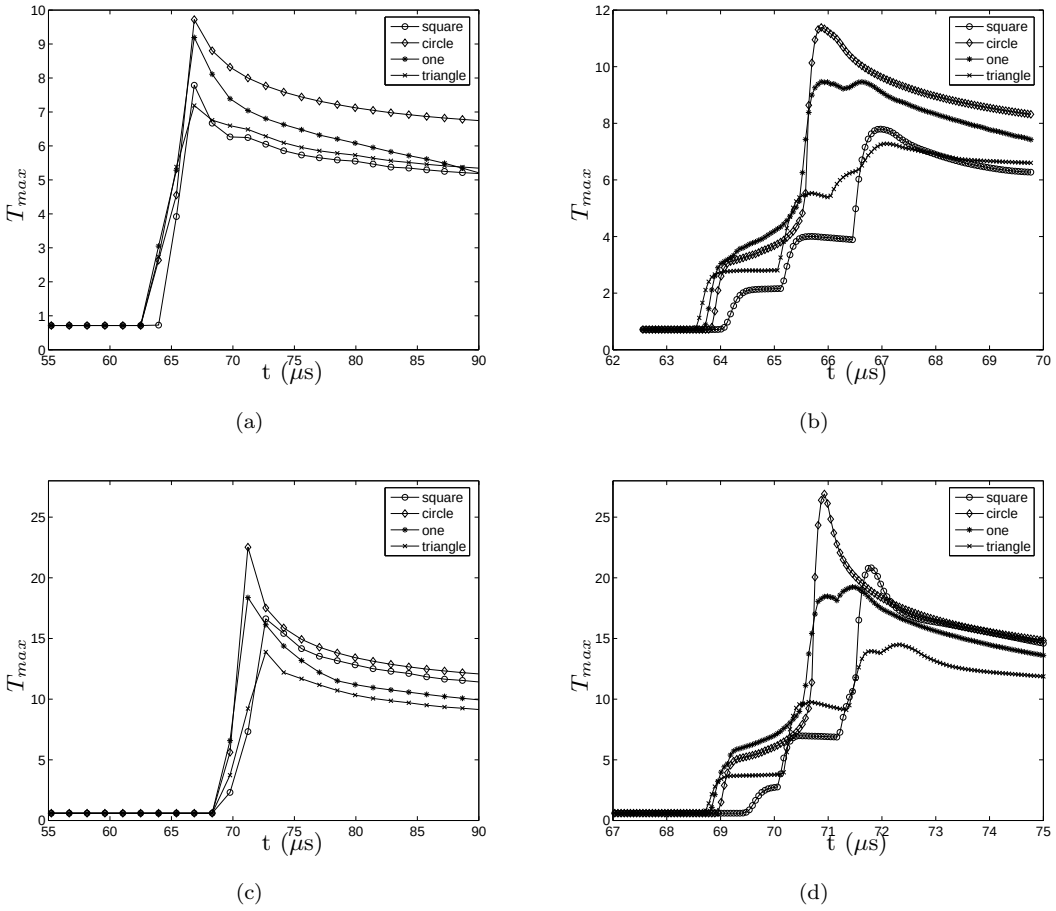

Figure 14: The maximum temperature in each time step in a 2 mm x 2 mm square region (a) a long and (b) a short time scale for air, (c) a long time and (d) a short time scale for argon.

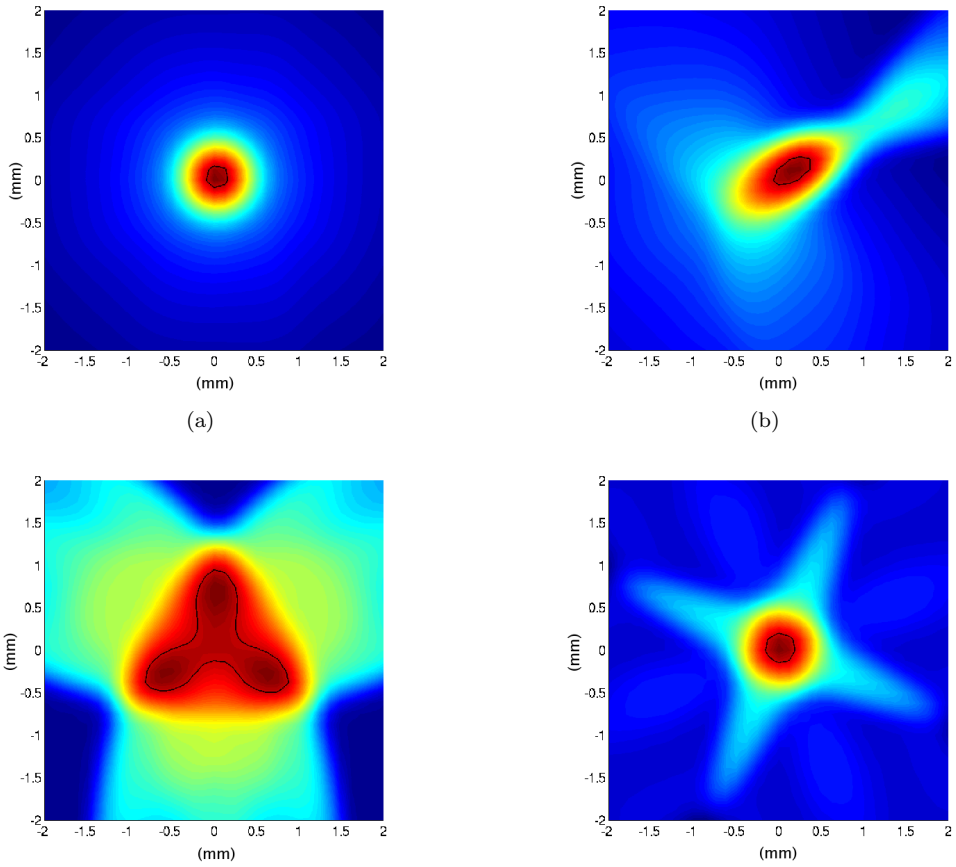

Figure 15: Maximum temperature, in non-dimensional units, for the (a) circular case, $T_{max} = 11.4$ (b) one cylinder case, $T_{max} = 9.5$ (c) three cylinder case, $T_{max} = 7.3$ and (d) four cylinder case $T_{max} = 7.8$. The region is a 2 mm x 2 mm square. The contours show the region with 95% of the maximum temperature.

Paper 6

6

On cylindrically converging shock waves shaped by obstacles

Veronica Eliasson,[1,2,*] William D. Henshaw,[3] and Daniel Appelö[3,†]

[1] *KTH Mechanics, KTH, SE-100 44 Stockholm, Sweden*
[2] *Department of Mechanical Engineering, University of California, Berkeley, CA 94720, USA*
[3] *Lawrence Livermore National Laboratory, Livermore, CA 94551 USA*

Motivated by recent experiments, numerical simulations were performed of cylindrically converging shock waves. The converging shocks impinged upon a set of zero to sixteen regularly space obstacles. For more than two obstacles the resulting diffracted shock fronts formed polygonal shaped patterns near the point of focus. The maximum pressure and temperature as a function of number of obstacles were studied. The self-similar behavior of cylindrical, triangular and square-shaped shocks were also investigated.

PACS numbers: 47.10.ab,47.40Nm

I. INTRODUCTION

Converging shock waves can be found in a broad range of situations, from astronomical size events like supernovae collapse, to microscopic events such as sonoluminescence when tiny bubbles collapse so strongly as to produce light. Shock waves are an effective method to generate high temperatures and pressures for experimental and engineering purposes and thus remain an area of continued research.

Over the years many experiments have been performed on cylindrically converging shock waves; see e.g. [1, 2]. It is common to use annular shock tubes to create and study converging shock waves. The converging shocks are often visualized by either schlieren photographs or interferograms taken during the focusing process. These methods give a measure of the shock position and shape development as a function of time. With these techniques, it is not possible to measure other quantities, like temperatures and pressures. In a recent paper [3] Eliasson et al. presented experimental results on the light emission occurring at the focal point for converging shock waves of different shapes. By analyzing the response from a photo mulitplier tube, Eliasson et al. found that the amount of emitted light depended on the shape of the converging shock wave. In [3] only a small number of obstacles were considered which resulted in polygons with a few number of sides.

In this paper we present numerical simulations of the experimental setup used in [3]. We consider cylindrically converging shock waves shaped by zero to sixteen obstacles, yielding seventeen different configurations. From monitoring the maximum pressure and temperature as the shocks converge, we find that a low number of obstacles gives a low maximum pressure and temperature, compared to the case with no obstacles. This is consistent with the amount of light observed in [3] for 0,1,3 and 4 obstacles. However, as we increase the number of obstacles we see a gradual increase in the maximum pressure and temperature; this is somewhat surprising since a greater portion of the initial cylindrical shock is reflected by the obstacles. The present model, the Euler equations for an ideal gas, does not take real gas and ionization effects into account, thus it is not possible to make detailed predictions on light production. Our numerical results suggest that further experiments for more than four obstacles would be of great interest.

Converging shock waves of different polygonal shapes have been studied for example in [4, 5]. For a polygonal shock the regions of high curvature, such as corners, generally travel faster than the planar parts. This leads to a reconfiguration of the shape of the shock wave during the focusing process. For example, a square-shaped shock wave will transform into an octagon and then back to a square again. This process repeats as the shock focuses provided there are no other disturbances to interrupt it.

In this work, we use the method suggested and tested in experiments by Eliasson et al. ,[4], to produce converging polygonal shock waves. The numerical simulations were performed using a state of the art adaptive mesh refinement (AMR) flow solver. Disturbances in the form of cylindrical obstacles were introduced in front of an initially cylindrical converging shock. The obstacles used to shape the shock are not small. Therefore it takes some time for the shock front to reach the asymptotic state described by the theory of Schwendeman and Whitham, [5]. From our highly resolved numerical simulations we find that, only at the very final stage of the convergence, a shock perturbed by four obstacles becomes square-shaped. At this stage, the mean radius of the shock is well described by Guderley's, [6], self-similar solution, giving a base solution around which geometrical shock dynamics, [5], can be utilized. The fact that the polygonal shape of the shock is attained only at the final stage, where characteristic length scales (the sides of the polygon) are very small compared to the initial scales (the diameter of initial shock), means that the numerical simulations become quite challenging.

*Electronic address: veronica@mech.kth.se

†This work was performed under the auspices of the U.S. Department of Energy by University of California, Lawrence Livermore National Laboratory under Contract W-7405-Eng-48.

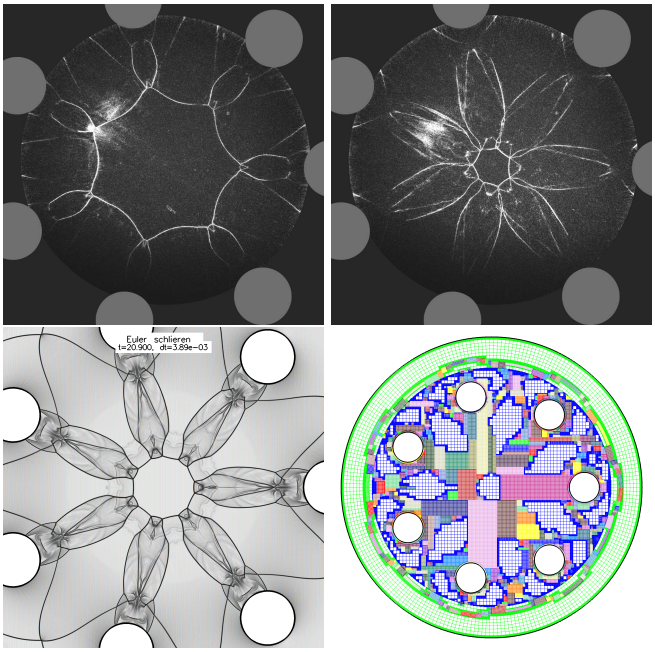

FIG. 1: Experimental and numerical schlieren photographs of a converging polygonal shock wave. Top: experimental results for seven obstacles. Lower left: numerical results. Lower right: An AMR grid with two levels of refinement adapted to the shock structures (every 8th line is plotted).

II. NUMERICAL METHOD

The Euler equations of gas dynamics are solved numerically using using a high-order accurate Godunov method, [7, 8]. The geometry is discretized with overlapping structured grids. Adaptive mesh refinement is used to dynamically track the shocks and contacts. The software, along with references describing the approach can be found at www.llnl.gov/casc/Overture.

III. NUMERICAL EXPERIMENTS

The initial conditions in front of the shock are set to be a gas at pressure $p = 13.33$ kPa (100 torr) and at room temperature $T = 294$ K, where $\gamma = 1.4$, $R_g = 287.06$ J/KgK and $p = \rho R_g T$. The shock front is given an initial shock Mach number of $M = 2.4$. The state behind the shock is determined by the standard shock relations. The diameter of the computational domain is set to 150 mm.

The following cases were simulated: an initially cylindrical shock wave perturbed by 0-16 obstacles (cylinders with a diameter of 15 mm) placed in a symmetrical pattern at a radial distance of 46.25 mm from the focal point, see Figure 1. The boundary conditions on the cylinders are modeled by slip wall conditions. Supersonic outflow boundary conditions are imposed at the perimeter of the computational domain.

In a first set of simulations we compute solutions with

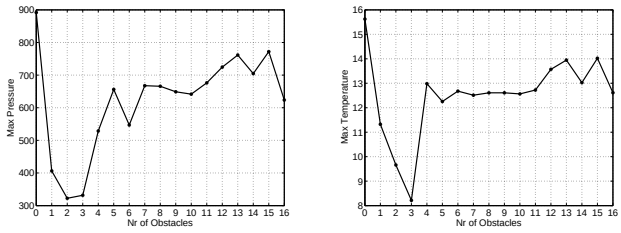

FIG. 2: Maximum pressure and temperature near the focal point as a function of the number of cylinders.

0–16 obstacles to study how quantities like the maximum pressure and temperature vary with the number of obstacles. For these computations the initial grid is composed of a Cartesian background grid (covering most of the domain), an annular perimeter grid and embedded cylindrical grids around each obstacle. The annular grids have a cell size adjusted to the (non-refined) Cartesian grid which has a grid-spacing of 0.2 mm. We use two levels of AMR with a refinement ratio of four yielding a smallest grid size of 50 μm.

In a second set of experiments, we use an initial grid with a Cartesian grid-spacing of 0.5 mm but with four levels of AMR with refinement ratio four, yielding a smallest grid size of 7.8125 μm. With this setup, we limit our simulations to the cases with 0, 3 and 4 obstacles and focus on the asymptotic behavior of the converging shocks.

A. Maximum pressure and temperature as a function of the number of cylinders

The pressure and temperature near the focal point were measured for all seventeen cases. Figure 2 shows the maximum pressure and temperature as a function of the number of cylinders. Figure 7 shows the numerically computed schlieren images for some of these cases. The results show that the undisturbed cylindrical shock gives the highest pressure and temperature near the focal point. This should be expected, since in all other cases, part of the flow is reflected by the obstacles and never reaches the focal point. For a low number of cylinders, 1–6, the maximum values are low. This is most likely caused by the fact that all parts of the shock front do not reach the focal point at the same time and hence the focusing effect is lost, see Figure 7. Higher pressure and temperatures are obtained for the cases with a larger number of obstacles, 7-13.

B. Comparison to Guderley's self-similar solution

Guderley, [6], derived a self-similar solution for the radius of the converging shock wave as a function of time,

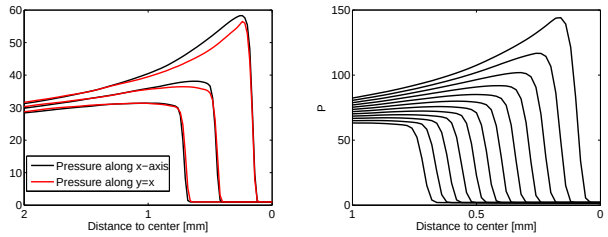

FIG. 3: The case with zero obstacles. Left: the solution along the neg. x axis and the line $y = x$, $x > 0$, at times 22.28, 22.38, 22.48. The difference between the solutions increases as the shock sharpens up. Right: the value of the pressure averaged along the pos. and neg. x and y axes at times $22.34 - 22.56$ with time spacing 0.02. Note that the shock is accelerating.

which can be expressed as

$$R = \xi_0 \left(t_c - t\right)^{\alpha}. \tag{1}$$

Here α is the self-similar power law exponent, R is the radius of the converging shock wave, t is the time, t_c is the time when the shock wave arrives at the center of convergence and ξ_0 is a constant. Guderley found the self-similar power law exponent for cylindrical shock waves to be $\alpha = 0.834$ and this has been confirmed by many other investigations, see Table I.

In this study, we investigate when the converging shocks shaped by obstacles are described by Guderely's solution. We fit data from the numerical experiments to equation (1) in order to find the similarity exponent, α. We do this for the three cases of a cylinder, a triangle and a square-shaped shock.

Zero Obstacles. To test the accuracy of the numerical algorithms we first consider an unperturbed converging shock and extract the distance between the shock front and the focal point. Starting at time 20 we save solutions every 0.02 time units until time 22.46. For each of the saved solutions we find the position along rays starting at the focal point, where the pressure is half of its global maximum. Precisely, we use rays along the positive and negative x and y axis and the four diagonals in between. We fit the extracted data to equation (1) by minimizing $\sum_i |R(t_i) - \xi_0 \left(t_c - t_i\right)^{\alpha}|^2$, thus finding α, t_c and ξ_0. Here $R(t_i)$ is taken as the average of the data from the eight rays at time t_i. The value of the self-similar power law exponent, $\alpha = 0.844$, agrees well with other values in the literature, see Table I. Note that for the rays used here, the anisotropy in the solution due to grid effects is largest (see Figure 3), thus the errors in the results obtained using these values are likely maximized.

Three Obstacles. The triangular shape was generated by placing three obstacles in an equilateral triangular pattern. Close to the focal point, the shock wave assumes a triangular shape and the similarity exponent can be found. The shock front just before the triangular shape appears is shown in Figure 4 (a)-(b). The

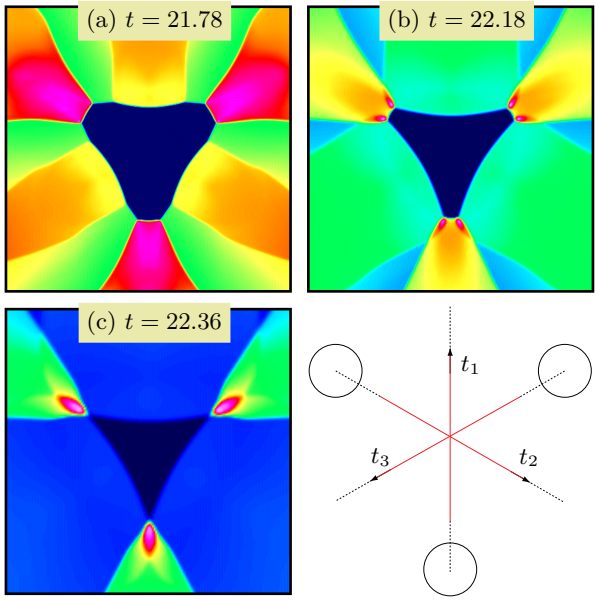

FIG. 4: Contours of the pressure for three obstacles showing the formation of the triangular converging shock.

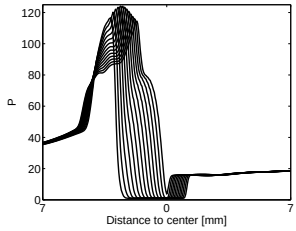

FIG. 5: The value of the pressure with three obstacles averaged along the lines t_1, t_2, t_3, of Figure 4. The solutions are displayed at times $22.28 - 22.5$ with time spacing 0.02. The solution to the left of the origin corresponds to the part of the lines t_1, t_2, t_3 closest to the obstacles.

plane sides develop as soon as the reflected part of the shock, originating from the reflection off the cylinder, has passed the whole side of the triangle. In Figure 4 (a) the reflected shock is still interacting with the sides of the triangle. In (b), the reflected shocks have passed the sides of the triangle and in (c) a triangle-shaped shock is observed. Once the triangle-shaped shock has formed, it remains for the duration of the focusing process since the plane sides undergo regular reflection,this is consistent with results in [9].

For this experiment the self-similar exponent was computed from solution data along the three lines shown in Figure 4 (d). The pressure, averaged along the three lines, is plotted in Figure 5. Referring to Figure 5, there is a significant difference in the profile of the pressure in the regions to the left and right of the focal point at the origin; we therefore make two fits to the data. Using the averaged values of the solutions at times 22.34 to 22.56 we get a self-similar exponent $\alpha = 1.155$ for the data to the left and $\alpha = 0.977$ to the data on the right. The

fact the similarity exponent is not exactly equal to unity probably results from the sides not being perfectly plane until the very last stages of the focusing process (see, Figure 4 (c)).

Four Obstacles. A square-shaped shock was obtained by perturbing a cylindrical shock with four obstacles placed in a square formation, see Figure 6. A square-shaped shock undergoes Mach reflection if the shock Mach number is larger than 1.24, [9], as is the case here. This means that when two plane sides meet in a corner, a new shock (Mach stem) is created. The Mach stem travels faster than the adjacent plane sides and will consume these; repeating for the rest of the focusing process. In the present setup, the Mach stem will form along the lines s_2 and s_4 (see Figure 6 (d)) and expand outwards towards the lines s_1 and s_3. When adjacent stems meet the square has turned 45 degrees.

Because of this reconfiguration process it is impractical to detect the location of the shock along rays. Instead we compute the area of the domain where the pressure is within 5% of its quiescent state. Assuming the area to be

	Self similar exponent
Present results (zero obstacles)	0.844
Present results (four obstacles)	0.835
Guderley (1942), [6]	0.834
Butler (1954)	0.835217
Stanyukovich (1960)	0.834
Welsh (1967)	0.835323
Mishkin & Fujimoto (1978)	0.828
Nakamura (1983)	0.8342, $M_s = 4.0$
	0.8345, $M_s = 10.0$
de Neef & Nechtman* (1978)	0.835±0.003
Kleine* (1985)	0.832 + 0.028, -0.043
Takayama* (1986)	0.831 ±0.002

TABLE I: Self similarity exponents for converging cylindrical shock waves. *Experiments.

proportional to the square of the mean radius, we can use the square root of the area instead of R to find α from (1). Using solutions from the final stages, corresponding to times 21.96 to 22.7 (with a time step of 0.02), we obtain a self-similar exponent $\alpha = 0.835$. This in agreement with the theory in [5].

It should be noted that in general the computed value of the self-similar exponent depends slightly on the data set used. In particular for the case of four obstacles, there is a tendency for the computed value of α to be somewhat larger when solutions at earlier times are included.

IV. CONCLUSIONS

The shape of the shock front and the diffraction pattern behind the shock in the numerical simulations agree well with the experimental results in [4]. The maximum pressure and temperature near the focal point were computed using 0–16 cylindrical obstacles. The highest maximum pressure and temperature occurred with zero obstacles. With a small number of obstacles, 1–6, the maximum pressure and temperature were lower than with a large number of obstacles, 7–16. During the final stages of the focusing process, a self-similar solution is obtained for the triangular and the square-shaped shock. The triangle-shaped shock undergoes regular reflection and the same shape remains during the focusing process. For the triangle, the self-similar exponent depends on the direction in which the location of the shock front is measured. For the two directions measured here, the exponents were $\alpha = 0.977$ and $\alpha = 1.155$, compared to the expected value of one. The square-shaped shock undergoes Mach reflection and the self-similar exponent was found to be $\alpha = 0.835$ in agreement with other published results.

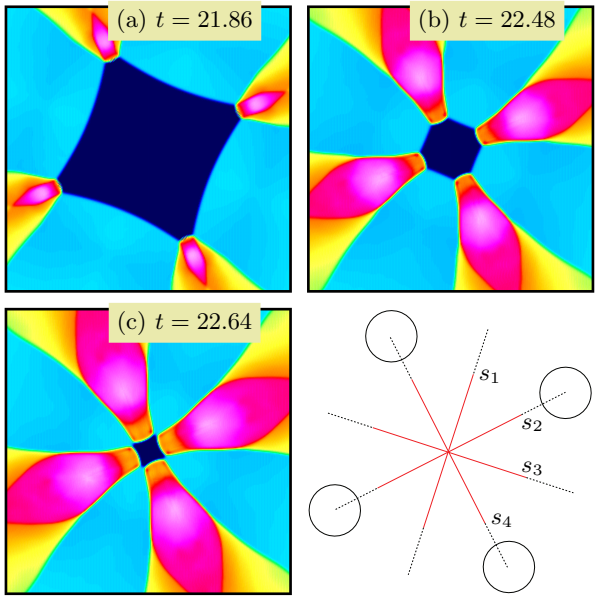

FIG. 6: Contours of the pressure for four obstacles. The square shaped shock front periodically reforms, rotated by 45 degrees.

Acknowledgments

V.E. thank Prof. A.J. Szeri at the Department of Mechanical Engineering, University of California, Berkeley, for hosting her visit and providing computational resources. The work of V.E. was supported by KTH Mechanics, Stiftelsens Bengt Ingeströms Stipendiefond and Helge Ax:son Johnsons Stiftelse. The authors acknowledge valuable discussions with Prof. D.W. Schwendeman.

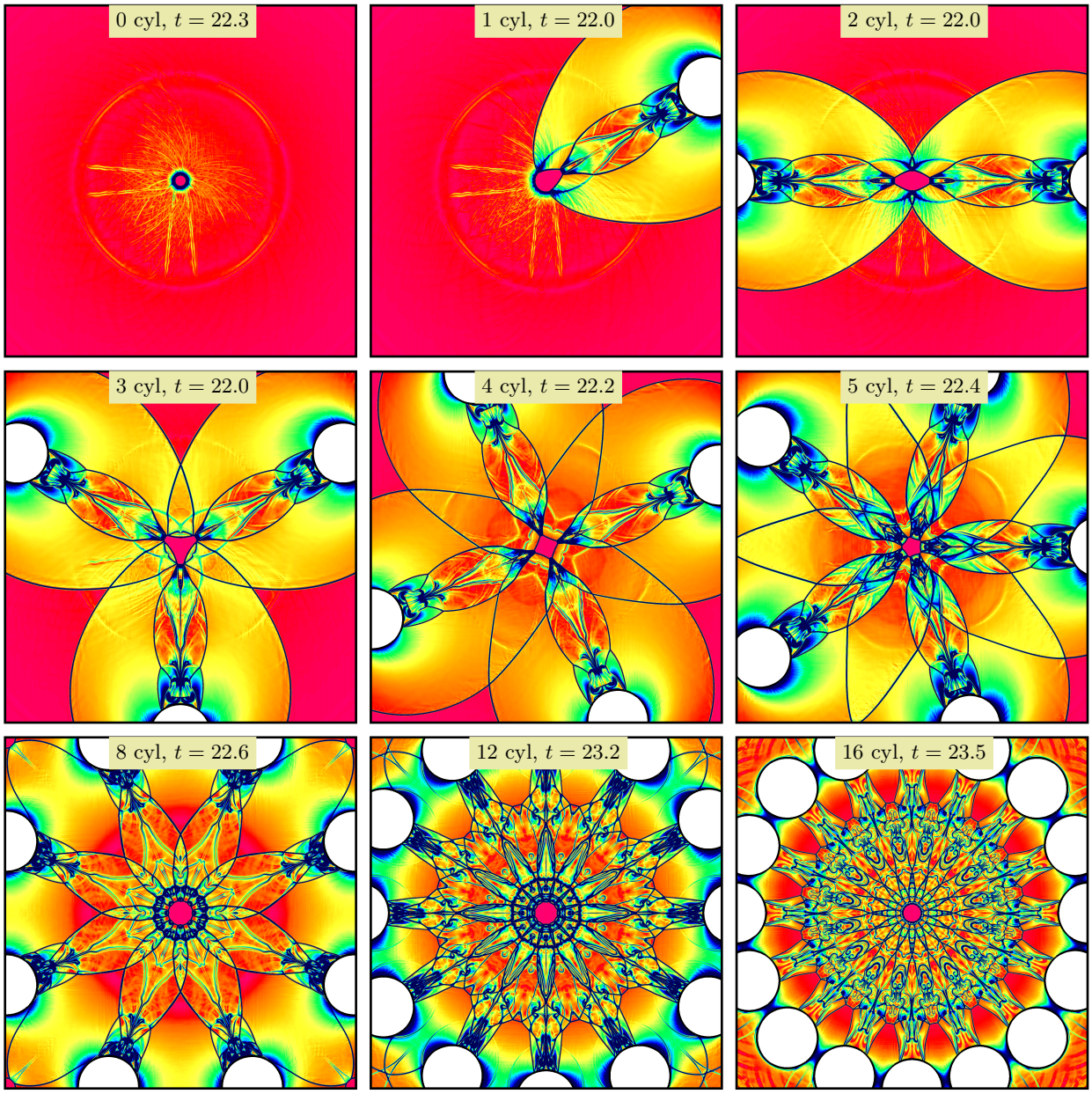

FIG. 7: Numerically computed schlieren images for a converging shock diffracted by 0, 1, 2, 3, 4, 5, 8, 12 and 16 cylindrical obstacles. The dominant portion of the shock is located near the focal point. This part of the shock front is far from circular in cases 1–5, whereas it is close to circular in cases 8–16.

[1] K. Takayama, H. Kleine, and H. Grönig, Exp. Fluids **5**, 315 (1987).

[2] M. Watanabe, O. Onodera, and K. Takayama, Shock Waves @ Marseille IV (1995).

[3] V. Eliasson, N. Apazidis, N. Tillmark, and A. J. Szeri, Submitted to Physics of Fluids (2007).

[4] V. Eliasson, N. Apazidis, N. Tillmark, and M. B. Lesser, Shock waves **15**, 205 (2006).

[5] D. W. Schwendeman and G. B. Whitham, Proc. R. Soc. Lond. A **A413**, 297 (1987).

[6] G. Guderley, Luftfahrt Forsch **19**, 302 (1942).

[7] W. D. Henshaw and D. W. Schwendeman, J. Comput. Phys. **191**, 420 (2003).

[8] W. D. Henshaw and D. W. Schwendeman, J. Comput. Phys. **216**, 744 (2006), ISSN 0021-9991.

[9] S. I. Betelu and D. G. Aronson, Phys. Rev. Lett. **87**, 074501 (2001).